

**STATIC BUCKLING AND FREE
VIBRATION BEHAVIOUR OF SKEW
MAGNETO-ELECTRO-ELASTIC
PLATES**

Thesis

Submitted in partial fulfilment of the requirements for the degree
of

DOCTOR OF PHILOSOPHY

by

KIRAN M. C.



**DEPARTMENT OF MECHANICAL ENGINEERING
NATIONAL INSTITUTE OF TECHNOLOGY
KARNATAKA
SURATHKAL, MANGALORE-575025
September, 2018**

DECLARATION

I hereby declare that the Research Thesis entitled “**STATIC BUCKLING AND FREE VIBRATION BEHAVIOUR OF SKEW MAGNETO-ELECTRO-ELASTIC PLATES**” which is being submitted to the **National Institute of Technology Karnataka, Surathkal** in partial fulfilment of the requirements for the award of the degree of **Doctor of Philosophy** in **Department of Mechanical Engineering** is a *bonafide report of the research work carried out by me*. The material contained in this Research Thesis has not been submitted to any other Universities or Institutes for the award of any degree.

Register Number: **155107 ME15F05**

Name of the Research Scholar: **KIRAN M. C.**

Signature of the Research Scholar:

Department of Mechanical Engineering

Place: NITK-Surathkal

Date:

C E R T I F I C A T E

This is to certify that the Research Thesis entitled “**STATIC BUCKLING AND FREE VIBRATION BEHAVIOUR OF SKEW MAGNETO-ELECTRO-ELASTIC PLATES**” submitted by **Mr. KIRAN M. C. (Register Number: 155107-ME15F05)** as the record of the research work carried out by him, *is accepted as the Research Thesis submission* in partial fulfilment of the requirements for the award of the degree of **Doctor of Philosophy**.

Dr. Subhaschandra Kattimani

Research Guide

Date:

Chairman-DRPC

Date:

ACKNOWLEDGEMENT

Foremost, I would like to express my sincere gratitude to my advisor Dr. Subhaschandra Kattimani, Associate Professor, Department of Mechanical Engineering, National Institute of Technology Karnataka (N.I.T.K), Surathkal, for the continuous support of my Ph.D. study and research, for his patience, motivation, enthusiasm, and immense knowledge. His guidance helped me in all the time of research and writing of this thesis. His vast knowledge and insight into the area of smart composites have helped me to overcome the hurdles throughout my dissertation. I could not have imagined having a better advisor and mentor for my Ph.D. study. For all this I will remain grateful to him throughout my career.

Besides my advisor, I would like to thank the research progress assessment committee: Dr. P. Jeyaraj, Associate Professor, Department of Mechanical Engineering, N.I.T.K., Surathkal, and Dr. H. Ramesh, Associate Professor, Department of Applied Mechanics, N.I.T.K., Surathkal, for their encouragement and insightful comments.

I would also extend my sincerest gratitude to Dr. S. Narendranath, Professor and Head, Mechanical Engineering Department, National Institute of Technology Karnataka (N.I.T.K), Surathkal, for all the support provided throughout the duration of the stay at the Institute.

I thank my fellow mates in Mechanical engineering department NITK: Vinyas, Permi Jagadeesh and Chetan for all the technical discussions and fun we have had in the last three years. Also I thank my friends outside the research domain: Raghavendra, Rachana, Srividya, Shivadarshan, Pradeep Kumar, Sanjay Patil, Sanjay

Shantaram, Praveen, Tejas, Chaitanya and Srinidhi for their constant motivation and support. I would also like to thank Dr. S. N. Omkar, Chief Research Scientist, Aerospace Department, Indian Institute of Science, Bengaluru, for enlightening me the first glance of research. In addition, I take this opportunity to thank the Science and Engineering Research Board, Department of Science and Technology, Government of India, for funding my visit to Wuhan, China, to attend the conference and present a part of my research work. Further, I extend my sincerest gratitude to Prof. K. N. Shantharam, Kuvempu University, Karnataka, for his suggestions towards the English language correction of this thesis.

Furthermore, I extend my devotion to his holiness Dr. Shree Jagadguru Prasanna Renuka Veera Someshwara Shivacharya Swamiji, Rambhapuri Peetha, Balehonnuru for his blessings throughout the journey of my life.

Last but not the least; I would like to thank my family: my parents Gowramma R and Chidananda Murthy, for giving birth to me at the first place and supporting me spiritually throughout my life.

Kiran M. C.

National Institute of Technology Karnataka, Surathkal

Date:

ABSTRACT

This dissertation comprises the investigation on structural characteristics of skew magneto-electro-elastic (SMEE) plates through static, buckling, and free vibration analysis. Magneto-electro-elastic plates with multilayered and functionally graded types are considered for the analysis. The numerical analysis is performed by developing a finite element model based on the coupled constitutive equations and shear deformation theories. A transformation matrix is developed to account for the skew edges introduced as a geometrical change, and utilized to specify boundary conditions on the skew edges. Influence of boundary conditions and material stacking sequences on the displacement, stresses, buckling load, and natural frequency of the SMEE plates has been investigated. Particular emphasis has been placed to study the effect of skew angles and aspect ratios on the stresses, electric displacement, magnetic induction, and natural frequencies. The present study reveals that the skew angle and the aspect ratio significantly influence the structural behaviour of the SMEE plates.

The buckling behaviour of multilayered SMEE plate under uniaxial and biaxial in-plane loading is investigated. The in-plane stress distribution within the SMEE plate due to the enacted force is considered to be equivalent to the applied in-plane compressive loads in the pre-buckling range and the same stress distribution is used to derive the potential energy functional of the SMEE plate. The non-dimensional critical buckling load is attained from the solution of the allied linear eigenvalue problem. Influence of skew angle, stacking sequence, span to thickness ratio, aspect ratio and boundary conditions on the critical buckling load and their corresponding mode shapes has been investigated comprehensively.

Further, the finite element formulation is extended to assess the static response and free vibration characteristics of a functionally graded skew magneto-electro-elastic (FGSMEE) plate. The material grading of FSMEE plate is considered across the thickness using power law distribution. The influence of skew angle on the primary quantities such as displacements, electric potential, and magnetic potential, and secondary quantities such as stresses, electric displacement, and magnetic

induction is studied in detail. In addition, the effect of power-law gradient, thickness ratio, boundary conditions, and aspect ratio on the static response and free vibration characteristics of FGSMEE plate has been investigated.

The major defect encountered in the preparation of functionally graded structures is porosity. Hence, the influence of porosity on the static responses and free vibration of functionally graded rectangular and skew magneto-electro-elastic plate is also considered for the investigation. The porosity in the FG material is accounted as local density using modified power law. The displacements, potentials, and stresses for the porous skew plate are established through static analysis. The influence of different porosity distributions on the FGSMEE plate has also been studied. The effect of porosity volume, skew angle, and the geometrical parameters such as aspect ratio, thickness ratio, and boundary conditions on the behaviour of porous FGSMEE plate is investigated.

KEYWORDS: magneto-electro-elastic; multilayered; skew MEE plate; functionally graded.

CONTENTS

Acknowledgements	i
Abstract	iii
List of Tables.....	ix
List of Figures.....	xiii
Nomenclature.....	xix
1. Introduction and Literature review	
1.1 SMART COMPOSITE MATERIALS.....	01
1.1.1 Piezoelectric and Piezomagnetic.....	02
1.1.2 Magneto-electro-elastic Materials.....	03
1.2 Applications of MEE composites.....	05
1.3 Origin and analysis of MEE structures.....	06
1.3.1 Free vibration studies of MEE structures.....	07
1.3.2 Free vibration studies of skew composite structures.....	09
1.3.3 Static studies of MEE structures.....	10
1.3.4 Static studies of skew composite structures.....	11
1.3.5 Buckling studies of MEE structures.....	11
1.3.6 Buckling of composite and skew composite structures.....	12
1.3.7 Porosity influence on MEE structures.....	13
1.4 Scope and objective of the dissertation.....	14
1.5 Contributions from the dissertation.....	16
1.6 Overview of the dissertation by chapter.....	16

2. Static and buckling behaviour of multilayered magneto-electro-elastic plates

2.1. Introduction.....	19
2.2. Problem Description And Governing Equation.....	20
2.3 Finite Element Formulation.....	25
2.4 Results And Discussion.....	29
2.4.1 Buckling analysis.....	29
2.4.2 Validation.....	30
2.4.3 Effect of uniaxial and biaxial compression.....	31
2.4.4 Effect of stacking sequence.....	32
2.4.5 Effect of lateral load parameter.....	34
2.4.6 Effect of aspect ratio (a/b).....	34
2.4.7 Effect of span to thickness (a/h) ratio.....	37
2.4.8 Effect of boundary condition.....	38
2.4.9 Static studies.....	39
2.5 Conclusions.....	42
3. Static characteristics and free vibration analysis of multilayered skew magneto-electro-elastic plates	
3.1 Introduction.....	43
3.2. Problem description and governing equation.....	44
3.2.1 Finite element formulation for skew magneto-electro-elastic plate.....	47
3.2.2 Skew boundary transformation.....	48
3.3. Results and discussions.....	50
3.3.1 Validation of present FE model.....	51
3.3.2 Free vibration analysis of skew magneto-electro-elastic plates.....	53
3.3.3 Static analysis of SMEE plates.....	57

3.3.4 Effect of geometrical parameters and stacking sequence.....	60
3.4. Conclusion.....	67
4. Buckling analysis of skew magneto-electro-elastic plates under in-plane loading	
4.1. Introduction.....	69
4.2. Problem Description And Governing Equation.....	70
4.2.1 Skew boundary transformation.....	71
4.3 Results and Discussion.....	72
4.3.1 Validation.....	72
4.3.2 Effect of skew angle on buckling load.....	73
4.3.3 Effect of uniaxial and biaxial compression.....	75
4.3.4 Effect of material stacking sequence.....	77
4.3.5 Effect of span to thickness ratio (a/h).....	79
4.3.6 Effect of aspect ratio (a/b).....	80
4.3.7 Buckling behaviour of SMEE plate through mode shapes.....	84
4.4 Conclusions.....	86
5. Static analysis and free vibration characteristics of functionally graded skew magneto-electro-elastic plate	
5.1. Introduction.....	89
5.2. Problem Description And Governing Equation.....	90
5.3. Results And Discussion.....	92
5.3.1 Validation studies.....	93
5.3.2 Free vibration of FGSME plate.....	94
5.3.3 Static analysis of FGSME plates.....	95
5.4. Conclusions.....	119

6. Influence of porosity on structural behaviour of functionally graded magneto-electro-elastic plate

6.1 Introduction.....	121
6.2 Problem description.....	122
6.3 Results and discussion.....	123
6.3.1 Free vibration assessment of porous FGSMEE plate.....	123
6.3.2 Static characteristics of porous FGSMEE plate.....	132
6.4. Conclusions.....	162

7. Conclusions and future scope

7.1 Major findings.....	165
7.2 Scope for the future work.....	167

Appendix.....	169
---------------	-----

References.....	171
-----------------	-----

LIST OF TABLES

Table No.	Description	Page No.
1.1	Various constituent phases used for MEE composite.....	6
2.1	Material properties of BaTiO ₃ and CoFe ₂ O ₄	31
2.2	Non-dimensional critical buckling load for three layered composite plate under uniaxial and biaxial compression ($a/b = 1$).....	32
2.3	Critical buckling loads for B/F/B plates at different span to thickness ratio.....	37
3.1	Non-dimensional natural frequency modes for clamped B/F/B	52
3.2	Non-dimensional frequency parameter $\lambda = \omega b^2 / \pi^2 h (\rho/E_2)^{1/2}$ for the clamped laminated composite plate ($a/H = 10$).....	52
3.3	Non-dimensional frequency parameter $\lambda = \omega b^2 / \pi^2 h (\rho/E_2)^{1/2}$ for the simply supported laminated composite plate ($a/H = 10$).....	53
3.4	Normalized natural frequencies for SMEE plate ($a = 1$ m, $a = b$, $H = 0.3$ m).....	54
3.5	Normalized natural frequencies for different thickness ratio ($a = 1$ m, $a = b$, B/F/B, SSSS).....	55
3.6	Normalized natural frequencies for different thickness ratio ($a = 1$ m, $a = b$, B/F/B, CCCC).....	56
3.7	Normalized natural frequencies for different thickness ratio ($a = 1$ m, $a = b$, F/B/F, SSSS)	56
3.8	Normalized natural frequencies for different thickness ratio ($a = 1$ m, $a = b$, F/B/F, CCCC).....	57

4.1	Buckling load $\lambda_{cr} = \lambda a^2 / H^3 E_2$ for three ($0^0/90^0/0^0$) layered composite plate under in-plane load	72
4.2	Normalized natural frequencies $\bar{\omega} = \omega a \sqrt{\rho_{max} / C_{max}} / h$ of the BFB simply supported plate.....	73
4.3	Effect of skew angle on non-dimensional buckling load $\lambda_{cr} = \lambda a^2 / H^3 E_2$ for ($90^0/0^0/0^0/90^0$) cross-ply skew composite plate ($a/b = 1$; $a/h = 100$)	74
4.4	Effect of skew angle on buckling load parameter for B/F/B CCCC SMEE plate subjected to uniaxial compression ($a/b = 1$, $a/h = 100$)...	74
4.5	Effect of skew angle on buckling load parameter for B/F/B CCCF SMEE plate subjected to uniaxial compression ($a/b = 1$, $a/h = 100$) ...	75
4.6	Effect of skew angle on buckling load parameter for B/F/B FCFC SMEE plate subjected to uniaxial compression ($a/b = 1$, $a/h = 100$) ...	75
4.7	Effect of uniaxial and biaxial compression on buckling load parameter on B/F/B SMEE plate ($a/b = 1$, $a/h = 100$).....	77
4.8	Effect of thickness ratio on buckling load parameter of B/F/B CCCC SMEE plate ($a/b = 1$).....	79
4.9	Effect of thickness ratio on buckling load parameter of B/F/B CCCF SMEE plate ($a/b = 1$).....	80
4.10	Effect of to thickness ratio on buckling load parameter of B/F/B FCFC SMEE plate ($a/b = 1$).....	81
5.1	Convergence and validation studies of normalized natural frequencies of FGMEE plate.....	95
5.2	Normalized frequency parameter $\lambda = \omega b^2 / \pi^2 h (\rho/E_2)^{1/2}$ for the clamped-clamped laminated composite plate ($a/h = 10$).....	96

5.3	Normalized frequency parameter $\lambda = \omega b^2 / \pi^2 h (\rho/E_2)^{1/2}$ for the simply supported laminated composite plate ($a/h = 10$).....	97
5.4.	Skew angle influence on the natural frequency of FGSMEE plate ...	98
5.5	Influence of thickness ratio (a/h) on the natural frequency of simply supported FGSMEE plate.....	99
5.6	Influence of aspect ratio (b/a) on the natural frequency of FGSMEE plate	100
6.1	Effect of different porosity distribution on normalized natural frequencies of porous FGMEE plate.....	122
6.2	Effect of porosity factor, m on normalized natural frequencies of porous V_u FGMEE plate	122
6.3	Effect of porosity factor, m on normalized natural frequencies of porous V_o FGMEE plate	122
6.4	Effect of porosity factor, m on normalized natural frequencies of porous V_x FGMEE plate.....	123
6.5	Effect of porosity factor, m on normalized natural frequencies of porous V_v FGMEE plate	123
6.6	Effect of skew angle on natural frequency of porous FGSMEE plate (SSSS, $\eta = 0.2$, porosity factor, $m= 0.1$, $a/h=100$, $b/a = 1$).....	124
6.7	Effect of skew angle on natural frequency of porous FGSMEE plate (SSSS, $\eta = 0.5$, porosity factor, $m= 0.1$, $a/h=100$, $b/a = 1$).....	125
6.8	Effect of skew angle on natural frequency of porous FGSMEE plate (SSSS, $\eta = 2$, porosity factor, $m= 0.1$, $a/h=100$, $b/a = 1$).....	126
6.9	Effect of skew angle on natural frequency of porous FGSMEE plate (SSSS, $\eta = 5$, porosity factor, $m= 0.1$, $a/h=100$, $b/a = 1$).....	127

6.10	Effect of thickness ratio on natural frequency of porous FGSMEE plate (SSSS, $\alpha = 45^0$, $\eta = 2$, porosity factor, $m = 0.1$, $b/a = 1$).....	128
6.11	Effect of aspect ratio on natural frequency of porous FGSMEE plate (SSSS, $\alpha = 45^0$, $\eta = 2$, porosity factor, $m = 0.1$, $a/h = 100$).....	129

LIST OF FIGURES

Figure No	Description	Page No.
1.1	Magneto-electro-elastic coupling scheme	4
1.2	Multiferroic composite with piezoelectric and piezomagnetic phases... ..	6
2.1	Schematic representation of multilayered MEE plate.....	21
2.2	Schematic representation of uniaxial and biaxial compression on MEE plate.....	21
2.3	First six buckling mode shapes of B/F/B MEE plate under uniaxial and biaxial compression for CCCC boundary condition ($a/b = 1$, $a/h = 100$).....	33
2.4	Critical buckling load for B/F/B and F/B/F MEE plate subjected to uniaxial compression. (CCCC, $a/b = 1$, $a/h = 100$).....	34
2.5	First six non-dimensional critical buckling loads and mode shapes of B/F/B and F/B/F plate subjected to uniaxial compression under clamped-clamped (CCCC) boundary condition ($a/b = 1$, $a/h = 100$)... ..	35
2.6	Effect of load factor on non-dimensional critical buckling load.....	36
2.7	Effect of aspect ratio on Non-dimensional buckling load of CCCC MEE (B/F/B) plate	36
2.8	Effect of aspect ratio on Non-dimensional buckling load of CCCF MEE (B/F/B) plate.....	36
2.9	Effect of aspect ratio on non-dimensional buckling load of FCFC MEE (B/F/B) plate.....	37
2.10	Comparison of first six non-dimensional buckling mode shapes of B/F/B at a/h $= 10$ and 50 subjected to uniaxial compression under clamped-clamped (CCCC) boundary condition	38

2.11	Comparison of first six non-dimensional buckling loads and their mode shapes for different boundary condition of B/F/B MEE plate ($a/b = 1, a/h = 100$).....	39
2.12	Static deflection (in meters) of BFB MEE plate subjected to sinusoidal load.....	40
2.13	Static deflection (in meters) of FBF MEE plate subjected to sinusoidal load.....	40
2.14	Static deflection (in meters) of BFB MEE plate subjected to UDL.....	41
2.15	Static deflection (in meters) of FBF MEE plate subjected to UDL.....	41
3.1	(a) SMEE plate with B/F/B stacking (b) Top view of the SMEE plate.....	44
3.2	Transverse shear stress (τ_{xz}) across the thickness for (a) B/F/B (b) F/B/F MEE plate ($\alpha = 0$).....	55
3.3	Influence of α on (a) u (b) v (c) w (d) ϕ (e) ψ (f) σ_{xx} (g) σ_{yy} (h) τ_{xy} (i) τ_{xz} (j) D_z (k) B_z of the simply supported B/F/B SMEE plate ($a/b = 1, H = 0.3$ m).....	60
3.4	Influence of boundary condition on (a) u (b) v (c) ϕ (d) ψ (e) σ_{xx} (f) σ_{yy} (g) τ_{xy} (h) τ_{xz} (i) D_z (j) B_z of the B/F/B SMEE plate ($a/b = 1, H = 0.3$ m).....	62
3.5	Normal stress (σ_{xx}) for different thickness ratio.....	62
3.6	Normal stress (σ_{yy}) for different thickness ratio	63
3.7	In-plane shear stress (τ_{xy}) for different thickness ratio.....	64
3.8	Transverse shear stress (τ_{xz}) for different thickness ratio	64
3.9	Electric displacement (D_z) for different thickness ratio	64
3.10	Magnetic induction (B_z) for different thickness ratio	65
3.11	Influence of stacking sequence on (a) u (b) v (c) ϕ (d) ψ (e) σ_{xx} (f) σ_{yy} (g) τ_{xy} (h) τ_{xz} (i) D_z (j) B_z of the B/F/B SMEE plate ($a/b = 1, H = 0.3$ m).....	67
4.1	SMEE plate subjected to biaxial and uniaxial compression.....	70

4.2	First three buckling modes at different skew angles for CCCC SMEE plate ($a/b = 1, a/h = 100$).....	77
4.3	First three buckling modes for uniaxial and biaxial compression of CCCC SMEE plate ($a/b = 1, a/h = 100, \alpha = 45^0$).....	79
4.4	Non-dimensional buckling loads of CCCC SMEE plate subjected to uniaxial load for ($a/b = 1, a/h = 100$) B/F/B and F/B/F stacking sequence.....	83
4.5	Influence of stacking sequence on buckling mode shapes of SMEE plate at $\alpha = 30^0$ ($a/b = 1, a/h = 100$).....	83
4.6	Effect of aspect ratio on buckling load parameter ($a/h = 100$).....	84
4.7	Effect of boundary condition on buckling load parameter ($a/b = 1, a/h = 100$)...	85
4.8	First six buckling modes of SMEE plate at skew angles $\alpha = 15^0$ and $\alpha = 45^0$	86
5.1	Schematic representation of (a) Functionally graded skew MEE plate. (b) Top view of FGSMEE plate.....	91
5.2	Variation of C_{II} for different gradient index values η	93
5.3	Through thickness variation of displacement u for different skew angles at power-law values (a) $\eta = 0$ (b) $\eta = 0.2$ (c) $\eta = 0.5$ (d) $\eta = 2$ (e) $\eta = 5$	103
5.4	Through thickness variation of displacement v for different skew angles at power-law index values (a) $\eta = 0$ (b) $\eta = 0.2$ (c) $\eta = 0.5$ (d) $\eta = 2$ (e) $\eta = 5$	104
5.5	Through thickness variation of displacement w for different skew angles at power-law index values (a) $\eta = 0$ (b) $\eta = 0.2$ (c) $\eta = 0.5$ (d) $\eta = 2$ (e) $\eta = 5$	105
5.6	Through thickness variation of electric potential ϕ_z for different skew angles at power-law index values (a) $\eta = 0$ (b) $\eta = 0.2$ (c) $\eta = 0.5$ (d) $\eta = 2$ (e) $\eta = 5$	107
5.7	Through thickness variation of magnetic potential Ψ_z for different skew angles at power-law index values (a) $\eta = 0$ (b) $\eta = 0.2$ (c) $\eta = 0.5$ (d) $\eta = 2$ (e) $\eta = 5$	108

5.8	Through thickness variation of normal stress σ_{xx} for different skew angles at power-law index values (a) $\eta = 0$ (b) $\eta = 0.2$ (c) $\eta = 0.5$ (d) $\eta = 2$ (e) $\eta = 5$	109
5.9	Through thickness variation of normal stress σ_{yy} for different skew angles at power-law index values (a) $\eta = 0$ (b) $\eta = 0.2$ (c) $\eta = 0.5$ (d) $\eta = 2$ (e) $\eta = 5$	110
5.10	Through thickness variation of normal stress σ_{xy} for different skew angles at power-law index values (a) $\eta = 0$ (b) $\eta = 0.2$ (c) $\eta = 0.5$ (d) $\eta = 2$ (e) $\eta = 5$	111
5.11	Through thickness variation of shear stress τ_{xz} for different skew angles at power-law index values (a) $\eta = 0$ (b) $\eta = 0.2$ (c) $\eta = 0.5$ (d) $\eta = 2$ (e) $\eta = 5$	112
5.12	Through thickness variation of magnetic induction B_z for different skew angles at power-law index values (a) $\eta = 0$ (b) $\eta = 0.2$ (c) $\eta = 0.5$ (d) $\eta = 2$ (e) $\eta = 5$	113
5.13	Through thickness variation of electric displacement D_z for different skew angles at power-law index values (a) $\eta = 0$ (b) $\eta = 0.2$ (c) $\eta = 0.5$ (d) $\eta = 2$ (e) $\eta = 5$	114
5.14	Effect of aspect ratio (b/a) on (a) u (b) v (c) ϕ_z (d) ψ_z (e) σ_{xx} (f) σ_{yy} (g) τ_{xy} (h) τ_{xz} (i) B_z (j) D_z	116
5.15	Effect of thickness ratio (a/h) on (a) u (b) v (c) ϕ_z (d) ψ_z (e) σ_{xx} (f) σ_{yy} (g) τ_{xy} (h) τ_{xz} (i) B_z (j) D_z	118
5.16	Effect of boundary condition on (a) ϕ_z (b) ψ_z (c) B_z (d) D_z	119
6.1	Porosity distribution (a) V_u (b) V_o (c) V_x (d) V_v	123
6.2	Effect of gradient index on natural frequency of porous plate (a) V_u (b) V_o (c) V_x (d) V_v	129
6.3	Effect of porosity volume on natural frequency of porous plate	130
6.4	Effect of different porosity distribution on (a) u (b) v (c) w (d) ϕ_z (e) Ψ_z (f) σ_{xx} (g) σ_{yy} (h) σ_{xy} (i) τ_{xz} (j) B_z (k) D_z	134
6.5	Effect of porosity distribution on porous FGSME plate for u ($\eta = 2$).....	136

6.6	Effect of porosity distribution on porous FGSMEE plate for v ($\eta = 2$).....	137
6.7	Effect of porosity distribution on porous FGSMEE plate for w ($\eta = 2$).....	137
6.8	Effect of porosity distribution on porous FGSMEE plate for ϕ ($\eta = 2$)	138
6.9	Effect of porosity distribution on porous FGSMEE plate for ψ ($\eta = 2$).....	139
6.10	Effect of porosity distribution on porous FGSMEE plate for σ_{xx} ($\eta = 2$).....	139
6.11	Effect of porosity distribution on porous FGSMEE plate for σ_{yy} ($\eta = 2$).....	140
6.12	Effect of porosity distribution on porous FGSMEE plate for σ_{xy} ($\eta = 2$).....	141
6.13	Effect of porosity distribution on porous FGSMEE plate for τ_{xz} ($\eta = 2$).....	141
6.14	Effect of porosity distribution on porous FGSMEE plate for B_z ($\eta = 2$)	142
6.15	Effect of porosity distribution on porous FGSMEE plate for D_z ($\eta = 2$).....	143
6.16	Comparison of porous and non-porous plate for u displacement ($\eta = 2$; $\alpha = 45^0$)..	144
6.17	Porous and non-porous plate for v displacement ($\eta = 2$; $\alpha = 45^0$)....	144
6.18	Comparison of porous and non-porous plate for ϕ ($\eta = 2$; $\alpha = 45^0$).....	145
6.19	Comparison of porous and non-porous plate for ψ ($\eta = 2$; $\alpha = 45^0$).....	146
6.20	Comparison of porous and non-porous plate for σ_x ($\eta = 2$; $\alpha = 45^0$).....	146
6.21	Comparison of porous and non-porous plate for σ_y ($\eta = 2$; $\alpha = 45^0$).....	147
6.22	Comparison of porous and non-porous plate for σ_{xy} ($\eta = 2$; $\alpha = 45^0$)	148
6.23	Comparison of porous and non-porous plate for τ_{xz} ($\eta = 2$; $\alpha = 45^0$).....	148
6.24	Comparison of porous and non-porous plate for B_z ($\eta = 2$; $\alpha = 45^0$).....	149
6.25	Comparison of porous and non-porous plate for D_z ($\eta = 2$; $\alpha = 45^0$).....	150
6.26	Effect of aspect ratio on ($\eta = 2$; Vu ; $\alpha = 45^0$) (a) u (b) v (c) ϕ_z (d) ψ_z (e) σ_{xx} (f)	152

	σ_{yy} (g) σ_{xy} (h) τ_{xz} (i) B_z (j) D_z	
6.27	Effect of thickness ratio on ($\eta = 2$; Vu ; $\alpha = 45^0$) (a) u (b) v (c) ϕ_z (d) ψ_z (e) σ_{xx} (f) σ_{yy} (g) σ_{xy} (h) τ_{xz} (i) B_z (j) D_z	154
6.28	Effect of boundary condition on ($\eta = 2$; Vu ; $\alpha = 45^0$) (a) u (b) v (c) ϕ_z (d) ψ_z (e) σ_{xx} (f) σ_{yy} (g) σ_{xy} (h) τ_{xz} (i) B_z (j) D_z	155
6.29	Effect of porosity volume on u ($\eta = 2$; $\alpha = 45^0$)	156
6.30	Effect of porosity volume on v ($\eta = 2$; $\alpha = 45^0$)	157
6.31	Effect of porosity volume on ϕ ($\eta = 2$; $\alpha = 45^0$)	157
6.32	Effect of porosity volume on ψ ($\eta = 2$; $\alpha = 45^0$)	158
6.33	Effect of porosity volume on σ_x ($\eta = 2$; $\alpha = 45^0$)	159
6.34	Effect of porosity volume on σ_y ($\eta = 2$; $\alpha = 45^0$)	159
6.35	Effect of porosity volume on σ_{xy} ($\eta = 2$; $\alpha = 45^0$)	160
6.36	Effect of porosity volume on τ_{xz} ($\eta = 2$; $\alpha = 45^0$)	161
6.37	Effect of porosity volume on B_z ($\eta = 2$; $\alpha = 45^0$)	161
6.38	Effect of porosity volume on D_z ($\eta = 2$; $\alpha = 45^0$)	162

NOMENCLATURE

ESL	Equivalent Single Layer Theory
LW	Layerwise Theory
$SMEE$	Skew-magneto-electro-elastic
MEE	Magneto-electro-elastic
N	Total number of layers
k	Layer number under consideration
$FGMEE$	Functionally graded magneto-electro-elastic
$FGSMEE$	Functionally graded skew magneto-electro-elastic
$\mathbf{u}, \mathbf{v}, \mathbf{w}$	Displacement components along x -, y - and z - directions
V_f	Volume fraction of Barium Titanate ($BaTiO_3$) and Cobalt Ferrite ($CoFe_2O_4$)
z	Position of the point of interest from the bottom layer
σ_x, σ_y and σ_z	Normal stresses along x -, y - and z -directions
σ_{xy}	In-plane shear stress
τ_{xz} and τ_{yz}	Transverse shear stresses along xz - and yz - directions
$[\bar{C}_b(z)]$ and $[\bar{C}_s(z)]$	Functionally graded material coefficient matrices
$\xi_{33}(z)$ and $\mu_{33}(z)$	Dielectric constant and the magnetic permeability constant
$d_{33}(z)$	The electromagnetic coefficient.
D_z	Electric displacement
E_z	Electric field
B_z	Magnetic induction
H_z	Magnetic field
$\{e_b(z)\}$	The electric coefficient matrix
$\{q_b(z)\}$	The magnetic coefficient matrix
ϕ	The electric potential.
ψ	The magnetic potential
$[M^{el}]$	Elemental mass matrix
$[k_{tt}^{el}], [k_{tr}^{el}]$ and $[k_{rr}^{el}]$	Elemental elastic stiffness matrices

$[k_{t\phi}^{el}], [k_{r\phi}^{el}]$	The elemental electro-elastic coupling stiffness matrices
$[k_{t\psi}^{el}], [k_{r\psi}^{el}]$	The elemental magneto-elastic coupling stiffness matrices
$[k_{\phi\phi}^{el}]$	The elemental electric stiffness matrices
$[k_{\psi\psi}^{el}]$	The elemental magnetic stiffness matrices
$\{F_t^{el}\}$	The elemental mechanical load vector
$[M]$	The global mass matrix
$[k_{tt}^g], [k_{rr}^g]$ and $[k_{rr}^g]$	The global elastic stiffness matrices
$[k_{t\phi}^g]$ and $[k_{r\phi}^g]$	The global electro-elastic coupling stiffness matrices
$[k_{t\psi}^g]$ and $[k_{r\psi}^g]$	The global magneto-elastic coupling stiffness matrices
$[k_{\phi\phi}^g]$	The global electric stiffness matrices
$[k_{\psi\psi}^g]$	The global magnetic stiffness matrices
$\{F_t\}$	The global mechanical load vector

CHAPTER 1

INTRODUCTION AND LITERATURE REVIEW

In this chapter, a brief introduction and a comprehensive literature survey on smart composite materials are presented. In particular, magneto-electro-elastic (MEE) smart composites composed of piezoelectric and magnetostrictive phases and their unique coupling characteristics associated with the MEE materials are unveiled. Significant contributions of many researchers with respect to MEE materials and their wide spectrum of applications have been discussed. The literature concerning the basic structural characteristics such as static, buckling, and free vibration analysis with various configurations are discussed in brief. In addition, the porosity influence on the structural characteristic of MEE composites is presented comprehensively. From the extensive literature survey, the prominent research gaps have been identified and incorporated as research objective of this dissertation. In the end, organization of the thesis chapters has been delineated.

1.1 SMART COMPOSITE MATERIALS

A composite material is a material consisting of two or more combined constituents at a macroscopic level and are insoluble in each other. A class of materials which exhibit changes in material properties with the external stimuli such as heat, light, moisture, electric field, magnetic field etc., are called smart materials. The composites comprising of smart materials such as piezoelectric, piezomagnetic etc., inherently exhibit multifunctional capabilities such as sensing, actuation and energy storage in addition to the load bearing characteristics. Such multifunctional abilities are achieved through the coupling characteristics among the elastic, electric and magnetic fields. One such multifunctional smart material with increasing popularity among the scientific community is the magneto-electro-elastic (MEE) material. The interaction between the piezoelectric and magnetostrictive constituents of MEE composite has a key role in attracting many researchers. A brief description of MEE and its constituent materials is illustrated in the following sections.

1.1.1 Piezoelectric and Piezomagnetic materials

Materials that exhibit electric polarization or magnetisation when subjected to strain due to applied load are called piezoelectrics or piezomagnetics. Most of the piezoelectric materials are ceramic in nature. The concept of piezoelectric effect was proposed by Curie brothers in 1880. The piezoelectric effect is generally observed in Tourmaline, Quartz, Topaz, and Rochelle salt. The dipoles within the domains either contract or expand when an electric field is applied to a piezoelectric material. If a strain is applied, the dipoles are again forced to contract or expand producing a potential difference. The piezoelectric and converse piezoelectric effects can be effectively used in an application of sensors and actuators. In addition, these materials can be effectively used to control vibration of structures (Kundalwal *et al.*, 2013 Kumar and Ray, 2013; Ray and Pradhan, 2008). The constitutive equation for a piezoelectric material can be expressed in matrix form as follows:

$$\begin{Bmatrix} \sigma \\ D \end{Bmatrix} = \begin{bmatrix} C & -e \\ e^T & \varepsilon \end{bmatrix} \begin{Bmatrix} \gamma \\ E \end{Bmatrix} \quad (1.1)$$

where, σ is the elastic stress vector in N/m^2 , D is the electric displacement vector in C/m^2 , γ is the elastic strain vector, E is the electric field vector in N/C or V/m , C is the elastic stiffness coefficient matrix in N/m^2 , ε is the electric permittivity matrix in $\text{C}/(\text{Vm})$, and e is the electro-mechanical coupling matrix in $\text{N}/(\text{Vm})$. Some of the commonly used piezoelectric materials are Polyvinylidene fluoride, Zinc Oxide, Barium Titanate and Aluminium nitride.

The magnetostriction was discovered by James Joule in 1842. Magnetostriction corresponds to the change in the geometry of the material under the influence of externally applied magnetic field. In a sample of magnetostrictive material considered, the magnetic domains in the material are arranged randomly in the absence of external magnetic field, while in the presence of magnetic field these materials undergo deformation. As the magnetic field is applied, the magnetic domains orient along the direction of the applied magnetic field and thereby induce strain. Analogously, the constitutive equation for the magnetostrictive material is expressed in matrix form as follows:

$$\begin{Bmatrix} \sigma \\ B \end{Bmatrix} = \begin{bmatrix} C & -q \\ q^T & \mu \end{bmatrix} \begin{Bmatrix} \gamma \\ H \end{Bmatrix} \quad (1.2)$$

where, B is the magnetic induction vector in Wb/m^2 or $\text{Ns}/(\text{Cm})$, H is the magnetic intensity vector in N/Wb or A/m , μ is the magnetic permeability matrix in $\text{Wb}/(\text{Nm})$, and q is the matrix of piezomagnetic constants in $\text{N}/(\text{Am})$. The prominent magnetostrictive materials available are Terfenol-D, Cobalt Ferrite etc.

1.1.2 Magneto-electro-elastic materials

In the 19th century, electricity and magnetism combined into one common form through Maxwell's equation. Consequently, Suchtelen (1972) proposed the concept of a product property in two-phase composite materials arising from an elastic coupling between two phases of different properties. Such coupling between electric and magnetic responses presents a material property called magneto-electric (ME) effect as shown in Figure 1.1. It can be seen from Figure 1.1 that the MEE coupling scheme is divided into seven regions. The regions 1, 2, and 3 represent individual phases of magnetic, electric, and elastic character, respectively. The coupling between two phases is represented by the regions 4, 5, and 6 corresponding to electro-elastic, magneto-elastic and magneto-electric coupling, respectively. The coupling among the magnetic, electric, and elastic phases is represented by the region 7 and is termed as magneto-electro-elastic coupling. Further, such materials with ME effect are also termed as multiferroic. The term multiferroic was originally understood by Schmid (1994, 2008) as the simultaneous presence of two or all three primary ferric properties i.e., ferroelasticity, ferroelectricity, and ferromagnetism. On the other hand, a composite with piezoelectric and piezomagnetic phases could demonstrate a strong ME effect (Zheng *et al.*, 2004). A multiferroic material can exhibit an electric polarization under a magnetic field or a magnetization under an electric field. Some of the single-phase materials exhibit a weak ME effect e.g., Ferroelectric perovskites such as PZT (Yuan *et al.*, 2006). The phenomenon of ME effect (Suchtelen, 1972; Newnham, 1978) is a product property due to the cross interaction between the two phases (i.e., piezomagnetic and piezoelectric) in a composite. Neither the piezoelectric nor the piezomagnetic phase has the ME effect, but composites of these two phases

exhibit a remarkable ME effect. Thus, the ME effect is a result of the product of magnetostrictive effect (magnetic/mechanical effect) in the piezomagnetic phase and piezoelectric effect (mechanical/electrical effect) in the piezoelectric phase, namely,

$$ME_H \text{ effect} = \frac{\text{magnetic}}{\text{mechanical}} \times \frac{\text{mechanical}}{\text{electric}} \quad (1.3a)$$

$$ME_E \text{ effect} = \frac{\text{electric}}{\text{mechanical}} \times \frac{\text{mechanical}}{\text{magnetic}} \quad (1.3b)$$

The ME effect is a coupled electric and magnetic phenomenon via elastic interaction. That is, for the ME_H effect, when a magnetic field is applied to a MEE composite, the piezomagnetic phase changes its shape magnetostrictively. The strain is then passed along to the piezoelectric phase, resulting in an electric polarization as shown in Figure 1.2. Thus, the ME effect in MEE composites is extrinsic dependent on the composite microstructure and coupling interaction across magnetostrictive-piezoelectric interfaces (Nan *et al.*, 2008).

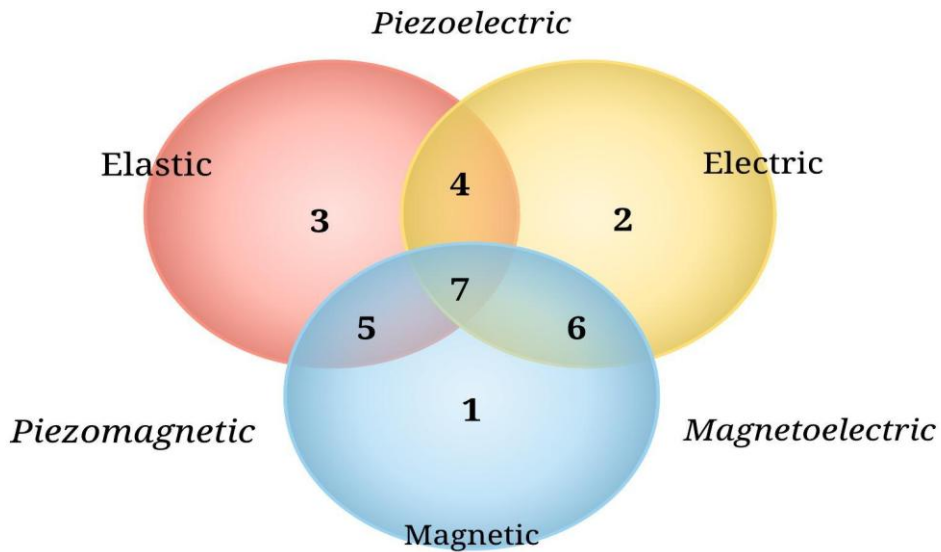


Figure 1.1: Magneto-electro-elastic coupling scheme

The MEE material consisting of a magnetostrictive phase and a piezoelectric phase along with mechanical coupling is described by Eqs.(1.3a) and (1.3b). If an input magnetic field H is applied to such composite material, then the piezomagnetic and piezoelectric coefficients can be obtained respectively for the piezomagnetic phase and the piezoelectric phase as follows:

$$\frac{\partial S}{\partial H} = e^m \quad (1.4a)$$

and

$$\frac{\partial P}{\partial S} = e \quad (1.4b)$$

where, S is the strain, P is the potential difference and e^m and e are, piezomagnetic and piezoelectric coefficients, respectively. As a result, the two-phase composite material can be expressed as

$$\frac{\partial P}{\partial H} = \alpha = k_c e^m e \quad (1.4c)$$

where, k_c is a coupling factor ($0 \leq |k_c| \leq 1$) between the two phases (Nan, 1994) and α is the ME coefficient of the composite. Thus, a new property (i.e., nonzero ME coefficient) appears in the composite consisting of piezomagnetic and piezoelectric phases, since neither constituent phase possess magnetoelectric effect. High piezoelectric (PE) and piezomagnetic (PM) coefficients and strong coupling (large k_c) favour a large ME coefficient. Computational analyses have also helped to understand the coupling between piezomagnetic, piezoelectric, and elastic coefficients.

So far, three kinds of bulk magnetoelectric composites have been investigated in experimental and theoretical studies, i.e., composites of (a) Ferrite and piezoelectric ceramics (e.g., lead zirconate titanate) (b) Magnetic metals/alloys (e.g., Terfenol-D and Metglas) and piezoelectric ceramics, and (c) Terfenol-D and piezoelectric ceramics and polymer. In the past decades, various ceramic composites consisting of piezoelectric and magnetic oxide ceramics have been investigated experimentally. Table 1.1 provides some of the MEE ceramic composites. Among all the combinations, Barium Titanate (BaTiO_3) and Cobalt Ferrite (CoFe_2O_4) MEE composite furnish the highest ME effect (Zheng *et al.*, 2004).

1.2 APPLICATIONS OF MEE COMPOSITES

The unique behaviour of MEE composites/structures have attracted many applications in the fields of aerospace, marine, medical instruments, energy harvesting etc., Their intelligent behaviour (Gracia *et al.*, 2014), sensitivity and their ability to control vibration meet the requirement of many mechanical, civil (Song *et al.*, 2006)

and electronic applications. The ability to convert one form of energy to other fits them into many multifunctional components. They mainly find their presence in critical aerospace and marine structures (Koma and Zimick, 2003). In addition, their sensitivity makes them most suitable for surface sensitive electronic probes, devices (Nan *et al.*, 2008) and in many sensors and actuators (Zhang *et al.*, 2014). Applications of multiferroic bulk composites (Terfenol-D) are related to high-frequency devices such as filters and oscillators that could be tuned by magnetic field, and to electrically tuneable microwave applications such as filters, oscillators and phase shifters (Nan *et al.*, 2008). Further, they are also used in stress monitoring and non destructive testing devices (Kurlyandskaya *et al.*, 2009 & Barandiaran *et al.*, 2009).

Table 1.1: Various constituent phases used for MEE composite (Nan *et al.*, 2008)

Piezoelectric phase	Piezomagnetic phase
BaTiO ₃ (BTO)	Ni ferrites (e.g., NFO)
PZT	Co ferrites (e.g., CFO , CoFe ₂ O ₄)
Pb (Mg Nb)O ₃ (PMN)	Li ferrites (LFO)
PbTiO ₃ (PTO)	Cu ferrite, Mn ferrite

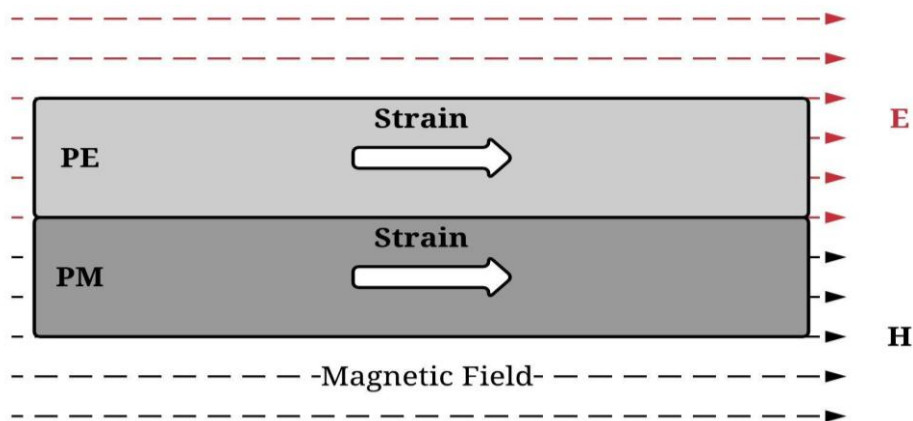


Figure 1.2: Multiferroic composite with piezoelectric and piezomagnetic phases

1.3 ORIGIN AND ANALYSIS OF MEE STRUCTURES

The first production of multiferroic BaTiO₃-CoFe₂O₄ composite made by Boomgaard and Born (1978) via unidirectional solidification from eutectic compositions initiated the investigation on MEE composites. Since then, numerous

investigations on the MEE composites have been carried out. To be specific, different approaches such as, analytical solutions (Jian and Ding 2007; Babei and Chen 2008; Haitao *et al.*, 2008; Biju *et al.*, 2009; Dai *et al.*, 2010; Badri and Al-Kayiem 2013; Cook and Vel 2013; Jabbari and Barati 2015), semi-analytical (Akbarzadeh *et al.*, 2012, 2013, 2014; Zhong *et al.*, 2015; Narendar 2016), state-space (Dong 2008; Chang 2013; Yu *et al.*, 2014; Zheng *et al.*, 2018) and finite element (FE) (Daga *et al.*, 2008, 2009a, 2009b; Biju *et al.*, 2010, 2011, 2012) models have been implemented to understand the behaviour of MEE plates. In this chapter, the most significant contributions by few researchers on free vibration, static and buckling analysis of MEE structure are discussed. Extra attention has been given to the literature dealing with the laminated skew composite structures. The review of the literature is discussed under the following sections:

- Free vibration studies of MEE and skew composite structures.
- Static studies of MEE and skew composite structures.
- Buckling of MEE, composite and skew composite structures.

1.3.1 Free vibration studies of MEE structures

Extensive research has been carried out to assess the structural behaviour of MEE plates (Pan 2001; Pan and Heyliger 2002; 2003; Pan and Han 2005; Liu 2011). The natural frequency of the MEE structures were extracted using free vibration studies through various methodologies such as analytical (Jandaghian and Rahamani 2016; Razavi 2016), State-vector (Wang *et al.*, 2003), Finite element method (Bhangale and Ganesan 2005; Jiang and Li 2007), Semi-analytical (Ramirez *et al.*, 2006) etc. Buchanan (2003, 2004) investigated the free vibration characteristics of MEE infinite cylinder and a comparative study for layered and multiphase MEE plate was performed. Chen *et al.*, (2007) proposed the state vector approach to analyse the free vibration characteristics of MEE plate and they found that the state vector approach accurately assesses the behavior of MEE plates. The free vibration characteristics of MEE plates resting on elastic foundation have been studied and the influence of foundation coefficients is extensively investigated (Li and Zhang 2014; Razavi and Shoostari 2014). Alaimo *et al.*, (2013) developed a four noded MITC element to study the structural behaviour of MEE multilayered plate. Amiri *et al.*, (2015) analysed the free vibration of circular MEE nano-plates based on Kirchhoff's

plate theory considering the small scale effect. Many researchers employed hybrid analysis by combining the state space (SS) approach and discrete singular convolution (DSC) algorithm to study the free vibration of simply-supported and multilayered and FG MEE plates (Chen *et al.*, 2005; Jiyangi *et al.*, 2006; Huang *et al.*, 2007; Chen *et al.*, 2007; Wang *et al.*, 2010; Xin and Hu, 2015). Razavi and Shoostari (2015, 2017) also discussed the nonlinear free and forced vibration of a transversely isotropic rectangular MEE thin plate with simply supported boundary conditions based on the thin plate theory along with the nonlinear strains.

The material properties variation at different proportion along the thickness of structures, results in desired material properties and superior structural behaviour. Such materials with functional variation of properties are called functionally graded (FG) materials. The structural characteristics of functionally graded MEE plates are comprehensively studied and the free vibration behaviour is well established through various methodologies such as State-space model (Chen *et al.*, 2005), FE method (Bhangale and Ganesan 2005, 2006, 2007), Exact solutions (Ramirez *et al.*, 2006a, b; Ramirez and Heyliger 2005), Analytical solution (Wu and Lu 2009; Tsai and Wu 2010; Kiani *et al.*, 2018; Mohammedimehr *et al.*, 2018) etc. Annigeri *et al.*, (2006a, b, 2007) proposed a semi-analytical method to investigate the free vibration behaviour of magneto-electro-elastic structures. The MEE bimorph beam was studied using an analytical solution method by Milazzo *et al.*, (2009) to assess the forced vibration characteristics. Tsai and Wu (2008) proposed a three-dimensional finite element approach to investigate the dynamic response of MEE shells with open-circuit surface foundation. Wu and Wang *et al.*, (2010) established state variable formulation for free vibration of the bonded and embedded laminated structures for actuators and sensors application. Milazzo (2012, 2013, 2014) proposed an equivalent single layer (ESL) model to understand the MEE plate dynamics. Davi and Milazzo (2011) proposed a regular variational boundary model for free vibration of MEE structures. Non-linear vibration of MEE structures is considerably available in the open literature (Ebrahimi *et al.*, 2009; Ansari *et al.*, 2015a, b; Razavi and Shoostari 2015a, b; Ansari and Gholami 2016a, b, c). The non-linear vibration control was studied through active constrained layer damping of MEE structures by Kattimani and Ray (2014a, b, 2015,

2017a, b). Benedetti and Milazzo (2017) proposed a new model in the framework of unified formulation to assess the free vibration and static characteristics.

1.3.2 Free vibration studies of skew composite structures

This section includes the literature concerned to the free vibration behaviour of composite skew plates. It may also be noted that most of the studies concerned to MEE structures were restricted to regular rectangular or square plates. However, the geometrical change in terms of plate skewness introduces an effective behavioural change in the plate structure. The free vibration characteristics of isotropic, orthotropic, layered, anisotropic and sandwich laminate skew plate are studied comprehensively in the literature (Farag and Ashour, 2000; Garg *et al.*, 2006; Singha and Daripa, 2007; Civalek, 2007; Mohazzab and Dozio, 2015; Setoodeh and Shojaee, 2016, Azam *et al.*, 2017; Shojaee *et al.*, 2017; Mandal *et al.*, 2017; Parida and Mohanty 2017, 2018; Watts *et al.*, 2018; Xue *et al.*, 2018; Chakraverty and Pradhan, 2018). Ashour (2009) investigated the free vibration of thin laminated skew plates with fully clamped edges. The governing differential equation for skew plate was obtained by transforming the differential equation in Cartesian coordinates into skew coordinates. Wang *et al.*, (2014) proposed modified differential quadrature method to obtain the accurate vibration behaviour of isotropic skew plates. The natural frequencies of the plate were then calculated by using the finite strip transition matrix (FSTM) method. Naghash and Azhari (2015) employed element-free Galerkin method to analyze the large amplitude free vibration of point supported laminated composite skew plates by including the geometrical non-linearity based on the von Karman's assumptions. Based on thin plate theory and Von Karman strain, Houmat (2015) developed a skew p-element for the nonlinear free vibration of variable stiffness symmetric skew laminates. The complex problem of skew plate was analysed via modified finite strip method using the combination of the Kantorovich method and the transition matrix. Chakraverty and Pradhan (2018) investigated the flexural vibration of functionally graded skew plates resting on Winkler and Pasternak elastic foundation. The studies involving the evaluation of structural characteristics of skew FG plates have also been reported profoundly in the literature. Free vibration of FG quadrilateral microplates in the thermal environment was studied by Shenan and Malekzadeh (2016). Ruan and Wang (2016) investigated the transverse vibrations of

moving skew plates made of FG material. Adineh and Kadkhodayan (2017) carried out three-dimensional thermo-elastic analysis and also obtained the dynamic response of a multi-directional FG skew plate on elastic foundation. Free vibration characteristics of FG-CNT reinforced composite skew plates were assessed by Kiani (2016). Ardestani *et al.*, (2017) developed isogeometric analysis to assess the effect of CNT orientation on the static and vibration response of CNT-reinforced skew composite plates. An analytical investigation of dynamic instability of FG skew plate under periodic axial compression was carried out by Kumar *et al.*, (2017).

1.3.3 Static studies of MEE structures

Under different loading conditions, the primary quantities such as displacements, potentials, and secondary quantities such as electrical displacement, magnetic induction, and the stresses display unique behaviour (Heyliger and Pan 2004; Hou *et al.*, 2006; Carrera *et al.*, 2009; Phoenix *et al.*, 2006; Huang *et al.*, 2010; Kuang 2011, 2014; Zhou and Zhu 2016; Vinyas and Kattimani 2017a, b, c, d;). Since, MEE structures act as precision structures in some of the applications, such responses are considered to be significant in design and analysis of MEE components. Pan (2001) presented exact solutions for a simply supported and multilayered MEE plates under static loading using the Stroh formalism. The solutions for multilayered plate were expressed in terms of propagator matrix. The importance of higher order polynomial to evaluate the electric and magnetic quantities for a thin plate was demonstrated by Pan and Heyliger (2003) through analytical solution. Lage *et al.*, (2004) presented a partial mixed layerwise (LW) FE model for adaptive plate structures to perform static analysis of MEE laminated plate structures. The mixed FE formulation was obtained by considering a Reissner mixed variational theorem (RMVT). Phoenix *et al.*, (2009) analysed multi-layered plates with surface bonded piezoelectric/magnetostrictive layers using LW mixed FE method. Exact deformation analysis of fiber reinforced MEE thin plates with closed circuit electric restriction was evaluated analytically by Liu (2011). Among them, Milazzo (2014) investigated the large deflection of MEE plates and the displacement fields were assumed to be based on FSDT. Alaimo *et al.*, (2014) developed an original FE formulation for the analysis of large deflections in MEE multilayered plates. Later, the active control of MEE structures received much of the attention due to its efficient controlling ability.

Kattimani and Ray (2014) developed a 3D coupled FE formulation of the MEE plate with active constrained layer damping (ACLD) treatment. Kattimani and Ray (2014) also investigated the active damping of geometrically nonlinear vibrations of FG-MEE plates integrated with the patches of the active constrained layer damping (ACLD). Recently, Pan and Waksanski (2016) presented an analytical solution using pseudo-Stroh formalism and propagator matrix method to study the non-local effect on MEE plates.

1.3.4 Static studies of skew composite structures

Skew composite plates and laminates occupy an importance in many engineering applications, as the geometric changes implemented to the rectangular plate influence various response characteristics. In addition, such plates specifically exhibit high strength to weight ratio and excellent fatigue resistance makes them to attract the attention of many researchers (McGee *et al.*, 1994; Upadhyay and Shukla 2012; Nagash and Azari 2015; Joodaky and Joodaky 2015; García *et al.*, 2016; Ahmed and Kapuria 2017; Jafari and Azhari 2017). Butalia and Kant (1990) carried out critical analysis of parallelogram-shaped plates under bending. They used Mindlin plate theory and nine-node Heterosis element for the plate modelling. The performance of the different elements was evaluated for uniformly distributed as well as point loads on the isotropic rhombic skew plates for different skew angles. Wankhade (2011) presented geometric nonlinear analysis of skew plates using FE formulation. It was based on Reissener /Mindlin thick plate theory which included effect of transverse shear. Active vibration control of skew composite plates was studied by Kanasogi and Ray (2013). Asemi *et al.*, (2014) presented the static and dynamic behavior of FG skew plates based on three-dimensional theory of elasticity. García-Macías (2016) studied the static and free vibration characteristics of carbon nano tube reinforced functionally graded skew plates based on Hu-Washizu principle. He *et al.*, (2017) investigated the static behaviour of size-dependent composite laminated skew plate based on modified couple stress theory

1.3.5 Buckling studies of MEE structures

The structures operating under axial loads are prone to buckling. Hence, it is important to understand the buckling behaviour of MEE plates. Recently, stability

studies concerned with MEE structures are gaining much attention among the researchers (Kumaravel *et al.*, 2007, 2010; Miehe *et al.*, 2016; Xu *et al.*, 2016; Li *et al.*, 2016; Jamalpoor *et al.*, 2016; Farajpour and Rastgoo 2017). Li (2014) performed the buckling analysis of MEE plate resting on Pasternak foundation based on the Mindlin plate theory. The numerical results revealed the effects of electric and magnetic potentials, Winkler spring, and Pasternak shear coefficients on the buckling load. Ansari (2016) investigated the buckling and post-buckling of magneto-electro-thermo-elastic (METE) nanoplates under magneto-electro-thermo-mechanical (METM) loads considering the nonlocal elasticity theory. Ebrahimi *et al.*, (2016) developed a nonlocal four-variable refined plate theory to examine the buckling behaviour of nanoplates made of FG-MEE materials resting on Winkler–Pasternak foundation.

1.3.6 Buckling of composite and skew composite structures

Stability analysis of composite structures was also studied, as most of the buckling studies for MEE plate were restricted to plates resting on elastic foundation. Among many researchers, Moita *et al.*, (1996) developed a discrete FE model using higher-order theory for the linear buckling analysis of multi-laminated composite plate-shell structures. The geometric stiffness matrix was developed by taking into consideration the effects of the higher order terms on the initial in-plane and transverse shear stresses. Wang (1996) presented a B-spline Rayleigh-Ritz method (RRM) based on FSDT for buckling analysis of skew fibre-reinforced composite laminates. The laminates considered had arbitrary lay-ups which include coupling between in-plane and out-of plane behaviour. Luccioni *et al.*, (1998) studied free vibration and stability of laminated composite rectangular plates based on both classical and FSDT using Levy-type FE model. The buckling behaviour of skew composite plates was also studied to understand the effect of geometrical changes on the structural stability. Here, in order to analyse the buckling behaviour of skew fibre reinforced composite and sandwich laminates Babu and Kant (1999) established C° iso-parametric finite element formulations based on FSDT and higher-order shear deformation theory. Vuksanović (2000) proposed a single layered higher-order discrete model which allowed a parabolic distribution of shear strains through the

plate thickness as well as a cubic variation of in-plane displacements. Hu *et al.*, (2000) also studied elastic stability of skew composite laminate plates subjected to uniaxial inplane compressive forces. Hu *et al.*, (2006) employed a nonlinear material constitutive model with nonlinear in-plane shear formulation and the Tsai–Wu failure criterion. Grover *et al.*, (2014) developed a computationally efficient C^0 finite element model for laminated composite and sandwich plates using inverse hyperbolic shear deformation theory. Kumar *et al.*, (2015) investigated the buckling behaviour of composite skew plate with different skew angles and boundary conditions under different types of linearly varying in-plane loadings (γ). The analysis was based on higher order shear deformation theory. The total energy functional was derived using in-plane stress distributions and transformed from physical domain to computational domain using transformation relations.

1.3.7 Porosity influence on MEE structures

The recent development in FGM includes the graded porosity structures. The pores in the microstructures of such structural materials are accounted via local density of the material. The methods to prepare FGMs are a trending area of research capturing attention of many researchers. The preparation method includes powder metallurgy, vapour deposition, self propagation, centrifugal casting, and magnetic separation (Khor *et al.*, 2000; Watanabe *et al.*, 2001; Song *et al.*, 2007; Peng *et al.*, 2007; Wang and Zhao *et al.*, 2017; Barati, 2018; Wu *et al.*, 2018; Zenkour 2018; Heshmati and Daneshmand 2018; Thang *et al.*, 2018). Although many preparation methods are available, the sintering process is preferred due to its cost effectiveness. The FGMs prepared using sintering process possesses micro-voids or porosities due to the different solidification rate of material constituents (Zhu *et al.*, 2001). A study by Wattanasakulpong *et al.*, (2012) projects the importance of considering porosity factor in the design and analysis of FGMs. Wang *et al.*, (2017) investigated the vibration characteristics of FG plates with porosities. Recently, Ebrahimi *et al.*, (2017a, b, c, d, e, f) analysed the various structural characteristics of MEE porous material plates. Aero-hygro-thermal stability analysis of higher-order refined supersonic FGM panels with even and uneven porosity distributions was studied by Barati and Shahverdi (2017). Using refined four-variable theory, Barati *et al.*, (2017)

studied the electro-mechanical vibration of smart piezoelectric FG plates with porosities. Ebrahimi *et al.*, (2017) studied the free vibration of smart porous plates subjected to various physical fields considering neutral surface position. Shafiei *et al.*, (2017) characterized the vibration behaviour of two-dimensional imperfect FG porous nano and micro-beams.

1.4 SCOPE AND OBJECTIVE OF THE DISSERTATION

The study of smart structures has increased considering the ability to design and establish multifunctional components. Hence, a new era of smart structures composed of smart composites has emerged. In particular, magneto-electro-elastic (MEE) composites composed of piezoelectric (BaTiO_3) and magnetostrictive (CoFe_2O_4) materials have attracted the attention of researchers. An increasing demand for structures that are more adaptable to the applied load might have motivated the recent developments in MEE composites.

The comprehensive literature survey provides a larger insight on the various quantities influencing the structural behaviour of MEE plates. The literature concerning the skew plates in section 1.3 suggests that the geometric changes influence on the plate behaviour significantly. Several methodologies such as analytical, semi-analytical, state-space models, FE models are employed to investigate the structural behaviour of plates. However, FE modelling is widely accepted for its simplicity, adaptability, and effectiveness. Thus, the FE modelling is suitable for the study of skew structures.

The evaluation of structural behaviour of MEE plates through static, free vibration, buckling, and various other analysis is extensively investigated in the past. The research on the laminated and reinforced composite skew plates is considerably available, while the studies related to the skew MEE plate are scarce in the open literature. Hence, MEE plates with multilayered and FG are considered to investigate the influence of skew angle. Most often multilayered plates are prone to delamination with the shear stress developed in the adjacent layers. The thickness grading of the material is being implemented to overcome the delamination. The material grading is governed by the power law. However, the unavailability of the studies related to the

effect of skew angle and coupling fields on the structural behaviour of MEE plates provides an opportunity in the present investigation.

The FG structures prepared by sintering process are most likely to inherit porosity defects. Some studies in evaluating the influence of porosity in FG structures are available in the open literature (Wang *et al.*, 2017; Barati *et al.*, 2017; Ebrahimi *et al.*, 2017). However, there is larger scope for the study of porosity influence on the structural behaviour of skew MEE plates. The effect of skew angle and porosity volume on the coupled fields are little-known until now and provides an ample opportunity for further research. The prominent aim of the dissertation is to develop a finite element formulation to investigate the structural characteristics of skew MEE plates. Further, to extend the analysis, the influence of porosity defects on the structural behaviour of FGSMEE plate is being assessed. In addition, the influence of different parameters such as skew angle, material gradient index, porosity distribution, porosity volume, aspect ratio, thickness ratio, and boundary conditions need to be analysed. In this regard, the following analyses have been carried out as objectives of the dissertation.

- To develop a finite element formulation based on shear deformation theory for layered skew magneto-electro-elastic (SMEE) plates.
- To investigate the static and free vibration behaviour of multilayered SMEE plates.
- To analyse the static and free vibration characteristics of functionally graded SMEE plates.
- To evaluate the effect of skew angle, volume fraction, boundary conditions, aspect ratio and width to thickness ratio on static and free vibration performance of SMEE plates.
- To perform buckling analysis for the multilayered MEE and SMEE plates subjected to uni-axial and bi-axial compression.
- To assess the influence of skew angle, porosity distribution and different geometrical conditions on the static and free vibration behaviour of porous functionally graded SMEE plates.

1.5 CONTRIBUTIONS FROM THE DISSERTATION

The following contributions have been made in the area of MEE structures towards the preparation of the dissertation:

- The FE formulation based on shear deformation theory for layered, functionally graded, and porous functionally graded skew magneto-electro-elastic (SMEE) plates are successfully developed.
- The structural behaviour of multilayered SMEE plate is investigated. Some of the major influences on the static and free vibration behaviour for various geometrical aspects are studied.
- Buckling behaviour of rectangular and skew multilayered MEE plates are investigated.
- Functionally graded MEE plates are analysed and the influence of geometric modification on structural behaviour is studied.
- Prediction of porosity influence on functionally graded skew MEE plates is developed and its influence on structural behaviour is investigated.

1.6 OVERVIEW OF THE DISSERTATION BY CHAPTER

The present dissertation is devoted to investigate the influence of geometrical changes on the static, free vibration and buckling response of MEE plates using the FE formulation. Further, the effect of different porosity distribution on the static and free vibration behaviour of skew FG plates is thoroughly studied. The geometrical changes introduced in terms of skew angle are achieved by transforming the skew edges on to the original coordinates by implementing the transformation matrix. The emphasis is made on evaluating the influence of skew angle, material gradient index, porosity distribution, porosity volume, aspect ratio, and the thickness ratio.

This thesis has been divided into six chapters. In the first chapter, a brief introduction and a comprehensive literature review on the smart materials, MEE materials, MEE structures, skew structures, and porous structures have been presented. Subsequently, the scope of present work is explored and the objectives of the present work have been defined.

In chapter 2, a detailed finite element formulation based on first order shear deformation theory (FSDT) is presented to study the static and buckling behaviour of

multilayered rectangular MEE plate. Buckling loads and corresponding mode shapes are presented for uniaxial and biaxial in-plane loads. Influence of load factor, stacking sequence, thickness ratio, and aspect ratio on the static and buckling behaviour of multilayered MEE plate is investigated.

Chapter 3 includes the detailed finite element formulation based on 1-2 shear deformation theory to assess the static and free vibration characteristics of multilayered skew magneto-electro-elastic (SMEE) plate. A comparative study for two different stacking sequences is presented. The influence of geometrical changes introduced in terms of skew angle on the structural behaviour of the SMEE plate is assessed.

Chapter 4 is concerned with the assessment of buckling characteristics of multilayered SMEE plate subjected to in-plane loads. The FE formulation is developed based on the FSDT, and the skew co-ordinates are transformed by suitable transformation matrix. Critical buckling loads and corresponding mode shapes are presented for uniaxial and biaxial in-plane loads. The influence of skew angle on critical buckling loads and corresponding mode shapes are studied in detail. Further, various geometrical parameters influencing the stability characteristics of the SMEE plate is thoroughly investigated.

The static and free vibration characteristics of functionally graded magneto-electro-elastic (FGMEE) plate are discussed in chapter 5. The functional variation of material properties through the thickness is achieved using modified power law. The influence of power law and skew angle on the structural characteristics of FGMEE plate is investigated. The geometrical aspects such as thickness ratio, aspect ratio, and boundary condition affecting the natural frequency and static behaviour of FGMEE plate are studied.

The influence of porosity on the rectangular and skew FGMEE plate is encapsulated in chapter 6. Porosity is accounted as the local density and the material properties are obtained using modified power law. Four different porosity distributions are investigated and their influence on the static behaviour and free vibration characteristics of porous plates is also studied. The influence of skew angle on the structural characteristics of the porous FGMEE plate is thoroughly

investigated. In addition, various parameters such as porosity volume, boundary condition, aspect ratio, and thickness ratio are studied in detail.

At last, chapter 7 encapsulates the major findings of the dissertation. The future possible work for the improvement in the application of MEE structures has also been outlined. The appendix and the list of references are shown at the end of the dissertation.

CHAPTER 2

STATIC AND BUCKLING CHARACTERISTICS OF MULTILAYERED MAGNETO-ELECTRO-ELASTIC PLATES

This chapter deals with the analysis of buckling behaviour of multilayered magneto-electro-elastic (MEE) plate subjected to uniaxial and biaxial compressive (in-plane) loads. The constitutive equations of MEE material are used to derive a finite element (FE) formulation involving the coupling among the electric, magnetic, and elastic fields. The displacement field corresponding to the first order shear deformation theory (FSDT) has been employed. The in-plane stress distribution within the MEE plate existing due to the enacted force is considered to be equivalent to the applied in-plane compressive load in the pre-buckling range. The same stress distribution is used to derive the potential energy functional. The non-dimensional critical buckling load is accomplished from the solution of allied linear eigenvalue problem. Influence of stacking sequence, span to thickness ratio, aspect ratio, load factor, and boundary condition on critical buckling load, and their corresponding mode shape is investigated. In addition, static deflection of MEE plate under the sinusoidal and the uniformly distributed loads has been studied for different stacking sequences and boundary conditions.

2.1. INTRODUCTION

An increasing application of MEE composites in the field of aerospace, surface sensitive electronic probes, stress monitoring devices, electrically and magnetically tuneable high frequency oscillators, sensors, and actuators has attracted the attention of many researchers. The MEE composites facilitate the energy conversion among the electric, magnetic, and elastic quantities. The conversion of various form of energy within the composite makes it most suitable for multifunctional devices.

In this chapter, a finite element model based on first order shear deformation theory (FSDT) to assess the buckling characteristics of the multilayered MEE plate is

developed. The in-plane stress distribution within the MEE plate existing due to the enacted force is considered to be equivalent to the applied in-plane compressive loads in the pre-buckling range. Buckling characteristics are well presented in terms of non-dimensional critical buckling load and their corresponding mode shapes which are obtained by solving a linear eigenvalue problem. In addition, parametric studies such as the effect of uniaxial and biaxial compression, aspect ratio, span to thickness ratio and boundary conditions are studied in detail. Further, the static deflection of MEE plate under different boundary and loading conditions is also presented.

2.2. PROBLEM DESCRIPTION AND GOVERNING EQUATION

A three layered MEE plate illustrated in Figure 2.1 whereas Figure 2.2 illustrates the MEE plate subjected to uniaxial and biaxial compression. The length, the width and the total thickness of the plate are a , b and H , respectively. The MEE plate consists of three layers of equal thickness h_i ($i = 1, 2, 3$). The top and the bottom layers are made of identical material either piezoelectric (BaTiO_3) commonly represented by B or magnetostrictive (CoFe_2O_4) commonly represented by F, while the middle layer is of the other material i.e., magnetostrictive or piezoelectric. Based on the stacking sequence of the material, the MEE composite is called B/F/B or F/B/F, indicating the top/middle/bottom layer, respectively, wherein, B represents barium titanate and F represents cobalt ferrite. The displacement field of such MEE plate is considered as the first order expansion of Taylor's series of the mid-plane variables with respect to the plate thickness. Hence, the displacement fields are given by (Reddy 2004)

$$u = u_0 + z\theta_x, \quad v = v_0 + z\theta_y, \quad w = w_0 \quad (2.1)$$

where, u_0 , v_0 , w_0 are the initial displacements at the midplane and θ_x , θ_y are the rotations of the line initially normal to the midplane relative to the y - and x - axis respectively. For the ease of computation, the displacement components are split into translational and rotational displacement vectors as follows:

$$\{d_t\} = [u_0 \ v_0 \ w_0]^T \quad \{d_r\} = [\theta_x \ \theta_y]^T \quad (2.2)$$

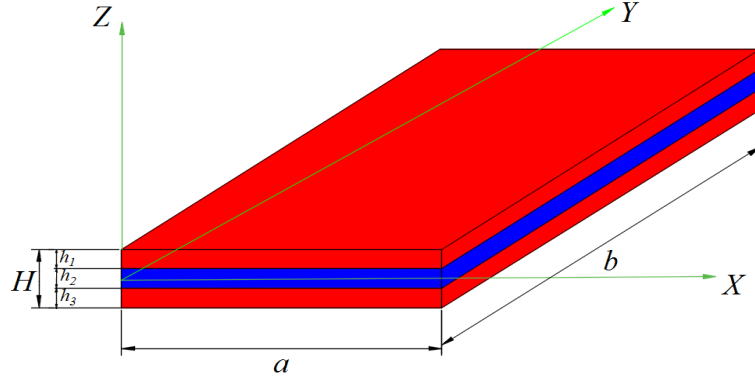


Figure 2.1: Schematic representation of multilayered MEE plate

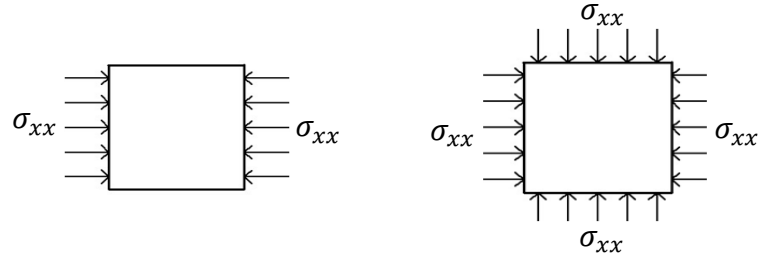


Figure 2.2: Schematic representation of uniaxial and biaxial compression on MEE plate

Since, the thin plate analysis is involved, to avoid shear locking, selective integration scheme is employed. In addition, to emphasize the effect of transverse shear deformation, the strain $\{\varepsilon\}$ at any point in the MEE plate is divided into bending strain vector $\{\varepsilon_b\}$ and shear strain vector $\{\varepsilon_s\}$ and are written as follows:

$$\{\varepsilon\} = \{\varepsilon_x \quad \varepsilon_y \quad \varepsilon_z \quad \gamma_{xy} \quad \gamma_{xz} \quad \gamma_{yz}\}^T,$$

$$\{\varepsilon_b\} = \{\varepsilon_x \quad \varepsilon_y \quad \varepsilon_z \quad \gamma_{xy}\}^T, \quad \{\varepsilon_s\} = [\gamma_{xz} \quad \gamma_{yz}]^T \quad (2.3)$$

Utilizing the displacement field from Eq. (2.1) and the strain components in Eq. (2.3) along with the strain-displacement relations, the state of bending and transverse shear stress components at any point in the plate can be expressed as:

$$\{\varepsilon_b\} = \{\varepsilon_{bt}\} + [Z_1]\{\varepsilon_{br}\}, \quad \{\varepsilon_s\} = \{\varepsilon_{st}\} + [Z_2]\{\varepsilon_{sr}\} \quad (2.4)$$

in which, $[Z_1]$ and $[Z_2]$ are the transformation matrices given as

$$[Z_1] = \begin{bmatrix} z & 0 & 0 \\ 0 & z & 0 \\ 0 & 0 & 0 \\ 0 & 0 & z \end{bmatrix}, [Z_2] = \begin{bmatrix} 1 & 0 \\ 0 & 1 \end{bmatrix} \quad (2.5)$$

correspondingly, the various strain components appearing in Eq. (2.4) are given by

$$\begin{aligned} \{\varepsilon_{bt}\} &= \begin{bmatrix} \frac{\partial u_0}{\partial x} & \frac{\partial v_0}{\partial y} & 0 & \frac{\partial u_0}{\partial y} + \frac{\partial v_0}{\partial x} \end{bmatrix}, \{\varepsilon_{ts}\} = \begin{bmatrix} \frac{\partial w_0}{\partial x} & \frac{\partial w_0}{\partial y} \end{bmatrix} \\ \{\varepsilon_{br}\} &= \begin{bmatrix} \frac{\partial \theta_x}{\partial x} & \frac{\partial \theta_y}{\partial y} & 0 & \frac{\partial \theta_x}{\partial y} + \frac{\partial \theta_y}{\partial x} \end{bmatrix} \end{aligned} \quad (2.6)$$

Analogous to the strain vectors presented in Eq. (2.3), the state of stress any given point in the MEE plate can be expressed as follows:

$$\{\sigma_b\} = [\sigma_x \ \sigma_y \ \sigma_z \ \tau_{xy}]^T, \{\sigma_s\} = [\tau_{xz} \ \tau_{yz}]^T \quad (2.7)$$

wherein, σ_x , σ_y and σ_z along the x -, y - and z -directions are the corresponding normal stresses, τ_{xy} is the in-plane stress component, τ_{xz} and τ_{yz} are the transverse shear stresses along xz - and yz - directions, respectively. Considering the effect of coupled fields, the constitutive equations for the MEE plate can be written as follows:

$$\{\sigma_b^k\} = [\bar{C}_b^k] \{\varepsilon_b^k\} - \{e_b^k\} E_z - \{q_b^k\} H_z, \{\sigma_s^k\} = [\bar{C}_s^k] \{\varepsilon_s^k\} \quad (2.8a)$$

$$D_z = \{\bar{e}_b^k\}^T \{\varepsilon_b^k\} + \bar{\xi}_{33}^k E_z + \bar{d}_{33}^k H_z \quad (2.8b)$$

$$B_z = \{\bar{q}_b^k\}^T \{\varepsilon_b^k\} + \bar{d}_{33}^k E_z + \bar{\mu}_{33}^k H_z \quad (2.8c)$$

here $k = 1, 2, 3$ denotes the layer number initiating from the bottom layer of the MEE plate and

$$[\bar{C}_b^k] = \begin{bmatrix} \bar{C}_{11}^k & \bar{C}_{12}^k & \bar{C}_{13}^k & 0 \\ \bar{C}_{12}^k & \bar{C}_{22}^k & \bar{C}_{23}^k & 0 \\ \bar{C}_{13}^k & \bar{C}_{23}^k & \bar{C}_{33}^k & 0 \\ 0 & 0 & 0 & \bar{C}_{66}^k \end{bmatrix}, [\bar{C}_s^k] = \begin{bmatrix} \bar{C}_{55}^k & \bar{C}_{45}^k \\ \bar{C}_{45}^k & \bar{C}_{44}^k \end{bmatrix} \quad (2.9)$$

where $\begin{bmatrix} \bar{C}_b^k \\ \bar{C}_s^k \end{bmatrix}$ and $\begin{bmatrix} \bar{C}_s^k \\ \bar{C}_b^k \end{bmatrix}$ represent the reduced coefficient matrices, $\bar{\xi}_{33}^k$ is the reduced dielectric constant and $\bar{\mu}_{33}^k$ represent the reduced magnetic permeability coefficient, \bar{d}_{33}^k is the reduced electromagnetic coefficient and are given by (Farajpour *et al.*, 2016). Since the plate is considered to be thin, the electric displacement, the electric field, the magnetic induction and the magnetic field along the z -direction are only considered (Milazzo, 2014; Sladek *et al.*, 2013; Li, 2014) and are represented by D_z , E_z , B_z and H_z , respectively. The components of reduced elastic coefficient matrices $\{\bar{C}_{ij}^k\}$, the reduced electric coefficient matrix $\{\bar{e}_b^k\}$ and the reduced magnetic coefficient matrix $\{\bar{q}_b^k\}$ are given by

$$\begin{aligned} \bar{C}_{11}^k &= C_{11}^k - \frac{(C_{13}^k)^2}{C_{33}^k}, \quad \bar{C}_{12}^k = C_{12}^k - \frac{(C_{13}^k)^2}{C_{33}^k}, \quad \bar{C}_{22}^k = C_{22}^k - \frac{(C_{13}^k)^2}{C_{33}^k}, \quad \bar{C}_{13}^k = 0, \quad \bar{C}_{23}^k = 0, \quad \bar{C}_{33}^k = 0, \\ \bar{C}_{44}^k &= C_{44}^k \\ \bar{C}_{55}^k &= C_{55}^k, \quad \bar{C}_{66}^k = C_{66}^k, \quad \bar{e}_{31}^k = e_{31}^k - \frac{C_{13}^k e_{33}^k}{C_{33}^k}, \quad \bar{e}_{32}^k = e_{32}^k - \frac{C_{13}^k e_{33}^k}{C_{33}^k}, \quad \bar{q}_{31}^k = q_{31}^k - \frac{C_{13}^k q_{33}^k}{C_{33}^k}, \\ \bar{q}_{32}^k &= q_{32}^k - \frac{C_{13}^k q_{33}^k}{C_{33}^k} \\ \bar{\xi}_{33}^k &= \xi_{33}^k - \frac{e_{33}^k q_{33}^k}{C_{33}^k}, \quad \bar{\mu}_{33}^k = \mu_{33}^k - \frac{e_{33}^k q_{33}^k}{C_{33}^k} \quad \text{and} \quad \bar{d}_{33}^k = d_{33}^k - \frac{e_{33}^k q_{33}^k}{C_{33}^k} \\ \{\bar{e}_b^k\} &= \{\bar{e}_{31}^k \quad \bar{e}_{32}^k \quad \bar{e}_{33}^k \quad \bar{e}_{36}^k\}^T, \quad \{\bar{q}_b^k\} = \{\bar{q}_{31}^k \quad \bar{q}_{32}^k \quad \bar{q}_{33}^k \quad \bar{q}_{36}^k\}^T \end{aligned} \quad (2.10)$$

Employing the principle of virtual work the governing equations for the MEE plate is established as

$$\delta \Pi = \delta U + \delta V = 0 \quad (2.11)$$

wherein, the strain energy (δU) is given by

$$\begin{aligned} \delta U &= \sum_{k=1}^3 \left(\int_{\Lambda^k} \delta \{\varepsilon_b^k\} \{\sigma_b^k\} d\Lambda^k + \int_{\Lambda^k} \delta \{\varepsilon_s^k\} \{\sigma_s^k\} d\Lambda^k \right) - \int_{\Lambda^t} \delta E_z^t D_z^t d\Lambda^t - \int_{\Lambda^b} \delta E_z^b D_z^b d\Lambda^b \\ &\quad - \int_{\Lambda^m} \delta H_z B_z d\Lambda^m - \int_{A^{el}} \delta \{d_t\}^T F_t dA^{el} \end{aligned} \quad (2.12)$$

the work of in-plane loads (δV) can be expressed as

$$\delta V = \int_0^a \int_0^b \begin{bmatrix} \frac{\partial w}{\partial x} \\ \frac{\partial w}{\partial y} \end{bmatrix}^T [\sigma_0] \begin{bmatrix} \frac{\partial w}{\partial x} \\ \frac{\partial w}{\partial y} \end{bmatrix} dx dy \quad (2.13)$$

where A^k ($k = 1, 2, 3$) designates the respective layer volume, F_t corresponds to the applied surface traction force on the top surface area A^{el} . A^t and A^b represent the volume of the top and bottom piezoelectric layer while the middle magnetostrictive layer is represented by A^m . $[\sigma_0]$ is the initial stress matrix. E_z^t , E_z^b and D_z^t , D_z^b are the electric fields and the electric displacements of the top and the bottom layers of the MEE plate, whereas H_z^m and B_z^m are the magnetic field and magnetic induction in the middle layer, respectively. The transverse electric field (E_z) related to the electric potential $\{\phi\}$ and the transverse magnetic field (H_z) is related to the magnetic potential $\{\psi\}$ in accordance with Maxwell's equation as follows:

$$E_z^t = -\frac{\partial \phi^t}{\partial z}, E_z^b = -\frac{\partial \phi^b}{\partial z} \text{ and } H_z^m = -\frac{\partial \psi^m}{\partial z} \quad (2.14)$$

where, the superscript t , b , and m represent the top, bottom, and middle layer of the MEE plate, respectively. The interface connectivity of piezoelectric layer and magnetostrictive layer are assumed to be properly grounded. Since the MEE plate layers possess very small thickness, the variation of the electric and magnetic potential across the thickness can be suitably assumed to be linear. Correspondingly, the electric potential functions ϕ^t and ϕ^b pertaining to the top and the bottom piezoelectric layers, and ψ^m the magnetic potential pertaining to the middle magnetostrictive layer of the MEE plate can be represented as (Kattimani 2015)

$$\phi^t = \frac{z - z_b}{h} \phi_1, \phi^b = -\frac{z - h_2}{h} \phi_2 \text{ and } \psi^m = \frac{z - h_2}{h} \bar{\psi} \quad (2.15)$$

where z_b denotes the z -coordinate of the bottom surface of the top piezoelectric layer; h_2 represent the z -coordinate of the top face of the bottom piezoelectric layer; The

electric potentials ϕ_1 and ϕ_2 corresponding to the top and the bottom surfaces of the top and the bottom piezoelectric layers.

2.3 FINITE ELEMENT FORMULATION

The MEE plate is discretized by using four noded quadrilateral elements. Considering Eq. (2.2), the displacement vectors in generalized form $\{d_{ti}\}$ and $\{d_{ri}\}$ are linked with the i^{th} node (where, $i = 1, 2, 3, 4$) of an element can be articulated as

$$\{d_{ti}\} = [u_{oi} \ v_{oi} \ w_{oi}]^T \text{ and } \{d_{ri}\} = [\theta_{xi} \ \theta_{yi}]^T \quad (2.16)$$

At any given point within the element, the displacement vectors in generalized form $\{d_t\}$ and $\{d_r\}$, the generalized electric potential vector $\{\phi\}$ and the generalized magnetic potential vector $\{\psi\}$ can be expressed in terms of nodal generalized displacement vectors $\{d_t^{\text{el}}\}$ and $\{d_r^{\text{el}}\}$, the nodal magnetic potential vector $\{\psi^{\text{el}}\}$ and the nodal electric potential vector $\{\phi^{\text{el}}\}$, respectively, as follows:

$$\begin{aligned} \{d_t\} &= [n_t] \{d_t^{\text{el}}\}, \quad \{d_r\} = [n_r] \{d_r^{\text{el}}\}, \\ \{\phi\} &= [\phi_1 \ \phi_2]^T = [n_\phi] \{\phi^{\text{el}}\}, \quad \{\psi\} = [\psi_1 \ \psi_2]^T = [n_\psi] \{\psi^{\text{el}}\} \\ \text{and } \{\psi^{\text{m}}\} &= [n_\psi^{\text{m}}] \{\psi^{\text{el}}\} \end{aligned} \quad (2.17)$$

in which,

$$\begin{aligned} \{d_t^{\text{el}}\} &= \left[\{d_{t1}^{\text{el}}\}^T \ \{d_{t2}^{\text{el}}\}^T \ \dots \ \{d_{t4}^{\text{el}}\}^T \right]^T, \quad \{d_r^{\text{el}}\} = \left[\{d_{r1}^{\text{el}}\}^T \ \{d_{r2}^{\text{el}}\}^T \ \dots \ \{d_{r4}^{\text{el}}\}^T \right]^T, \\ \{\phi^{\text{el}}\} &= \{\phi_{11} \ \phi_{21} \ \phi_{12} \ \phi_{22} \ \dots \ \phi_{14} \ \phi_{24}\}^T, \quad \{\bar{\psi}^{\text{el}}\} = \{\bar{\psi}_1 \ \bar{\psi}_2 \ \dots \ \bar{\psi}_4\}^T, \\ [n_t] &= [n_{t1} \ n_{t2} \ \dots \ n_{t4}]^T, \quad [n_r] = [n_{r1} \ n_{r2} \ \dots \ n_{r4}]^T, \\ [n_\phi] &= \begin{bmatrix} n_{\phi_{11}} & 0 & n_{\phi_{12}} & 0 & \dots & n_{\phi_{14}} & 0 \\ 0 & n_{\phi_{21}} & 0 & n_{\phi_{22}} & \dots & 0 & n_{\phi_{24}} \end{bmatrix}^T, \quad [n_\psi] = [n_{\psi/1} \ n_{\psi/2} \ \dots \ n_{\psi/4}]^T, \\ n_{ti} &= N_i I_t, \quad n_{ri} = N_i I_r \end{aligned} \quad (2.18)$$

where $[n_t]$, $[n_r]$, $[n_\phi]$ and $[n_\psi]$ are the shape function matrices, I_t and I_r are the identity matrices. The shape function N_i corresponding to the natural coordinate is linked with the i^{th} node. The degrees of freedom corresponding to the electric potential and magnetic potential are ϕ_{1i} , ϕ_{2i} and $\bar{\psi}_i$ (where, $i = 1, 2, 3, 4$), respectively. Utilizing Eqs. (2.12) - (2.16), the transverse electric field for the top and the bottom layer (E_z^t , E_z^b) and the transverse magnetic field for the middle layer (H_z^m) are given by

$$E_z^t = -\frac{1}{h}[1 \quad 0][n_\phi]\{\phi^{\text{el}}\}, \quad E_z^b = -\frac{1}{h}[0 \quad 1][n_\phi]\{\phi^{\text{el}}\}$$

$$\text{and } H_z^m = -\frac{1}{h}[n_\psi]\{\psi^{\text{el}}\} \quad (2.19)$$

Now, considering Eqs. (2.4) and (2.16), the strain vectors in generalized form at any given point in the element can be presented in the form of nodal generalized strain vectors as

$$\{\varepsilon_{bt}\} = [b_{bt}]\{d_t^{\text{el}}\}, \quad \{\varepsilon_{br}\} = [b_{br}]\{d_r^{\text{el}}\}$$

$$\{\varepsilon_{st}\} = [b_{st}]\{d_t^{\text{el}}\}, \quad \{\varepsilon_{sr}\} = [b_{sr}]\{d_r^{\text{el}}\} \quad (2.20)$$

in which, $[b_{tb}]$, $[b_{rb}]$, $[b_{ts}]$ and $[b_{rs}]$ are the nodal strain-displacement matrices. The explicit form of the matrices is given in the appendix. Substituting Eqs. (2.4), (2.10), (2.13), (2.19) and (2.20) into Eq. (2.11) and simplifying, we obtain the elemental equations of motion for the MEE plate as follows:

$$[k_{tt}^{\text{el}}]\{d_t^{\text{el}}\} + [k_{tr}^{\text{el}}]\{d_r^{\text{el}}\} + [k_{t\phi}^{\text{el}}]\{\phi^{\text{el}}\} + [k_{t\psi}^{\text{el}}]\{\psi^{\text{el}}\} + [k_G^{\text{el}}]\{d_t\} = \{F_t^{\text{el}}\} \quad (2.21)$$

$$[k_{tr}^{\text{el}}]^T \{d_t^{\text{el}}\} + [k_{rr}^{\text{el}}]\{d_r^{\text{el}}\} + [k_{r\phi}^{\text{el}}]\{\phi^{\text{el}}\} + [k_{r\psi}^{\text{el}}]\{\psi^{\text{el}}\} = 0 \quad (2.22)$$

$$[k_{t\phi}^{\text{el}}]^T \{d_t^{\text{el}}\} + [k_{r\phi}^{\text{el}}]^T \{d_r^{\text{el}}\} - [k_{\phi\phi}^{\text{el}}]\{\phi^{\text{el}}\} = 0 \quad (2.23)$$

$$[k_{t\psi}^{\text{el}}]^T \{d_t^{\text{el}}\} + [k_{r\psi}^{\text{el}}]^T \{d_r^{\text{el}}\} - [k_{\psi\psi}^{\text{el}}]\{\psi^{\text{el}}\} = 0 \quad (2.24)$$

The matrices and the vectors displayed in Eqs. (2.21) - (2.24) are the elemental elastic stiffness matrices $[k_{tt}^{el}]$, $[k_{tr}^{el}]$ and $[k_{rr}^{el}]$, the elemental electro-elastic coupling stiffness and magneto-elastic coupling stiffness matrices are $[k_{t\phi}^{el}]$, $[k_{r\phi}^{el}]$ and $[k_{t\psi}^{el}]$, $[k_{r\psi}^{el}]$, respectively; $[k_G^{el}]$ is the elemental geometric stiffness matrix; $\{F_t^{el}\}$ is the elemental mechanical load vector; $[k_{\phi\phi}^{el}]$ and $[k_{\psi\psi}^{el}]$ are the elemental electric and elemental magnetic stiffness matrices, respectively. The elemental matrices and vectors are given by

$$\begin{aligned}
[k_{tt}^{el}] &= [k_{tb}^{el}] + [k_{ts}^{el}], [k_{tr}^{el}] = [k_{trb}^{el}] + [k_{trs}^{el}], [k_{rr}^{el}] = [k_{rrb}^{el}] + [k_{rrs}^{el}], \\
[k_{t\phi}^{el}] &= [k_{\phi t}^{el}]^T, [k_{t\psi}^{el}] = [k_{\psi t}^{el}]^T, [k_{t\phi}^{el}] = \int_0^{a_{el}} \int_0^{b_{el}} [b_{tb}]^T [D_{t\phi}] [n_\phi] dx dy, \\
[k_{r\phi}^{el}] &= \int_0^{a_{el}} \int_0^{b_{el}} [b_{rb}]^T [D_{r\phi}] [n_\phi] dx dy, [k_{r\psi}^{el}] = \int_0^{a_{el}} \int_0^{b_{el}} [b_{rb}]^T [D_{r\psi}] [n_\psi] dx dy, \\
[k_{r\psi}^{el}] &= \int_0^{a_{el}} \int_0^{b_{el}} [b_{rb}]^T [D_{r\psi}] [n_\psi] dx dy, [k_{\phi\phi}^{el}] = \int_0^{a_{el}} \int_0^{b_{el}} [n_\phi]^T [D_{\phi\phi}] [n_\phi] dx dy, \\
[k_{\psi\psi}^{el}] &= \int_0^{a_{el}} \int_0^{b_{el}} [n_\psi]^T [D_{\psi\psi}] [n_\psi] dx dy, [k_G^{el}] = \int_0^{a_{el}} \int_0^{b_{el}} [b_G]^T [\sigma_0] [b_G] dx dy \quad (2.25)
\end{aligned}$$

where, $[D_{t\phi}]$, $[D_{r\phi}]$, $[D_{t\psi}]$, $[D_{r\psi}]$, $[D_{\phi\phi}]$ and $[D_{\psi\psi}]$ are the rigidity matrices appearing in Eq.(2.25) are given as follows:

$$\begin{aligned}
[D_{t\phi}] &= \int_{h_3}^{h_4} \{e_b\} \frac{1}{h} [1 \ 0] dz + \int_{h_1}^{h_2} \{e_b\} \frac{1}{h} [1 \ 0] dz, [D_{t\psi}] = \int_{h_2}^{h_3} \{q_b\} \frac{1}{h} dz, \\
[D_{r\phi}] &= \int_{h_3}^{h_4} [z_1]^T \{e_b\} \frac{1}{h} [1 \ 0] dz + \int_{h_1}^{h_2} [z_1]^T \{e_b\} \frac{1}{h} [1 \ 0] dz, [D_{r\psi}] = \int_{h_2}^{h_3} [z_1]^T \{q_b\} \frac{1}{h} dz, \\
[D_{\phi\phi}] &= \frac{\xi_{33}}{h} \begin{bmatrix} 1 & 0 \\ 0 & 1 \end{bmatrix}, D_{\psi\psi} = \frac{1}{h} \mu_{33}, [\sigma_0] = \begin{bmatrix} \sigma_{xx}^0 & \sigma_{xy}^0 \\ \sigma_{xy}^0 & \sigma_{yy}^0 \end{bmatrix} \quad (2.26)
\end{aligned}$$

The global equations of motion are obtained by assembling the elemental equations of motion of the MEE plate as follows:

$$\left[k_{tt}^g \right] \{d_t\} + \left[k_{tr}^g \right] \{d_r\} + \left[k_{t\phi}^g \right] \{\phi\} + \left[k_{t\psi}^g \right] \{\psi\} + [K_G] \{d_t\} = \{F_t\} \quad (2.27)$$

$$\left[k_{tr}^g \right]^T \{d_t\} + \left[k_{rr}^g \right] \{d_r\} + \left[k_{r\phi}^g \right] \{\phi\} + \left[k_{r\psi}^g \right] \{\psi\} = 0 \quad (2.28)$$

$$\left[k_{t\phi}^g \right]^T \{d_t\} + \left[k_{r\phi}^g \right]^T \{d_r\} - \left[k_{\phi\phi}^g \right] \{\phi\} = 0 \quad (2.29)$$

$$\left[k_{t\psi}^g \right]^T \{d_t\} + \left[k_{r\psi}^g \right]^T \{d_r\} - \left[k_{\psi\psi}^g \right] \{\psi\} = 0 \quad (2.30)$$

where, $\left[k_{tt}^g \right]$, $\left[k_{tr}^g \right]$ and $\left[k_{rr}^g \right]$ are the elastic global stiffness matrices; $\left[k_{t\phi}^g \right]$ and $\left[k_{r\phi}^g \right]$ are the electro-elastic coupling global stiffness matrices; $\left[k_{t\psi}^g \right]$ and $\left[k_{r\psi}^g \right]$ are the magneto-elastic coupling global stiffness matrices; $[K_G]$ is the global geometric stiffness matrix; $\{F_t\}$ is the global mechanical load vector; $\left[k_{\phi\phi}^g \right]$ and $\left[k_{\psi\psi}^g \right]$ are the global electric and the global magnetic stiffness matrices, respectively. Solving the global equations of motion (Eqs. (2.28) - (2.30)) to obtain the global generalized displacement vector $\{d_t\}$ and $\{d_r\}$ by condensing the global degrees of freedom for $\{\phi\}$ and $\{\psi\}$ in terms of $\{d_r\}$ as follows:

$$\begin{aligned} \{\psi\} &= \left[k_{\psi\psi}^g \right]^{-1} \left[k_{t\psi}^g \right]^T \{d_t\} + \left[k_{\psi\psi}^g \right]^{-1} \left[k_{r\psi}^g \right]^T \{d_r\}, \\ \{\phi\} &= \left[k_{\phi\phi}^g \right]^{-1} \left[k_{t\phi}^g \right]^T \{d_t\} + \left[k_{\phi\phi}^g \right]^{-1} \left[k_{r\phi}^g \right]^T \{d_r\}, \\ \{d_r\} &= -[K_3]^{-1} [K_2]^T \{d_t\} \end{aligned} \quad (2.31)$$

Now, substituting Eq. (2.31) in Eq. (2.27) and upon simplification, we obtain the global equations of motion in terms of the global translational degrees of freedom as follows:

$$\begin{aligned} & \left([K_1] - [K_2][K_3]^{-1}[K_2]^T \right) \{d_t\} + [K_G] \{d_t\} = \{F_t\}, \\ & [K] \{d_t\} + [K_G] \{d_t\} = \{F_t\} \\ & \text{and } [K] = \left([K_1] - [K_2][K_3]^{-1}[K_2]^T \right) \end{aligned} \quad (2.32)$$

where, the global aggrandized matrices are given as follows:

$$\begin{aligned}
[K_1] &= [k_{tt}^g] + [k_{t\phi}^g][k_{\phi\phi}^g]^{-1}[k_{t\phi}^g]^T + [k_{t\psi}^g][k_{\psi\psi}^g]^{-1}[k_{t\psi}^g]^T, \\
[K_2] &= [k_{tr}^g] + [k_{t\phi}^g][k_{\phi\phi}^g]^{-1}[k_{r\phi}^g]^T + [k_{t\psi}^g][k_{\psi\psi}^g]^{-1}[k_{r\psi}^g]^T, \\
[K_3] &= [k_{rr}^g] + [k_{r\phi}^g][k_{\phi\phi}^g]^{-1}[k_{r\phi}^g]^T + [k_{r\psi}^g][k_{\psi\psi}^g]^{-1}[k_{r\psi}^g]^T. \quad (2.33)
\end{aligned}$$

The buckling criterion is achieved based on the neutral equilibrium method (Jadhav and Bajoria 2013). According to this method, the corresponding load at which the structure attains equilibrium in both straight and the slightly bent configuration is defined as a critical load. The geometric matrix is represented by $\lambda[K_G]$, where λ is the scalar multiplier. The scalar multiplier is obtained such that, the equilibrium is established for both the reference configuration $\{d_t\}$ and slightly deformed configuration $\{d_t\} + \{\delta d_t\}$ (Jadhav and Bajoria 2013).

$$([K] + \lambda[K_G])\{d_t\} = \{F_t\} \quad (2.34)$$

$$([K] + \lambda[K_G])(\{d_t\} + \{\delta d_t\}) = \{F_t\} \quad (2.35)$$

Subtracting Eq. (2.35) from Eq. (2.34) yields the eigenvalue problem

$$([K] + \lambda[K_G])\{\delta d_t\} = 0 \quad (2.36)$$

here, the critical buckling load is the eigenvalue with the lowest magnitude and the displacement vector $\{\delta d_t\}$ represents the corresponding buckled mode shape. Further, the static behaviour of the MEE plate is assessed by neglecting the geometrical stiffness matrix from Eq. (2.34).

2.4. RESULTS AND DISCUSSION

2.4.1 Buckling analysis

Buckling analysis of layered MEE plate is carried out in order to assess the nature of stability by solving an eigenvalue problem. Such eigenvalue problem yields eigen values i.e., critical buckling loads and their corresponding mode shapes in terms

of eigen vectors. The material property of the MEE composite is specified in Table 2.1. The commonly used two types of stacking sequence are studied in the present analysis, one being B/F/B i.e., the magnetostrictive layer being sandwiched between two piezoelectric layers and the other F/B/F, wherein the piezoelectric layer is sandwiched between two magnetostrictive layers. The buckling characteristics of the MEE plate are evaluated for different span to thickness ratio, aspect ratio, and boundary condition. In addition, the effect of load factor on the critical buckling load is subsequently investigated. The MEE plate considered for the analysis is having an aspect ratio of $a/b = 1$ and a span to thickness ratio of $a/h = 100$ with each layer has equal thickness. The non-dimensional critical buckling load is obtained using the relation $\lambda_{cr} = \lambda a^2 / H^3 C_{11}$. In this chapter, buckling analysis is performed for three boundary conditions i.e., CCCC (all sides clamped), CCCF (three clamped sides and one being free), FCFC (two clamped and two free sides) and are given as follows (Ansari and Gholami, 2016):

Clamped edge

$$\text{at } x = 0, x = a \quad u_0 = v_0 = w_0 = \theta_x = \theta_y = \theta_z = \phi = \psi = 0$$

$$\text{at } y = 0, y = b \quad u_0 = v_0 = w_0 = \theta_x = \theta_y = \theta_z = \phi = \psi = 0$$

Free edge

$$\text{at } x = y, x = a \quad u_0 = v_0 = w_0 = \theta_x = \theta_y = \theta_z = \phi = \psi \neq 0$$

$$\text{at } y = 0, y = b \quad u_0 = v_0 = w_0 = \theta_x = \theta_y = \theta_z = \phi = \psi \neq 0 \quad (2.37)$$

2.4.2 Validation

To the best of author's knowledge, the research on buckling of layered MEE plate is not found in the open literature. Hence, to assess the effectiveness of proposed formulation in solving a stability problem, the buckling analysis of multilayered laminate composites studied by Reddy (2004) has been considered. A three layer simply supported symmetric cross-ply square plates having material properties $E_1 = 25E_2$, $G_{12} = G_{13} = 0.5E_2$, $G_{23} = 0.2E_2$, $\nu_{12} = 0.25$, $K = 5/6$ is considered to analyse the buckling behaviour. In this regard, the coupled constitutive equations of the MEE

plate is decoupled and implemented for the analysis of laminated composite plate. The convergence study has been carried out by considering different FE mesh sizes. For the mesh size of 20×20 , the present solutions are well in agreement with the existing ones as shown in Table 2.2, and apparently for all the subsequent analysis, a mesh size of 20×20 (400 elements) has been imparted. Since, the validation is executed for the buckling behaviour, buckling characteristics of MEE plate under in-plane loads are discussed at first in the following section.

Table 2.1: Material properties of BaTiO₃ and CoFe₂O₄ (Pan and Heyliger 2003)

Material properties	BaTiO ₃	CoFe ₂ O ₄
$C_{11} = C_{22}$ (10^9 N/m ²)	166	286
C_{12} (10^9 N/m ²)	77	173
$C_{13} = C_{23}$ (10^9 N/m ²)	78	170.5
C_{33} (10^9 N/m ²)	162	269.5
$C_{44} = C_{55}$ (10^9 N/m ²)	43	45.3
C_{66} (10^9 N/m ²)	44.5	56.5
ρ (kg/m ³)	5300	5800
$e_{31} = e_{32}$ (C/m ²)	- 4.4	-
e_{33} (C/m ²)	18.6	-
$e_{24} = e_{15}$ (C/m ²)	11.6	-
$\zeta_{11} = \zeta_{22}$ (10^{-9} C/Nm ²)	11.2	0.08
$\mu_{11} = \mu_{22}$ (10^{-6} Ns ² /C ²)	5	- 590
μ_{33} (10^{-6} Ns ² /C ²)	10	157
$q_{31} = q_{32}$ (N/Am)	-	180.3
q_{33} (N/Am)	-	699.7
$q_{24} = q_{15}$ (N/Am)	-	550

2.4.3 Effect of uniaxial and biaxial compression

Firstly, buckling analysis of CCCC MEE plates subjected to uniaxial and biaxial compression is investigated. The influence of in-plane compression on the non-dimensional critical buckling load and their corresponding mode shapes are analysed. The buckling mode shapes and their respective buckling loads are presented

in Figure 2.3. It can be observed from Fig. 2.3 that the buckling loads get halved for the bi-axial load in comparison with uniaxial loading case. It is also evident from the results that the first, fifth and sixth modes of the MEE plate under biaxial compression buckled in the opposite direction in comparison with uniaxial compression, while the nature of buckling mode remains the same in both the cases.

Table 2.2: Non-dimensional critical buckling load for the simply supported three layered composite plate under uniaxial and biaxial compression ($a/b = 1$)

a/h ratio	Type of load	Non-dimensional critical buckling load				
		Present (12×12)	Present (16×16)	Present (20×20)	Present (30×30)	Reddy (2004)
10	Uniaxial	15.2636	14.9178	14.8690	14.8694	15.2890
	Biaxial	7.6318	7.4589	7.4345	7.4347	7.6445
50	Uniaxial	22.4276	22.1628	22.0418	22.0422	22.9781
	Biaxial	11.2138	11.0814	11.0209	11.0211	11.4890
100	Uniaxial	23.0434	22.8826	22.8461	22.8467	23.3633
	Biaxial	11.5217	11.4413	11.4230	11.4233	11.6820

2.4.4 Effect of stacking sequence

In this section, the effect of stacking sequence on the buckling behaviour of MEE plates is considered for the evaluation. Two stacking sequences of MEE plate are investigated under CCCC boundary condition. Figure 2.4 displays the buckling behaviour of the B/F/B and the F/B/F MEE plates. It may be observed from the plots shown in Fig. 2.4 that the MEE plate with F/B/F stacking sequence yield higher critical buckling load than the B/F/B stacking configuration. It may be due to the fact that the F/B/F configuration exhibits higher stiffness and hence larger buckling load. Figure 2.5 illustrates the first six non-dimensional critical buckling loads and their corresponding mode shapes for both the B/F/B and F/B/F stacking sequences of the

MEE plate. It may be observed from these results that the stacking sequence not only affects the critical buckling loads but also their corresponding mode shapes. In addition, as noticed from Figure 2.5, the first, third, fifth and sixth modes display buckling in opposite direction for F/B/F sequence in comparison with the B/F/B stacking sequence while the nature of buckling remains the same for both.

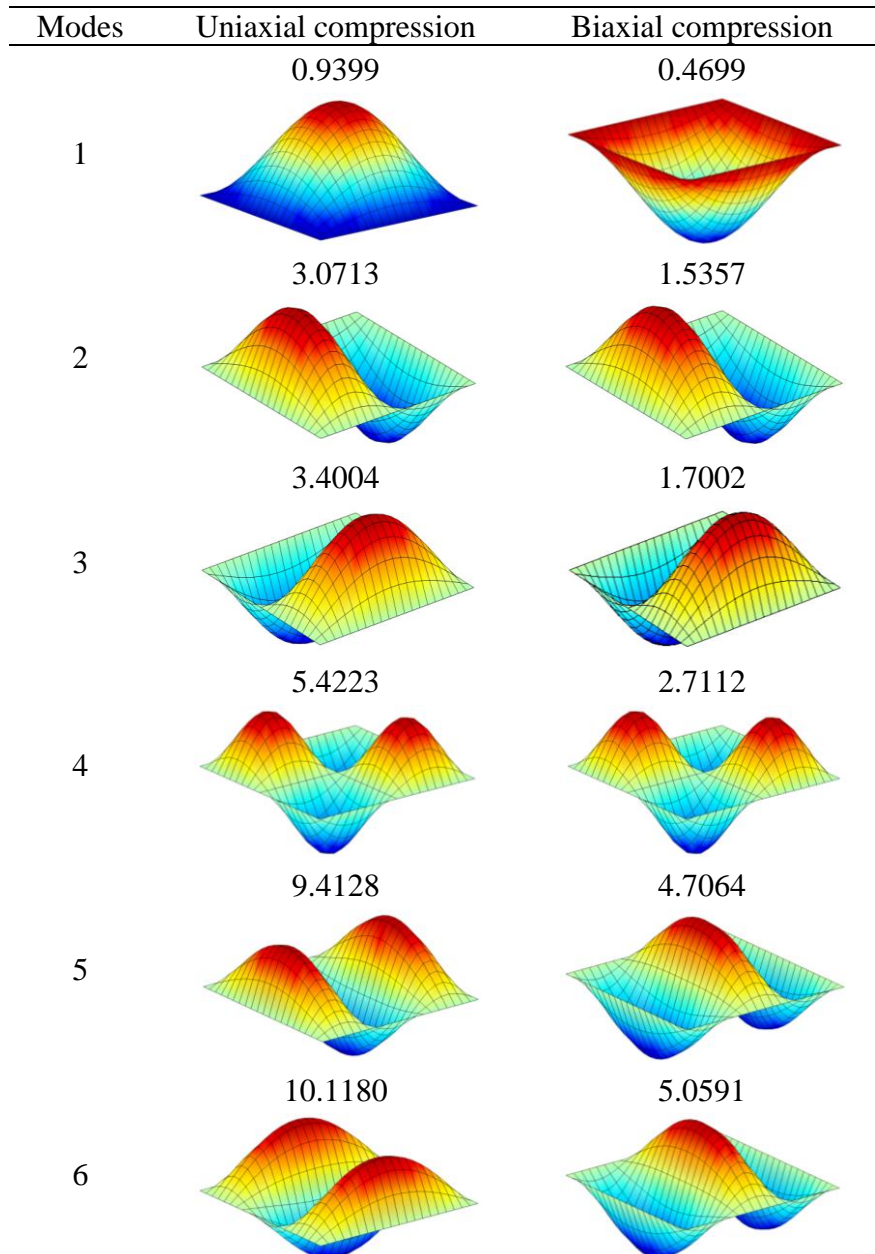


Figure 2.3: First six buckling mode shapes of B/F/B MEE plate under uniaxial and biaxial compression for CCCC boundary condition ($a/b = 1$, $a/h = 100$)

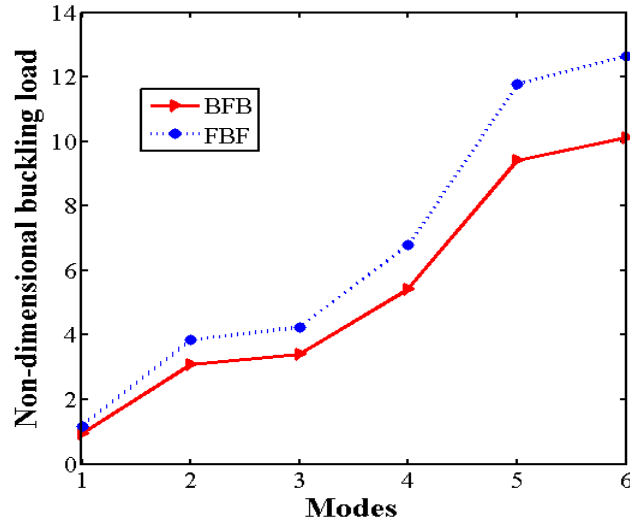


Figure 2.4: Critical buckling load ($\lambda_{cr} = \lambda a^2 / H^3 C_{11}$) for B/F/B and F/B/F MEE plate subjected to uniaxial compression (CCCC, $a/b = 1$, $a/h = 100$).

2.4.5 Effect of lateral load parameter

In a bi-axial buckling condition, the lateral load on one of the in-plane directions is increased incrementally while in the other direction, the load is kept constant. The effect of such incremental loading on the buckling behaviour of the MEE plate is investigated. A bar graph plotted for buckling load against the load factor in Figure 2.6 demonstrates the decrease in non-dimensional buckling load with the incremental increase in load factor. It can also be observed that the CCCC boundary condition possesses the highest buckling load. This can be attributed to the fact that the CCCC plate possesses larger flexural rigidity at the plate edges in comparison to other two boundary conditions.

2.4.6 Effect of aspect ratio (a/b)

The buckling characteristics of the MEE plate is studied for different aspect ratio (a/b). The non-dimensional critical buckling loads are obtained for different aspect ratio (a/b). The study of influence of aspect ratio (a/b) is extended for four different span to thickness ratio and boundary condition as shown in Figure 2.7 - Figure 2.9. It is evident from the plots (Figure 2.7 - Figure 2.9) that the buckling load decreases with increase in aspect ratio irrespective of the boundary condition and a/h ratio involved. The buckling load decreases rapidly for the lower aspect ratio (a/b) while

for the higher aspect ratio, decay is marginal. In the case of CCCF plate, it is observed that for all the a/h ratios evaluated, buckling load converges at higher aspect ratios.

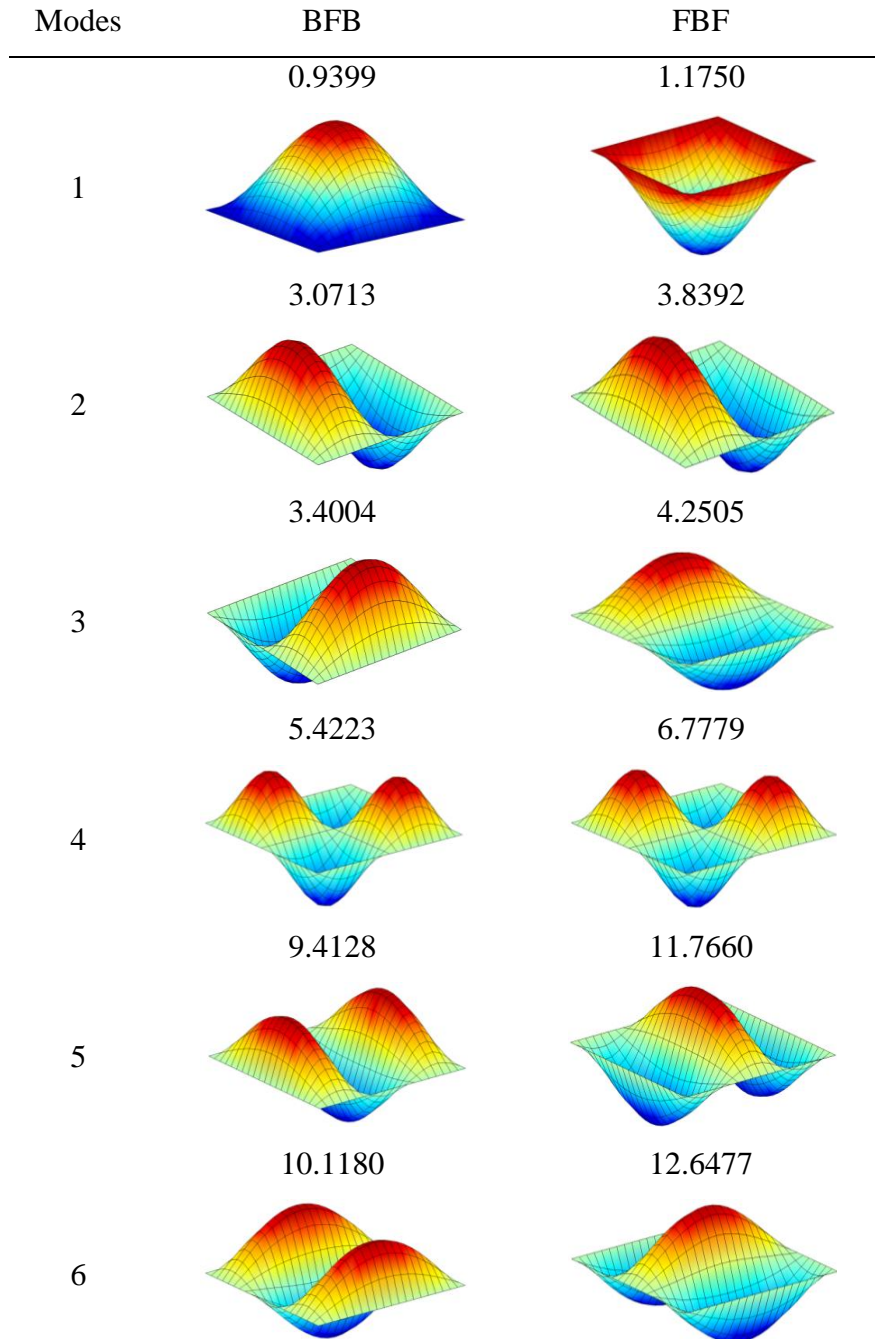


Figure 2.5: First six non-dimensional critical buckling loads ($\lambda_{cr} = \lambda a^2 / H^3 C_{11}$) and mode shapes of B/F/B and F/B/F plate subjected to uniaxial compression under clamped-clamped (CCCC) boundary condition ($a/b = 1$, $a/h = 100$)

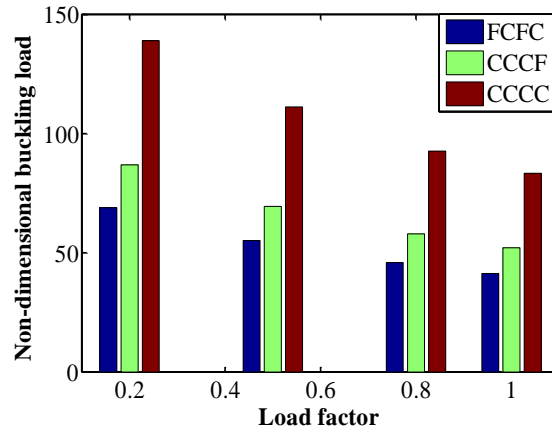
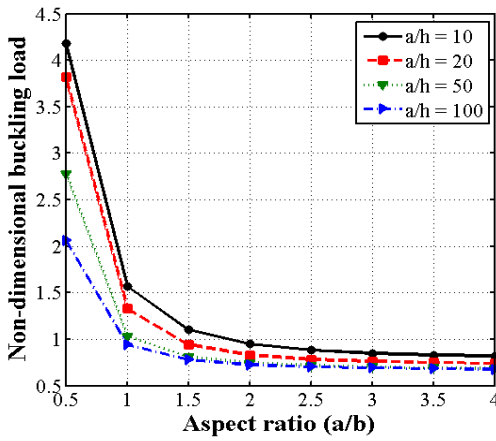
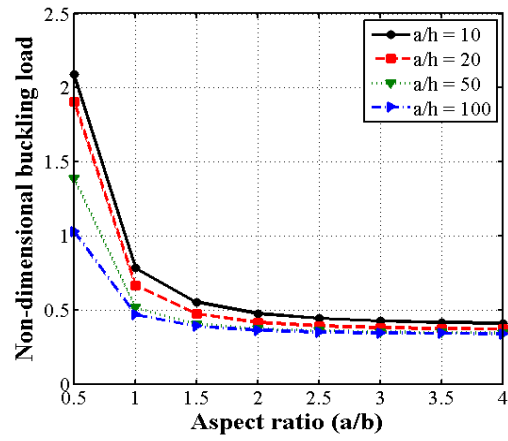


Figure 2.6: Effect of load factor on non-dimensional critical buckling load

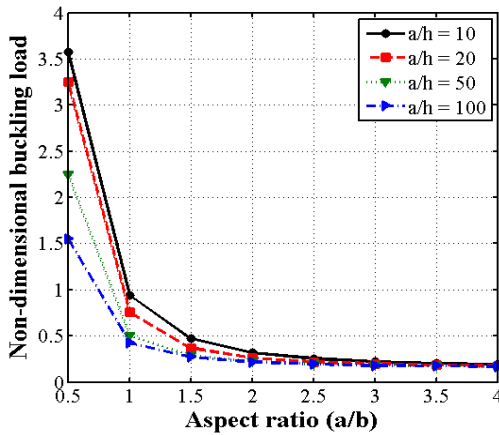


(a) Uniaxial compression

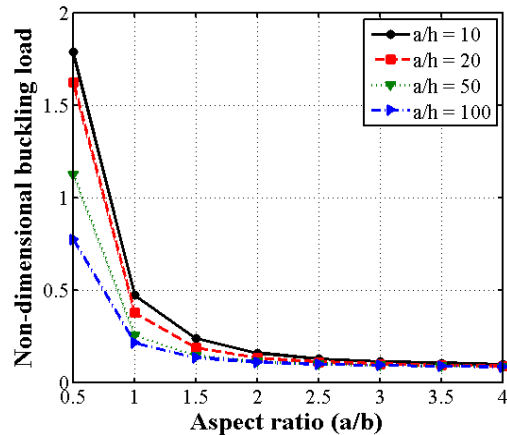


(b) Biaxial compression

Figure 2.7: Effect of aspect ratio on non-dimensional buckling load of CCCC MEE (B/F/B) plate



(a) Uniaxial compression



(b) Biaxial compression

Figure 2.8: Effect of aspect ratio on non-dimensional buckling load of CCCF MEE (B/F/B) plate.

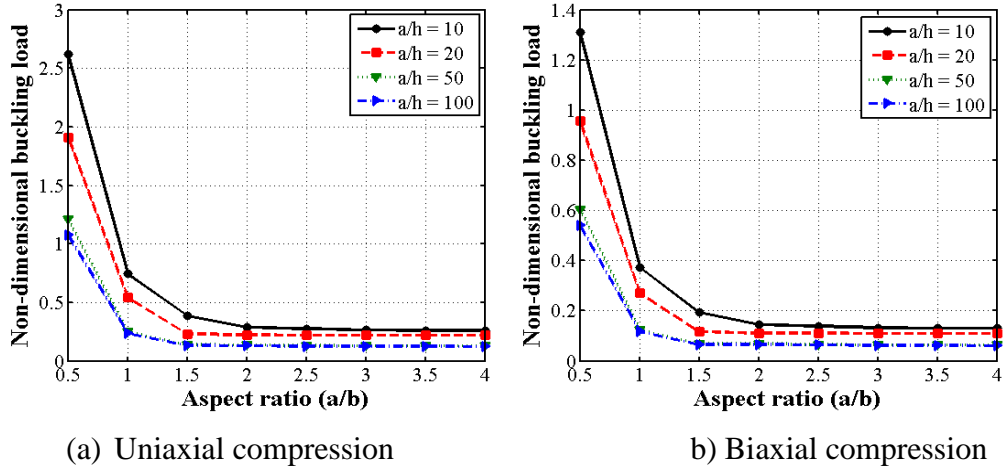


Figure 2.9: Effect of aspect ratio on non-dimensional buckling load of FCFC MEE (B/F/B) plate.

2.4.7 Effect of span to thickness (a/h) ratio

The buckling behaviour of CCCC MEE plate is evaluated for different a/h ratios to analyse their effect on buckling loads. Table 2.3 presents the critical buckling loads obtained for the different span to thickness ratio ($a/h = 20, 50$ and 100) of the MEE plate under uniaxial and biaxial loading conditions. It is observed that with the increase in thickness ratio, the critical buckling load decreases. The effect of the span to thickness ratio on the corresponding mode shapes is also presented in Figure 2.10. From the plots, it is evident that the mode shapes and their corresponding critical buckling loads are influenced by the span to thickness ratio of the plate. Further, it can be observed that the nature of the modes remains the same for both the a/h ratio compared; while for the first, third, fourth and fifth modes, only the direction of buckling changes. It can be noted that for an eigenvalue buckling problem, the direction of mode shape distribution retains less importance and the nature of buckling mode shape for both the span to thickness ratio can be considered identical.

Table 2.3: Critical buckling loads for B/F/B plate at different span to thickness ratio

a/h ratio	Uniaxial compression					Biaxial compression				
	CCCC	CCCF	FCFC	FFFF	FFFC	CCCC	CCCF	FCFC	FFFF	FFFC
20	1.3335	0.7559	0.5405	0.0914	0.4630	0.6667	0.3779	0.2702	0.0457	0.2315
50	1.0312	0.4317	0.2703	0.0174	0.1888	0.5156	0.2158	0.1351	0.0087	0.0944
100	0.9399	0.4289	0.2519	0.0024	0.1364	0.4699	0.2144	0.1259	0.0012	0.0682

2.4.8 Effect of boundary conditions

Three different boundary conditions are studied and their effects on buckling loads and corresponding mode shapes are assessed. Figure 2.11 presents the buckling loads and corresponding mode shapes for CCCC, CCCF and FCFC boundary conditions. It can be noticed that the largest buckling load is obtained for the most constrained CCCC plate and the lowest for the least constrained FCFC plate. Additionally, the effect of different boundary conditions is highlighted via corresponding mode shapes.

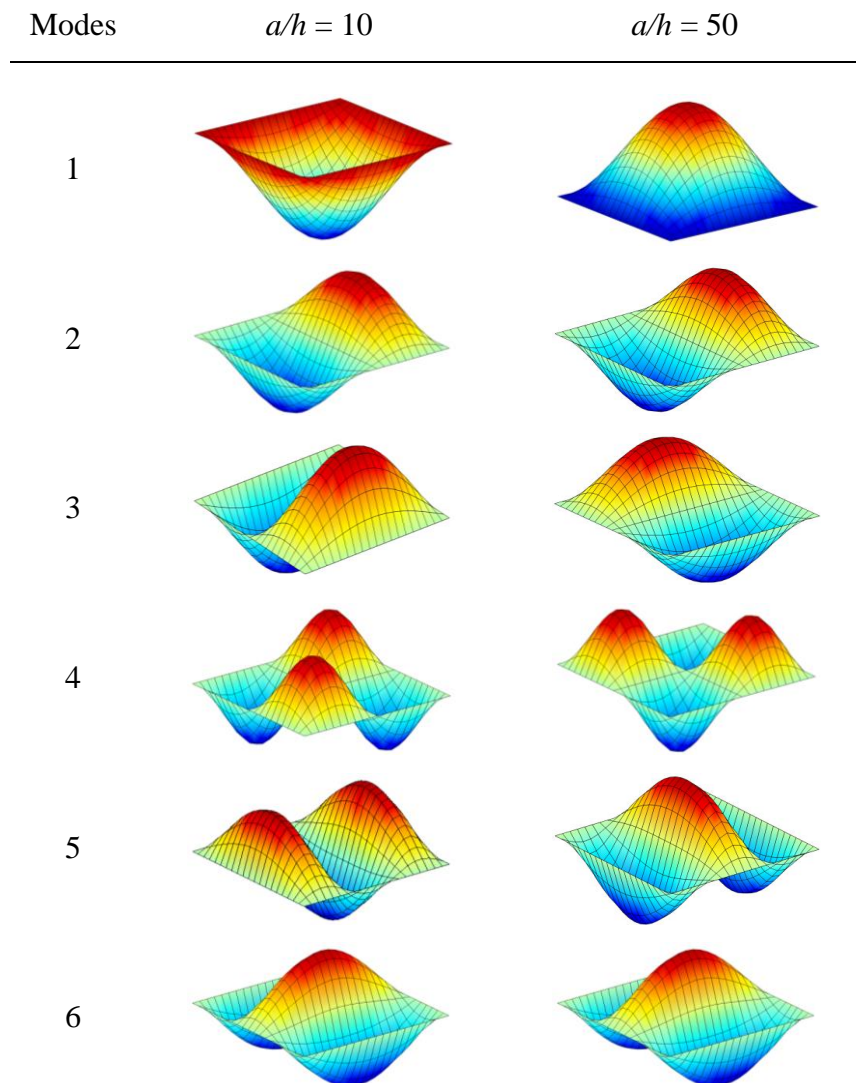


Figure 2.10: Comparison of first six non-dimensional buckling mode shapes of B/F/B at $a/h = 10$ and 50 subjected to uniaxial compression under clamped-clamped (CCCC) boundary condition

2.4.9 Static studies

The static deflection of MEE plate subjected to sinusoidal and uniformly distributed load (UDL) is studied for different boundary conditions. The static deflection for different boundary conditions of the B/F/B MEE plate subjected to sinusoidal load is presented in Figure 2.12(a)-(d) while Figure 2.13(a)-(d) depicts for the F/B/F MEE plate. Further, Figure 2.14(a)-(c) and Figure 2.15(a)-(c) illustrate the results for the B/F/B and F/B/F MEE plate subjected to UDL, respectively. The static deflection of the F/B/F plate is observed to be lower than the B/F/B plate for all the investigated boundary conditions.

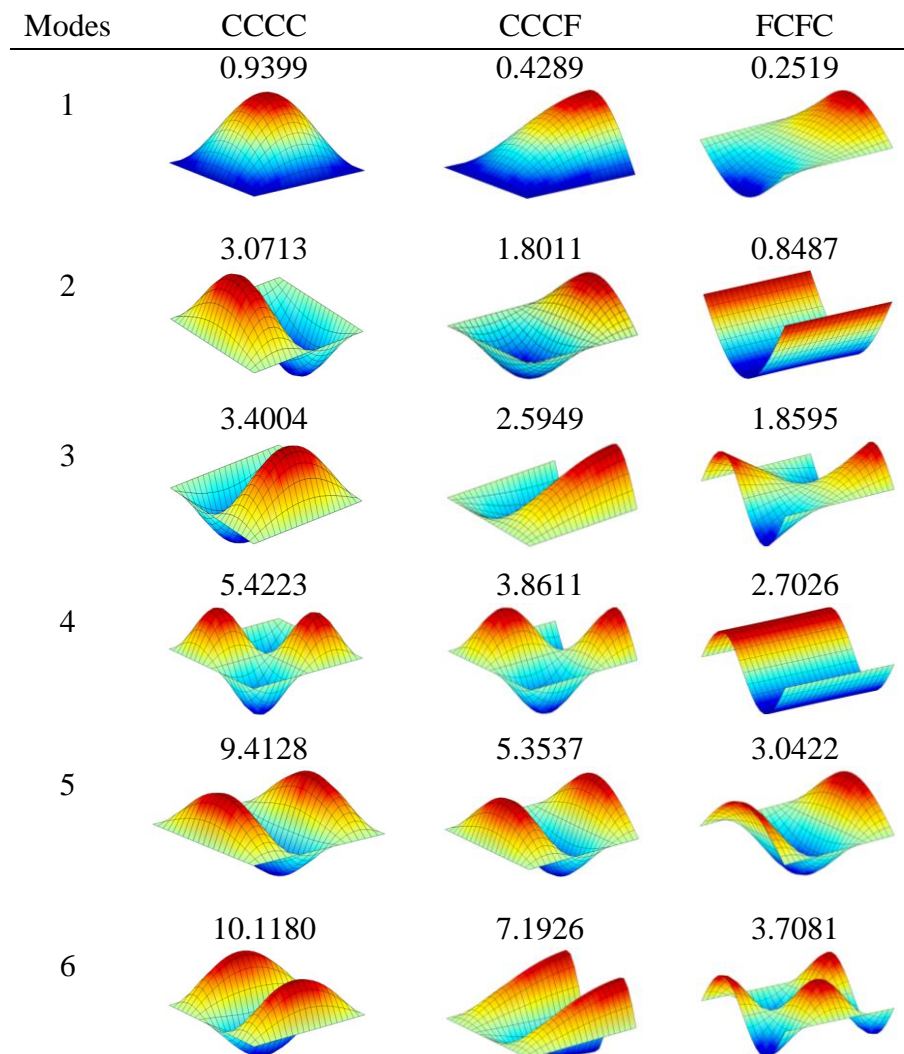
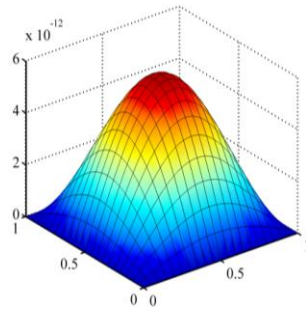
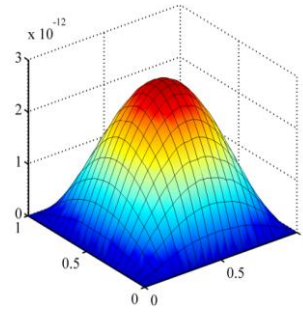


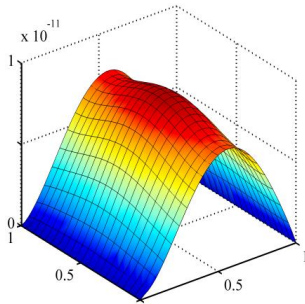
Figure 2.11: Comparison of first six non-dimensional buckling loads and their mode shapes for different boundary condition of B/F/B MEE plate ($a/b = 1$, $a/h = 100$)



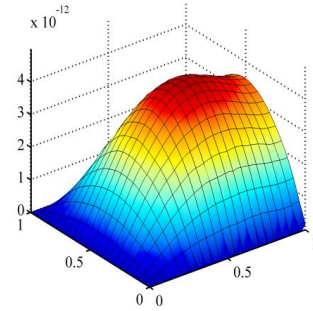
(a) SSSS



(b) CCCC

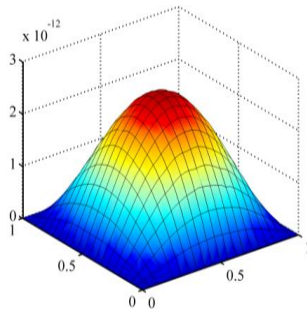


(c) FCFC

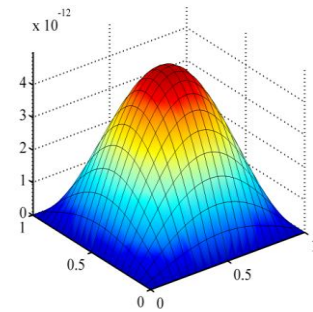


(d) CCCF

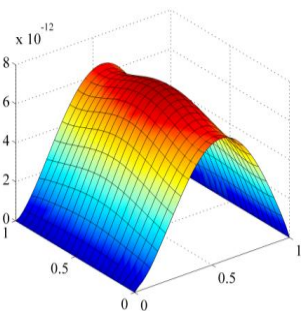
Figure 2.12: Static deflection (in meters) of BFB MEE plate under sinusoidal load



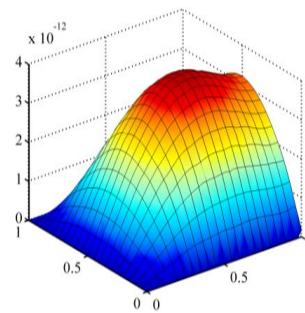
(a) SSSS



(b) CCCC



(c) FCFC



(d) CCCF

Figure 2.13: Static deflection (in meters) of FBF MEE plate under sinusoidal load

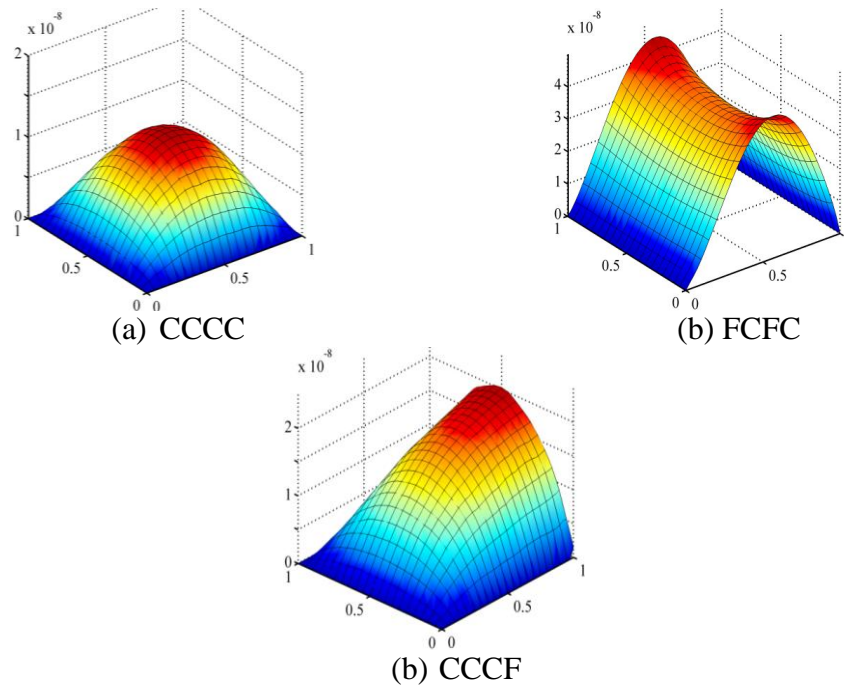


Figure 2.14: Static deflection (in meters) of BFB MEE plate subjected to UDL

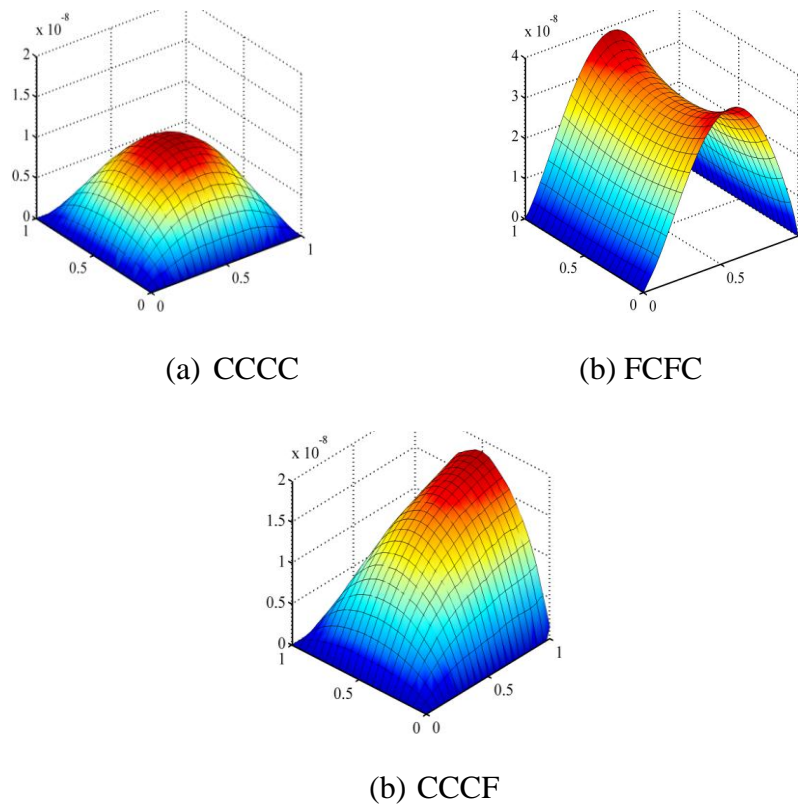


Figure 2.15: Static deflection (in meters) of FBF MEE plate subjected to UDL

2.5 CONCLUSIONS

The present chapter describes the buckling analysis of multilayered MEE plates using finite element approach considering the FSDT for displacement fields. The influence of boundary conditions, aspect ratio, stacking sequence, span to thickness ratio and load factor was studied. From the present evaluation on the parameters of critical buckling load and mode shapes, the following conclusions could be drawn. Under the biaxial compression, the critical buckling loads halved in comparison with uniaxial compression and their corresponding mode shapes are also affected by the type of compression applied. The effect of stacking sequence is found to be significant for the F/B/F stacking sequence exhibiting larger buckling strength over B/F/B configuration. Further, the buckling load decreases with increase in aspect ratio and span to thickness ratio of the MEE plate. Also, the highest constrained CCCC MEE plate witnessed largest buckling strength. In addition, the effect of load factor also exhibited a significant influence on critical buckling load. Further, for all the considered boundary conditions, the FBF plate exhibits the lowest deflection in the thickness direction.

Chapter 3

STATIC CHARACTERISTICS AND FREE VIBRATION ANALYSIS OF MULTILAYERED SKEW MAGNETO-ELECTRO-ELASTIC PLATES

This chapter presents a finite element (FE) model for static analysis and free vibration behaviour of layered skew magneto-electro-elastic (SMEE) plates by incorporating the shear deformation theory. The coupled constitutive equations of the MEE materials are used to derive the FE model accounting the effect of electro-elastic and magneto-elastic couplings. The displacement, electric potential, and magnetic potential are considered as primary variables while the stresses, electric displacement, and magnetic induction are derived from the primary variables using constitutive equations. Influence of boundary conditions and material stacking sequences on the natural frequency, displacement, and stresses of the SMEE plates has been investigated. Particular emphasis has been placed to study the effect of skew angles and thickness ratios on the natural frequencies, stresses, electric displacement, and magnetic induction. The present study reveals that skew angle and thickness ratio significantly influence the structural behaviour of SMEE plates.

3.1 INTRODUCTION

Skew plates occupy importance in many engineering applications as geometric changes implemented to the rectangular plate influence various response characteristics. Consequently, this chapter presents the development of FE model to investigate the static analysis and the free vibration behaviour of layered skew magneto-electro-elastic (SMEE) plates using shear deformation theory. Special attention has been paid to study the effect of skew angle on the natural frequencies, displacements, potentials, stresses, electric displacement, and magnetic induction of the SMEE plates. Effect of thickness ratios, layer stacking sequence, and boundary conditions on the behavior of SMEE plates has been thoroughly investigated.

3.2. PROBLEM DESCRIPTION AND GOVERNING EQUATION

A schematic diagram of a SMEE plate is illustrated in Figure 3.1(a), while Figure 3.1(b) illustrates the top view of the SMEE plate. The geometrical dimensions of the SMEE plate are a , b and H representing the length, the width and the total thickness of the plate, respectively. The skew angle of the SMEE plate is α and the layers have identical thickness h_i ($i = 1, 2, 3$). Since, the structure is composed of layers of dissimilar materials, the kinematics of deformation of the SMEE plate may be difficult to define by using an equivalent single layer displacement theory because of the fact that the material properties of the adjacent continua of the overall plate differ in order. Hence, the 1-2 shear deformation theory has been incorporated to derive the deformations of the SMEE plate.

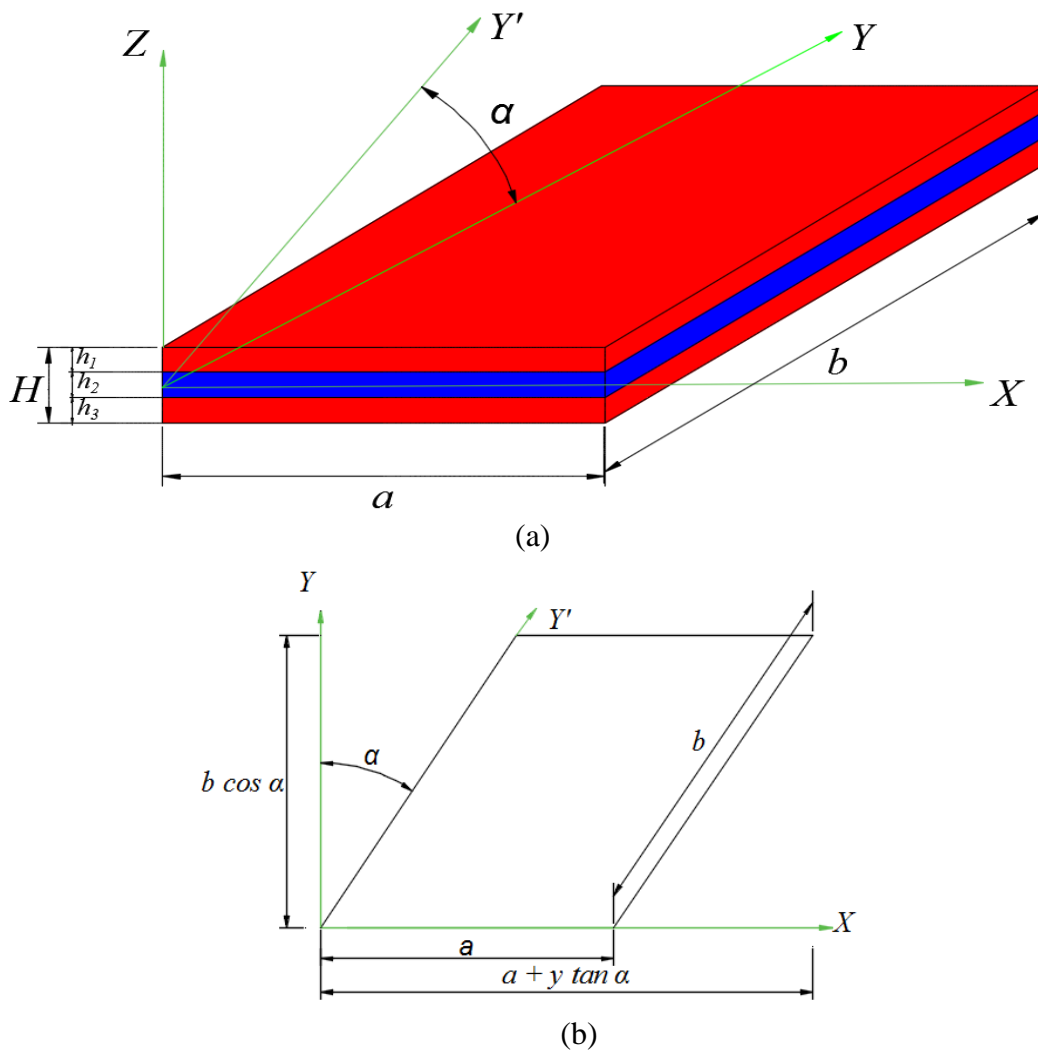


Figure 3.1: (a) SMEE plate with B/F/B stacking (b) Top view of the SMEE plate

Consequently, the axial displacements u and v at any point in the SMEE plate along the x - and y - direction, and the transverse displacement w at any point in the SMEE plate can be expressed as (Hildebrand et al. 1949)

$$\begin{aligned} u(x, y, z, t) &= u_0(x, y, t) + z \theta_x(x, y, t) \\ v(x, y, z, t) &= v_0(x, y, t) + z \theta_y(x, y, t) \\ w(x, y, z, t) &= w_0(x, y, t) + z \theta_z(x, y, t) + z^2 \kappa_z(x, y, t) \end{aligned} \quad (3.1)$$

where, u_0 and v_0 are the translational displacements at any point on the mid-plane of the plate along x - and y - directions while w_0 is the transverse displacement along z - direction at any point in the SMEE plate. θ_x and θ_y denote the generalized rotation of the normal to the middle plane of the SMEE plate about the y - and x - axis, respectively. θ_z and κ_z are the generalized rotational displacements for the SMEE plate with respect to the thickness coordinate. For the ease of computation, rotational and translational displacements are considered separately as follows:

$$\{d_t\} = [u_0 \ v_0 \ w_0]^T, \{d_r\} = [\theta_x \ \theta_y \ \theta_z \ \kappa_z]^T \quad (3.2)$$

To overcome the shear locking in thin structures and to emphasize the computation of elemental stiffness matrices linked with the transverse shear deformation, the selective integration rule has been employed. To address such specific need, the state of strain at any point in the plate is separated by in-plane and transverse normal strain vector ε_b and the transverse shear strain vector ε_s can be expressed similar to Eq. (2.3). Making use of the displacement field given in Eq. (3.1) and from the linear strain-displacement relations, the strain vectors ε_b and ε_s defining the state of in-plane, transverse normal and transverse shear strain at any point in the SMEE plate can be expressed as

$$\{\varepsilon_b^k\} = \{\varepsilon_{bt}\} + [Z_1]\{\varepsilon_{rb}\}, \{\varepsilon_s^k\} = \{\varepsilon_{ts}\} + [Z_2]\{\varepsilon_{rs}\} \quad (3.3)$$

wherein k designates the layer number for the overall plate, the transformation matrices $[Z_1]$ and $[Z_2]$ are expressed as

$$[Z_1] = \begin{bmatrix} z & 0 & 0 & 0 & 0 \\ 0 & z & 0 & 0 & 0 \\ 0 & 0 & 0 & 1 & 2z \\ 0 & 0 & z & 0 & 0 \end{bmatrix}, [Z_2] = \begin{bmatrix} 1 & 0 & z & 0 & z^2 & 0 \\ 0 & 1 & 0 & z & 0 & z^2 \end{bmatrix} \quad (3.4)$$

while the generalized strain vectors appearing in Eq. (3.3) are given by

$$\begin{aligned} \{\varepsilon_{bt}\} &= \begin{bmatrix} \frac{\partial u_0}{\partial x} & \frac{\partial v_0}{\partial y} & 0 & \frac{\partial u_0}{\partial y} + \frac{\partial v_0}{\partial x} \end{bmatrix}, \{\varepsilon_{ts}\} = \begin{bmatrix} \frac{\partial w_0}{\partial x} & \frac{\partial w_0}{\partial y} \end{bmatrix} \text{ and} \\ \{\varepsilon_{rb}\} &= \begin{bmatrix} \frac{\partial \theta_x}{\partial x} & \frac{\partial \theta_y}{\partial y} & \frac{\partial \theta_x}{\partial x} + \frac{\partial v_0}{\partial x} & \theta_z & \kappa_z \end{bmatrix} \end{aligned} \quad (3.5)$$

Analogous to the strain vectors given in Eq. (2.3), the state of stress at any point in the SMEE plate can be written similar to Eq. (2.7). Considering the effect of coupled fields, the constitutive equations for the SMEE plate are similar to Eqs.(2.8) – (2.9).

The electric coefficient matrix $\{e_b^k\}$ and the magnetic coefficient matrix $\{q_b^k\}$ are given by

$$\{e_b^k\} = \{e_{31} \ e_{32} \ e_{33} \ e_{36}\}^T, \{q_b^k\} = \{q_{31} \ q_{32} \ q_{33} \ q_{36}\}^T \quad (3.6)$$

Employing the principle of virtual work the governing equations for the SMEE plate is established as

$$\begin{aligned} \sum_{k=1}^3 \left(\int_{A^k} \delta \{ \varepsilon_b^k \} \{ \sigma_b^k \} dA^k + \int_{A^k} \delta \{ \varepsilon_s^k \} \{ \sigma_s^k \} dA^k + \int_{A^k} \delta \{ d_t \}^T \rho^k \{ \ddot{d}_t \} dA^k \right) - \int_{A^t} \delta E_z^t D_z^t dA^t \\ - \int_{A^b} \delta E_z^b D_z^b dA^b - \int_{A^m} \delta H_z^m B_z^m dA^m - \int_{A^{el}} \delta \{ d_t \}^T F_t dA^{el} = 0 \end{aligned} \quad (3.7)$$

where, A^k ($k = 1, 2, 3$) indicates the volume of the respective layer, F_t is the applied surface traction force on the top surface area A^{el} , ρ^k denotes the mass density of the k^{th} layer and δ is the symbol representing the first variation. A^t , A^b and A^m represents the volume of the top piezoelectric, the bottom piezoelectric and the middle magnetostrictive layer, respectively. E_z^t , E_z^b and D_z^t , D_z^b are the electric fields and the electric displacements of the top and bottom layers of the SMEE plate whereas H_z^m and B_z^m are the magnetic field and magnetic induction in the middle layer, respectively. The transverse electric field (E_z) related to the electric potential and the transverse magnetic field (H_z) is related to the magnetic potential in accordance with the Maxwell's equation similar to the derived equations (Eqs. (2.14) – (2.15)) in the previous chapter.

3.2.1. Finite element formulation for skew magneto-electro-elastic plate

The SMEE plate is discretized by using eight noded iso-parametric elements. In accordance with Eq. (3.2), the generalized displacement vectors $\{d_{ti}\}$ and $\{d_{ri}\}$ associated with the i^{th} node (where, $i = 1, 2, 3, \dots, 8$) of an element can be expressed as

$$\{d_{ti}\} = [u_{0i} \ v_{0i} \ w_{0i}]^T \text{ and } \{d_{ri}\} = [\theta_{xi} \ \theta_{yi} \ \theta_{zi} \ \kappa_{zi}]^T \quad (3.8)$$

At any point within the element, the generalized displacement vectors $\{d_t\}$ and $\{d_r\}$, the magnetic potential vector $\{\psi\}$ and the electric potential vector $\{\phi\}$ can be expressed in terms of nodal generalized displacement vectors $\{d_t^{\text{el}}\}$ and $\{d_r^{\text{el}}\}$, the nodal magnetic potential vector $\{\psi^{\text{el}}\}$ and the nodal electric potential vector $\{\phi^{\text{el}}\}$, respectively, as follows:

$$\begin{aligned} \{d_t\} &= [n_t] \{d_t^{\text{el}}\}, \quad \{d_r\} = [n_r] \{d_r^{\text{el}}\}, \\ \{\phi\} &= [\phi_1 \ \phi_2]^T = [n_\phi] \{\phi^{\text{el}}\}, \quad \{\psi\} = [\psi_1 \ \psi_2]^T = [n_\psi] \{\psi^{\text{el}}\} \\ \text{and } \{\psi^{\text{m}}\} &= [n_\psi^{\text{m}}] \{\psi^{\text{el}}\} \end{aligned} \quad (3.9)$$

in which,

$$\begin{aligned} \{d_t^{\text{el}}\} &= \left[\{d_{t1}^{\text{el}}\}^T \ \{d_{t2}^{\text{el}}\}^T \ \dots \ \{d_{t8}^{\text{el}}\}^T \right]^T, \quad \{d_r^{\text{el}}\} = \left[\{d_{r1}^{\text{el}}\}^T \ \{d_{r2}^{\text{el}}\}^T \ \dots \ \{d_{r8}^{\text{el}}\}^T \right]^T, \\ \{\phi^{\text{el}}\} &= \{\phi_{11} \ \phi_{21} \ \phi_{12} \ \phi_{22} \ \dots \ \phi_{18} \ \phi_{28}\}^T, \quad \{\bar{\psi}^{\text{el}}\} = \{\bar{\psi}_1 \ \bar{\psi}_2 \ \dots \ \bar{\psi}_8\}^T, \\ [n_t] &= [n_{t1} \ n_{t2} \ \dots \ n_{t8}]^T, \quad [n_r] = [n_{r1} \ n_{r2} \ \dots \ n_{r8}]^T, \\ [n_\phi] &= \begin{bmatrix} n_{\phi_{11}} & 0 & n_{\phi_{12}} & 0 & \dots & n_{\phi_{18}} & 0 \\ 0 & n_{\phi_{21}} & 0 & n_{\phi_{22}} & \dots & 0 & n_{\phi_{28}} \end{bmatrix}^T, \quad [n_\psi] = [n_{\psi 1} \ n_{\psi 2} \ \dots \ n_{\psi 8}]^T, \\ n_{ti} &= N_i I_t, \quad n_{ri} = N_i I_r \end{aligned} \quad (3.10)$$

where $[n_t]$, $[n_r]$, $[n_\phi]$ and $[n_\psi]$ are the (3×24) , (4×32) , (2×16) and (1×8) shape function matrices, respectively. I_t and I_r are the (3×3) and (5×5) identity matrices, respectively. N_i is the shape function of natural coordinate associated with the i^{th} node. ϕ_{1i} , ϕ_{2i} (where, $i = 1, 2, 3, \dots, 8$) are the electric potential degrees of freedom

and $\bar{\psi}_i$ are the magnetic potential degrees of freedom. The transverse electric field for the top and the bottom layer (E_z^t, E_z^b) and the transverse magnetic field for the middle layer (H_z^m) can be given similar to Eq. (2.19). Now, using Eqs. (3.3) and (3.10), the generalized strain vectors at any point within the element can be expressed similar to Eq. (2.20). The elemental equations of motion and corresponding elemental stiffness matrices for the SMEE plate can be adapted from the previous chapter and are expressed identical to Eqs. (2.21) – (2.25).

3.2.2. Skew boundary transformation

In case of skew MEE plates, the supported adjacent edges of the boundary element are not parallel to the global axes (x, y, z). Hence, in order to specify the boundary conditions at the skew edges of the plate, the displacements u^l, v^l and w^l at any point on the skew edges of the local coordinates must be restrained along the x^l, y^l - and z^l -directions. The boundary conditions can be specified conveniently by transforming the element matrices corresponding to the global axis to the local axis along the edges. A simple transformation relation can be expressed between the local degrees of freedom and the global degrees of freedom for the generalized displacement vectors of a point lying on the skew edges of the plate as follows:

$$\{d_t\} = [L_t]\{d_t^l\}, \quad \{d_r\} = [L_r]\{d_r^l\} \quad (3.11)$$

$$\{d_t^l\} = [u_0^l \ v_0^l \ w_0^l]^T, \quad \{d_r^l\} = [\theta_x^l \ \theta_y^l \ \theta_z^l \ \phi_z^l]^T \quad (3.12)$$

where, $\{d_t\}, \{d_r\}$ and $\{d_t^l\}, \{d_r^l\}$ are the displacements on the global and the local edge coordinate system, respectively. $[L_t]$ and $[L_r]$ are the transformation matrices for a node on the skew boundary and is given by

$$[L_t] = \begin{bmatrix} c & s & 0 \\ -s & c & 0 \\ 0 & 0 & 1 \end{bmatrix}, \quad [L_r] = \begin{bmatrix} c & s & 0 & 0 \\ -s & c & 0 & 0 \\ 0 & 0 & 1 & 0 \\ 0 & 0 & 0 & 1 \end{bmatrix} \quad (3.13)$$

in which, $c = \cos\alpha$ and $s = \sin\alpha$, the skew angle of the plate is α . It may be noted that for the nodes which do not lie on the skew edges, the transformation from global coordinates to the local coordinates is not required. The transformation matrices in

such cases are the diagonal matrices in which the values of the principal diagonal elements are unity. Thus, considering Eq. (2.25), the elemental stiffness matrices of the element containing the nodes laying on the skew edges are given as follows:

$$\begin{aligned} \left[\bar{k}_{tt}^{el} \right] &= [T_1]^T [k_{tt}^{el}] [T_1], \quad \left[\bar{k}_{tr}^{el} \right] = [T_1]^T [k_{tr}^{el}] [T_2], \\ \left[\bar{k}_{rr}^{el} \right] &= [T_2]^T [k_{rr}^{el}] [T_2], \quad [M^{el}] = [T_1]^T [M^{el}] [T_1] \end{aligned} \quad (3.14)$$

where, the transformation matrices $[T_1]$ and $[T_2]$ are given by

$$\begin{aligned} [T_1] &= \begin{bmatrix} [L_t] & \tilde{0} & \tilde{0} & \tilde{0} & \tilde{0} & \tilde{0} & \tilde{0} & \tilde{0} \\ \tilde{0} & [L_t] & \tilde{0} & \tilde{0} & \tilde{0} & \tilde{0} & \tilde{0} & \tilde{0} \\ \tilde{0} & \tilde{0} & [L_t] & \tilde{0} & \tilde{0} & \tilde{0} & \tilde{0} & \tilde{0} \\ \tilde{0} & \tilde{0} & \tilde{0} & [L_t] & \tilde{0} & \tilde{0} & \tilde{0} & \tilde{0} \\ \tilde{0} & \tilde{0} & \tilde{0} & \tilde{0} & [L_t] & \tilde{0} & \tilde{0} & \tilde{0} \\ \tilde{0} & \tilde{0} & \tilde{0} & \tilde{0} & \tilde{0} & [L_t] & \tilde{0} & \tilde{0} \\ \tilde{0} & \tilde{0} & \tilde{0} & \tilde{0} & \tilde{0} & \tilde{0} & [L_t] & \tilde{0} \\ \tilde{0} & \tilde{0} & \tilde{0} & \tilde{0} & \tilde{0} & \tilde{0} & \tilde{0} & [L_t] \end{bmatrix}; \\ [T_2] &= \begin{bmatrix} [L_r] & \tilde{0} & \tilde{0} & \tilde{0} & \tilde{0} & \tilde{0} & \tilde{0} & \tilde{0} \\ \tilde{0} & [L_r] & \tilde{0} & \tilde{0} & \tilde{0} & \tilde{0} & \tilde{0} & \tilde{0} \\ \tilde{0} & \tilde{0} & [L_r] & \tilde{0} & \tilde{0} & \tilde{0} & \tilde{0} & \tilde{0} \\ \tilde{0} & \tilde{0} & \tilde{0} & [L_r] & \tilde{0} & \tilde{0} & \tilde{0} & \tilde{0} \\ \tilde{0} & \tilde{0} & \tilde{0} & \tilde{0} & [L_r] & \tilde{0} & \tilde{0} & \tilde{0} \\ \tilde{0} & \tilde{0} & \tilde{0} & \tilde{0} & \tilde{0} & [L_r] & \tilde{0} & \tilde{0} \\ \tilde{0} & \tilde{0} & \tilde{0} & \tilde{0} & \tilde{0} & \tilde{0} & [L_r] & \tilde{0} \\ \tilde{0} & \tilde{0} & \tilde{0} & \tilde{0} & \tilde{0} & \tilde{0} & \tilde{0} & [L_r] \end{bmatrix} \end{aligned} \quad (3.15)$$

in which, $\tilde{0}$ and $\tilde{0}$ are the (3×3) and (4×4) null matrices, respectively and the number of $[L_t]$ and $[L_r]$ matrices are equal to the number of nodes in the element. The elemental equations of motion are assembled to obtain the global equations of motion of the SMEE plate as follows:

$$[M] \{ \ddot{d}_t \} + [k_{tt}^g] \{ d_t \} + [k_{tr}^g] \{ d_r \} + [k_{t\phi}^g] \{ \phi \} + [k_{t\psi}^g] \{ \psi \} = \{ F_t \} \quad (3.16)$$

$$[k_{tr}^g]^T \{ d_t \} + [k_{rr}^g] \{ d_r \} + [k_{r\phi}^g] \{ \phi \} + [k_{r\psi}^g] \{ \psi \} = 0 \quad (3.17)$$

$$[k_{t\phi}^g]^T \{ d_t \} + [k_{r\phi}^g]^T \{ d_r \} - [k_{\phi\phi}^g] \{ \phi \} = 0 \quad (3.18)$$

$$[k_{t\psi}^g]^T \{ d_t \} + [k_{r\psi}^g]^T \{ d_r \} - [k_{\psi\psi}^g] \{ \psi \} = 0 \quad (3.19)$$

where, $[M]$ is the global mass matrix; $[k_{tt}^g]$, $[k_{tr}^g]$ and $[k_{rr}^g]$ are the global elastic stiffness matrices; $[k_{t\phi}^g]$ and $[k_{r\phi}^g]$ are the global electro-elastic coupling stiffness

matrices; $[k_{t\psi}^g]$ and $[k_{r\psi}^g]$ are the global magneto-elastic coupling stiffness matrices; $\{F_t\}$ is the global mechanical load vector; $[k_{\phi\phi}^g]$ and $[k_{\psi\psi}^g]$ are the global electric and the global magnetic stiffness matrices, respectively. Solving the global equations of motion (Eqs. (3.17) - (3.19)) to obtain global generalized displacement vector $\{d_t\}$ and $\{d_r\}$ by condensing the global degrees of freedom for $\{\phi\}$ and $\{\psi\}$ in terms of $\{d_r\}$ as follows:

$$\begin{aligned}\{\psi\} &= [k_{\psi\psi}^g]^{-1} [k_{t\psi}^g]^T \{d_t\} + [k_{\psi\psi}^g]^{-1} [k_{r\psi}^g]^T \{d_r\}, \\ \{\phi\} &= [k_{\phi\phi}^g]^{-1} [k_{t\phi}^g]^T \{d_t\} + [k_{\phi\phi}^g]^{-1} [k_{r\phi}^g]^T \{d_r\}, \\ \{d_r\} &= -[K_3]^{-1} [K_2]^T \{d_t\}\end{aligned}\quad (3.20)$$

Now, substituting Eq. (3.19) in Eq. (3.16) and upon simplification, we obtain the global equations of motion in terms of the global translational degrees of freedom as follows:

$$\begin{aligned}[M]\{\ddot{d}_t\} + \left([K_1] - [K_2][K_3]^{-1}[K_2]^T \right) \{d_t\} &= \{F_t\}, \\ [M]\{\ddot{d}_t\} + [K]\{d_t\} &= \{F_t\} \\ \text{and } [K] &= \left([K_1] - [K_2][K_3]^{-1}[K_2]^T \right)\end{aligned}\quad (3.21)$$

where, the global assembled matrices are given as follows:

$$\begin{aligned}[K_1] &= [k_{tt}^g] + [k_{t\phi}^g][k_{\phi\phi}^g]^{-1}[k_{t\phi}^g]^T + [k_{t\psi}^g][k_{\psi\psi}^g]^{-1}[k_{t\psi}^g]^T, \\ [K_2] &= [k_{tr}^g] + [k_{t\phi}^g][k_{\phi\phi}^g]^{-1}[k_{r\phi}^g]^T + [k_{t\psi}^g][k_{\psi\psi}^g]^{-1}[k_{r\psi}^g]^T, \\ [K_3] &= [k_{rr}^g] + [k_{r\phi}^g][k_{\phi\phi}^g]^{-1}[k_{r\phi}^g]^T + [k_{r\psi}^g][k_{\psi\psi}^g]^{-1}[k_{r\psi}^g]^T.\end{aligned}\quad (3.22)$$

3.3. RESULTS AND DISCUSSIONS

This section comprises the investigation of SMEE plate to assess the static and free vibration characteristics. The influence of skew angle, stacking sequence, boundary conditions, and width to thickness ratios on the behaviour of SMEE plate is explicitly studied. The validity of the proposed FE formulation is established

considering different benchmark solutions available in the literature. The SMEE plate consists of three layers of equal thickness h_i , the geometric parameters $a = b = 1$ m, and the total thickness $H = 0.3$ m. The material properties for the BaTiO₃ and the CoFe₂O₄ are tabulated in Table 2.1. The skew boundary conditions considered for the analysis of the SMEE plate are given as follows:

(a) Simply supported boundary condition

$$\begin{aligned} \text{at } x = y \tan\alpha, x = a + y \tan\alpha \quad & v_0^I = w_0^I = \theta_y^I = \theta_z^I = \phi^I = \psi^I = 0 \\ \text{at } y = 0, y = b \cos\alpha \quad & u_0 = w_0 = \theta_z = \phi = \psi = 0 \end{aligned} \quad (3.23)$$

(b) Clamped-clamped boundary condition

$$\begin{aligned} \text{at } x = y \tan\alpha, x = a + y \tan\alpha \quad & u_0^I = v_0^I = w_0^I = \theta_x^I = \theta_y^I = \theta_z^I = \phi^I = \psi^I = 0 \\ \text{at } y = 0, y = b \cos\alpha \quad & u_0 = v_0 = w_0 = \theta_x = \theta_y = \theta_z = \phi = \psi = 0 \end{aligned} \quad (3.24)$$

3.3.1 Validation of present FE model

The validity of the proposed FE formulation is verified with the various benchmark solutions available in the literature. To the best of our knowledge, the studies pertaining to structural behaviour of SMEE plate is unavailable in the open literature. Hence, the results are verified for the rectangular MEE plate reported by Chen et al. (2014). For the identical geometric parameters and material properties, the natural frequencies of the skew MEE plate with the skew angle $\alpha = 0$ are computed for different mesh size to understand the convergence behaviour as depicted in Table 3.1. It may be observed from Table 3.1 that the present FE formulation displayed a good convergence for the mesh size of 20×20 . Hence, the same mesh size is employed for all the subsequent analysis. The transverse shear stresses across the thickness of the SMEE plate for two different stacking sequence with $\alpha = 0$ are presented in Figure 3.2 (a) and (b). It may be seen from these figures that the results are in excellent agreement with that of Lage et al. (2004) and Moita et al. (2009). Further, it may be noted that the present FE formulation of MEE plate can be utilized to study the purely elastic laminated composite plates by neglecting the coupled fields. Hence, to verify the correctness of the transformation matrix generated, the free vibration behaviour of skew laminated composite plate is studied. It may be noticed from Table 3.2 and Table 3.3 that the results reported from the present FE model display a good agreement with

the results available in the literature (Kanasogi and Ray 2013; Garg et al. 2006) facilitating the further investigation on SMEE plates. The non-dimensional natural frequency is calculated by $\bar{\omega} = \omega a \sqrt{\rho_{max} / C_{max}}$ where, $\rho_{max} = 5800 \text{ kg/m}^3$ and $C_{max} = 286 \cdot 10^9 \text{ N/m}^2$. Since the validation is presented for free vibration behaviour of MEE plates, static studies are presented after the free vibration characteristics of SMEE plates in the next section.

Table 3.1: Non-dimensional natural frequency $\bar{\omega} = \omega a \sqrt{\rho_{max} / C_{max}}$ modes for clamped B/F/B plate

Source	Mode				
	1	2	3	4	5
Present (8 × 8)	1.3586	2.2481	2.2481	2.6342	2.6342
Present (16 × 16)	1.3498	2.2319	2.2319	2.6222	2.6222
Present (20 × 20)	1.3496	2.2316	2.2316	2.6217	2.6217
Chen <i>et al.</i> (2014)	1.3452	2.2231	2.2231	2.6178	2.6178

Table 3.2: Non-dimensional frequency parameter $\lambda = \omega b^2 / \pi^2 h (\rho/E_2)^{1/2}$ for the clamped laminated composite plate (a/H = 10)

Skew angle (α)	Source	$(0^0/90^0/0^0/90^0)$ $(45^0/-45^0/45^0/-45^0)$			
		Mode		Mode	
		1	2	1	2
0^0	Present	2.2621	3.6072	2.2352	3.5152
	Upadhyay and Shukla (2012)	2.2990	3.7880	2.2119	3.7339
	Liew and Wang (2004)	2.3315	3.6531	2.2433	3.6000
15^0	Present	2.3014	3.5143	2.2864	3.4982
	Upadhyay and Shukla (2012)	2.3809	3.7516	2.3099	3.6997
	Liew and Wang (2004)	2.3741	3.5856	2.3049	3.5346
30^0	Present	2.4614	3.6997	2.4835	3.5612
	Upadhyay and Shukla (2012)	2.6666	3.9851	2.6325	3.9549
	Liew and Wang (2004)	2.5240	4.1943	2.4945	3.6113

Table 3.3: Non-dimensional frequency parameter $\lambda = \omega b^2 / \pi^2 h (\rho/E_2)^{1/2}$ for the simply supported laminated composite plate ($a/H = 10$)

Skew angle (α)	Source	$(0^0/90^0/0^0/90^0)$		$(45^0/-45^0/45^0/-45^0)$	
		Mode		Mode	
		1	2	1	2
	Present	1.4848	2.4439	1.8125	3.2411
0^0	Upadhyay and Shukla (2012)	1.4829	2.4656	1.7974	3.3351
	Liew and Wang (2004)	1.5076	2.4380	1.8493	3.3359
	Present	1.5701	2.7091	1.8236	3.1258
15^0	Upadhyay and Shukla (2012)	1.5741	2.5351	1.8313	3.2490
	Liew and Wang (2004)	1.5796	2.5775	1.8675	3.2075
	Present	1.8416	3.1581	1.9429	3.1683
30^0	Upadhyay and Shukla (2012)	1.8871	2.9372	2.0270	3.4431
	Liew and Wang (2004)	1.8226	2.9585	1.9894	3.2365

3.3.2 Free vibration analysis of skew magneto-electro-elastic plates

In this section, the free vibration behaviour of SMEE plate is investigated. Influence of skew angle on the natural frequency of the SMEE plate is presented. The effect of stacking sequence and geometric parameters are extensively studied. Table 3.4 present the influence of different skew angle, stacking sequence and the boundary conditions on the natural frequency of the plate. The increase in skew angle increases the natural frequency of the SMEE plate. It is interesting to note that the natural frequency increases rapidly for $\alpha = 45^0$. This increase in natural frequency can be attributed to the reduction in the area of the SMEE plate. Also, the plate stiffness increases with the increase in skew angle contributing to higher natural frequency. Further, the F/B/F stacked SMEE plate attains higher natural frequency than the B/F/B plate. It may be due to the fact that the F/B/F plate possesses larger stiffness and elastic properties because of two magnetostrictive layers. Furthermore, it can be noticed from Table 3.4 that the fully clamped plate attains higher natural frequency over simply supported SMEE plate. This can be attributed to the increase in flexural rigidity at the plate edges for higher constraints and hence higher natural frequency. Influence of different thickness ratio (a/H) for various skew angles on the natural

frequencies of the simply supported and fully clamped B/F/B SMEE plate is tabulated in Table 3.5 and Table 3.6, respectively. Similarly, Table 3.7 and Table 3.8 present the same for F/B/F SMEE plate. It may be observed from these tables (Table 3.5 – Table 3.8) that the increase in thickness ratio decreases the natural frequencies for different skew angles. This may be attributed to the lower stiffness of the thin plate over thick plate and hence lower natural frequency. Further, it is interesting to note that the effect of thickness ratio on the natural frequencies is significant as compared to the effects of skew angle, boundary conditions, and the stacking sequences.

Table 3.4: Normalized natural frequencies $\bar{\omega} = \omega a \sqrt{\rho_{max} / C_{max}}$ for SMEE plate ($a = 1$ m, $a = b, H = 0.3$ m)

Skew angle (α)	Stacking sequence	Boundary condition	Modes of natural frequencies				
			1	2	3	4	5
0°	B/F/B	SSSS	1.7919	2.4637	2.4637	3.4856	3.5657
		CCCC	2.4152	3.9625	3.9625	5.0231	5.0231
	F/B/F	SSSS	1.9063	2.5633	2.5633	3.6266	3.6994
		CCCC	2.4375	3.2775	3.2775	4.6370	4.7300
15°	B/F/B	SSSS	1.8898	2.5364	2.5678	3.5210	3.5744
		CCCC	2.5103	3.9281	4.2728	4.9191	5.2142
	F/B/F	SSSS	1.9312	2.6279	2.6279	3.7124	3.7124
		CCCC	2.4692	3.3600	3.3600	4.7467	4.7467
30°	B/F/B	SSSS	2.2237	2.7778	2.9360	3.7765	3.8681
		CCCC	2.8301	4.1812	4.9507	5.1027	5.4823
	F/B/F	SSSS	2.3992	2.9969	3.1676	4.0745	4.1733
		CCCC	3.0676	3.8319	4.0501	5.2096	5.3360
45°	B/F/B	SSSS	2.9506	3.2845	3.7684	4.4722	4.4849
		CCCC	3.5143	4.8625	5.7152	6.2263	6.2772
	F/B/F	SSSS	3.1834	3.5437	4.0658	4.8250	4.8388
		CCCC	4.0704	4.5309	5.1985	6.1693	6.1869

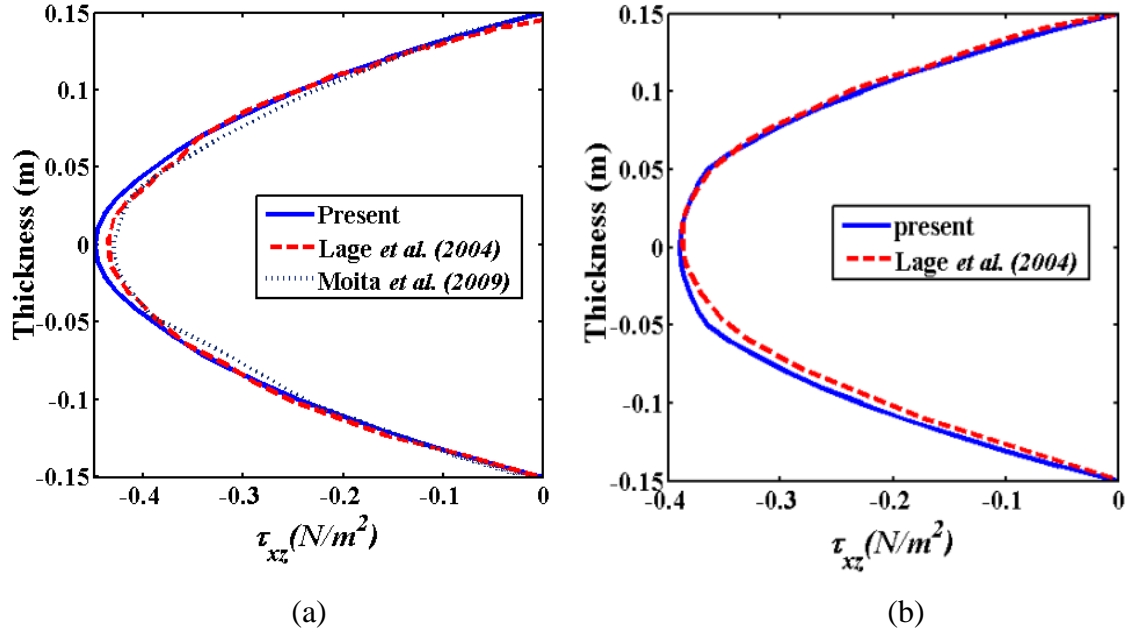


Figure 3.2: Transverse shear stress (τ_{xz}) across the thickness for (a)B/F/B (b) F/B/F MEE plate ($\alpha = 0$)

Table 3.5: Normalized natural frequencies $\bar{\omega} = \omega a \sqrt{\rho_{max} / C_{max}}$ for different thickness ratio ($a = 1$ m, $a = b$, B/F/B, SSSS)

Skew angle (α)	a/H	Mode			
		1	2	3	4
0°	10	0.2462	0.8212	0.9133	1.1397
	20	0.0631	0.2540	0.3206	0.4106
	50	0.0101	0.0455	0.0543	0.0858
	100	0.0098	0.0455	0.0530	0.0850
15°	10	0.2687	0.8454	0.9325	1.2037
	20	0.0714	0.2633	0.3598	0.4227
	50	0.0129	0.0476	0.0643	0.0951
	100	0.0122	0.0466	0.0629	0.0907
30°	10	0.3450	0.9256	1.0287	1.4232
	20	0.0962	0.3037	0.4628	0.4840
	50	0.0177	0.0577	0.0898	0.1169
	100	0.0164	0.0556	0.0875	0.1155
45°	10	0.5200	1.2533	1.3167	1.8010
	20	0.1500	0.4003	0.6037	0.6265
	50	0.0272	0.0808	0.1348	0.1731
	100	0.0261	0.0787	0.1318	0.1592

Table 3.6: Normalized natural frequencies $\bar{\omega} = \omega a \sqrt{\rho_{max} / C_{max}}$ for different thickness

ratio ($a = 1$ m, $a = b$, B/F/B, CCCC)

Skew angle (α)	a/H	Mode			
		1	2	3	4
0°	10	0.4247	1.1534	1.4216	1.6633
	20	0.1163	0.3559	0.4410	0.5489
	50	0.0204	0.0672	0.0779	0.1012
	100	0.0059	0.0180	0.0202	0.0268
15°	10	0.4486	1.1786	1.5260	1.6737
	20	0.1234	0.3678	0.4780	0.6101
	50	0.0216	0.0710	0.0846	0.1119
	100	0.0062	0.0192	0.0218	0.0294
30°	10	0.5332	1.2886	1.6976	1.8604
	20	0.1489	0.4134	0.6043	0.7590
	50	0.0262	0.0837	0.1086	0.1425
	100	0.0074	0.0236	0.0280	0.0376
45°	10	0.7332	1.5795	2.0966	2.5157
	20	0.2124	0.5310	0.7733	0.9463
	50	0.0377	0.1110	0.1683	0.2144
	100	0.0105	0.0333	0.0436	0.0573

Table 3.7: Normalized natural frequencies $\bar{\omega} = \omega a \sqrt{\rho_{max} / C_{max}}$ for different thickness

ratio ($a = 1$ m, $a = b$, F/B/F, SSSS)

Skew angle (α)	a/H	Mode			
		1	2	3	4
0°	10	0.2732	0.8544	1.0033	1.2607
	20	0.0709	0.2919	0.3826	0.4272
	50	0.0115	0.0577	0.0712	0.1140
	100	0.0106	0.0544	0.0660	0.1113
15°	10	0.2923	0.8757	1.0191	1.2762
	20	0.0847	0.3078	0.4018	0.4378
	50	0.0186	0.0703	0.0920	0.1308
	100	0.0160	0.0658	0.0884	0.1279
30°	10	0.3388	0.9396	1.0638	1.3225
	20	0.1069	0.3450	0.4509	0.4697
	50	0.0229	0.0902	0.1294	0.1621
	100	0.0203	0.0856	0.1263	0.1564
45°	10	0.3929	1.0504	1.1291	1.3962
	20	0.1228	0.3853	0.5103	0.5250
	50	0.0247	0.1051	0.1596	0.1881
	100	0.0220	0.0982	0.1501	0.1716

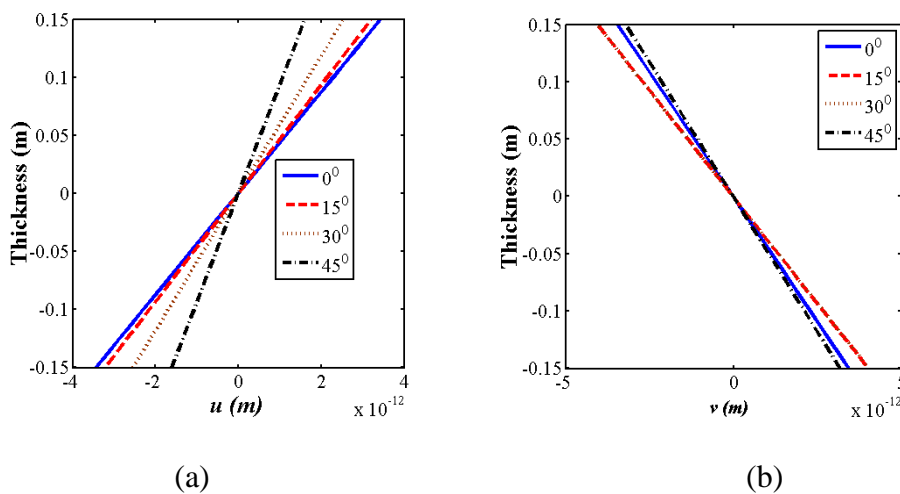
Table 3.8: Normalized natural frequencies $\bar{\omega} = \omega a \sqrt{\rho_{max} / C_{max}}$ for different thickness ratio ($a = 1$ m, $a = b$, F/B/F, CCCC)

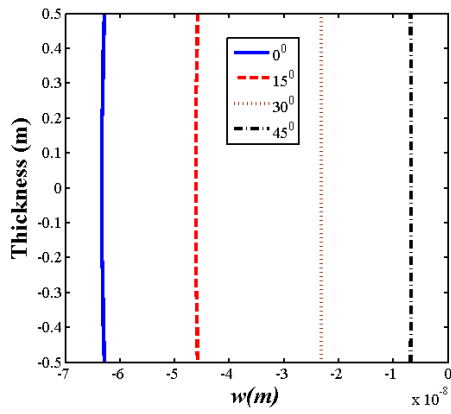
Skew angle (α)	a/H	Mode			
		1	2	3	4
0^0	10	0.4813	1.2796	1.5618	1.7377
	20	0.1389	0.4447	0.5981	0.7136
	50	0.0268	0.1251	0.1897	0.2219
	100	0.0237	0.1206	0.1748	0.2013
15^0	10	0.5075	1.3113	1.6292	1.7018
	20	0.1474	0.4619	0.6260	0.7186
	50	0.0285	0.1299	0.1973	0.2269
	100	0.0261	0.1247	0.1791	0.2033
30^0	10	0.5996	1.4367	1.7651	1.9837
	20	0.1778	0.5224	0.7224	0.7948
	50	0.0347	0.1465	0.2237	0.2526
	100	0.0326	0.1366	0.2097	0.2390
45^0	10	0.8134	1.7487	1.9767	2.3560
	20	0.2515	0.6656	0.9420	0.9874
	50	0.0499	0.1859	0.2842	0.3121
	100	0.0458	0.1597	0.2567	0.2701

3.3.3. Static analysis of SMEE plates

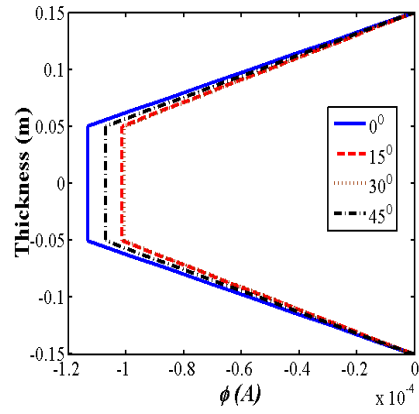
In this section, the static analysis of the plate subjected to a sinusoidal load (Lage et al. 2004) on its top surface is presented. The geometrical parameters of the SMEE plate are similar to that of the dimensions considered for the free vibration analysis. The results are obtained at the Gauss points near to the nodes at $x = 0.75$ m, $y = 0.25$ m coordinates. The effect of skew angle on the primary and secondary parameters is presented in Figure 3.3 (a) – (k). The displacements (u , v , and w) decreases with the increase in skew angle as depicted in Figure 3.3(a) and (c), respectively. The electric potential shown in Figure 3.3(d) decreases with the increase in skew angle while the magnetic potential in Figure 3.3(e) is higher for $\alpha = 45^0$. The effect of skew angle on the stresses of the simply supported B/F/B SMEE plate has been presented in Figure 3.3(f) - (i). It may be observed from these figures that the normal stresses (σ_x and σ_y)

are compressive on the top layer and tensile in the bottom layer with zero stress in the midplane of the SMEE plate. The normal stress components are discontinuous at the interface of the layers of dissimilar materials. It can be attributed to the difference in material properties and displacement gradient across the thickness. It may also be noticed from these figures (Figure 3.3 (a) – (k)) that the effect of skew angle on the stress components is minimum for $\alpha = 45^\circ$. A similar trend has been observed for the in-plane shear stress (τ_{xy}). The magnitude of transverse shear stress (τ_{xz}) also decreases with the increase in the skew angle. Further, it may be observed from the results that the stiffness of the SMEE plate changes with the change in skew angle, thereby directly affecting various parameters as shown in Figure 3.3 (a) – (k). It may also be observed that the transverse shear stress (τ_{xz}) is zero at the top and the bottom layers of the plate while satisfying the continuity at the interface of the layers exhibiting the maximum at the mid-plane. Figure 3.3(j) and (k) illustrate the effect of the skew angle on the electric displacement (D_z) and magnetic induction (B_z), respectively. From these figures (Figure 3.3(j) and (k)), it may be observed that the electric displacement (D_z) varies linearly in the top and the bottom layers while the effect of skew angle appears to be negligible in the middle layer. In addition, electric displacement (D_z) decreases with the increase in the skew angle as the electric potential (ϕ) decrease for higher skew angles. A similar trend has been noticed in the behavior of the magnetic induction (B_z) also. The minimum electric displacement and magnetic induction are observed for $\alpha = 45^\circ$.

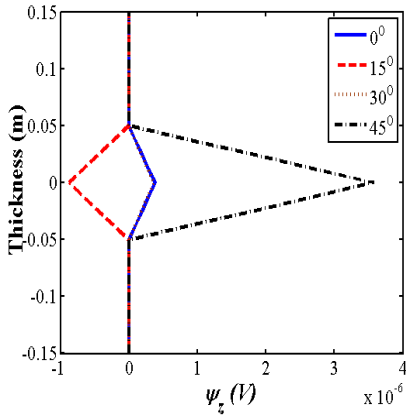




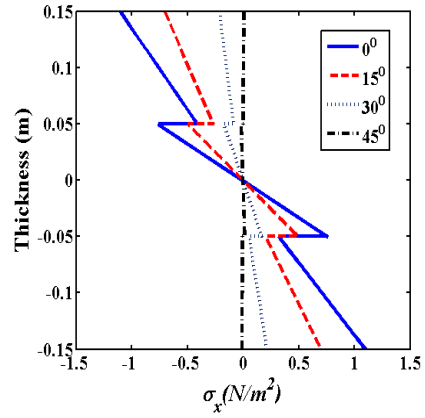
(c)



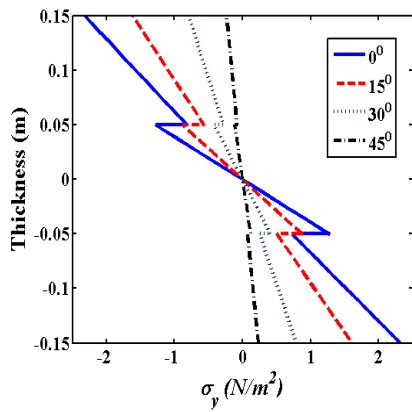
(d)



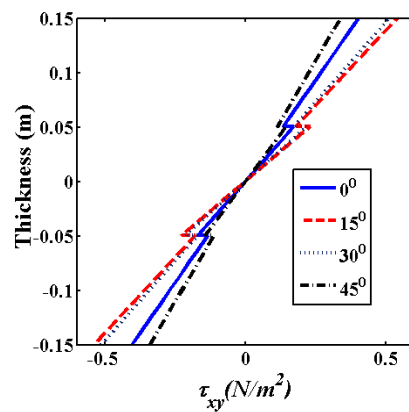
(e)



(f)



(g)



(h)

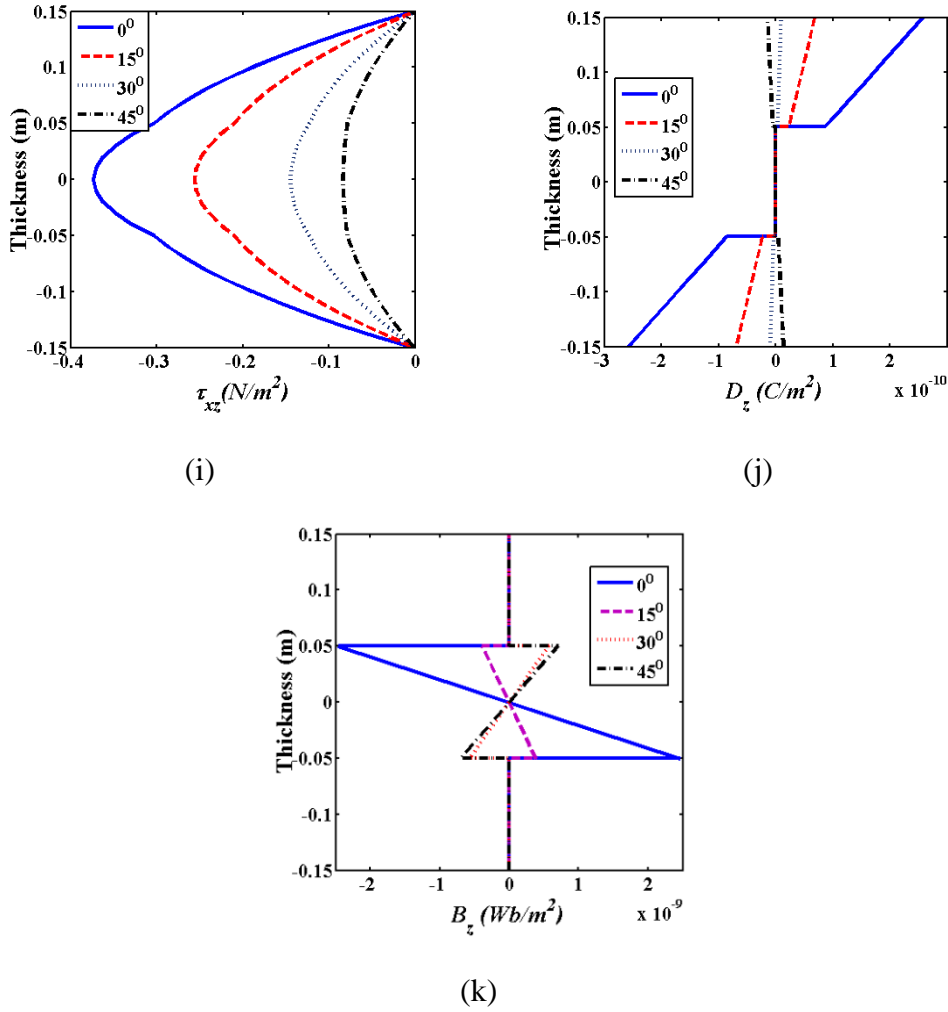
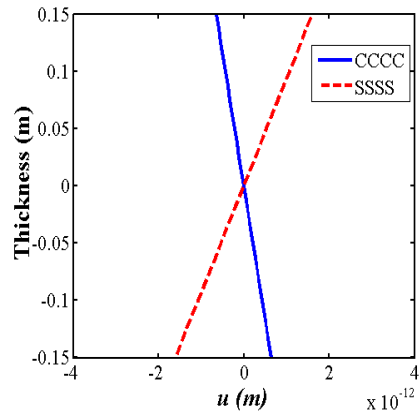


Figure 3.3. Influence of α on (a) u (b) v (c) w (d) ϕ (e) ψ (f) σ_x (g) σ_y (h) τ_{xy} (i) τ_{xz} (j) D_z (k) B_z of the simply supported B/F/B SMEE plate ($a/b = 1$, $H = 0.3$ m)

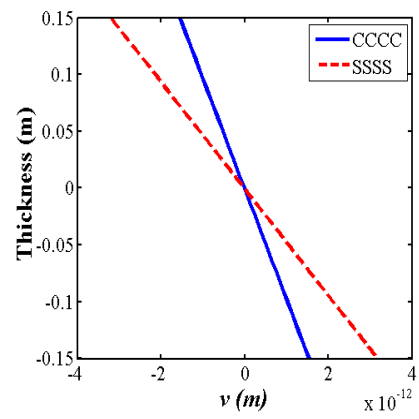
3.3.4. Effect of geometrical parameters and stacking sequence

The assessment of influence of geometric parameters and boundary conditions on the static behaviour of SMEE plate is discussed in this section. In addition, the effect of material stacking sequence on the static response characteristics of SMEE plate is also presented. The influence of different boundary conditions applied to the SMEE plate is presented in Figure 3.4(a) – (j). The displacements (u and v) shown in Figure 3.4(a) and (b) are lower for the simply supported (SSSS) plate in comparison with the fully clamped (CCCC) plate. The increase in flexural rigidity at the plate edges contribute to the lower displacements for CCCC plate. The electric and the

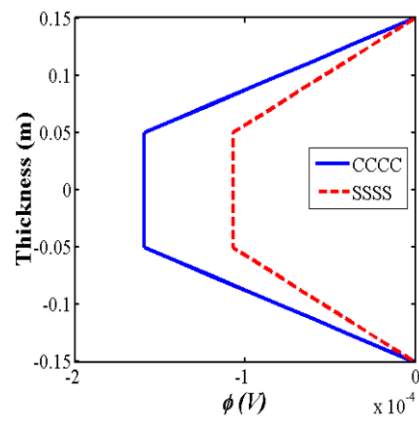
magnetic potential are higher for fully clamped plate as depicted in Figure 3.4(c) and (d), respectively.



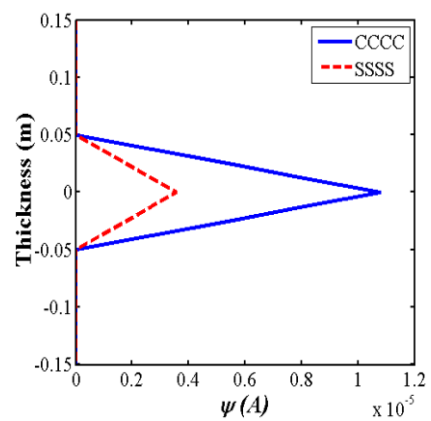
(a)



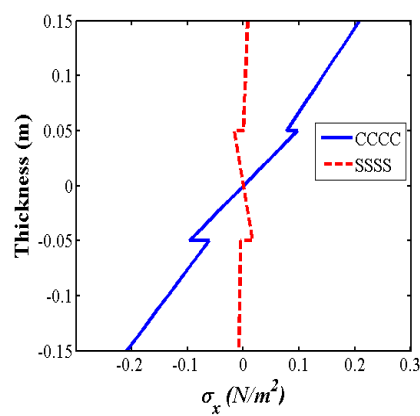
(b)



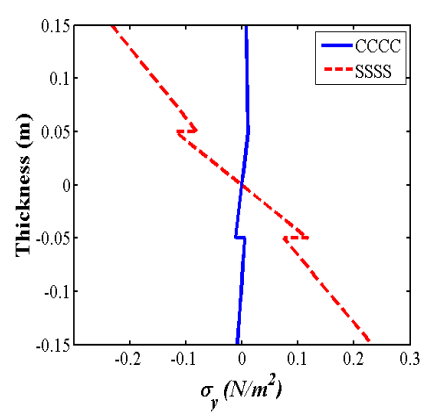
(c)



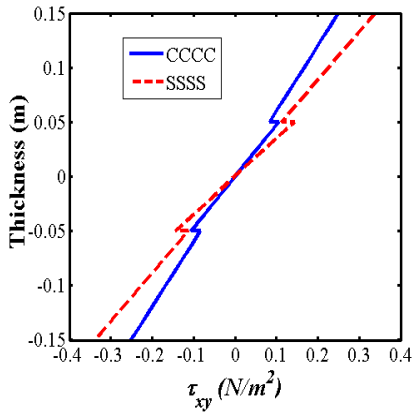
(d)



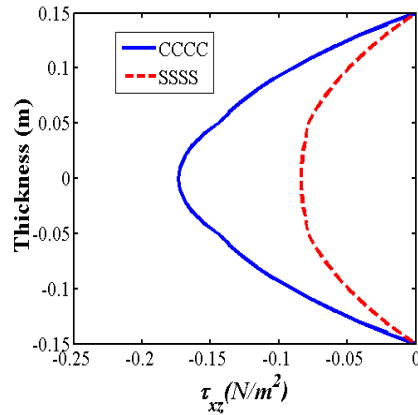
(e)



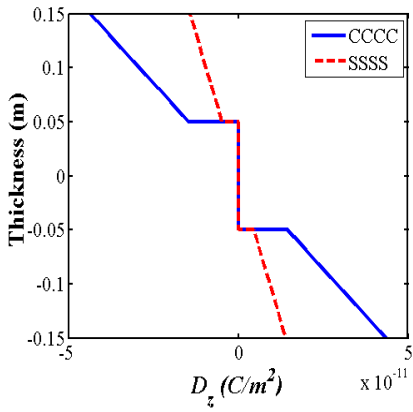
(f)



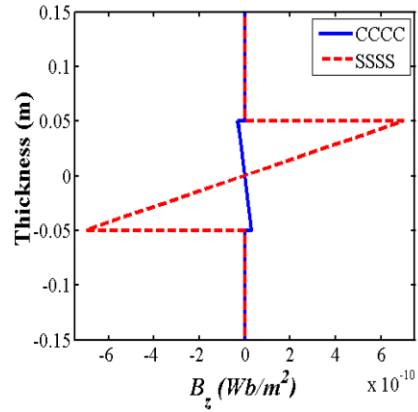
(g)



(h)



(i)



(j)

Figure 3.4. Influence of boundary condition on (a) u (b) v (c) ϕ (d) ψ (e) σ_x (f) σ_y (g) τ_{xy} (h) τ_{xz} (i) D_z (j) B_z of the B/F/B SMEE plate ($a/b = 1$, $H = 0.3$ m)

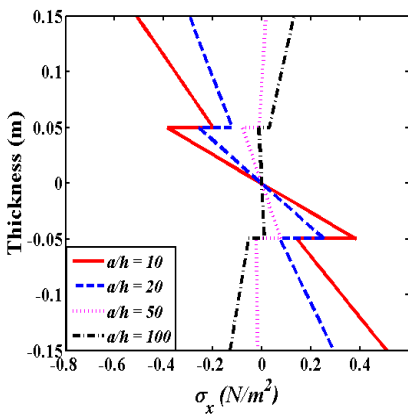
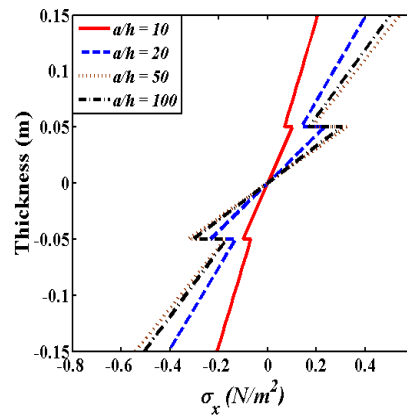
(a) $\alpha = 15^\circ$ (b) $\alpha = 45^\circ$

Figure 3.5: Normal stress (σ_x) for different thickness ratio

The stresses σ_x and τ_{xy} are higher for fully clamped plate while the stress σ_y in the y - direction is higher for SSSS plate. The transverse shear stress is higher for fully clamped plate in comparison with SSSS plate as shown in Figure 3.4(h). The electric displacement is higher for CCCC plate while the magnetic induction is seen to be higher for SSSS plate as shown in Figure 3.4(i) and (j), respectively. In addition, the effect of thickness ratio on the stresses, electric displacement, and magnetic induction is investigated. Figure 3.5 and Figure 3.6 illustrate the variation of normal stresses σ_x and σ_y for different thickness ratio and skew angles, respectively. It can be observed from these figures that the normal stresses decrease with the increase in thickness ratios for different skew angles. The in-plane shear stress (τ_{xy}) presented in the Figure 3.7(a) and (b) show a minimal variation for all the thickness ratios and skew angles considered. The transverse shear stress (τ_{xz}), the electric displacement (D_z) and the magnetic induction (B_z) are presented in Figure 3.8 – Figure 3.10, respectively. It may be noticed from these figures that the transverse shear stress (τ_{xz}), the electric displacement (D_z) and the magnetic induction (B_z) follow a similar trend of the normal stresses.

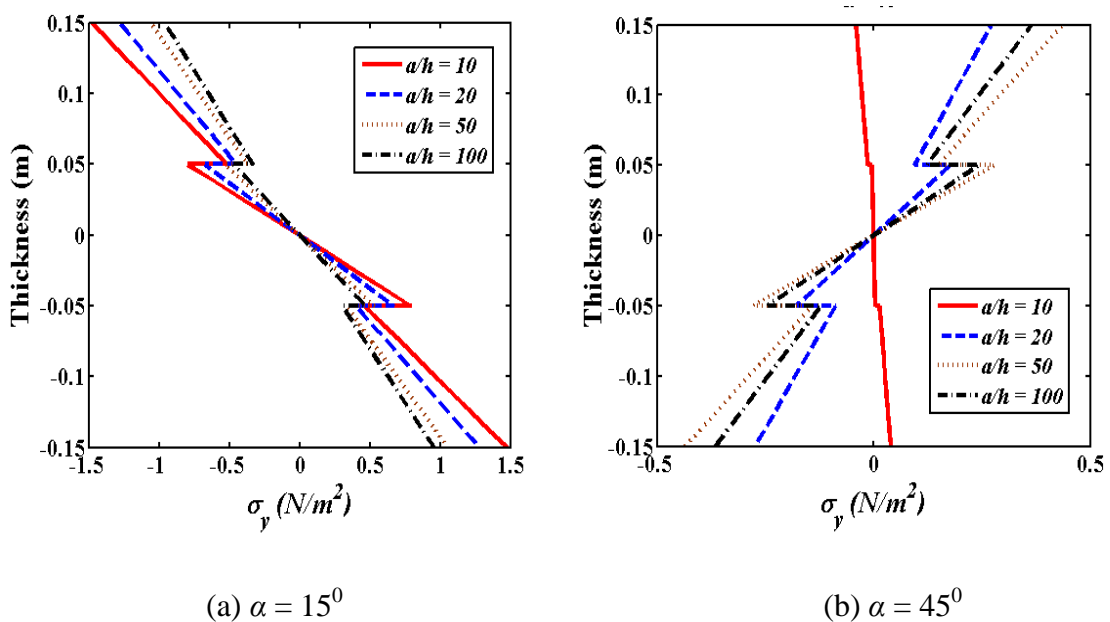
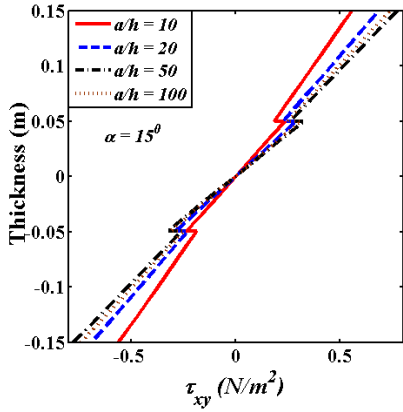
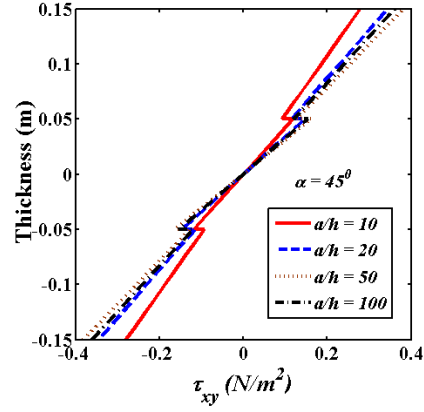


Figure 3.6: Normal stress (σ_y) for different thickness ratio

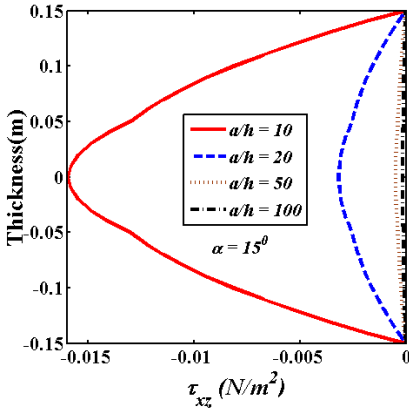


(a) $\alpha = 15^\circ$

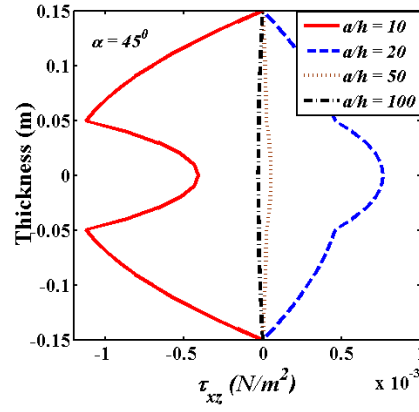


(b) $\alpha = 45^\circ$

Figure 3.7: In-plane shear stress (τ_{xy}) for different thickness ratio

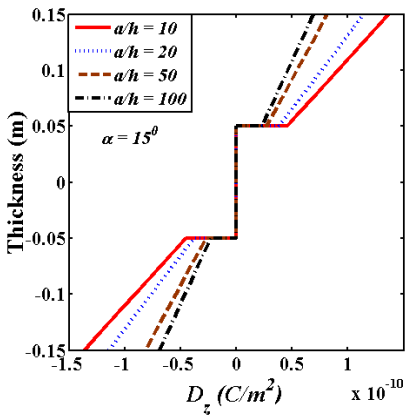


(a) $\alpha = 15^\circ$

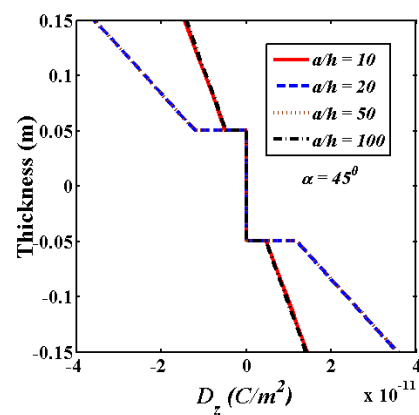


(b) $\alpha = 45^\circ$

Figure 3.8: Transverse shear stress (τ_{xz}) for different thickness ratio



(a) $\alpha = 15^\circ$



(b) $\alpha = 45^\circ$

Figure 3.9: Electric displacement (D_z) for different thickness ratio

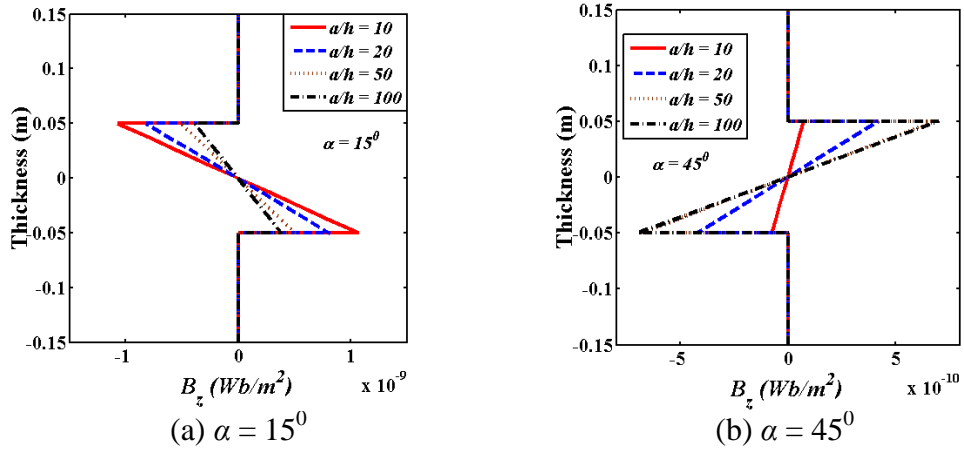
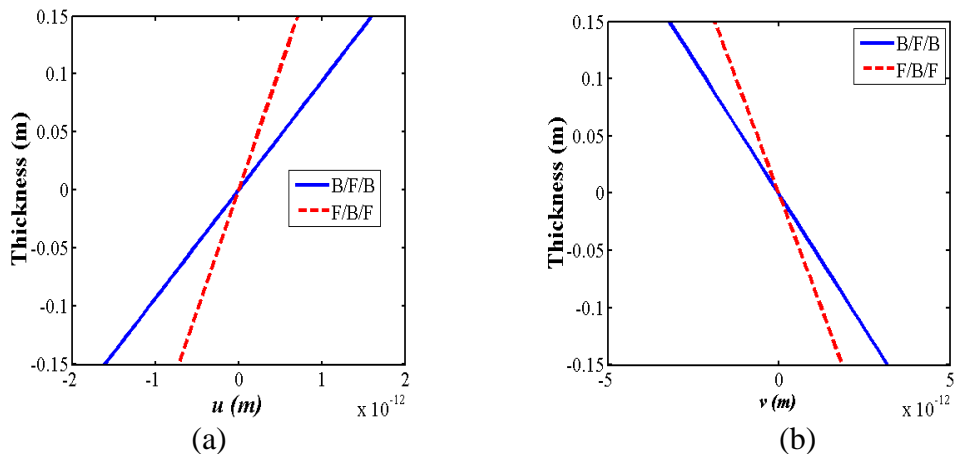
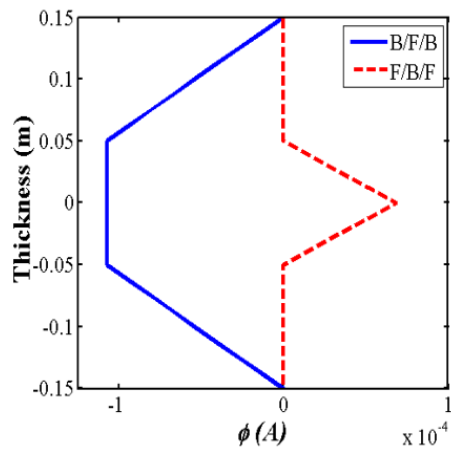


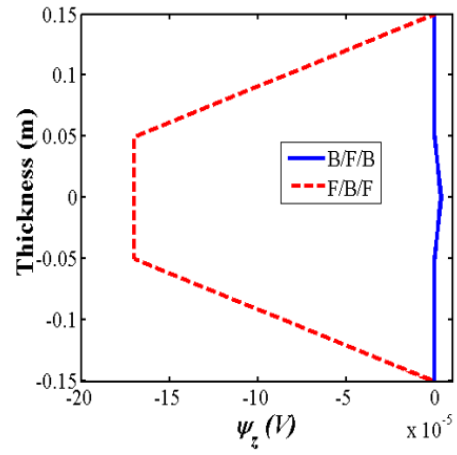
Figure 3.10: Magnetic induction (B_z) for different thickness ratio

The effect of material stacking sequence on the static response characteristics of the SMEE plate is presented in Figure 3.11(a) – (j). The displacements u and v are higher for B/F/B plate over F/B/F plate. This can be attributed to the lower stiffness associated with B/F/B plate in comparison with F/B/F plate. The electric potential in the B/F/B SMEE plate and the magnetic potential in the F/B/F SMEE plate are observed to be constant in the middle layer while it varies linearly in the top and the bottom layer. However, the electric potential in F/B/F plate and the magnetic potential in B/F/B plate are found to be zero at the top and the bottom layer. The stresses are found to be higher for B/F/B stacking sequence over F/B/F stacking. The electric displacement in the B/F/B SMEE plate and the magnetic induction in the F/B/F SMEE plate are observed to be zero in the middle layer while it varies linearly in the top and the bottom layer. However, the electric displacement in F/B/F plate and the magnetic induction in the B/F/B plate are found to be zero at the top and the bottom layer while they vary linearly in the middle layer.

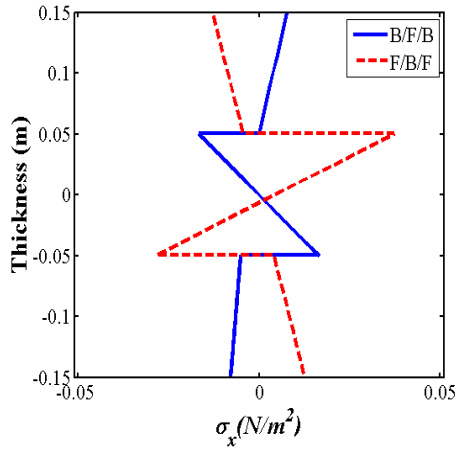




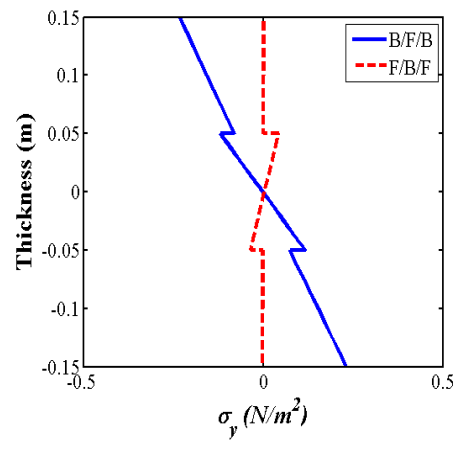
(c)



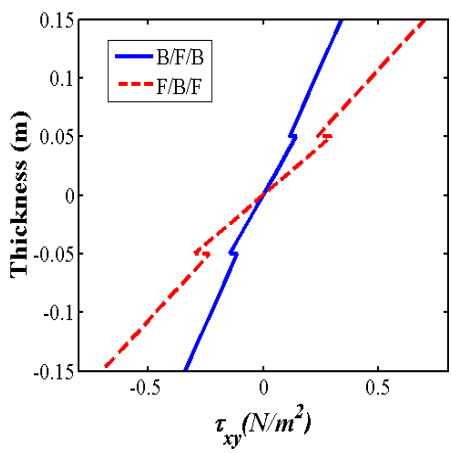
(d)



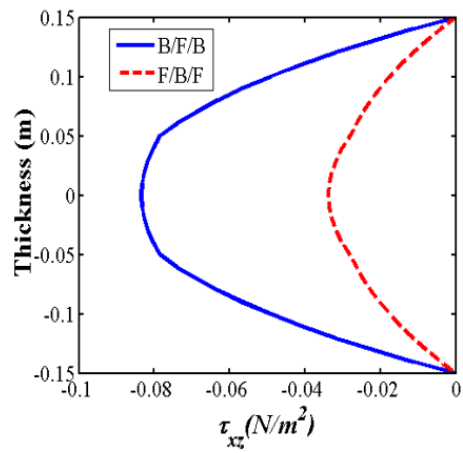
(e)



(f)



(g)



(h)

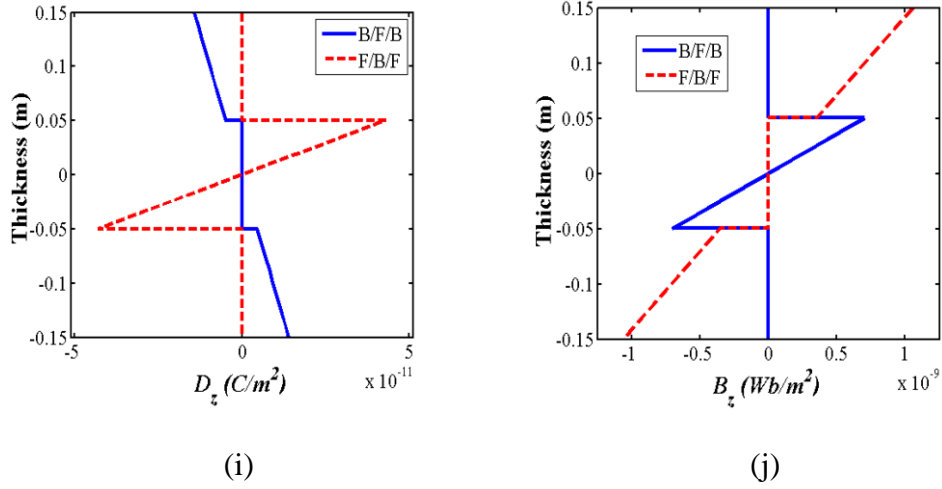


Figure 3.11: Influence of stacking sequence on (a) u (b) v (c) ϕ (d) ψ (e) σ_x (f) σ_y (g) τ_{xy} (h) τ_{xz} (i) D_z (j) B_z of the B/F/B SMEE plate ($a/b = 1$, $H = 0.3$ m)

3.4. CONCLUSION

In this chapter, a finite element analysis has been carried out to investigate the static and free vibration behavior of the layered skew-magneto-electro-elastic plates. The kinematics of the SMEE plate is described by 1-2 shear deformation theory. The transformation matrix between the global and local degrees of freedom for the nodes lying on the skew edges has been successfully incorporated to investigate the behavior of the SMEE plate. The natural frequencies of the SMEE plate increases with an increase in the skew angle for both the plates of B/F/B and F/B/F stacking sequence. However, for $\alpha = 45^\circ$, an accelerated increase in the natural frequency is seen. In addition, F/B/F SMEE plate produces higher natural frequency over B/F/B plate. The displacements and the electric potential decrease with the increase in skew angle while the magnetic potential is higher for $\alpha = 45^\circ$. The magnitude of the normal stresses decreases with the increase in a skew angle. Further, it is observed that the transverse shear stresses in the thickness direction decrease with increase in the skew angle while the influence on the in-plane shear stresses is marginal. The boundary condition, the thickness ratio, and the stacking sequence exhibit noticeable influence on the induced magnetic, electric and the elastic fields.

Chapter 4

BUCKLING ANALYSIS OF SKEW MAGNETO-ELECTRO-ELASTIC PLATES UNDER IN-PLANE LOADING

This chapter deals with the study of buckling behaviour of multilayered skew magneto-electro-elastic (SMEE) plate under uniaxial and biaxial in-plane loading. The finite element formulation derived in the previous chapters has been extended for the buckling analysis of SMEE plates. The in-plane stress distribution within the SMEE plate due to the enacted force is considered to be equivalent to the applied in-plane compressive loads in the pre-buckling range and the same stress distribution is used to derive the potential energy functional of the SMEE plate. The non-dimensional critical buckling load is attained from the solution of the allied linear eigenvalue problem. Influence of skew angle, stacking sequence, span to thickness ratio, aspect ratio, and boundary condition on the critical buckling load and their corresponding mode shapes is investigated.

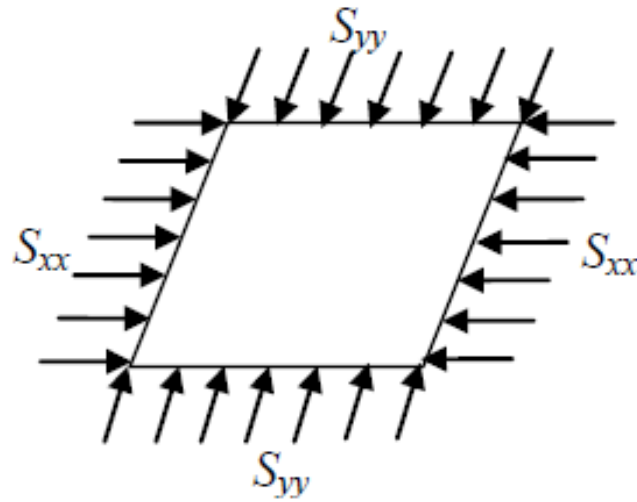
4.1. INTRODUCTION

Studies related to free vibration, static, buckling, nonlinear, dynamic behaviour etc., have gained more importance with the increase in the application spectrum of MEE composites. The studies concerning the buckling behaviour of MEE plates resting on an elastic foundation are recently reported in the literature (Alibeigi et al. 2018; Kamali et al. 2018; Li et al. 2016; Jamalpoor et al. 2016; Farajpour and Rastgoo 2017). However, studies related to buckling of multilayered SMEE plate is an overlooked area. Consequently, this chapter presents a finite element model based on FSDT to assess the buckling characteristics of the multilayered SMEE plate. The buckling characteristics are well presented in terms of non-dimensional critical buckling load and their corresponding mode shapes which are obtained by solving a linear eigenvalue problem. In addition, parametric studies such as the effect of skew

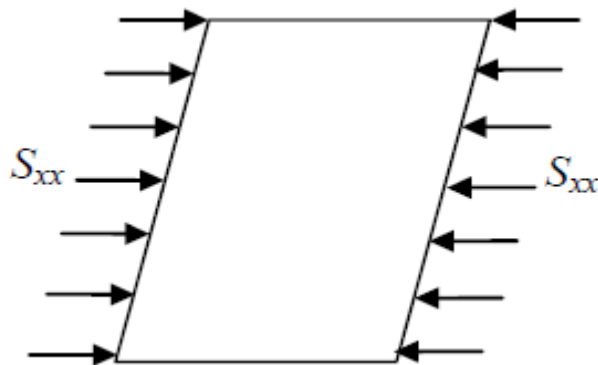
angle, uniaxial and biaxial compression, aspect ratio, span to thickness ratio and boundary conditions on buckling behaviour of SMEE plate are studied in detail.

4.2. PROBLEM DESCRIPTION AND GOVERNING EQUATION

The geometric details of the SMEE plate considered for the analysis is similar to the SMEE plate studied in Chapter 3. However, the SMEE plate considered in this chapter is subjected to uniaxial and biaxial in-plane loads as shown in Figure 4.1. The displacement equations, the constitutive equations, the governing equations, and the FE formulation are represented identical to Section 2.2 and 2.3 of Chapter 2.



(a) Biaxial compression



(b) Uniaxial compression

Figure 4.1: SMEE plate subjected to biaxial and uniaxial compression

4.2.1. Skew boundary transformation

The skew boundary transformation is implemented similarly to the Eqs. 3.11 and 3.12. However, the transformation matrices $[L_t]$ and $[L_r]$ differ in order and is given by

$$[L_t] = \begin{bmatrix} c & s & 0 \\ -s & c & 0 \\ 0 & 0 & 1 \end{bmatrix}, [L_r] = \begin{bmatrix} c & s \\ -s & c \end{bmatrix} \quad (4.1)$$

in which, $c = \cos\alpha$ and $s = \sin\alpha$, the skew angle of the plate is α . The elemental equations of motion and corresponding elemental stiffness matrices for the SMEE plate can be adapted from Chapter 2 and are identical to Eqs. (2.21) – (2.25). Then, the elemental stiffness matrices for the element containing the nodes laying on the skew edges can be given as follows:

$$\begin{aligned} [\bar{k}_{tt}^{el}] &= [T_1]^T [k_{tt}^{el}] [T_1], [\bar{k}_{tr}^{el}] = [T_1]^T [k_{tr}^{el}] [T_2], \\ [\bar{k}_{rr}^{el}] &= [T_2]^T [k_{rr}^{el}] [T_2], [M^{el}] = [T_1]^T [M^{el}] [T_1] \\ [\bar{k}_G^{el}] &= [T_2]^T [k_G^{el}] [T_2] \end{aligned} \quad (4.2)$$

where, the transformation matrices $[T_1]$ and $[T_2]$ are given by

$$\begin{aligned} [T_1] &= \begin{bmatrix} [L_t] & \tilde{0} & \tilde{0} & \tilde{0} \\ \tilde{0} & [L_t] & \tilde{0} & \tilde{0} \\ \tilde{0} & \tilde{0} & [L_t] & \tilde{0} \\ \tilde{0} & \tilde{0} & \tilde{0} & [L_t] \end{bmatrix}, \\ [T_2] &= \begin{bmatrix} [L_r] & \tilde{0} & \tilde{0} & \tilde{0} \\ \tilde{0} & [L_r] & \tilde{0} & \tilde{0} \\ \tilde{0} & \tilde{0} & [L_r] & \tilde{0} \\ \tilde{0} & \tilde{0} & \tilde{0} & [L_r] \end{bmatrix} \end{aligned} \quad (4.3)$$

in which, $\tilde{0}$ and $\check{0}$ are the (3×3) and (2×2) null matrices, respectively, and the number of $[L_t]$ and $[L_r]$ matrices are equal to the number of nodes in the element. The global equation of motion and the final form of the eigen buckling problem is outlined similar to Eq. (2.32) – (2.36).

4.3. RESULTS AND DISCUSSION

Buckling analysis of layered SMEE plate is carried out in order to assess the nature of stability by forming an eigenvalue problem. Such eigenvalue problem yields eigenvalues i.e., critical buckling loads and their corresponding mode shapes in terms of eigenvectors. The multilayered SMEE plate involved in the previous chapter is adapted without any modification. The material property of the SMEE plate is given in Table 2.1. The non-dimensional critical buckling load for SMEE plate is given by $\lambda_{cr} = \lambda a^2 / H^3 C_{11}$ where C_{11} corresponds to the largest elastic constant value of MEE material, a corresponds to the width of the plate and H is the total thickness of the SMEE plate. The stability characteristics of the SMEE plate is evaluated for different skew angles, aspect ratio, span to thickness ratio and boundary conditions. Effect of boundary conditions on the buckling behaviour of the SMEE plate has been studied. The boundary conditions employed in the present analysis for clamped, and simply-supported edges considered are identical to Eq. (3.36) and Eq. (3.37), respectively, while for the free edges the boundary conditions are given as follows:

Free edge

$$\begin{aligned} \text{at } x = \tan\alpha, \quad x = a + y \tan\alpha \quad & u_0^l = v_0^l = w_0^l = \theta_x^l = \theta_y^l = \theta_z^l = \phi^l = \psi^l \neq 0 \\ \text{at } y = 0, \quad y = b \cos\alpha \quad & u_0 = v_0 = w_0 = \theta_x = \theta_y = \theta_z = \phi = \psi \neq 0 \end{aligned} \quad (4.4)$$

4.3.1 Validation

It may be noted that the proposed FE formulation to solve a buckling problem is validated with the results reported by Reddy (2004) for the simply-supported multilayered laminate composite plate with the material properties $E_1 = 25E_2$, $G_{12} = G_{13} = 0.5E_2$, $G_{23} = 0.2E_2$, $\nu_{12} = 0.25$, $k = 5/6$ are considered here for the validation because of the unavailability of MEE plate solutions in the literature. In this regard, the coupled constitutive equations of the SMEE plate have been decoupled (by setting electric and magnetic couple effect to zero) and implemented for the analysis of laminated composite plate. The convergence studies were performed by considering the different mesh sizes. For a mesh size of 20×20 , the results obtained are well in agreement with existing results (Reddy, 2004) as shown in Table 4.1. Hence, for all the subsequent analysis, a mesh size of 20×20 has been implemented. In addition, the effectiveness of the present model in solving a multifield problem is

assessed. In this regard, the free vibration behaviour of B/F/B MEE plate studied by Millazo (2016) using refined kinematic models is considered for the validation, and the corresponding results are presented in Table 4.2. The free vibration analysis presented in Table 4.2 is performed by considering the stiffness matrix and the mass matrix while the geometrical stiffness matrix is neglected. The results show a close agreement with each other. Further, Table 4.3 depicts the stability behaviour of the simply-supported and clamped laminated skew composite plate (Chakrabarti and Sheikh, 2010; Hu and Tzeng, 2009). It may be noted that the laminated skew composite plate is studied here to emphasize the correctness of the present formulation for the investigation of skew plates. The material properties concerned to the skew composite plate are $E_1 = 128 \text{ Gpa}$, $E_2 = 11 \text{ Gpa}$, $G_{12} = G_{13} = 4.48 \text{ Gpa}$, $G_{23} = 1.53 \text{ Gpa}$, $\nu_{12} = 0.25$.

Table 4.1: Buckling load $\lambda_{cr} = \lambda a^2 / H^3 E_2$ for three ($0^0/90^0/0^0$) layered composite plate under in-plane load

a/h ratio	Type of load	Buckling load				
		Reddy (2004)	Present study			
			4×4	8×8	16×16	20×20
10	uniaxial	15.2890	15.0319	14.8981	14.8694	14.8690
	biaxial	7.6445	7.5159	7.4490	7.4347	7.4345
50	uniaxial	22.9781	22.4591	22.1085	22.0464	22.0418
	biaxial	11.4890	11.2295	11.0542	11.0232	11.0209
100	uniaxial	23.3633	23.0521	22.9703	22.8492	22.8461
	biaxial	11.6820	11.5260	11.4851	11.4246	11.4230

4.3.2 Effect of skew angle on buckling load

This section discusses the influence of skew angle (α) on the non-dimensional buckling load. The buckling characteristics of the SMEE plate under different boundary conditions are investigated for skew angles of $0^0 - 60^0$. Table 4.4 presents the buckling load for CCCC SMEE plate with B/F/B stacking sequence subjected to uniaxial compression. It may be observed from Table 4.4 that the increase in skew angle effectively increases the buckling strength of the SMEE plate. Further, Table

4.5 and Table 4.6 display the effect of skew angle on buckling load for CCCF and FCFC SMEE plates, respectively. It may be observed from these tables (Table 4.5 and Table 4.6) that the introduction of free edge boundary conditions to the plate reduces the magnitude of buckling loads. This may be due to the reduced flexural rigidity with the introduction of free edges to the plate. In general, for all the considered boundary conditions, the buckling load increases with the increase in skew angle. However, the rate of increase in buckling load is observed higher for $\alpha = 45^0$ and 60^0 . It may be due to the fact that stiffness of the SMEE plate increases at higher skew angles. The first three mode shapes corresponding to CCCF SMEE plate are presented in Figure 4.2 for $\alpha = 0^0, 30^0$ and 60^0 . It may be noticed from Figure 4.2 that formation of buckling mode is shifting towards the corners of the SMEE plate with an increase in the skew angle.

Table 4.2: Normalized natural frequencies $\bar{\omega} = \omega a \sqrt{\rho_{\max}/C_{\max}}/h$ of the B/F/B simply supported plate

a/h ratio	Approach	Mode			
		1	2	3	4
10	FSDT(Milazzo, 2016)	3.83	9.17	12.74	14.12
	ESL2 (Milazzo, 2016)	3.84	9.19	12.74	14.14
	ESL3 (Milazzo, 2016)	3.82	9.12	12.74	13.98
	ESL4 (Milazzo, 2016)	3.82	9.12	12.74	13.97
	LW1 (Milazzo, 2016)	3.90	9.30	12.74	14.26
	LW2 (Milazzo, 2016)	3.81	9.10	12.74	13.96
	LW3 (Milazzo, 2016)	3.81	9.11	12.74	13.96
	LW4 (Milazzo, 2016)	3.83	9.17	12.74	14.12
	Present model	3.82	9.12	12.74	13.98
	100	FSDT(Milazzo, 2016)	3.95	9.89	15.82
ESL2 (Milazzo, 2016)		3.96	9.91	15.86	19.97
ESL3 (Milazzo, 2016)		3.96	9.91	15.85	19.97
ESL4 (Milazzo, 2016)		3.96	9.91	15.85	19.96
LW1 (Milazzo, 2016)		4.04	10.10	16.15	20.35
LW2 (Milazzo, 2016)		3.95	9.89	15.82	19.92
LW3 (Milazzo, 2016)		3.95	9.89	15.82	19.92
LW4 (Milazzo, 2016)		3.95	9.89	15.82	19.92
Present model		3.95	9.84	15.79	19.87

Table 4.3: Effect of skew angle on non-dimensional buckling load $\lambda_{cr} = \lambda a^2 / H^3 E_2$ for (90⁰/0⁰/0⁰/90⁰) cross-ply skew composite plate ($a/b = 1$; $a/h = 100$)

Skew angle (α)	Simply-supported			Clamped		
	Chakrabarti and Sheikh (2010)	Hu and Tzeng (2009)	Present study (20×20)	Chakrabarti and Sheikh (2010)	Hu and Tzeng (2009)	Present study (20×20)
0 ⁰	12.138	12.045	11.634	37.418	37.272	36.987
10 ⁰	13.020	13.000	12.635	38.798	38.180	37.613
20 ⁰	15.915	15.636	15.343	42.308	42.100	42.009
30 ⁰	21.605	21.500	20.669	49.274	49.000	48.894
40 ⁰	25.917	25.500	25.234	52.970	52.200	52.121

Table 4.4: Effect of skew angle on buckling load parameter for B/F/B CCCC SMEE plate subjected to uniaxial compression ($a/b = 1$, $a/h = 100$)

Skew angle (α)	Buckling mode					
	1	2	3	4	5	6
0 ⁰	0.9399	3.0713	3.4003	5.4223	9.4127	10.1181
15 ⁰	1.0262	3.2248	3.7847	5.8462	10.1201	10.9020
30 ⁰	1.3436	3.9273	5.0607	7.4047	12.7022	13.7722
45 ⁰	2.1613	5.8867	8.2093	11.4246	19.3030	21.1458
60 ⁰	4.6567	12.0257	17.7547	23.7239	39.2709	43.5688

4.3.3 Effect of uniaxial and biaxial compression

The effect of uniaxial and biaxial compression on the buckling behaviour of SMEE plate is investigated. Their influence on the stability characteristics is assessed on the basis of non-dimensional critical buckling load and with the corresponding modes. The SMEE plate having an aspect ratio of $a/b = 1$ and a span to thickness ratio of $a/h = 100$ with different boundary conditions is considered for the analysis. Table 4.7 presents a comparison between uniaxial and biaxial loading at skew angle of $\alpha = 0^0, 30^0$ and 45^0 in terms of non-dimensional critical buckling load. It can be observed from the results of Table 4.7 that the buckling loads get halved for the bi-axial

compression loading in comparison with the uniaxial loading case irrespective of skew angle and boundary conditions. This is due to the fact that the increase in the load decreases the buckling strength of the SMEE plate. The first three buckling modes are presented in Figure 4.3 for both the uniaxial and biaxial loading cases. The effect of uniaxial and biaxial load on the mode shape of SMEE plate is significant and can be witnessed from the plate buckling direction in the Figure 4.3.

Table 4.5: Effect of skew angle on buckling load parameter for B/F/B CCCF SMEE plate subjected to uniaxial compression ($a/b = 1$, $a/h = 100$)

Skew angle (α)	Buckling mode					
	1	2	3	4	5	6
0^0	0.4289	1.8011	2.5949	3.8611	5.3537	7.1926
15^0	0.4763	1.8980	2.8671	4.1142	5.8291	7.7097
30^0	0.6517	2.2909	3.8311	5.0780	7.5396	9.6120
45^0	1.1044	3.3787	6.2228	7.6547	11.8588	14.5250
60^0	2.4842	6.7955	13.3330	15.7235	24.9038	29.5387

Table 4.6: Effect of skew angle on buckling load parameter for B/F/B FCFC SMEE plate subjected to uniaxial compression ($a/b = 1$, $a/h = 100$)

Skew angle (α)	Buckling mode					
	1	2	3	4	5	6
0^0	0.2519	0.8487	1.8595	2.7026	3.0422	3.7081
15^0	0.2726	0.9002	2.0055	2.8625	3.3845	4.8989
30^0	0.3767	1.1043	2.5460	3.4293	4.5842	6.4689
45^0	0.6529	1.6538	3.9343	5.1042	7.4910	9.7709
60^0	1.4970	3.3685	8.1144	10.4745	16.1308	19.8199

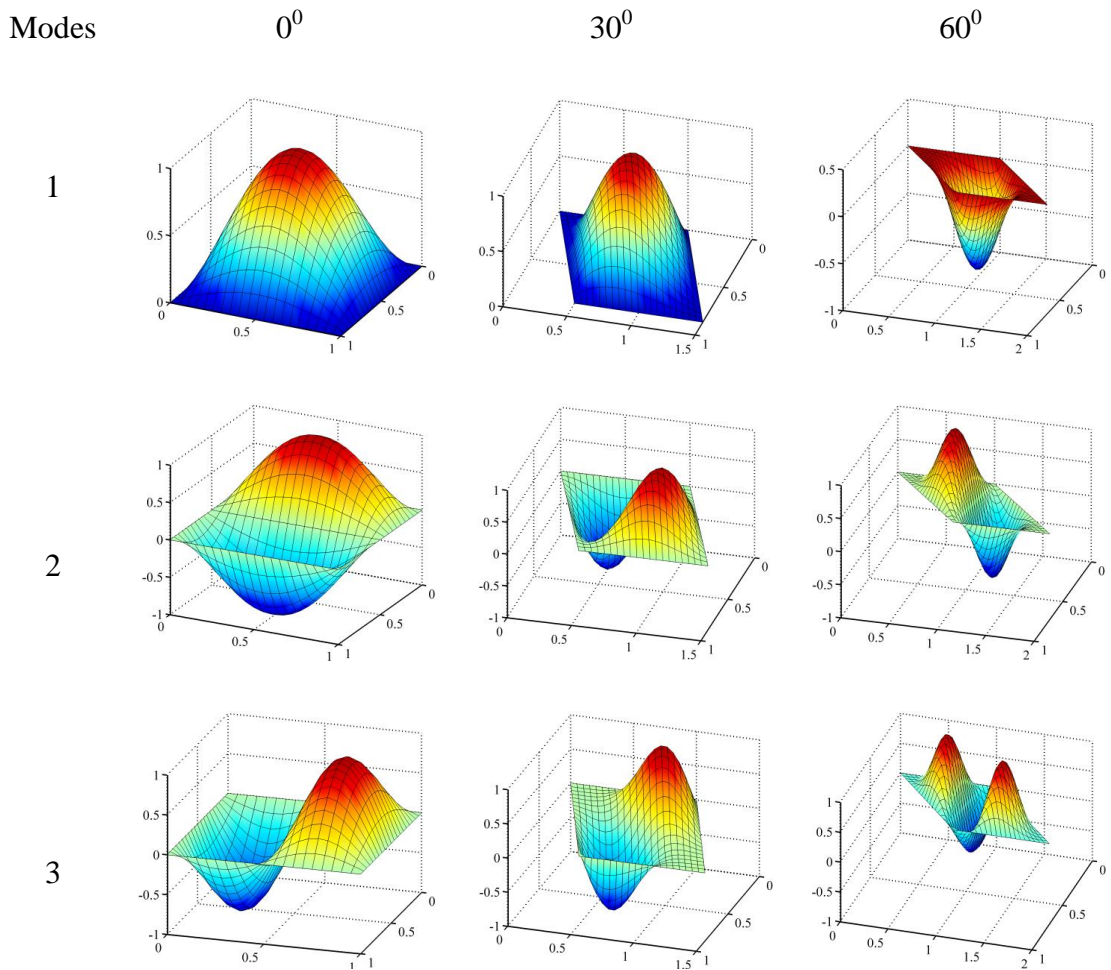


Figure 4.2: First three buckling modes at different skew angles for CCCC SMEE plate ($a/b = 1$, $a/h = 100$)

4.3.4 Effect of material stacking sequence

The buckling behaviour of the SMEE plate is analysed for different stacking sequence of the SMEE plate. The two generally used stacking sequences (B/F/B and F/B/F) of the SMEE plate are considered for the analysis. Both the stacking sequences of SMEE plate are investigated under clamped-clamped boundary condition for $\alpha = 0^0, 15^0, 30^0$ and 45^0 as shown in Figure 4.4. The SMEE plate having $a/b = 1$ and $a/h = 100$ is considered for the investigation. It may be observed from these plots that the SMEE plate with F/B/F stacking configuration yields higher critical buckling load than the B/F/B stacking configuration for all the skew angles of the SMEE plate. It may be due to the fact that the F/B/F configuration exhibits higher stiffness and hence larger buckling load. In addition, it may also be observed from Figure 4.4 that the

non-dimensional buckling load for F/B/F plate is larger than the B/F/B SMEE plate at $\alpha = 45^0$ while for $\alpha = 0^0$ the difference between two stacking sequence is minimum. Consequently, Figure 4.5 presents the comparison of first six buckling mode shapes for B/F/B and F/B/F stacking sequence. It can be seen that the increase in the stiffness of F/B/F plate influenced the mode shapes and for higher buckling modes the effect is largely evident. Further, it may be noticed from the mode shapes that the F/B/F SMEE plate exhibits higher buckling strength than the B/F/B SMEE plate.

Table 4.7: Effect of uniaxial and biaxial compression on buckling load parameter on B/F/B SMEE plate ($a/b = 1$, $a/h = 100$)

Boundary condition	Skew angle (α)	Buckling mode					
		1		2		3	
		uniaxial	biaxial	uniaxial	biaxial	uniaxial	biaxial
CCCC	0^0	0.9399	0.4699	3.0713	1.5356	3.4000	1.7000
	30^0	1.3436	0.6718	3.9273	1.9636	5.0600	2.5303
	45^0	2.1613	1.0806	5.8867	2.9433	8.2093	4.1046
CCCF	0^0	0.4289	0.2144	1.8011	1.5356	2.5949	1.7001
	30^0	0.6517	0.3258	2.2909	1.1454	3.8311	1.1454
	45^0	1.1044	0.5522	3.3787	1.6893	6.2228	3.1114
FCFC	0^0	0.2519	0.1259	0.8487	0.4243	1.8595	0.9297
	30^0	0.3767	0.1883	1.1043	0.5521	2.5460	1.2730
	45^0	0.6529	0.3264	1.6538	0.8269	3.9343	1.9671

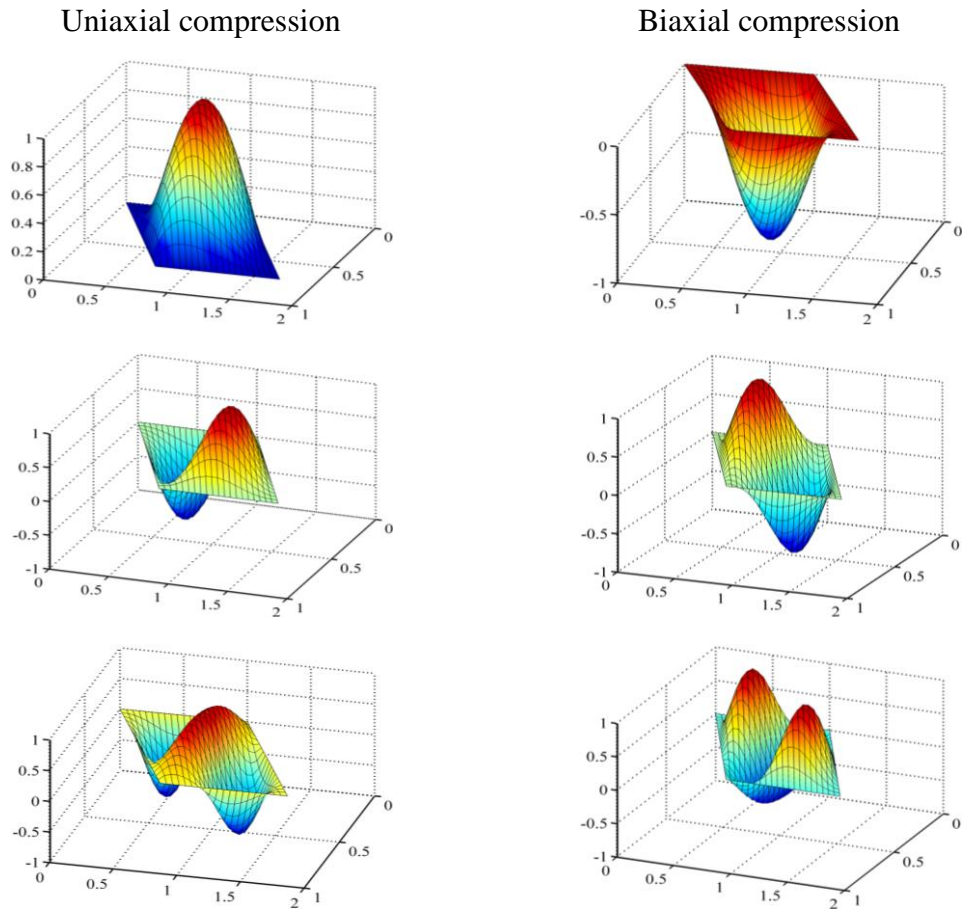


Figure 4.3: First three buckling modes for uniaxial and biaxial compression of CCCC SMEE plate ($a/b = 1$, $a/h = 100$, $\alpha = 45^0$)

4.3.5 Effect of span to thickness ratio (a/h)

In this section, the effect of the span to thickness ratio (a/h) of the SMEE plate on the stability behaviour is investigated. Four different a/h ratios are studied and their corresponding effect on the critical buckling load is analysed under uniaxial compression. Table 4.8 presents the critical buckling load for CCCC SMEE plate obtained for the span to thickness ratios of $a/h = 10, 20, 50, 100$ and $a/b = 1$. Further, the analysis is extended to the CCCF and FCFC support conditions and the corresponding results are tabulated in Table 4.9 and Table 4.10, respectively. From the tabulated results (Table 4.8 - Table 4.10), it may be observed that the critical buckling load increases for smaller thickness ratio while for the higher span to thickness ratio, minimal influence is seen irrespective of the edge conditions and skew inclination of the SMEE plate.

Table 4.8: Effect of thickness ratio on buckling load parameter of B/F/B CCCC SMEE plate ($a/b = 1$)

Skew angle (α)	a/h ratio	Buckling mode					
		1	2	3	4	5	6
0^0	10	1.5726	4.4355	4.4520	7.3330	10.0748	11.2200
	20	1.3335	4.0207	4.1097	6.7823	9.8394	10.7785
	50	0.9368	3.0698	3.3987	5.4183	9.4011	10.0989
	100	0.9399	3.0713	3.4003	5.4223	9.4127	10.1181
15^0	10	1.6767	4.4679	5.0402	7.7721	10.854	12.0721
	20	1.4268	4.0885	4.6403	7.2248	10.593	11.6063
	50	1.0262	3.2248	3.7847	5.8462	10.1204	10.9020
	100	1.0064	3.1599	3.7303	5.7352	10.0906	10.8688
30^0	10	2.0624	5.1943	6.5973	9.3966	13.6671	15.2041
	20	1.7826	4.8095	6.1443	8.8586	13.3375	14.6686
	50	1.3436	3.9273	5.0607	7.4047	12.7022	13.7722
	100	1.3225	3.8632	4.9821	7.2729	12.6576	13.7227
45^0	10	3.0660	7.3308	10.3528	13.6358	18.3952	20.7635
	20	2.7375	6.9491	9.80891	13.1198	20.3290	22.5895
	50	2.1613	5.8867	8.2093	11.4246	19.3030	21.1458
	100	2.1316	5.7957	8.0636	11.2150	19.2078	21.0333

4.3.6 Effect of aspect ratio (a/b)

The buckling behaviour of SMEE plate is studied for different aspect ratios. Figure 4.6 (a) - (c) present the non-dimensional critical buckling loads obtained for different aspect ratio at skew angles of $0^0 - 60^0$. The results are obtained for a plate keeping thickness ratio of $a/h = 100$ and varying aspect ratio from 0.5 to 4 over an interval of 0.5. The decline in the buckling load is observed with the increase in aspect ratio as depicted in Figure 4.6(a). The decline in the buckling load is rapid for smaller aspect ratio i.e., $a/b < 2$, while for $a/b \geq 2$ a steady decline is observed. The similar trend is observed for rest of the cases as shown in Figure 4.6 (b) - (c). It is noteworthy to mention that for the all the boundary conditions, the buckling load at α

$= 0^0$ and $\alpha = 15^0$ converges for $a/b \geq 1$, whereas in case of the FCFC boundary condition, the buckling load converged sharply for $a/b \geq 2.5$.

Table 4.9: Effect of thickness ratio on buckling load parameter of B/F/B CCCF SMEE plate ($a/b = 1$)

Skew angle (α)	a/h ratio	Buckling mode					
		1	2	3	4	5	6
0^0	10	0.9435	2.5059	3.7801	5.4342	6.4487	9.3252
	20	0.7559	2.2533	3.4297	4.9257	6.0331	8.6186
	50	0.4213	1.7985	2.5832	3.8421	5.3298	7.1758
	100	0.4289	1.8011	2.5949	3.8611	5.3537	7.1926
15^0	10	0.9962	2.6308	4.0610	5.6571	7.0538	9.8270
	20	0.8015	2.3661	3.7058	5.1548	6.5916	9.1304
	50	0.4763	1.8980	2.8671	4.1142	5.8291	7.7097
	100	0.4602	1.8722	2.8020	4.0350	5.7804	7.5970
30^0	10	1.1940	3.0929	5.0926	6.6209	9.1180	11.7455
	20	0.9813	2.8012	4.7227	6.1130	8.5449	11.0674
	50	0.6517	2.2909	3.8311	5.0780	7.5396	9.6120
	100	0.6360	2.2626	3.7614	4.9979	7.4681	9.4843
45^0	10	1.7182	4.3176	7.6965	9.3782	14.1269	15.0019
	20	1.4780	3.9999	7.3097	8.8526	13.4243	16.2599
	50	1.1044	3.3787	6.2228	7.6547	11.8588	14.5250
	100	1.0861	3.3399	6.1242	7.5444	11.7219	14.330

Table 4.10: Effect of to thickness ratio on buckling load parameter of B/F/B FCFC SMEE plate ($a/b = 1$)

Skew angle (α)	a/h ratio	Buckling mode					
		1	2	3	4	5	6
0^0	10	0.7076	1.3169	2.7575	3.7778	3.9722	6.0262
	20	0.5405	1.1495	2.4184	3.4730	3.5930	5.2517
	50	0.2415	0.8231	1.8431	2.6986	3.0287	3.6974
	100	0.2519	0.8487	1.8595	2.7026	3.0422	3.7081
15^0	10	0.7163	1.3779	2.9689	3.8842	4.3518	6.8440
	20	0.5474	1.2006	2.6245	3.5524	3.9876	6.1530
	50	0.2726	0.9002	2.0055	2.8625	3.3845	4.8989
	100	0.2590	0.8846	1.9618	2.8064	3.3496	4.7887
30^0	10	0.8180	1.6077	3.5799	4.4185	5.7458	8.3122
	20	0.6399	1.4103	3.2170	4.0759	5.3160	7.6387
	50	0.3767	1.1043	2.5460	3.4293	4.5842	6.4689
	100	0.3644	1.0891	2.4999	3.3809	4.5341	6.3754
45^0	10	1.1206	2.2101	5.0828	6.1620	9.1059	11.812
	20	0.9289	1.9906	4.6973	5.8240	8.5127	11.1107
	50	0.6529	1.6538	3.9343	5.1042	7.4910	9.7709
	100	0.6395	1.6361	3.8736	5.0454	7.4073	9.6400

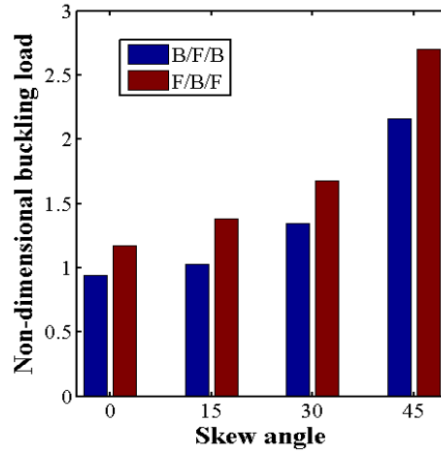


Figure 4.4: Non-dimensional buckling loads of CCCC SMEE plate subjected to uniaxial load for ($a/b = 1$, $a/h = 100$) B/F/B and F/B/F stacking sequence

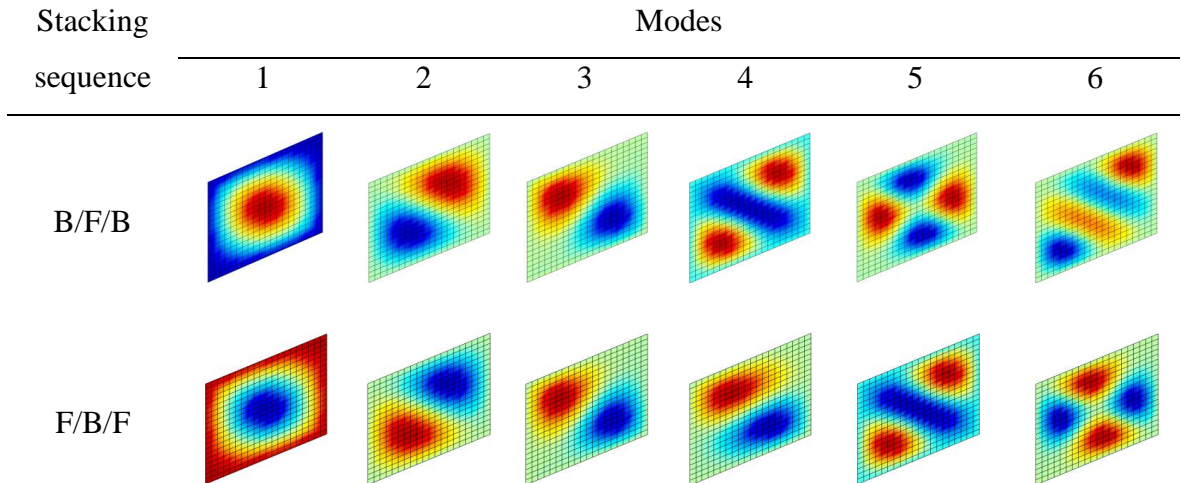
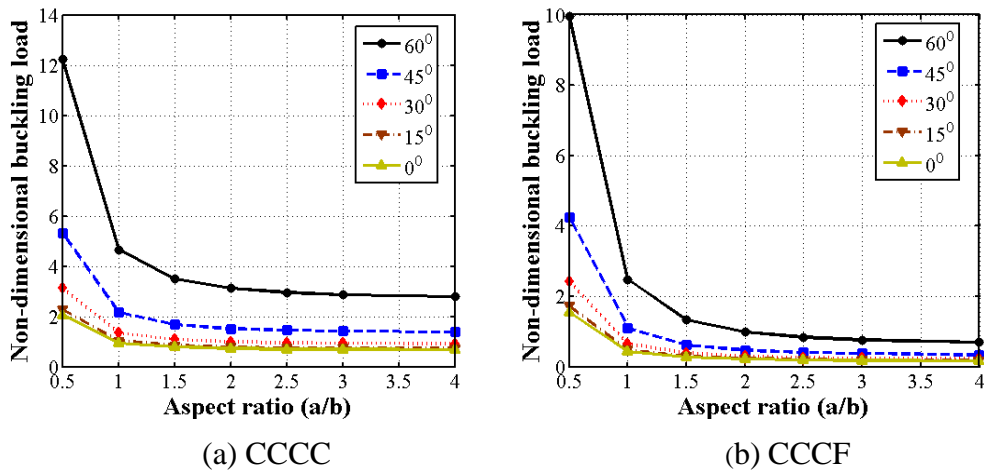
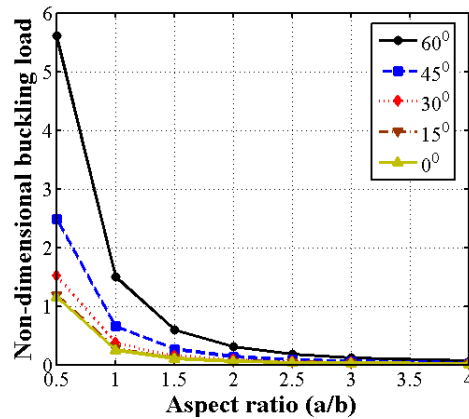


Figure 4.5: Influence of stacking sequence on buckling mode shapes of SMEE plate at $\alpha = 30^\circ$ ($a/b = 1$, $a/h = 100$)



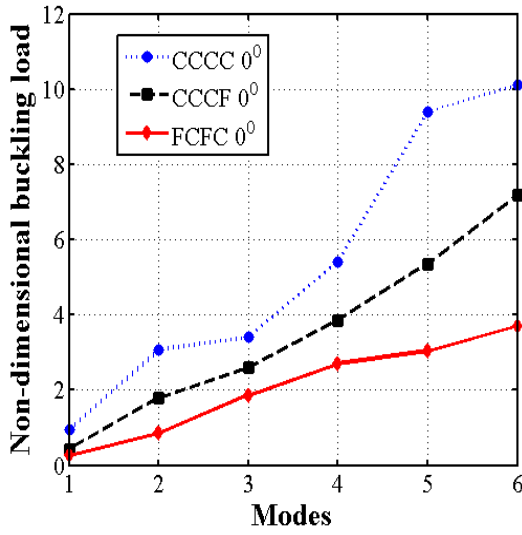


(c) FCFC

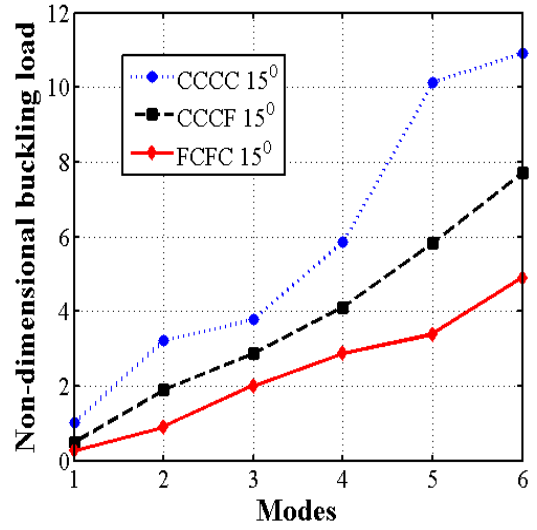
Figure 4.6: Effect of aspect ratio on buckling load parameter ($a/h = 100$)

4.3.7 Buckling behaviour of SMEE plate through mode shapes

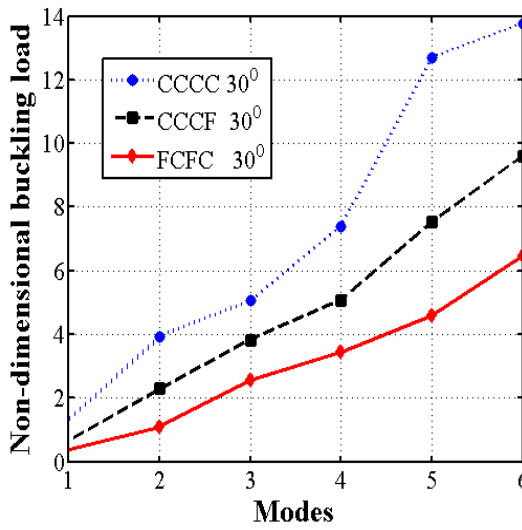
The buckling behaviour of SMEE plate influencing the buckling modes at various skew angles is demonstrated in Figure 4.7(a) - (d). In Figure 4.7, the effect of different boundary conditions on the non-dimensional buckling load for skew angles $\alpha = 0^\circ, 15^\circ, 30^\circ$ and 45° is considered while the plate dimensions are taken as $a/h = 100$ and $a/b = 1$. Effect of increase in skew angle affecting the buckling loads can be observed for all the three boundary conditions. However, the slope of CCCF plate is observed to be nearly constant for the first six modes at $\alpha = 0^\circ, 15^\circ$ and 30° . Consequently, the effect of different boundary conditions on the respective mode shapes for $\alpha = 15^\circ$ and 45° of the SMEE plate is demonstrated in Figure 4.8. In comparison with SMEE plate with $\alpha = 0^\circ$, the introduction of skew angle causes the mode formation near the corners of the plate for all three boundary conditions. It can also be observed from the Figure 4.8 that the number of half sine waves occurred is higher for $\alpha = 45^\circ$ when compared with $\alpha = 15^\circ$ for the third to sixth modes. The larger influence on higher buckling mode shapes can be attributed to the increase in stiffness of the SMEE plate. This stiffness increase is associated with the decrease in the plate area and a decrease in the perpendicular distance between the non-skew edges at higher skew angles.



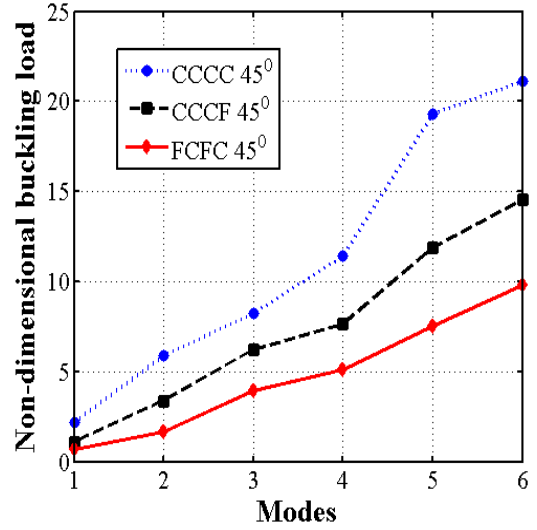
(a) $\alpha = 0^\circ$



(b) $\alpha = 15^\circ$



(c) $\alpha = 30^\circ$



(d) $\alpha = 45^\circ$

Figure 4.7: Effect of boundary condition on buckling load parameter

($a/b = 1$, $a/h = 100$)

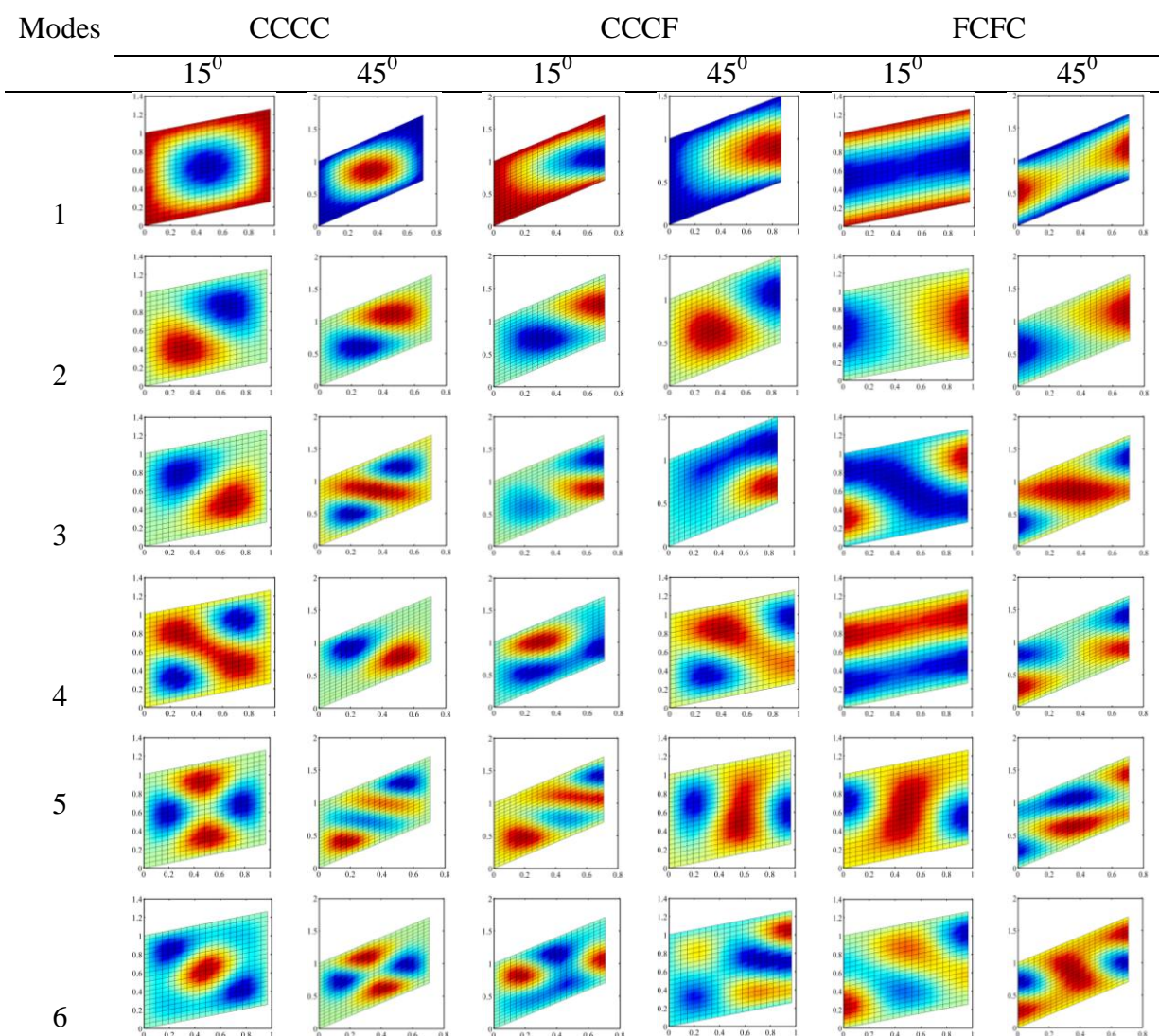


Figure 4.8: First six buckling modes of SMEE plate at skew angles $\alpha = 15^0$ and $\alpha = 45^0$

4.4 CONCLUSIONS

The buckling analysis of layered skew magneto-electro-elastic plate is performed for the uniaxial and biaxial in-plane loading. The skewness of the SMEE plate is achieved by using a suitable transformation matrix. The in-plane stress distribution within the SMEE plate existing due to the enacted force is considered to be equivalent to the applied in-plane compressive loads in the pre-buckling range. The corresponding stress distribution is used to derive the potential energy function. The important observations drawn from the present analysis are the buckling strength increases with increase in the skew angle for all the boundary conditions. Further, in

case of biaxial loading, the buckling load is half of the uniaxial buckling load. The F/B/F stacking sequence of the SMEE plate displayed higher buckling strength over the B/F/B SMEE plate for all the skew angles. Higher span to thickness ratio has minimum influence on the buckling behaviour. In addition, the buckling load decreases with increase in aspect ratio of the SMEE plate irrespective of boundary conditions and skew angles. It is also observed that the influence of boundary condition is significant on the stability behaviour of the SMEE plate.

Chapter 5

STATIC ANALYSIS AND FREE VIBRATION CHARACTERISTICS OF FUNCTIONALLY GRADED SKEW MAGNETO-ELECTRO-ELASTIC PLATE

This chapter presents a finite element (FE) model to assess the free vibration and static response of a functionally graded skew magneto-electro-elastic (FGSMEE) plate. FGSMEE plate is achieved through the thickness material grading using power-law distribution. The coupled constitutive equations along with the total potential energy approach are used to develop the FE model of FGSMEE plate. The transformation matrix is utilized in bringing out the element matrix corresponding to the global axis to a local axis along the skew edges to specify proper boundary conditions. The static behavior of FGSMEE plate for various skew angles is studied. The influence of skew angle on the primary quantities such as displacements, electric potential, and magnetic potential, and secondary quantities such as stresses, electric displacement, and magnetic induction is studied in detail. The effect of skew angle on the natural frequency of an FGSMEE plate is analyzed. In addition, the effect of power-law index, thickness ratio, boundary conditions, and aspect ratio on the free vibration and static response characteristics of FGSMEE plate has been investigated.

5.1. INTRODUCTION

The functionally graded [FG] material has been evolved with the technological advancements in developing a material with functional properties. This new class of material has attracted many researchers to assess their mechanical behaviour through basic structures like the beam, plate, and shells (Ray *et al.* 1992; Kondaiah *et al.* 2015, 2017; Jiang and Ding 2004, 2005, 2007; Wang and Ding 2007; Ray *et al.* 2001). The functionally graded magneto-electro-elastic (FGMEE) material is one such material with functional properties and exhibits coupled piezoelectric and magnetostrictive behavior. The possibility of coupling the different fields can be exploited in transducer application, structural health monitoring, vibration control, energy harvesting, and other applications.

In this chapter, the influence of geometric changes introduced in terms of plate skewness on the static and free vibration behaviour of the functionally graded skew magneto-electro-elastic (FGSMEE) plate is presented. A finite element formulation is developed incorporating the transformation of local skew coordinates on to the global plate coordinates. The influence of skew angle on the natural frequencies of the FGSMEE plate has been effectively investigated. Further, the static behavior of FGSMEE plate is evaluated thoroughly in terms of primary and secondary structural parameters such as the displacements, electric potential, magnetic potential, stresses, electric displacement, and magnetic induction. In addition, the influence of material gradient index is also studied. Further, the effect of boundary conditions, thickness ratio, and aspect ratio on the structural behaviour of the FGSMEE plates are investigated.

5.2. PROBLEM DESCRIPTION AND GOVERNING EQUATION

A schematic diagram of an FGSMEE plate with a Cartesian coordinate system attached to the corner of the plate is shown in Figure 5.1. The length, the width and the total thickness of the plate are a , b and h , respectively. The skew angle of the FGSMEE plate is α . The material properties of the FGSMEE plate are assumed to vary across the thickness according to Power law. The bottom surface of the plate is piezoelectric (BaTiO_3) and the top surface being magnetostrictive (CoFe_2O_4).

The displacement equations implemented in this chapter are identical to Eq. (3.1). However, accounting the continuous variation of material properties and considering the effect of coupled fields, the constitutive equations for the FGSMEE plate can be expressed as follows:

$$\{\sigma_b\} = [C_b(z)]\{\varepsilon_b\} - \{e_b(z)\}E_z - \{q_b(z)\}H_z, \quad \{\sigma_s\} = [C_s(z)]\{\varepsilon_s\} \quad (5.1a)$$

$$D_z = \{e_b(z)\}^T \{\varepsilon_b\} + \xi_{33}(z)E_z + d_{33}(z)H_z \quad (5.1b)$$

$$B_z = \{q_b(z)\}^T \{\varepsilon_b\} + d_{33}(z)E_z + \mu_{33}(z)H_z \quad (5.1c)$$

where, $[C_b(z)]$ and $[C_s(z)]$ are the FG material coefficient matrices given as

$$[C_b(z)] = \begin{bmatrix} C_{11}(z) & C_{12}(z) & C_{13}(z) & C_{16}(z) \\ C_{12}(z) & C_{22}(z) & C_{23}(z) & C_{26}(z) \\ C_{13}(z) & C_{23}(z) & C_{33}(z) & C_{36}(z) \\ C_{16}(z) & C_{26}(z) & C_{36}(z) & C_{66}(z) \end{bmatrix}, [C_s(z)] = \begin{bmatrix} C_{55}(z) & C_{45}(z) \\ C_{45}(z) & C_{44}(z) \end{bmatrix} \quad (5.2)$$

while, $\xi_{33}(z)$ and $\mu_{33}(z)$ are the dielectric constant and the magnetic permeability constant, respectively; $d_{33}(z)$ is the electromagnetic coefficient. The electric displacement, the electric field, the magnetic induction and the magnetic field along the z -direction are represented by D_z , E_z , B_z and H_z , respectively. The electric coefficient matrix $\{e_b(z)\}$ and the magnetic coefficient matrix $\{q_b(z)\}$ are given by

$$\{e_b(z)\} = \begin{Bmatrix} e_{31}(z) \\ e_{32}(z) \\ e_{33}(z) \\ e_{36}(z) \end{Bmatrix}, \{q_b(z)\} = \begin{Bmatrix} q_{31}(z) \\ q_{32}(z) \\ q_{33}(z) \\ q_{36}(z) \end{Bmatrix} \quad (5.3)$$

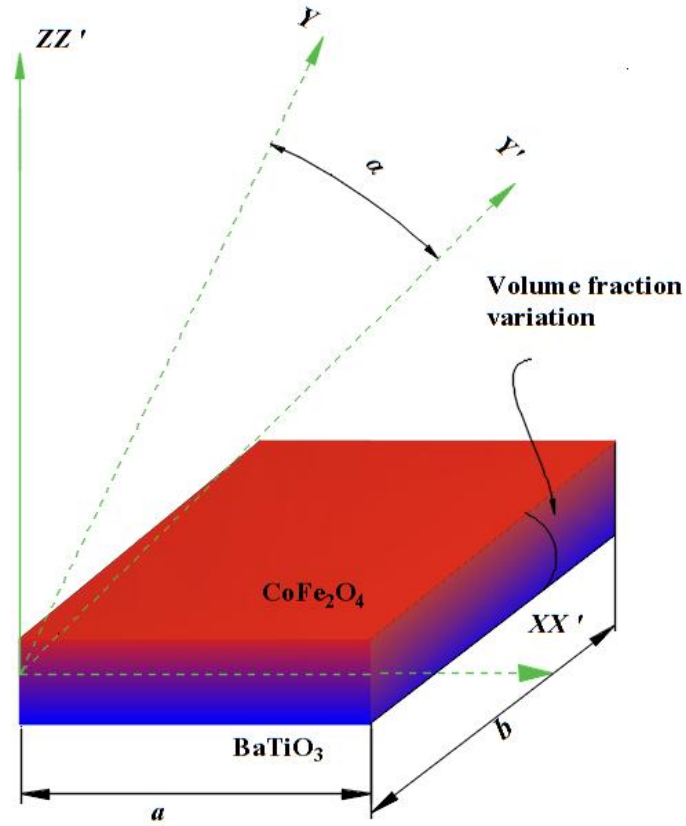


Figure 5.1: Schematic representation of functionally graded skew MEE plate

The material properties are graded along the thickness direction of the plate by implementing the volume fraction power law distribution. The present study considers smooth and continuous variation of the constituent materials governed by power law gradient index. A simple power law for a functionally graded material can be assumed as (Kattimani and Ray 2015)

$$V = \left\{ \left(\frac{z}{h} \right) + \left(\frac{1}{2} \right) \right\}^\eta$$

where, h is the thickness of the plate, z the thickness coordinate ($0 \leq z \leq h$), and η is the power law index.

According to the definition of the volume fraction and rule of mixtures (Bhangale and Ganesan, 2006), the various effective material properties can be written as follows:

$$\begin{aligned} \bar{C}_{fg}(z) &= C_F + (C_B - C_F)V, \quad \bar{\rho}_{fg}(z) = \rho_F + (\rho_B - \rho_F)V, \\ \bar{e}_{fg}(z) &= e_F + (e_B - e_F)V, \quad \bar{q}_{fg}(z) = q_F + (q_B - q_F)V \\ \bar{\xi}_{fg}(z) &= \xi_F + (\xi_B - \xi_F)V, \quad \bar{\mu}_{fg}(z) = \mu_F + (\mu_B - \mu_F)V \end{aligned} \quad (5.4)$$

where, $\rho_{fg}(z)$ corresponds to the functionally graded material density. The subscript “fg” and the over lines stands for the effective material properties obtained by the above equations for a particular power law gradient index η . For the sake of brevity, the variation of functionally graded material properties in accordance with the variation in the power law gradient index is represented for elastic constant C_{11} alone in Figure 5. 2. Further, the global equations of motion and the final form of equations corresponding to static analysis and free vibration can be expressed identical to the Eqs. (3.16) – (3.22).

5.3. RESULTS AND DISCUSSION

The material properties used in the present analysis are given in Table 2.1. The non-homogeneous transversely isotropic FGSME plate is functionally graded along the thickness by implementing the power law. For all the values of power law index (except for pure magnetostrictive and pure piezoelectric plate i.e., $\eta = 0$ and $\eta = \infty$), the variation of material properties in the bottom piezoelectric and the top magnetostrictive plate is achieved as shown in Figure 5. 2. Three point Gaussian integration rule is considered for computing the element matrices corresponding to

bending deformation while two point Gaussian of that are used for computing the element matrices corresponding to transverse shear deformation. The boundary conditions for the analysis are adapted from the previous chapter.

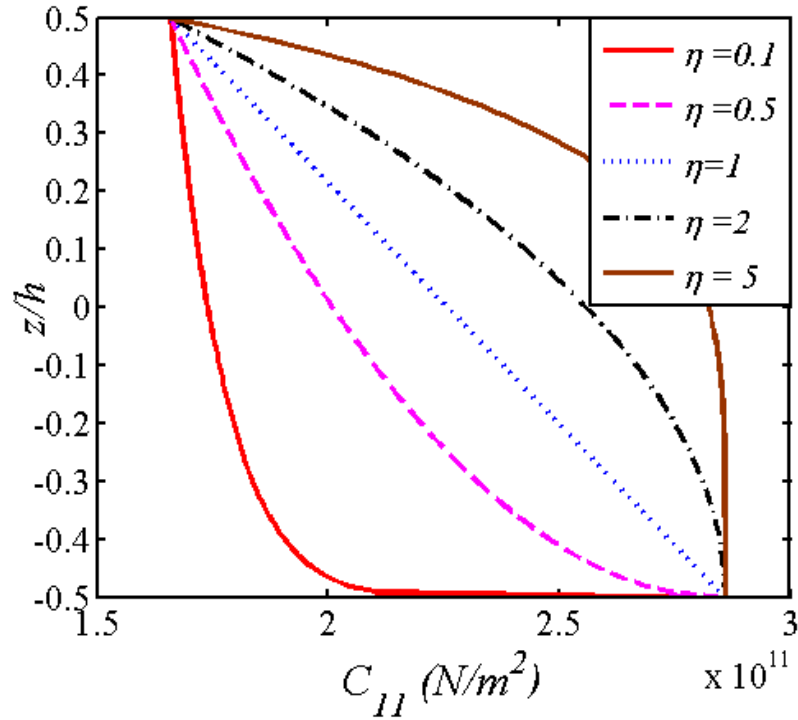


Figure 5. 2: Variation of C_{11} for different gradient index values η

5.3.1 Validation studies

The free vibration study of functionally graded magneto-electro-elastic (FGMEE) plate proposed by Milazzo (2014a) is considered for the validation. The natural frequencies for the simply supported FGMEE plate having the power-law index $\eta = 1$, aspect ratio of $b/a = 2$ and thickness ratio of $h/a = 0.1$ and 0.2 is presented in Table 5.2. The convergence study is also presented in Table 5.3. It can be seen from the tabulated results that for a 20×20 mesh size, an excellent agreement is achieved with the solutions available in literature. Therefore, for all the subsequent analysis, a mesh size of 20×20 is considered. It may be noted that to the best of our knowledge, the study related to skew MEE plates are not available in the literature. Hence, the effectiveness of the FE formulation to assess the influence of skew angle on the plate characteristics is evaluated for the laminated composite plate by decoupling the elastic and magnetic coupling co-efficients and considering only the

elastic co-efficients. The results are presented in Table 5.2 and Table 5.3 for the clamped-clamped and simply supported laminated composite plate, respectively, for different configurations. The material properties for the analysis are considered similar to Garg *et al.* (2006) and Kanasogi and Ray (2013) [$E_1/E_2 = 40$, $E_2 = E_3$, $G_{12} = 0.6E_2$, $G_{13} = G_{23} = 0.5E_2$, $\nu_{12} = \nu_{13} = \nu_{23} = 0.25$]. The tabulated results display an excellent agreement with the results available in the literature (Garg *et al.* 2006; Kanasogi and Ray 2013). Hence, the correctness of the present FE formulation is assessed and the same formulation is extended to evaluate the structural characteristics of FGSME plate. Since the free vibration study is validated, the natural frequencies corresponding to FGSME plates are presented before the static characteristics.

5.3.2 Free vibration of FGSME plate

In this section, the free vibration characteristic of FGSME plate is analysed. The material property distribution is governed by the power law. Further, the FGSME plate having an aspect ratio of $b/a = 1$ and thickness ratio of $a/h = 100$ is evaluated for various skew angles i.e., $\alpha = 0^0, 15^0, 30^0$ and 45^0 . The effect of skew angle (α) on the natural frequency corresponding to different power-law index (i.e., $\eta = 0, 0.2, 0.5, 1, 2, 5$ and 100) is presented in Table 5.4 for simply supported and clamped FGSME plates. It can be observed from this table that irrespective of η , the natural frequencies of the FGSME plate increase with the increase in skew angle. It can be attributed to the fact that the stiffness of the skew plate increases with the decrease in the plate area and the perpendicular distance between non-skew edges causing frequency enrichment. It can also be noticed that the increase in η values, effectively decreases the natural frequencies of the FGSME plate. The decrease in natural frequency with the increase in power-law index is due to the lower piezoelectric elastic properties than the magnetostrictive properties. It is evident from Table 5.4 that the clamped FGSME plate yields higher natural frequency over the simply supported plate. This trend is due to the increase in local flexural rigidity of the FGSME plate as the edge support stiffens.

The effect of thickness ratio (a/h) on the natural frequencies of simply supported FGSME plate is encapsulated in Table 5.5 for different power-law index

and its influence on free vibration characteristics is clearly evident. The aspect ratio is considered $b/a = 1$ to assess the influence of different thickness ratio. The skew angle largely affects thin plates over thick plates. Also, thin plates display higher natural frequency with the increase in skew angle compared to thick plates. Table 5.6 presents the effect of aspect ratio on the natural frequency of the simply supported FGSME plate $a/h = 100$. It can be observed from the results that the increase in aspect ratio leads to the decrease in natural frequency of the FGSME plate irrespective of the power-law index and skew angle. Since a and h are constants in non-dimensional frequency parameter, the increase in b will certainly decrease the frequency.

5.3.3 Static analysis of FGSME plates

This section addresses the static response characteristics of the FGSME plate for various geometrical conditions and power-law index. The sinusoidal distributed load (Lage *et al.* 2004) with a force F_0 is applied on the top surface of the FGSME plate to study the static behaviour as shown in Eq. (5.5). The geometrical parameters are considered as follows: simply supported boundary condition; $a/h = 100$; $b/a = 1$, unless otherwise stated. The effect of skew angle on the primary and secondary parameters is thoroughly investigated. The secondary parameters such as stresses, electric displacement, and magnetic induction are derived from the primary parameters such as displacement and potentials (electric and magnetic). Further, the effects of power-law index, boundary condition, thickness ratio, and aspect ratio on the static behavior of the FGSME plate are evaluated.

$$F_i = F_0 \sin\left(\frac{\pi x}{a}\right) \sin\left(\frac{\pi y}{b}\right) \quad (5.5)$$

The effect of skew angle on the displacement u across the thickness is shown in Figure 5.3(a) – (e) for different power law index η . It is evident from these figures that for all the power law index values, u decreases with increase in skew angle. This is due to the fact that the stiffness of the FGSME plate increases with increase in skew angle. It can also be observed from these figures that for $\eta = 0$ (i.e., pure magnetostrictive), the displacement is lower and steadily increases with the increase in η value. This may be attributed to the fact that with the increase in power-law index

(η), the volume fraction of BaTiO₃ increases. Since the elastic properties of BaTiO₃ are lower than CoFe₂O₄, the displacements produced are higher for higher value of η . Figure 5.3 also depicts the effect of skew angle on the displacement for various η values. It may be seen from Figure 5.3 that for all the skew angles, the displacement quantity u across the thickness direction experiences only bending. Figure 5.4(a) – (e) present the through-thickness behavior of the displacement quantity v across the z -direction. It can be observed from the Figure 5.4(a) that for $\eta = 0$, the FGSME plate experiences only bending for all the skew angles while stretching is dominant for other η values. The increase in η values witnessed an increase in stretching and decrease in bending of the plate. This phenomenon can be attributed to the piezoelectric material possessing a tendency to increase the stiffness of the plate in the polling direction by induced electric field due to the strains developed. Hence, the plate with low BaTiO₃ concentration experiences lower induced electric field resulting in bending only. The increase in BaTiO₃ concentration causes the increase in induced electric field in the polling direction i.e., z -direction, there by reduces the bending in the thickness direction and increases stretching along in-plane direction. The influence of skew angle on the w -displacement is shown in Figure 5.5(a) – (e). It can be observed from the plots that the increase in skew angle significantly decreases the w -deflection.

The effect of skew angle on electric and magnetic potentials is investigated. The slope in the z -direction for electric potential decreases with the increase in skew angle as observed from Figure 5.6(a) – (e). It can also be seen that the electric potential ϕ increases with the increase in η . This is due to the piezoelectric material enrichment of the FGSME plate for the higher η . Similarly, the effect of skew angle on the magnetic potential of FGSME plate for various power-law index η is shown in Figure 5.7(a) – (e). It is noticed from these figures that the magnetic potential varies linearly and symmetrically across the thickness (negative potential at the bottom and positive at the top). It can also be noticed that the magnetic potential decreases with the increase in skew angle irrespective of η . Further, the increase in η values had minimal influence on the magnetic potential.

Table 5.1: Convergence and validation studies of normalized natural frequencies of FGMEE plate

<i>h/a</i>	Mode									
	1	2	3	4	5	6	7	8	9	
0.2	Present (4×4)	6.798	7.923	11.283	13.595	13.642	15.202	18.982	18.693	19.326
	Present (8×8)	6.638	7.894	11.213	13.487	13.608	15.183	18.888	18.601	19.295
	Present (12×12)	6.623	7.872	11.208	13.462	13.592	15.172	18.854	18.592	19.283
	Present (16×16)	6.619	7.863	11.203	13.458	13.588	15.167	18.849	18.583	19.278
	Present (20×20)	6.618	7.860	11.198	13.455	13.583	15.161	18.843	18.579	19.273
	Milazzo (2014a)	6.735	8.223	11.882	13.463	15.049	16.951	19.027	20.178	20.415
0.1	Present (4×4)	9.720	13.598	14.909	23.158	27.195	27.290	28.106	31.411	35.006
	Present (8×8)	9.663	13.421	14.821	22.986	26.943	27.102	27.994	31.387	34.885
	Present (12×12)	9.652	13.417	14.811	22.963	26.932	27.082	27.979	31.372	34.869
	Present (16×16)	9.639	13.413	14.807	22.959	26.928	27.078	27.971	31.367	34.862
	Present (20×20)	9.637	13.408	14.801	22.952	26.921	27.069	27.967	31.361	34.858
	Milazzo (2014a)	9.584	12.852	14.733	22.577	25.701	28.339	28.734	32.391	36.341

Table 5.2: Normalized frequency parameter $\lambda = \omega b^2 / \pi^2 h (\rho/E_2)^{1/2}$ for the clamped-clamped laminated composite plate ($a/h = 10$)

Skew angle α	Source	$(0^0/90^0/0^0/90^0)$			$(-45^0/-45^0/-45^0/-45^0)$			$(90^0/0^0/90^0/0^0/90^0)$		
		Mode			Mode			Mode		
		1	2	3	1	2	3	1	2	3
0^0	Kanasogi and Ray (2013)	2.2990	3.7880	3.7880	2.2119	3.7339	3.7339	2.3687	3.5399	4.1122
	Garg et al. (2006)	2.3315	3.6531	3.6545	2.2433	3.6000	3.6012	2.3201	3.4769	4.4102
	Present	2.2990	3.5913	3.8695	2.1767	3.5746	3.5139	2.3400	3.3655	4.2382
15^0	Kanasogi and Ray (2013)	2.3809	3.7516	4.0785	2.3099	3.6997	4.0438	2.4663	3.6255	4.3418
	Garg et al. (2006)	2.3741	3.5856	3.8401	2.3049	3.5346	3.8092	2.3699	3.4821	4.4049
	Present	2.3992	3.5560	4.0841	2.2344	3.5111	3.9290	2.3160	3.4637	4.2346
30^0	Kanasogi and Ray (2013)	2.6666	3.9851	4.7227	2.6325	3.9549	5.2107	2.7921	3.9557	5.0220
	Garg et al. (2006)	2.5240	4.1943	4.5373	2.4945	3.6113	5.0932	2.5366	3.5696	4.4734
	Present	2.4903	3.8967	4.4609	2.4722	3.5807	5.0199	2.4896	3.6363	4.7949
45^0	Kanasogi and Ray (2013)	3.3015	4.6290	5.8423	3.3015	4.6290	5.8423	3.4739	4.7129	5.8789
	Garg et al. (2006)	2.8377	4.7614	5.6620	2.8377	4.7614	5.5162	2.8665	4.7074	5.4562
	Present	2.7948	4.5102	5.6270	2.8348	4.5102	5.4970	2.9439	4.6545	5.4362

Table 5.3: Normalized frequency parameter $\lambda = \omega b^2 / \pi^2 h (\rho/E_2)^{1/2}$ for the simply supported laminated composite plate ($a/h = 10$)

Skew angle α	Source	$(0^0/90^0/0^0/90^0)$			$(-45^0/-45^0/-45^0/-45^0)$			$(90^0/0^0/90^0/0^0/90^0)$		
		Mode			Mode			Mode		
		1	2	3	1	2	3	1	2	3
0^0	Kanasogi and Ray (2013)	1.4829	2.4656	3.2522	1.7974	3.3351	3.3351	1.5699	2.8917	3.7325
	Garg et al. (2006)	1.5076	2.4380	3.2254	1.8493	3.3370	3.3370	1.5635	2.4383	3.5033
	Present	1.4836	2.4392	3.1328	1.8111	3.4889	3.4889	1.5314	2.4392	3.6614
15^0	Kanasogi and Ray (2013)	1.5741	2.5351	3.0270	1.8313	3.6724	3.6724	1.6874	3.0458	3.9600
	Garg et al. (2006)	1.5796	2.5775	2.9892	1.8675	3.5810	3.5810	1.6571	2.9840	3.6505
	Present	1.5653	2.5961	3.0730	1.8219	3.4560	3.4560	1.6261	2.8245	3.5161
30^0	Kanasogi and Ray (2013)	1.8871	2.9372	3.4489	2.0270	4.2361	4.2361	2.0840	3.4023	4.6997
	Garg et al. (2006)	1.8226	2.9585	3.2357	1.9894	4.3208	4.3208	1.9596	3.1690	4.6796
	Present	1.8354	3.0573	3.4428	1.9409	4.1836	4.1836	1.9262	3.1844	4.4912
45^0	Kanasogi and Ray (2013)	2.5609	3.3126	4.0617	2.5609	4.2772	4.2772	2.8925	4.1906	5.4149
	Garg et al. (2006)	2.2996	3.4773	4.4889	2.3194	4.5009	4.5009	2.4811	4.4875	5.3289
	Present	2.3563	3.4126	4.3756	2.2676	4.3425	4.3425	2.4260	4.1908	5.2113

Table 5.4: Skew angle influence on the natural frequency of FGSMEE plate

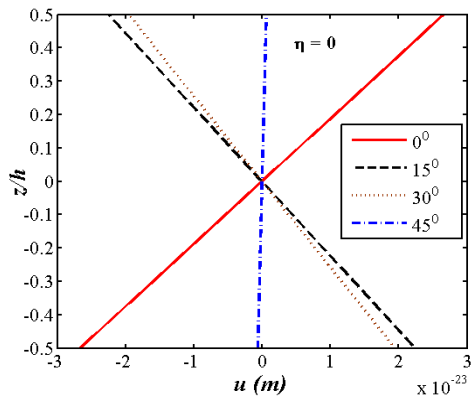
Skew angle (α)	η	Boundary condition	Mode				
			1	2	3	4	5
0°	0	SSSS	4.561	11.782	11.848	23.655	25.466
		CCCC	10.646	22.006	22.066	33.028	36.367
	0.2	SSSS	4.357	11.292	11.327	22.850	24.462
		CCCC	10.357	21.322	21.363	31.924	35.230
	0.5	SSSS	4.240	11.010	11.029	22.376	23.882
		CCCC	10.116	20.755	20.781	31.021	34.297
	2	SSSS	4.123	10.726	10.731	21.884	23.296
		CCCC	9.748	19.894	19.900	29.673	32.891
	5	SSSS	4.053	10.555	10.558	21.604	22.941
		CCCC	9.588	19.520	19.522	29.094	32.278
100	SSSS	3.927	10.240	10.255	21.110	22.293	
	CCCC	9.190	18.549	18.574	27.616	30.705	
15°	0	SSSS	6.600	12.600	14.638	24.289	28.824
		CCCC	11.231	22.753	23.996	35.284	39.202
	0.2	SSSS	6.346	12.081	14.038	23.396	27.660
		CCCC	10.923	22.065	23.236	34.111	37.980
	0.5	SSSS	6.197	11.783	13.692	22.876	26.990
		CCCC	10.668	21.493	22.607	33.149	36.980
	2	SSSS	6.045	11.483	13.342	22.342	26.312
		CCCC	10.277	20.621	21.656	31.711	35.477
	5	SSSS	5.957	11.306	13.137	22.034	25.917
		CCCC	10.107	20.243	21.247	31.092	34.824
100	SSSS	5.799	10.989	12.769	21.490	25.215	
	CCCC	9.685	19.283	20.201	29.514	33.147	
30°	0	SSSS	8.805	16.015	20.886	29.138	37.879
		CCCC	13.385	26.297	29.852	43.037	48.861
	0.2	SSSS	8.424	15.376	19.994	27.979	36.326
		CCCC	13.008	25.552	28.913	41.657	47.347
	0.5	SSSS	8.203	15.009	19.480	27.308	35.424
		CCCC	12.696	24.932	28.138	40.518	46.106
	2	SSSS	7.981	14.636	18.964	26.627	34.511
		CCCC	12.220	23.984	26.967	38.801	44.242
	5	SSSS	7.851	14.417	18.659	26.231	33.979
		CCCC	12.014	23.571	26.463	38.060	43.435
100	SSSS	7.618	14.028	18.112	25.530	33.025	
	CCCC	11.500	22.532	25.177	36.168	41.370	
45°	0	SSSS	13.156	22.879	34.065	41.884	57.023
		CCCC	18.884	34.854	44.131	59.703	71.843
	0.2	SSSS	12.553	21.988	32.526	40.222	54.670
		CCCC	18.336	33.891	42.749	57.994	69.709
	0.5	SSSS	12.205	21.474	31.642	39.255	53.297
		CCCC	17.883	33.095	41.608	56.571	67.954
	2	SSSS	11.858	20.951	30.759	38.271	51.908
		CCCC	17.195	31.880	39.886	54.393	65.303
	5	SSSS	11.654	20.647	30.238	37.700	51.099
		CCCC	16.896	31.352	39.145	53.444	64.152
100	SSSS	11.287	20.110	29.298	36.682	49.642	
	CCCC	16.149	30.042	37.253	51.045	61.219	

Table 5.5: Influence of thickness ratio (a/h) on the natural frequency of simply supported FGSME plate ($b/a = 1$)

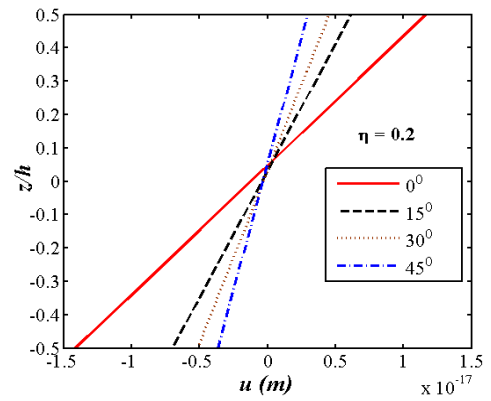
Skew angle (α)	a/h	$\eta = 0$			$\eta = 0.2$			$\eta = 1$			$\eta = 5$			$\eta = 100$		
		1	2	3	1	2	3	1	2	3	1	2	3	1	2	3
0°	10	4.296	10.206	10.253	4.181	9.963	9.996	4.007	9.589	9.601	3.881	9.315	9.316	3.721	8.952	8.971
	20	4.477	11.316	11.376	4.350	11.008	11.049	4.120	10.251	10.265	3.986	9.930	9.932	3.813	9.499	9.521
	100	4.561	11.782	11.848	4.357	11.292	11.327	4.173	10.846	10.858	4.053	10.555	10.558	3.927	10.240	10.255
15°	10	4.671	10.149	11.643	4.550	9.903	11.370	4.367	9.526	10.950	4.236	9.251	10.642	4.068	8.905	10.257
	20	4.985	11.075	12.837	4.853	10.777	12.498	4.655	10.326	11.985	4.512	10.003	11.617	4.331	9.590	11.146
	100	6.600	12.600	14.638	6.346	12.081	14.038	6.110	11.611	13.491	5.957	11.306	13.137	5.799	10.989	12.769
30°	10	5.960	11.379	15.015	5.817	11.118	14.692	5.598	10.716	14.191	5.439	10.421	13.820	5.241	10.054	13.363
	20	6.700	12.866	17.418	6.531	12.535	16.983	6.274	12.033	16.319	6.089	11.671	15.839	5.856	11.212	15.232
	100	8.805	16.015	20.886	8.424	15.376	19.994	8.075	14.795	19.183	7.851	14.417	18.659	7.618	14.028	18.112
45°	10	8.926	14.698	18.558	8.725	14.390	18.209	8.414	13.911	17.519	8.186	13.555	16.798	7.906	13.123	16.441
	20	10.464	17.471	27.455	10.197	17.039	26.832	9.788	16.379	25.856	9.492	15.900	25.114	9.122	15.298	24.183
	100	13.156	22.879	34.065	12.553	21.988	32.526	12.005	21.174	31.133	11.654	20.647	30.238	11.287	20.110	29.298

Table 5.6: Influence of aspect ratio (b/a) on the natural frequency of simply supported FGSMEE plate ($a/h = 100$)

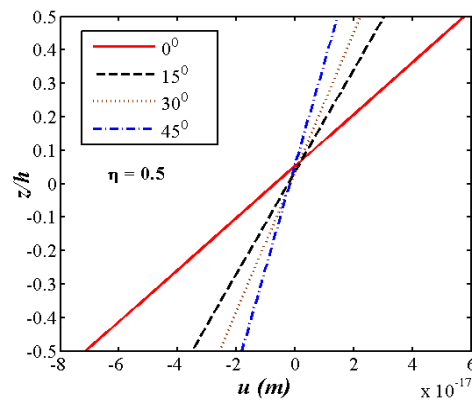
Skew angle (α)	b/a	$\eta = 0$			$\eta = 0.2$			$\eta = 1$			$\eta = 5$			$\eta = 100$		
		1	2	3	1	2	3	1	2	3	1	2	3	1	2	3
0°	0.5	9.611	16.192	29.925	10.000	16.809	30.965	10.434	17.508	32.156	10.792	18.089	33.149	11.164	18.694	34.166
	1	4.561	11.782	11.848	4.357	11.292	11.327	4.173	10.846	10.858	4.053	10.555	10.558	3.927	10.240	10.255
	1.5	2.790	5.946	8.842	2.906	6.153	9.201	3.036	6.389	9.609	3.144	6.586	9.948	3.257	6.788	10.305
15°	2	2.417	4.498	8.393	2.518	4.651	8.741	2.631	4.826	9.135	2.725	4.972	9.463	2.824	5.120	9.807
	0.5	14.830	20.501	33.669	15.287	21.166	34.759	15.811	21.933	36.018	16.246	22.575	37.074	16.675	23.226	38.144
	1	6.600	12.600	14.638	6.346	12.081	14.038	6.110	11.611	13.491	5.957	11.306	13.137	5.799	10.989	12.769
30°	1.5	3.790	6.533	9.965	3.928	6.766	10.3654	4.085	7.032	10.818	4.217	7.253	11.194	4.349	7.482	11.586
	2	3.067	4.885	9.175	3.186	5.056	9.557	3.321	5.251	9.990	3.434	5.414	10.349	3.548	5.579	10.727
	0.5	22.054	28.411	43.822	22.872	29.397	45.211	23.795	30.525	46.819	24.560	31.467	48.167	25.329	32.422	49.526
45°	1	8.805	16.015	20.886	8.424	15.376	19.994	8.075	14.795	19.183	7.851	14.417	18.659	7.618	14.028	18.112
	1.5	4.793	8.597	12.897	4.975	8.913	13.424	5.183	9.274	14.019	5.357	9.573	14.514	5.535	9.884	15.028
	2	3.859	6.293	11.586	4.012	6.525	12.071	4.184	6.789	12.618	4.328	7.010	13.073	4.474	7.237	13.549
45°	0.5	34.859	43.221	64.861	36.288	44.836	66.984	37.896	46.678	69.432	39.236	48.217	71.488	40.600	49.791	73.558
	1	13.156	22.879	34.065	12.553	21.988	32.526	12.005	21.174	31.133	11.654	20.647	30.238	11.287	20.110	29.298
	1.5	6.878	13.199	19.584	7.152	13.679	20.382	7.462	14.227	21.283	7.722	14.684	22.033	7.989	15.153	22.810
	2	5.557	9.715	17.426	5.774	10.083	18.146	6.020	10.501	18.957	6.226	10.850	19.630	6.435	11.208	20.332



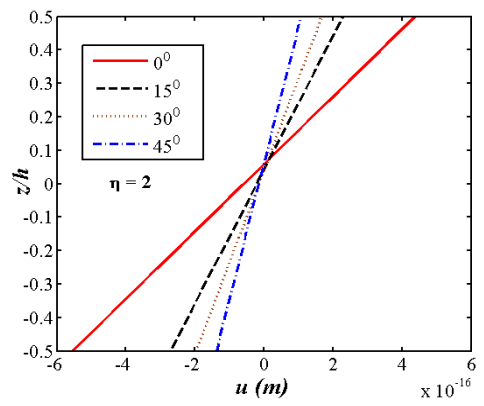
(a)



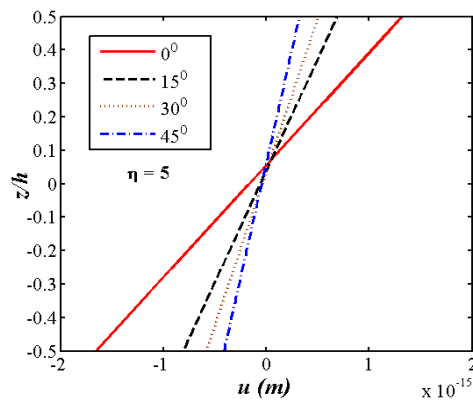
(b)



(c)



(d)



(e)

Figure 5.3: Through thickness variation of displacement u for different skew angles at power-law values (a) $\eta = 0$ (b) $\eta = 0.2$ (c) $\eta = 0.5$ (d) $\eta = 2$ (e) $\eta = 5$

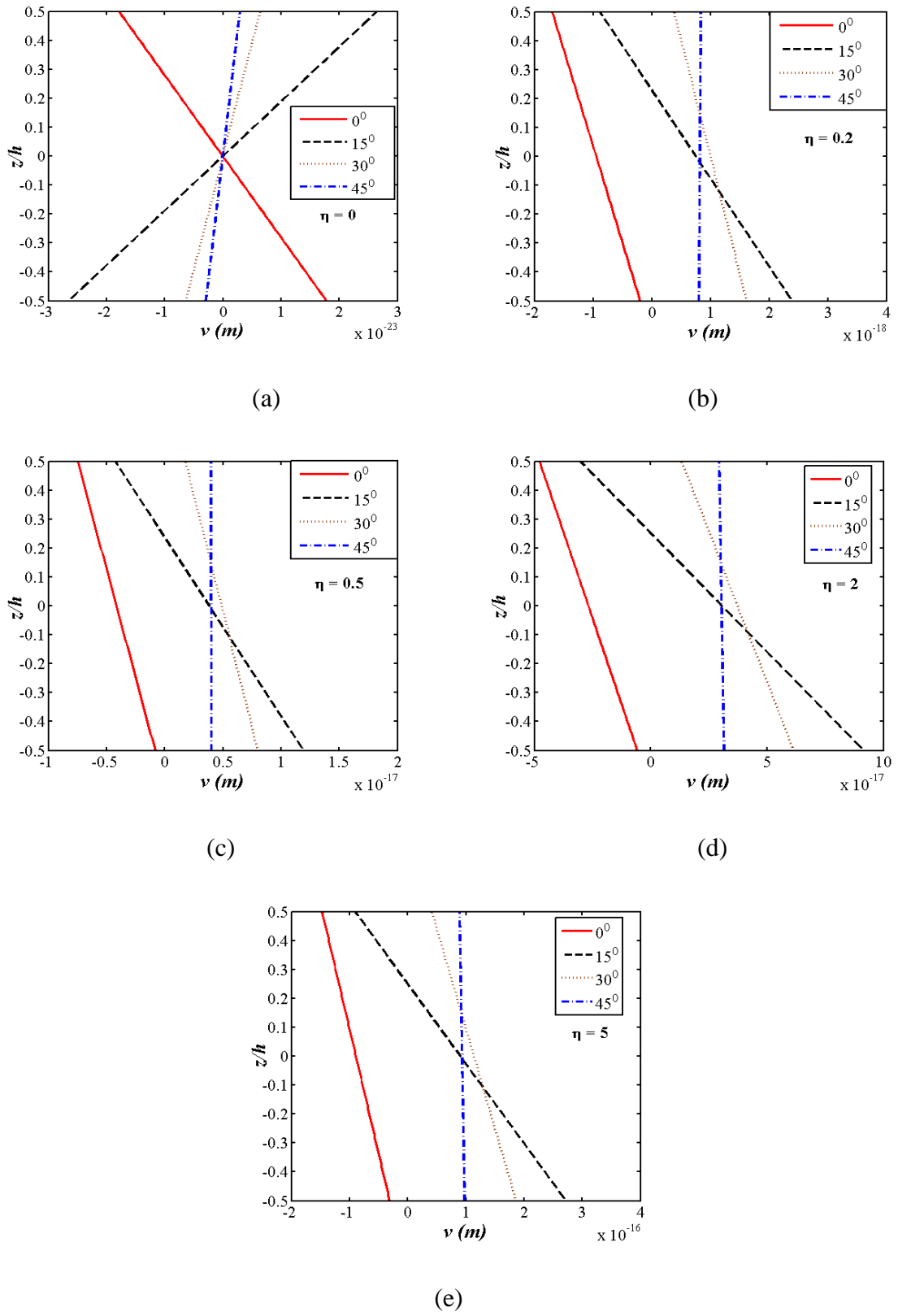
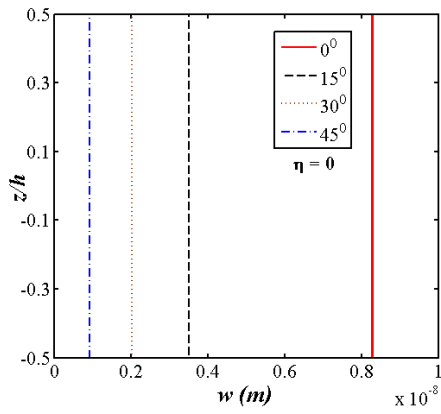
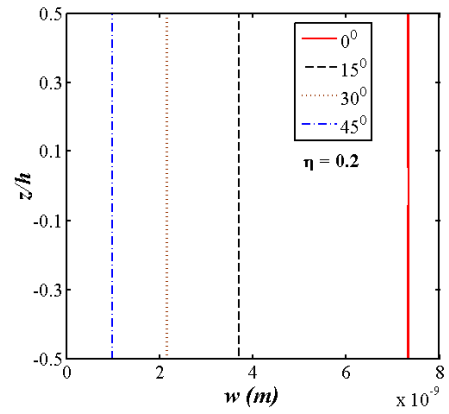


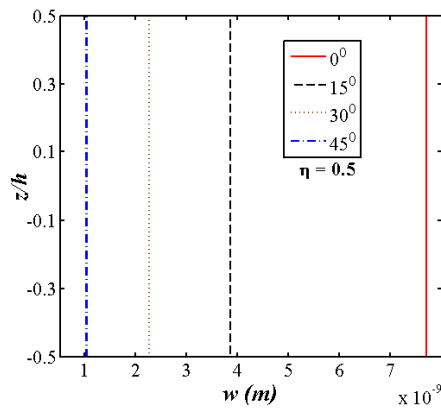
Figure 5.4: Through thickness variation of displacement v for different skew angles at power-law index values (a) $\eta = 0$ (b) $\eta = 0.2$ (c) $\eta = 0.5$ (d) $\eta = 2$ (e) $\eta = 5$



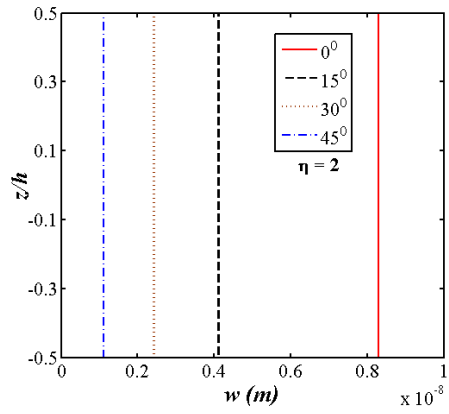
(b)



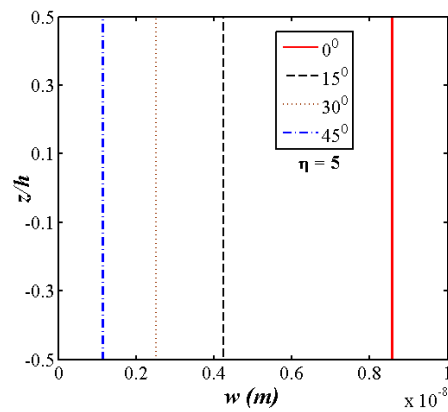
(b)



(c)



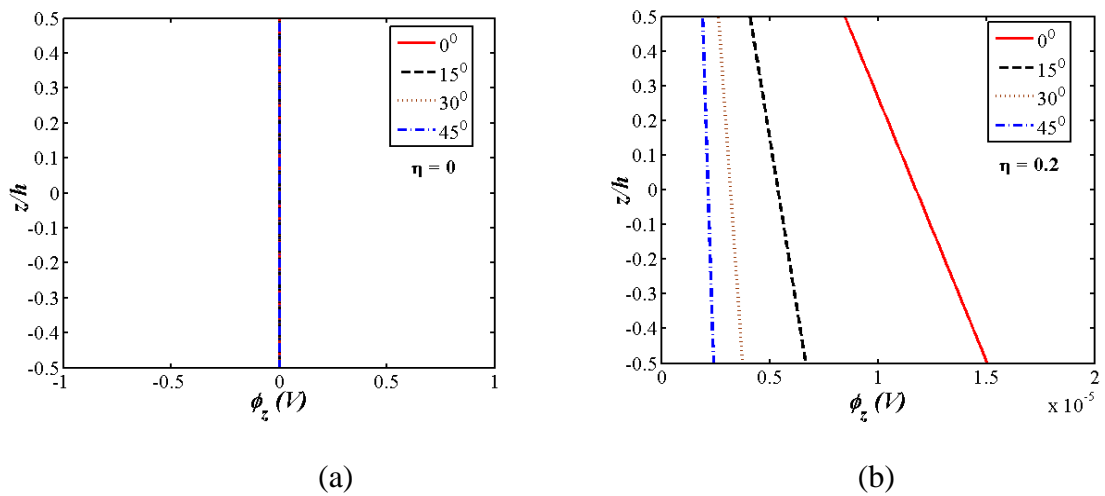
(d)

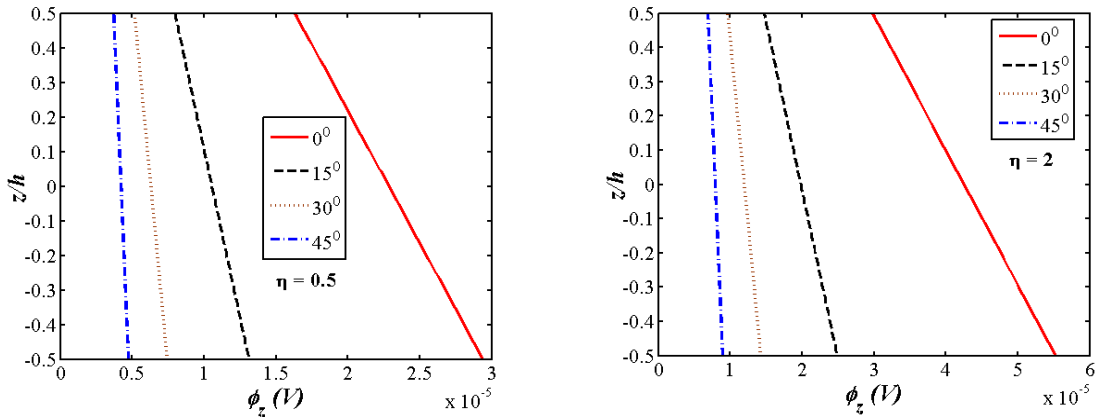


(e)

Figure 5.5: Through thickness variation of displacement w for different skew angles at power-law index values (a) $\eta = 0$ (b) $\eta = 0.2$ (c) $\eta = 0.5$ (d) $\eta = 2$ (e) $\eta = 5$

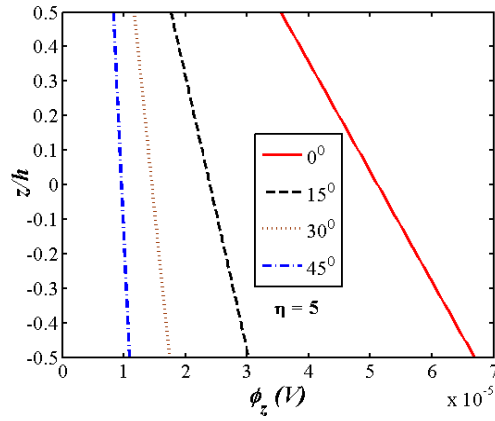
The effect of skew angle (α) on the normal stress (σ_x) for different gradient index is given in Figure 5.8(a) – (e). The normal stress (σ_x) for FGSMEE plate with zero skew angle ($\alpha = 0^0$) and $\eta = 0$, linearly varies across the thickness. The bottom half of the plate experiences compressive stress, while the top half of the plate experiences tensile stress as shown in Figure 5.8(a). For $\eta > 0$, the through-thickness variation of σ_x appears to be non-linear whereas at $\eta = 0$, the behavior is linear. For the FGSMEE plate with the skew angle $\alpha = 15^0$, 30^0 , and 45^0 , irrespective of η , the lower half of the plate experiences tensile stress while the upper half experiences compressive stress. Further, for $\eta = 0$, the normal stress (σ_x) increases for $\alpha = 15^0$ and 30^0 while for $\alpha = 45^0$, a decrease in the normal stress (σ_x) is observed. Similar trends are observed for other η values. Figure 5.9(a) – (e) illustrate the variation of normal stress (σ_y) for different skew angles. It may be seen from the figures that the behaviour of σ_y is similar to σ_x for all the cases considered. The effect of skew angle on the in-plane shear stress (τ_{xy}) of the FGSMEE plate is reported in Figure 5.10(a) – (e) corresponding to various η values. The in-plane shear stress (τ_{xy}) increases with the increase in skew angle for all the considered η values. Figure 5.11(a) – (e) present the transverse shear stress (τ_{xz}) distribution across the thickness of various η values. It can be clearly seen from the Figure 5.11 that the transverse shear stress decreases with the increase in skew angle.





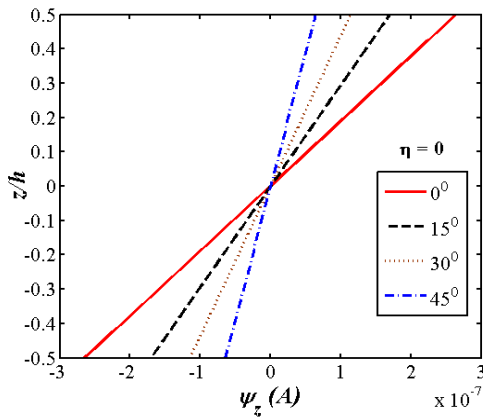
(c)

(d)

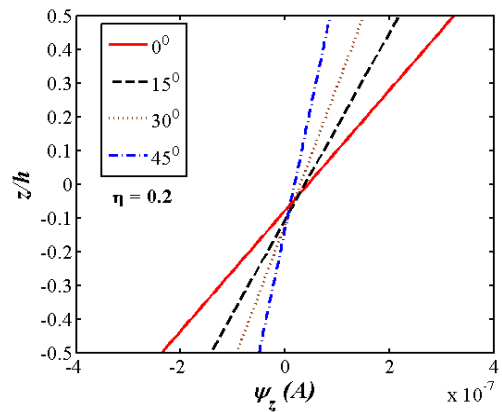


(e)

Figure 5.6: Through thickness variation of electric potential ϕ_z for different skew angles at power-law index values (a) $\eta = 0$ (b) $\eta = 0.2$ (c) $\eta = 0.5$ (d) $\eta = 2$ (e) $\eta = 5$



(a)



(b)

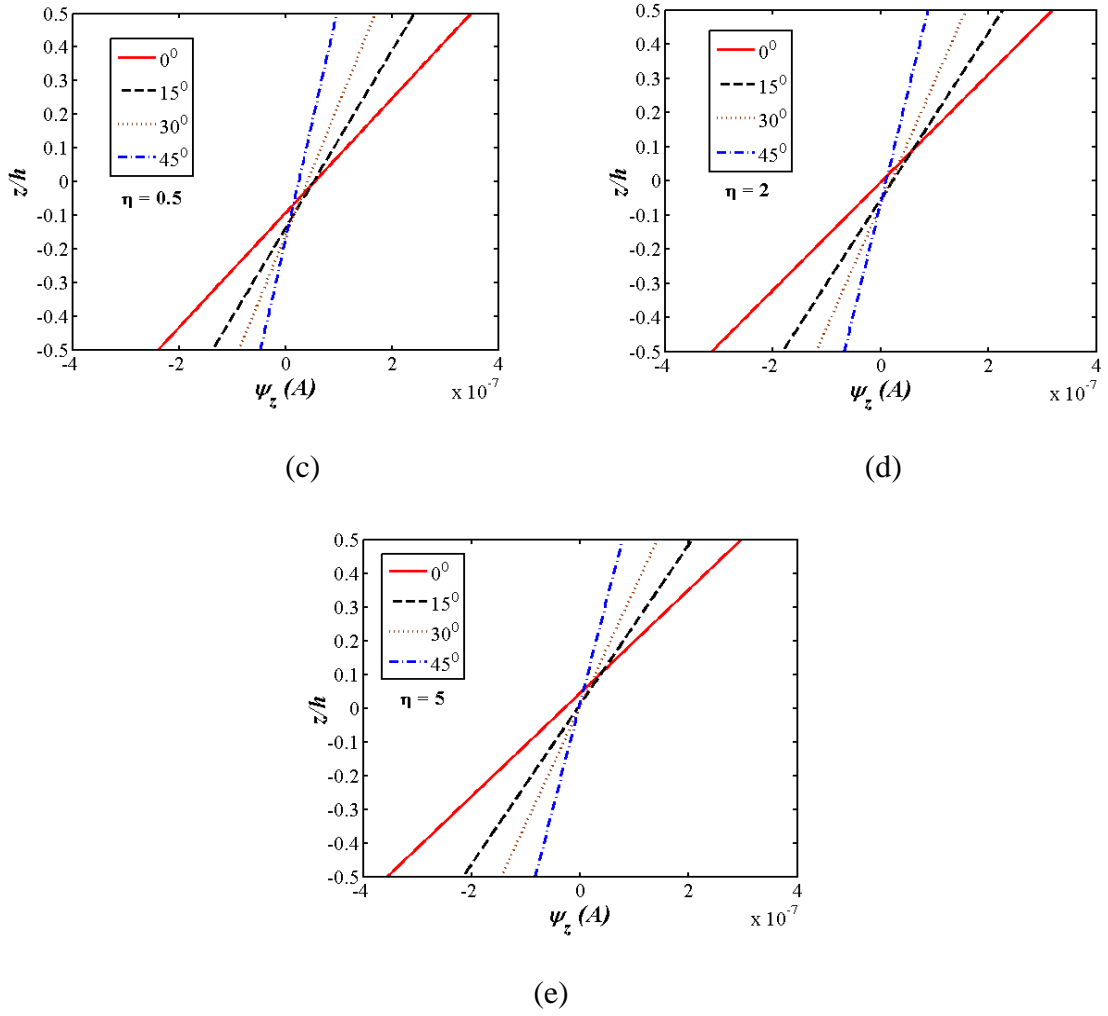
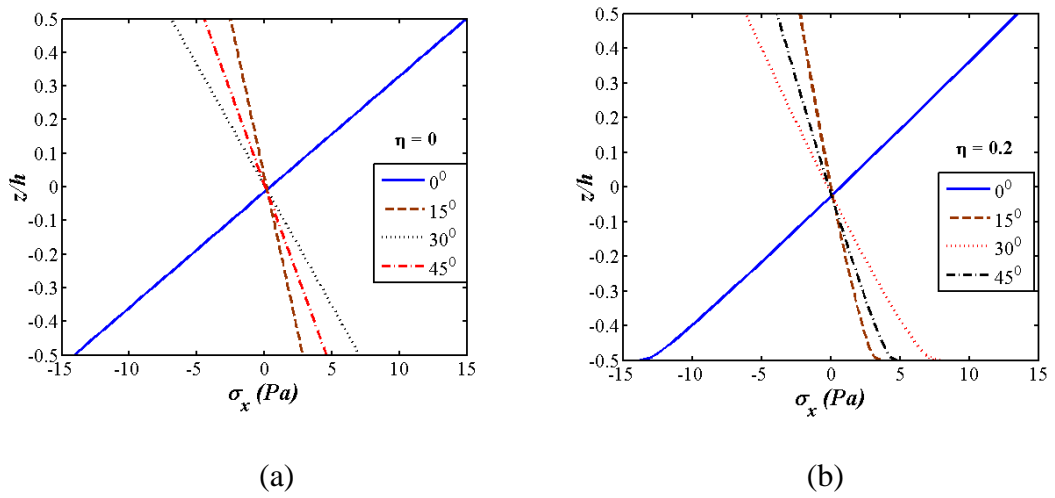
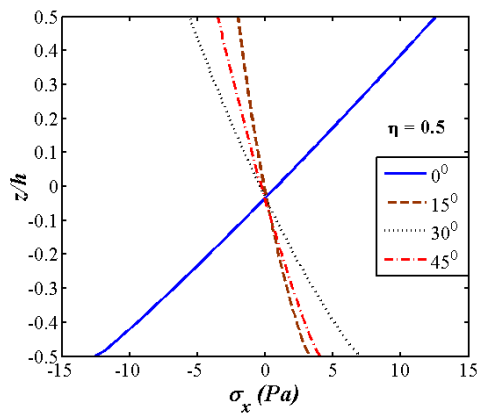
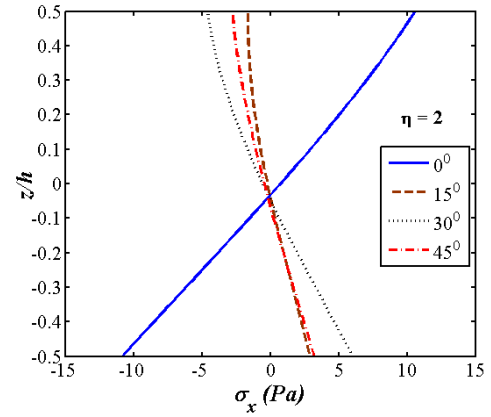


Figure 5.7: Through thickness variation of magnetic potential ψ_z for different skew angles at power-law index values (a) $\eta = 0$ (b) $\eta = 0.2$ (c) $\eta = 0.5$ (d) $\eta = 2$ (e) $\eta = 5$

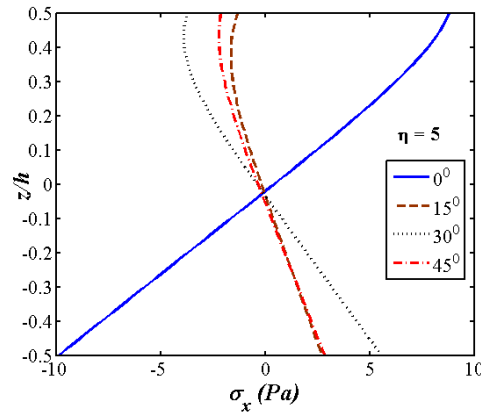




(c)

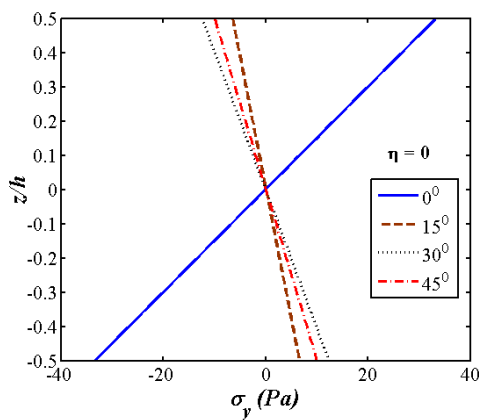


(d)

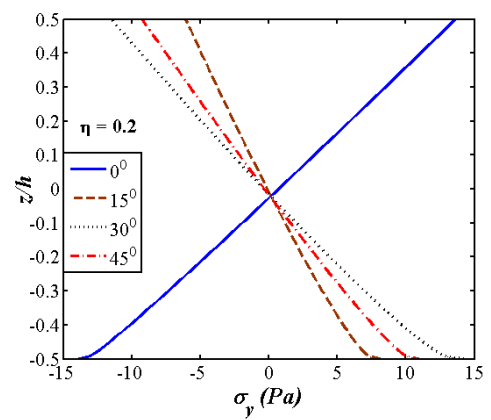


(e)

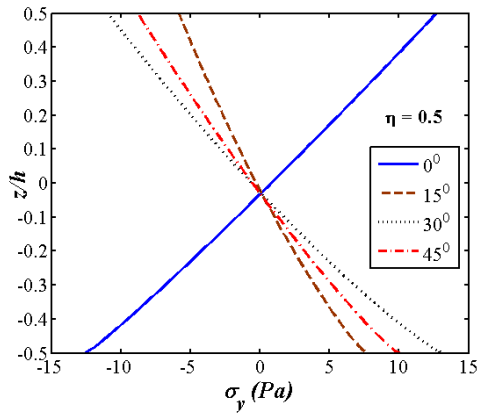
Figure 5.8: Through thickness variation of normal stress σ_x for different skew angles at power-law index values (a) $\eta = 0$ (b) $\eta = 0.2$ (c) $\eta = 0.5$ (d) $\eta = 2$ (e) $\eta = 5$



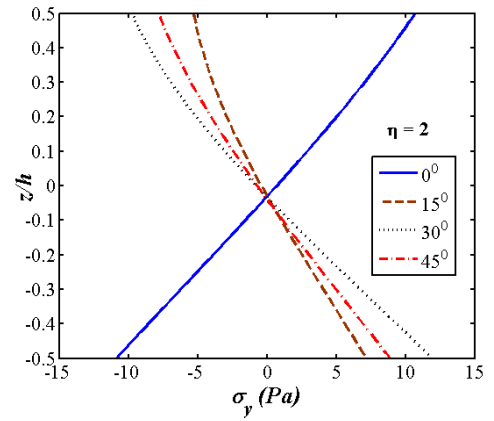
(a)



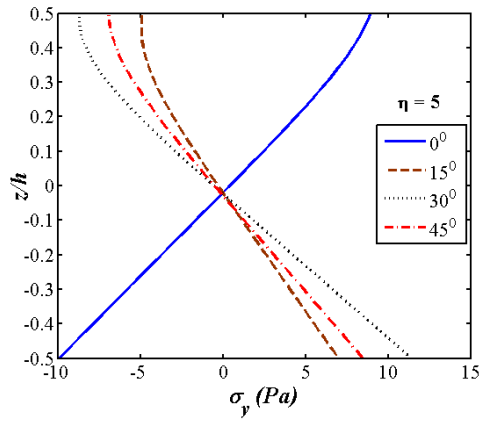
(b)



(c)

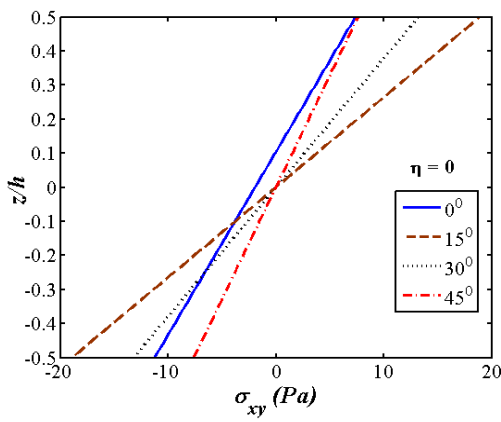


(d)

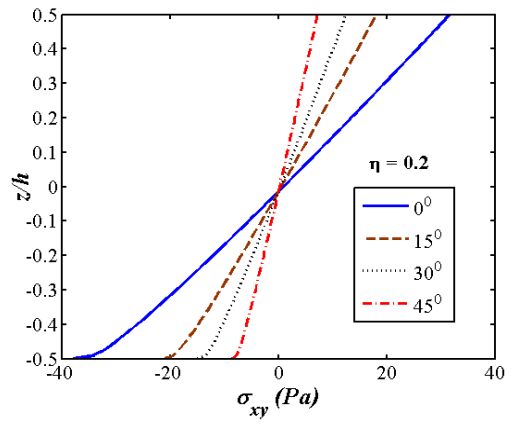


(e)

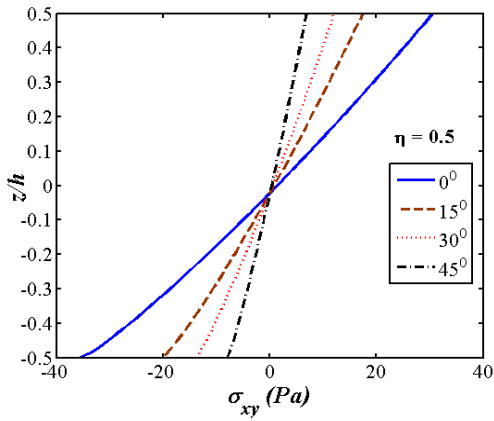
Figure 5.9: Through thickness variation of normal stress σ_y for different skew angles at power-law index values (a) $\eta = 0$ (b) $\eta = 0.2$ (c) $\eta = 0.5$ (d) $\eta = 2$ (e) $\eta = 5$



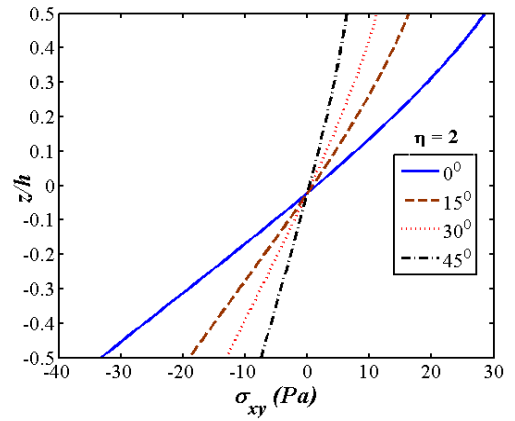
(a)



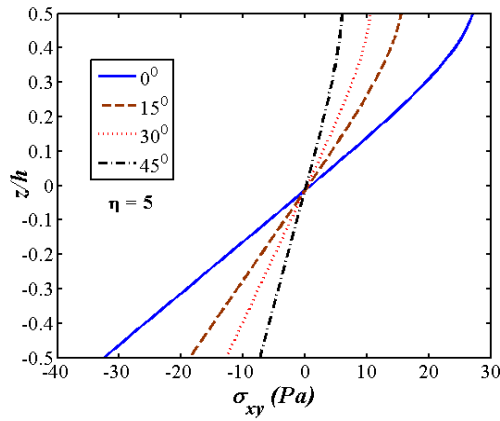
(b)



(c)

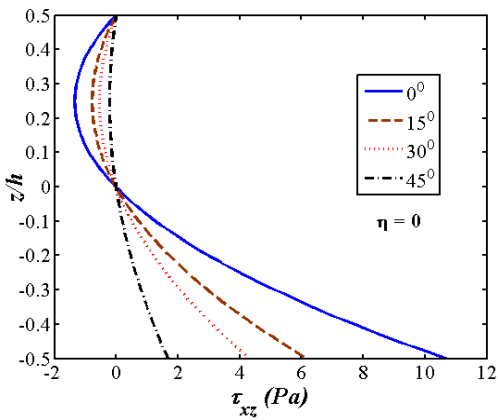


(d)

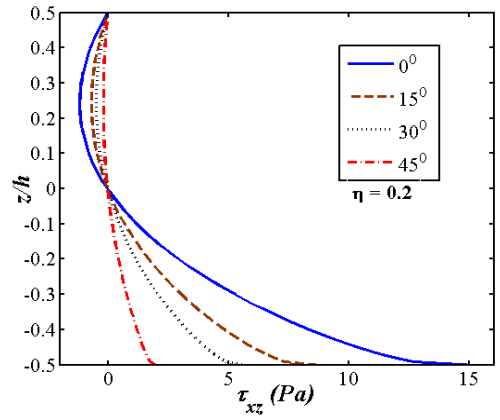


(e)

Figure 5.10: Through thickness variation of normal stress σ_{xy} for different skew angles at power-law index values (a) $\eta = 0$ (b) $\eta = 0.2$ (c) $\eta = 0.5$ (d) $\eta = 2$ (e) $\eta = 5$



(a)



(b)

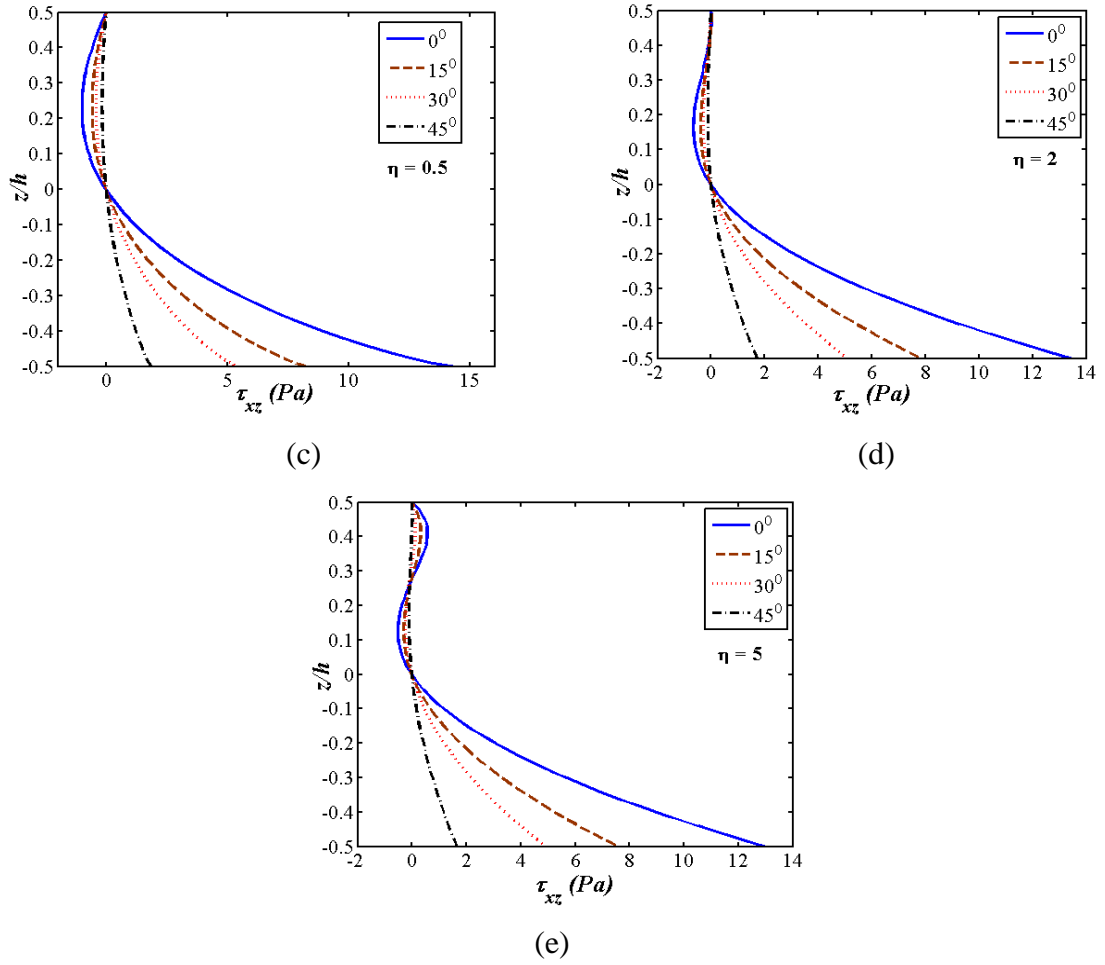


Figure 5.11: Through thickness variation of shear stress τ_{xz} for different skew angles at power-law index values (a) $\eta = 0$ (b) $\eta = 0.2$ (c) $\eta = 0.5$ (d) $\eta = 2$ (e) $\eta = 5$

The through thickness variation of magnetic induction (B_z) and electric displacement (D_z) for different skew angles and η values are presented in Figure 5.12(a) – (e) and Figure 5.13(a) – (e), respectively. For $\eta = 0$ (pure magnetostrictive plate), as seen in Figure 5.13(a), the magnetic induction decreases with the increase in skew angle for $\alpha \leq 30^\circ$. It can also be observed that for skew angle $\alpha \leq 30^\circ$, the plate experiences linear variation with positive B_z at the bottom surface of the plate and negative at the top surface. However, for $\alpha = 45^\circ$, the FGSME plate exhibit negative B_z at the bottom half of the plate and positive at the top half of the plate. For the power-law index values (i.e., $\eta = 0.2, 0.5, 2$ and 5), the bottom surface of the FGSME plate experiences nearly zero magnetic induction B_z irrespective of the skew angle. Further, it is seen from Figure 5.12(b) – (e) that the magnitude of B_z decreases with the increase in skew angle. For the case of a pure magnetostrictive

plate ($\eta = 0$) as seen in Figure 5.13(a), no influence of skew angle on the electric displacement D_z is observed. For the rest of η values (i.e., 0.2, 0.5, 2 and 5), the top surface of the FGSMEE plate experience zero electric displacement D_z , irrespective of skew angle (α). The magnitude of D_z decreases with the increase in α . The square ($\alpha = 0^\circ$) FGSMEE plate experiences positive D_z for all the η values while the increase in α leads to negative D_z .

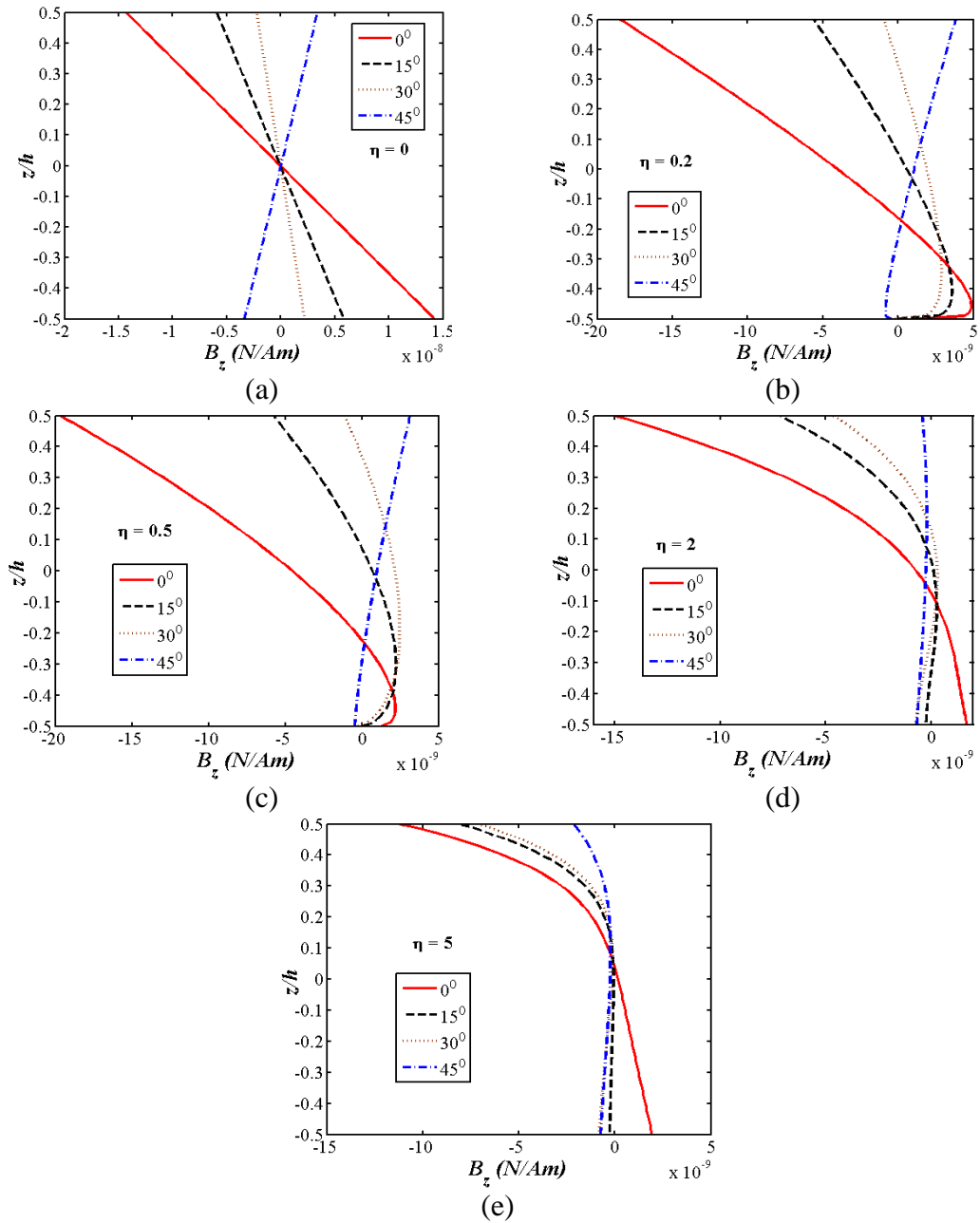


Figure 5.12: Through thickness variation of magnetic induction B_z for different skew angles at power-law index values (a) $\eta = 0$ (b) $\eta = 0.2$ (c) $\eta = 0.5$ (d) $\eta = 2$ (e) $\eta = 5$

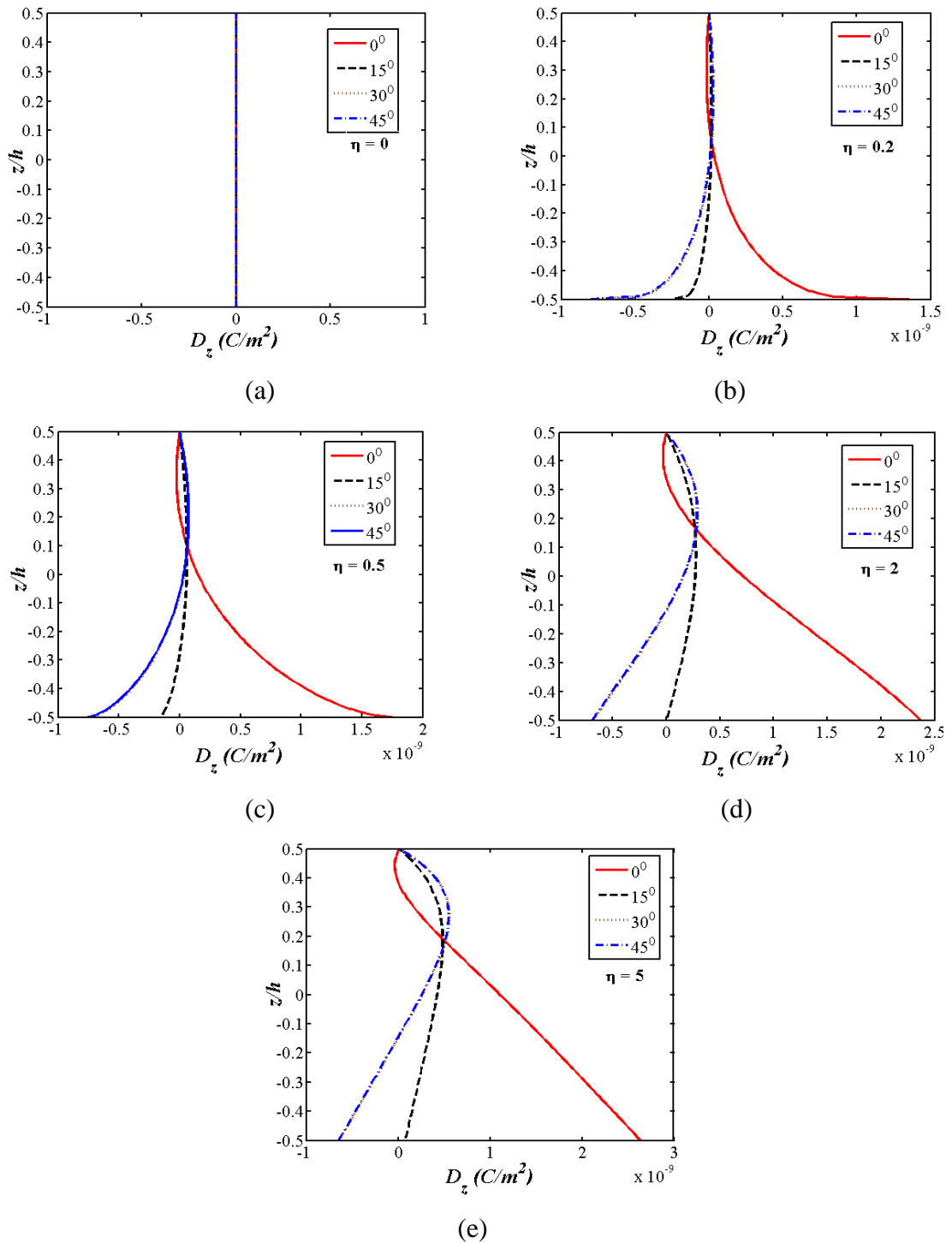
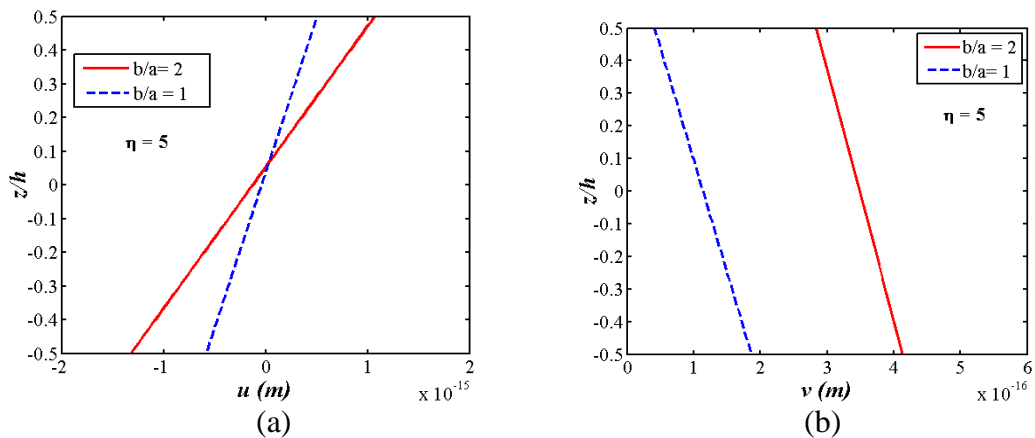


Figure 5.13: Through thickness variation of electric displacement D_z for different skew angles at power-law index values (a) $\eta = 0$ (b) $\eta = 0.2$ (c) $\eta = 0.5$ (d) $\eta = 2$ (e) $\eta = 5$

The effect of aspect ratio on the static behavior of FGSME plate is presented in Figure 5.14(a) – (j) for the thickness ratio of $a/h = 100$. It can be seen from the

figure that the aspect ratio has a significant influence on the primary and secondary quantities. The displacements u and v increases for the aspect ratio $b/a = 2$ in comparison with $b/a = 1$. The potentials (electric and magnetic) display an increase in the magnitude and amongst them, influence on the electric potential is found to be more dominant. The normal stress (σ_x) experiences tension at the bottom portion and compression at the top portion for the square FGSMEE plate while for a plate with $b/a = 2$, the bottom portion experiences compression and the top portion experiences tension. The normal stress σ_y and in-plane shear stress (τ_{xy}) increases with the increase in the lateral dimension of the plate. The transverse shear stress (τ_{xz}) and magnetic induction (B_z) decreases with the increase in aspect ratio while the higher aspect ratio produces a nearly constant electric displacement (D_z) at the bottom half of the FGSMEE plate. Figure 5.15(a) – (j) present the effect of geometrical parameter and thickness ratio on the primary and secondary parameters of FGSMEE plate subjected to a static load. It can be seen from the plots that the a/h ratio has considerable influence on the static behavior of FGSMEE plate. The effect of thickness ratio on static behavior is assessed for the FGSMEE plate having dimension $b/a = 1$. The primary quantities such as displacements (u and v) and potentials (electric and magnetic), increase with the increase in thickness ratio. The effect of boundary condition on the static response of FGSMEE plate is presented in Figure 5.16(a) – (d). These figures suggest that a considerable influence on the plotted parameters, i.e., ϕ_z , ψ_z , B_z , and D_z is observed as the boundary restraint changes from simply supported edges to clamped edges. The trend is due to the increase in local flexural rigidity of the plate with stiffening edge support.



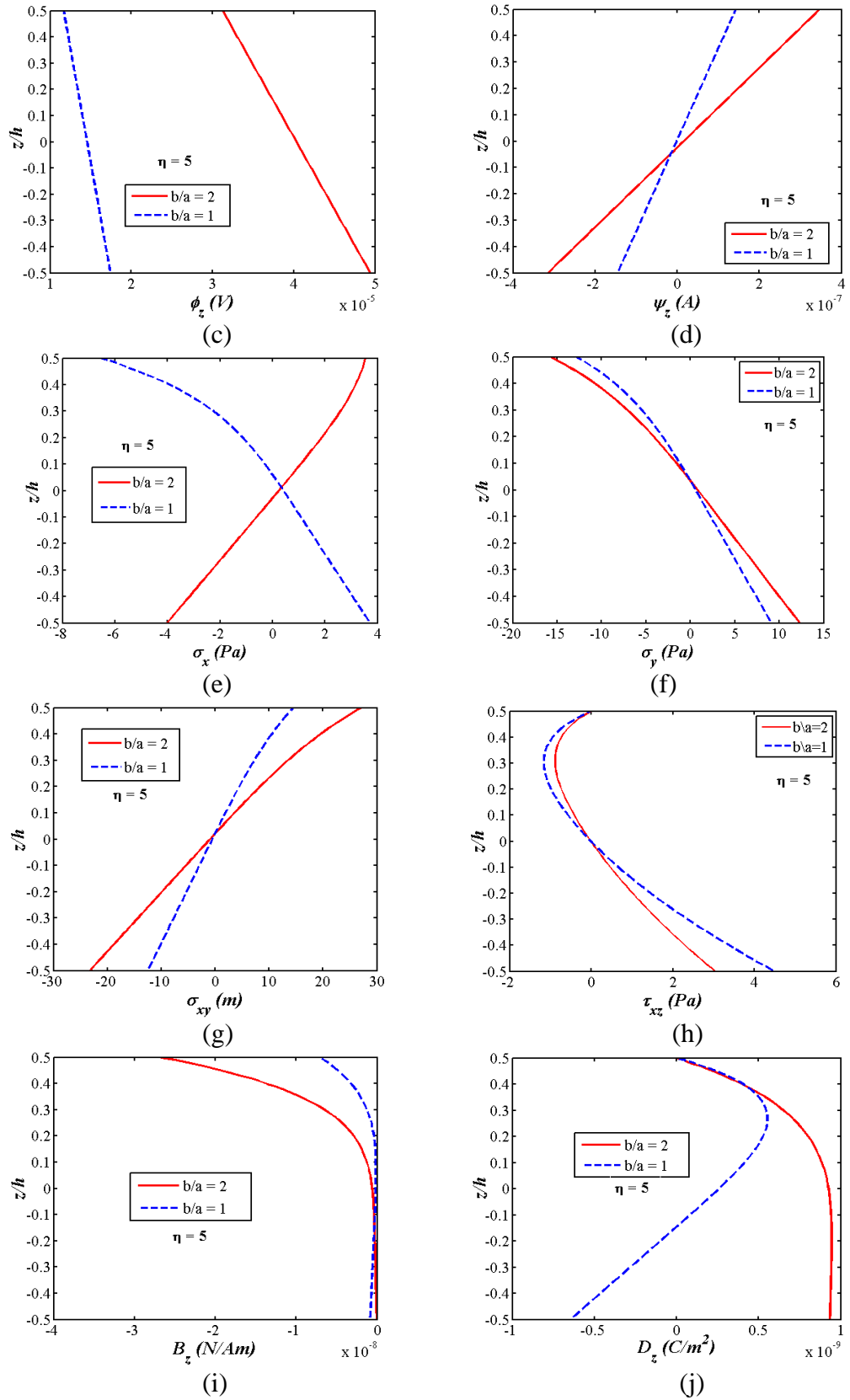
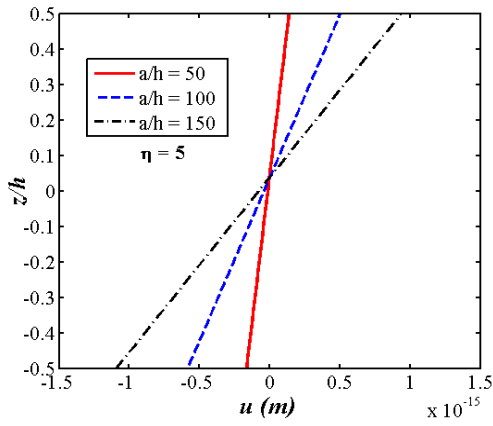
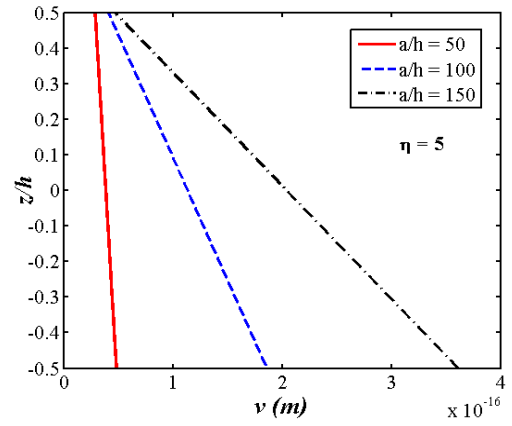


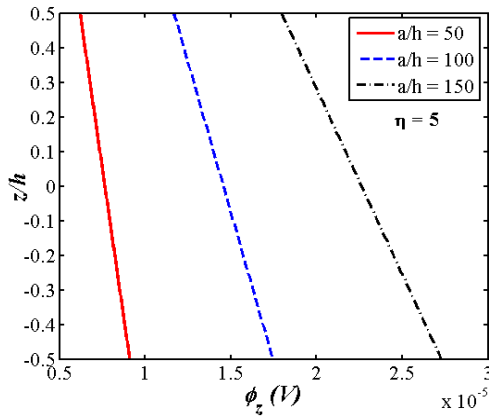
Figure 5.14: Effect of aspect ratio (b/a) on (a) u (b) v (c) ϕ_z (d) ψ_z (e) σ_x (f) σ_y (g) τ_{xy} (h) τ_{xz} (i) B_z (j) D_z



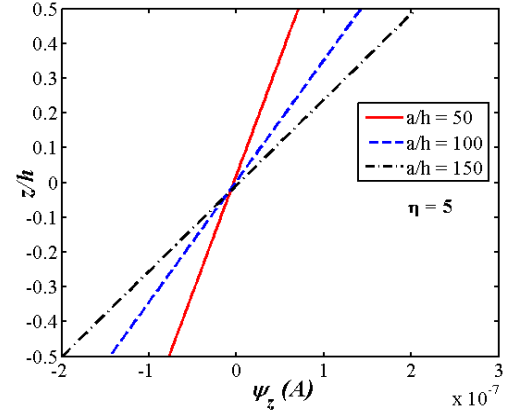
(a)



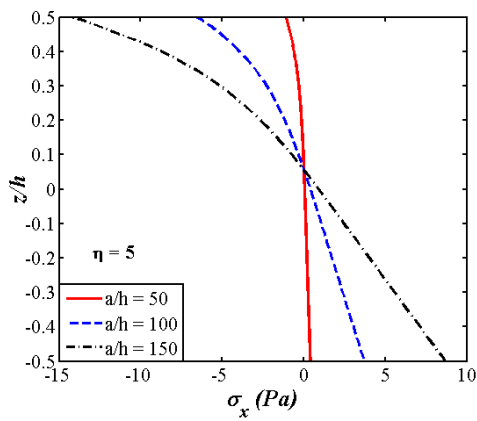
(b)



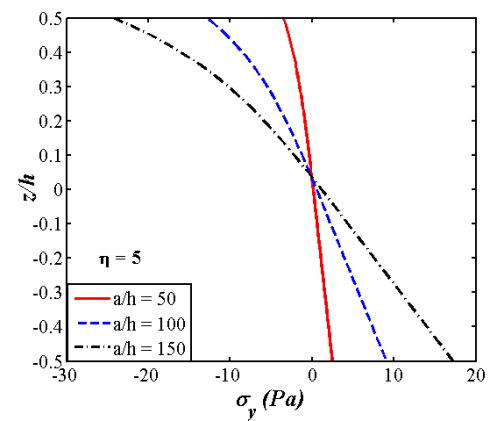
(c)



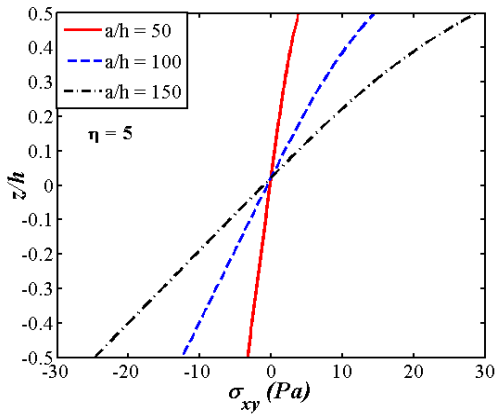
(d)



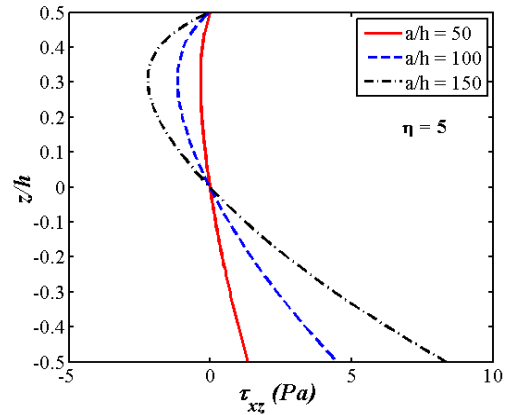
(e)



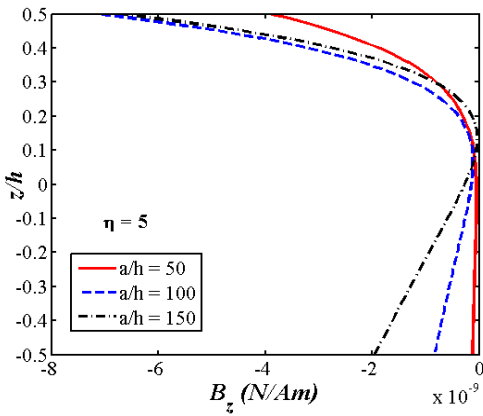
(f)



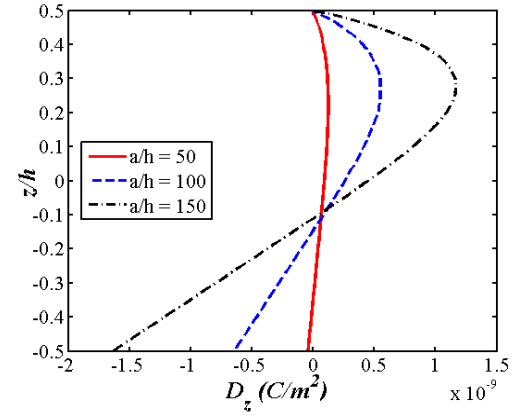
(g)



(h)

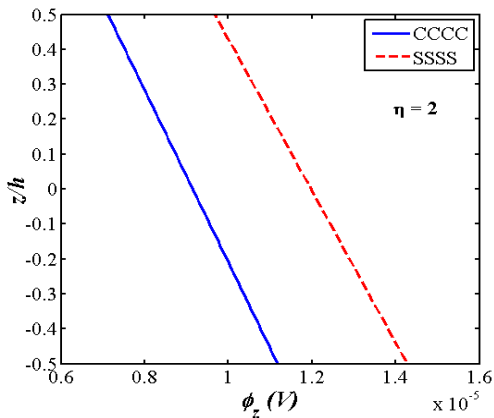


(i)

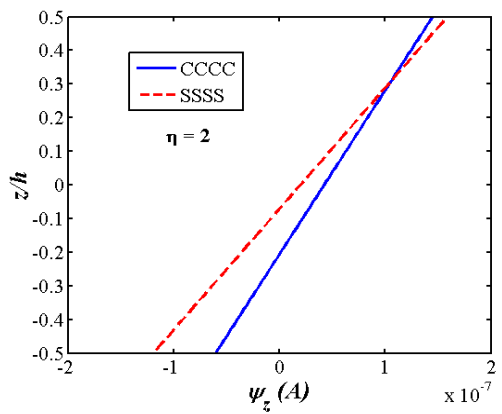


(j)

Figure 5.15: Effect of thickness ratio (a/h) on (a) u (b) v (c) ϕ_z (d) ψ_z (e) σ_x (f) σ_y (g) τ_{xy} (h) τ_{xz} (i) B_z (j) D_z



(a)



(b)

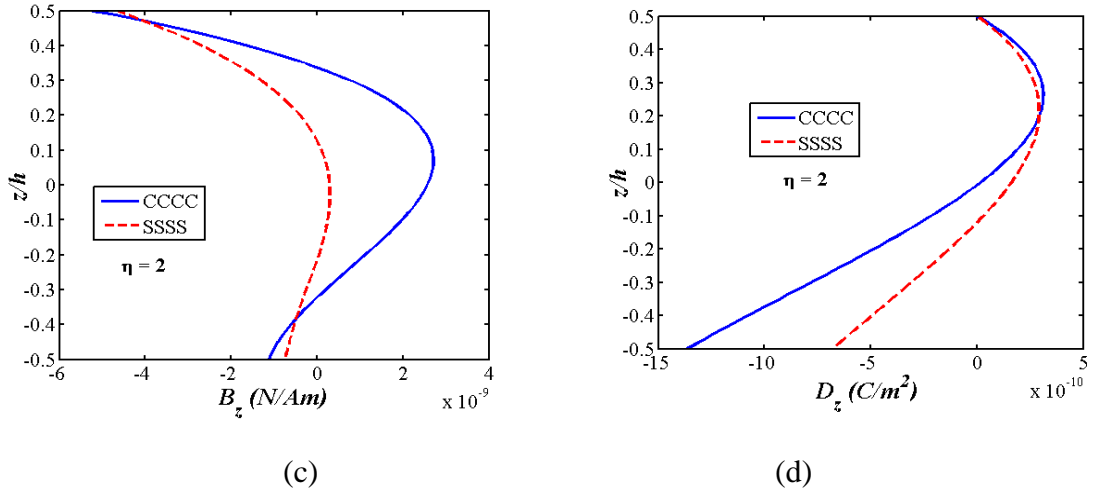


Figure 5.16: Effect of boundary condition on (a) ϕ_z (b) ψ_z (c) B_z (d) D_z

5.4. CONCLUSIONS

In this chapter, a finite element formulation to analyze the static and free vibration behaviour of FGSMEE plate is developed and implemented. To investigate the behavior of the FGSMEE plate, the transformation matrix between the global and local degrees of freedom for the nodes lying on the skew edges has been successfully incorporated. Graded material distribution along the thickness has been achieved using a simple power law and rule of mixture. The influence of skew angle on the natural frequencies of the FGSMEE plate has been effectively investigated. Further, the static behaviour of FGSMEE plate is evaluated thoroughly in terms of primary and secondary structural parameters such as the displacements, electric potential, magnetic potential, stresses, electric displacement, and magnetic induction. In addition, the influence of material gradient index on the behaviour of FGSMEE plate is also studied. The effect of boundary conditions, thickness ratio, and aspect ratio on the structural behaviour of the FGSMEE plates is thoroughly investigated. Some of the key findings of the present studies are listed below:

- The free vibration studies for FGSMEE plate unveiled that the natural frequency increases with the increase in the skew angle irrespective of the material gradient index values.
- It is observed that the natural frequency decreases with the increase in gradient-index values.

- The electric and magnetic potential decreases with the increase in the skew angle.
- The gradient index η exhibits major influence on the electric potential while its influence on the magnetic potential is observed to be minimal.
- The magnitude of electric displacement (D_z) and magnetic induction (B_z) decreases with the increase in the skew angle.
- The static response and free vibration are significantly affected by the thickness ratio, aspect ratio, and the boundary conditions.

Chapter 6

INFLUENCE OF POROSITY ON STRUCTURAL BEHAVIOUR OF FUNCTIONALLY GRADED MAGNETO-ELECTRO-ELASTIC PLATES

This chapter presents a finite element (FE) formulation to assess the influence of porosity on the static and free vibration responses of rectangular and skew functionally graded magneto-electro-elastic (FGMEE) plates. The porosity is accounted as local density using modified power law. The skew edges of the plate are achieved by implementing transformation matrix. The coupled constitutive relations establish the different couplings associated with MEE materials. The displacements, potentials, and stresses for the porous skew plate are established through static analysis. The influence of porosity on the natural frequency of the rectangular and skew plate is investigated via free vibration analysis. The influence of different porosity distributions on various skew angles of the FGMEE plate has been studied. The effect of porosity volume, skew angle, and geometrical parameters such as aspect ratio, thickness ratio, and boundary conditions on the porous FGMEE plate is investigated.

6.1. INTRODUCTION

Magneto-electro-elastic (MEE) materials find their presence in functionally graded (FG) form in addition to layered form depending on the requirement of the application. Functionally graded (FG) materials exhibit enhanced structural characteristics and are gradually expanding their presence in many commercial applications. In spite of tremendous developments in manufacturing techniques, porosity is the common defect most often associated with FG material structures. Hence, in this chapter a suitable FE model is developed for FGMEE plate accounting the porosity. Such FE formulation is utilized to evaluate the static and free vibration characteristics of porous FGMEE plate for different skew angles and porosity models. The effect of different skew angle, porosity distribution, porosity volume, and gradient index affecting the structural behaviour of rectangular and skew porous

FGMEE plate is extensively investigated. Further, the effect of thickness ratio, aspect ratio, and boundary conditions are also studied.

6.2. PROBLEM DESCRIPTION

The geometrical parameters of the FGSME plate considered in the present analysis are identical to the plate studied in the previous chapter as shown in Figure 5.1. In chapter 5, an FE formulation considering the shear deformation theory, coupled constitutive equations, and skew transformation matrices has been derived. The same formulation has been used for the analysis of porous FGSME plate also. However, the material properties by considering different porosity distribution have been derived using modified power law as explained in the subsequent section.

6.2.1 Porosity inclusion using modified power law

The material properties and all the coefficients are bound by power-law distribution given as follows:

$$\overline{P}_{fg}(z) = P_F + (P_B - P_F) \times V - (P_B + P_F) \times (m/2) \times V_p \quad (6.1)$$

where, \overline{P}_{fg} is the generalized term to represent the material property variables such as \overline{C} , $\overline{\rho}$, \overline{e} , \overline{q} , $\overline{\xi}$ and μ . The subscripts B and F refer to BaTiO_3 and CoFe_2O_4 , respectively. V_p is the generalized term to represent the different porosity distributions (i.e., V_u , V_o , V_x , V_v), while m is the porosity index ($0 < m < 1$) and V is the volume fraction and is given by

$$V = \left\{ \left(\frac{z}{h} \right) + \left(\frac{1}{2} \right) \right\}^\eta \quad (6.2)$$

wherein, η is the power law index, and different porosity distributions shown in Figure 6.1 are given by

(a) Uniform porosity distribution,

$$V_u = 1 \quad (6.3.a)$$

(b) Centralized porosity distribution,

$$V_o = \left\{ 1 - \frac{2|z|}{h} \right\} \quad (6.3.b)$$

(c) High density of porosity at the top and the bottom of the plate while low at the mid-span i.e.,

$$V_x = \left\{ \frac{2|z|}{h} \right\} \quad (6.3.c)$$

(d) High density of porosity at the top and low at the bottom,

$$V_v = \left\{ 1 + \frac{2|z|}{h} \right\} \quad (6.3.d)$$

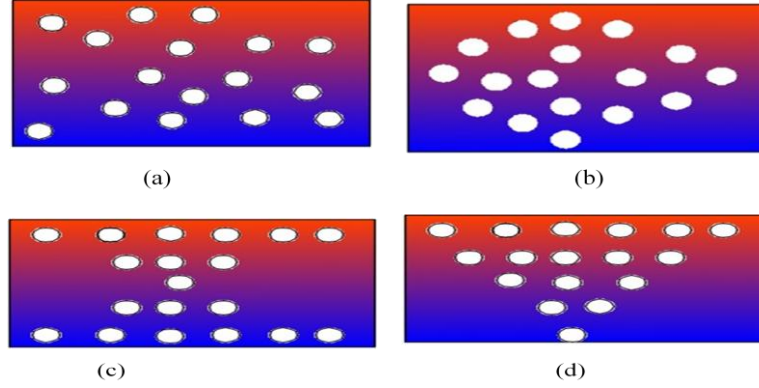


Figure 6. 1: Porosity distribution (a) V_u (b) V_o (c) V_x (d) V_v

6.3. RESULTS AND DISCUSSION

Validation studies presented in the section 5.3.1 have been implemented for the present analysis also. Since, the validation is executed for free vibration studies, the results corresponding to free vibration behaviour of porous FGSMEE plate appear before the static analysis in the subsequent section.

6.3.1 Free vibration assessment of porous FGSMEE plate

This section deals with the evaluation of free vibration characteristics for rectangular and skew FGMEE plates with porosities. Different porosity distributions (V_u , V_o , V_x , and V_v) and the porosity volume influencing the natural frequencies are explicitly investigated. The rectangular porous FGMEE plate considered for the analysis has the geometrical details as: $a/h = 100$; $b/a = 1$; $\eta = 2$. It is also evident from Table 6.1 that V_v distribution holds the largest influence on the natural frequency of the porous FGMEE plate while V_u displays the lowest influence. The effect of porosity volume ($0.1 \leq m \leq 0.5$) on the natural frequencies of porous FGMEE plate is presented in Table 6.2 – Table 6.5. It is evident from the tabulated results that the higher porosity volume reduces the stiffness of the plate and thereby results into lower natural frequencies.

Table 6.1: Effect of different porosity distribution on normalized natural frequencies of porous FGMEE plate

Plate Type	η	Mode				
		1	2	3	4	5
Perfect	0.5	4.269	11.075	11.100	22.477	24.014
FG	2	4.113	10.697	10.703	21.833	23.235
V_u	0.5	4.055	10.518	10.544	21.345	22.806
	2	3.888	10.114	10.119	20.657	21.974
V_o	0.5	4.216	10.929	10.954	22.107	23.677
	2	4.057	10.543	10.549	21.452	22.884
V_x	0.5	4.110	10.670	10.696	21.728	23.155
	2	3.946	10.274	10.279	21.052	22.341
V_v	0.5	4.068	10.550	10.577	21.399	22.872
	2	3.911	10.170	10.177	20.748	22.088

Table 6.2: Effect of porosity factor, m on normalized natural frequencies of porous V_u FGMEE plate

Porosity factor, m	Mode				
	1	2	3	4	5
0	4.113	10.697	10.703	21.833	23.235
0.1	3.888	10.114	10.119	20.657	21.974
0.2	3.648	9.493	9.496	19.406	20.630
0.5	2.782	7.255	7.260	14.943	15.795

Table 6.3: Effect of porosity factor, m on normalized natural frequencies of porous V_o FGMEE plate

Porosity factor, m	Modes				
	1	2	3	4	5
0	4.113	10.697	10.703	21.833	23.235
0.1	4.057	10.543	10.549	21.452	22.884
0.2	4.000	10.387	10.393	21.062	22.526
0.5	3.822	9.902	9.905	19.835	21.407

Table 6.4: Effect of porosity factor, m on normalized natural frequencies of porous

V_x FGMEE plate

porosity factor, m	Modes				
	1	2	3	4	5
0	4.113	10.697	10.703	21.833	23.235
0.1	3.946	10.274	10.279	21.052	22.341
0.2	3.772	9.833	9.837	20.237	21.407
0.5	3.190	8.361	8.361	17.530	18.299

Table 6.5: Effect of porosity factor, m on normalized natural frequencies of porous

V_v FGMEE plate

porosity factor, m	Modes				
	1	2	3	4	5
0	4.113	10.697	10.703	21.833	23.235
0.1	3.911	10.170	10.177	20.748	22.088
0.2	3.685	9.584	9.592	19.558	20.816
0.5	2.698	7.048	7.064	14.684	15.389

In addition, several other parameters influencing the free vibration characteristics of porous FGSME plate are discussed. Different skew angles, porosity distributions, power-law index, and porosity volume influencing the natural frequency of the plate are explicitly investigated. Table 6.6 - Table 6.9 display the influence of skew angle for different porosity distributions on the natural frequency of porous FGMEE plate. The boundary condition considered for the analysis is simply supported on all the edges and the porosity index is taken to be 0.1. It can be observed from the results that the increase in skew angle increases the natural frequency of the plate. However, the natural frequency drastically increases for $\alpha = 45^\circ$. In addition, the tabulated results suggest that the inclusion of porosity brings down the natural frequency in comparison with that of the perfect FG plate (without Porosity). This may be attributed to the lower stiffness of the porous material. Further, every porosity distribution displays a unique influence on the natural frequency with V_u distribution exhibiting the lowest natural frequency while V_o obtains the highest. The increase in skew angle causes the reduction in the plate area and imparts additional stiffness

causing the increase in natural frequency. The power-law index affecting the free vibration characteristics of porous FGSMEE plate is presented in Figure 6.2(a) – (d). These figures (Figure 6.2(a) – (d)) suggest that the increase in power-law index lowers the natural frequency for all the skew angles and porosity distributions. It is interesting to note that for V_o distribution at $\alpha = 45^0$, the increase in power-law index meagrely affects the natural frequencies. The influence of volume of porosity on the free vibration behaviour is presented in Figure 6.3. It can be seen that the increase in volume of the porosity, the natural frequency decreases significantly. Further, the influence of increase in porosity volume on V_o distribution is minimal in comparison with the other porosity distributions.

Table 6.6: Effect of skew angle on natural frequency of porous FGSMEE plate (SSSS, $\eta = 0.2$, porosity factor, $m = 0.1$, $a/h = 100$, $b/a = 1$)

Skew angle (α)	Porosity type	Modes				
		1	2	3	4	5
15^0	Pure FG	6.366	12.115	14.078	23.452	27.746
	V_u	6.060	11.535	13.403	22.321	26.416
	V_o	6.272	11.956	13.890	23.095	27.358
	V_x	6.157	11.699	13.597	22.689	26.817
	V_v	6.067	11.549	13.420	22.348	26.449
30^0	Pure FG	8.461	15.419	20.060	28.061	36.454
	V_u	8.057	14.679	19.102	26.715	34.708
	V_o	8.345	15.205	19.799	27.656	35.944
	V_x	8.177	14.900	19.372	27.133	35.236
	V_v	8.068	14.697	19.126	26.749	34.753
45^0	Pure FG	12.617	22.052	32.663	40.350	54.888
	V_u	12.018	20.993	31.109	38.414	52.260
	V_o	12.454	21.734	32.251	39.761	54.116
	V_x	12.187	21.321	31.536	39.021	53.058
	V_v	12.034	21.018	31.152	38.462	52.327

Table 6.7: Effect of skew angle on natural frequency of porous FGSMEE plate(SSSS, $\eta = 0.5$, porosity factor, $m = 0.1$, $a/h = 100$, $b/a = 1$)

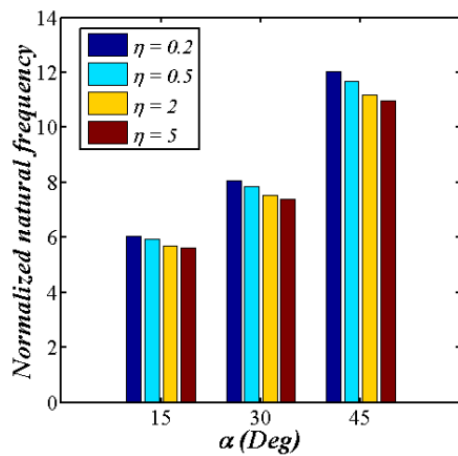
Skew angle (α)	Porosity type	Modes				
		1	2	3	4	5
15°	Pure FG	6.235	11.851	13.771	22.993	27.153
	Vu	5.922	11.255	13.079	21.837	25.789
	Vo	6.139	11.688	13.579	22.631	26.756
	Vx	6.021	11.424	13.279	22.211	26.200
	Vv	5.938	11.289	13.119	21.896	25.865
30°	Pure FG	8.265	15.093	19.604	27.468	35.657
	Vu	7.850	14.334	18.620	26.088	33.866
	Vo	8.147	14.874	19.337	27.055	35.136
	Vx	7.973	14.560	18.897	26.515	34.406
	Vv	7.876	14.376	18.679	26.164	33.969
45°	Pure FG	12.309	21.597	31.877	39.495	53.676
	Vu	11.691	20.511	30.279	37.511	50.979
	Vo	11.731	20.569	30.380	37.621	51.136
	Vx	11.865	20.847	30.718	38.129	51.794
	Vv	11.731	20.569	30.380	37.621	51.136

The influence of geometric parameters on the free vibration behaviour of the porous FGSMEE plate is investigated. The analysis is performed for the plate with $\alpha = 45^\circ$. Table 6.10 presents the effect of thickness ratio on the natural frequency of porous FGSMEE plate. It may be observed that the increase in the thickness ratio increases the natural frequency of the plate. The thick plate displays a rapid increase in the natural frequency while the thin plate ($a/h \geq 50$) witnesses a steady increase in the natural frequency. Furthermore, the effect of aspect ratio on the free vibration characteristics of the FGSMEE plate is also analysed, and the results are tabulated in Table 6.11. The increase in aspect ratio decreases the natural frequency of the plate. It is also observed that for the higher aspect ratio, the natural frequencies decrease steadily, while the rate of decrease is rapid for lower aspect ratio.

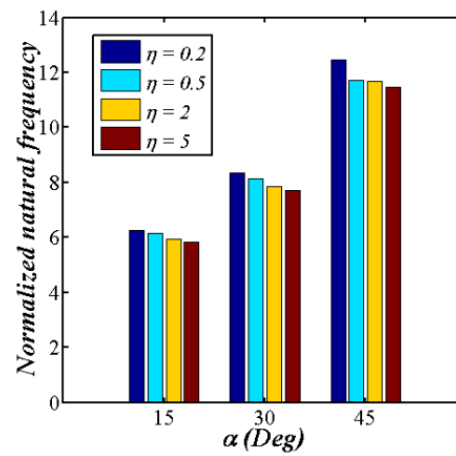
Table 6.8: Effect of skew angle on natural frequency of porous FGSMEE plate

(SSSS, $\eta = 2$, porosity factor, $m= 0.1$, $a/h=100$, $b/a = 1$)

Skew angle (α)	Porosity type	Mode				
		1	2	3	4	5
15^0	Pure FG	6.034	11.451	13.307	22.289	26.253
	Vu	5.706	10.829	12.583	21.084	24.827
	Vo	5.935	11.282	13.106	21.915	25.839
	Vx	5.809	11.006	12.792	21.473	25.257
	Vv	5.735	10.887	12.651	21.184	24.956
30^0	Pure FG	7.969	14.598	18.916	26.565	34.443
	Vu	7.533	13.806	17.884	25.124	32.568
	Vo	7.845	14.372	18.637	26.137	33.902
	Vx	7.662	14.042	18.175	25.568	33.131
	Vv	7.577	13.877	17.985	25.253	32.745
45^0	Pure FG	11.843	20.904	30.694	38.190	51.825
	Vu	11.193	19.772	29.014	36.117	49.000
	Vo	11.667	20.568	30.251	37.572	51.009
	Vx	11.377	20.121	29.477	36.758	49.849
	Vv	11.261	19.870	29.188	36.304	49.271



(a)



(b)

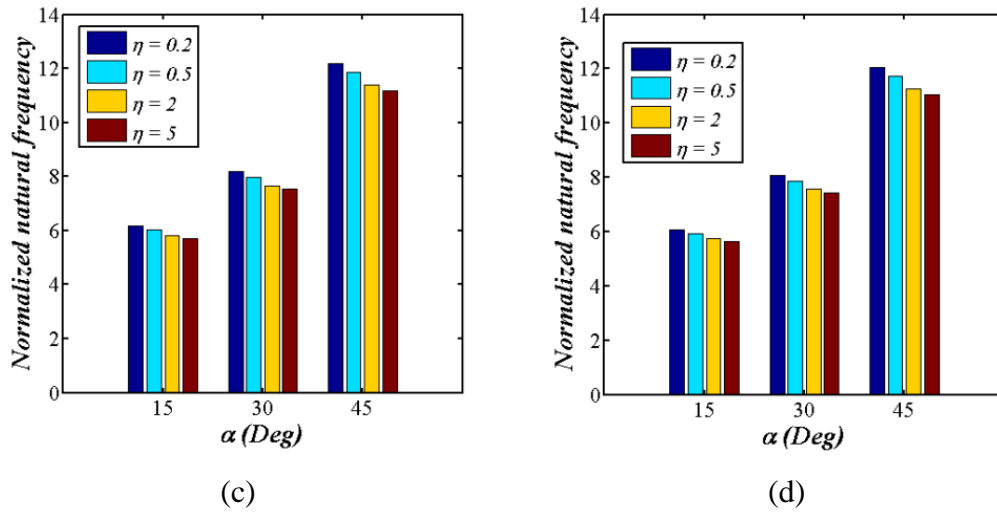


Figure 6.2: Effect of gradient index on natural frequency of porous plate (a)

Vu (b) Vo (c) Vx (d) Vv

Table 6.9: Effect of skew angle on natural frequency of porous FGSME plate

(SSSS, $\eta = 5$, porosity factor, $m = 0.1$, $a/h = 100$, $b/a = 1$)

Skew angle (α)	Porosity Type	Mode				
		1	2	3	4	5
15°	Pure FG	5.944	11.275	13.101	21.975	25.855
	Vu	5.613	10.644	12.368	20.756	24.411
	Vo	5.845	11.104	12.899	21.599	25.438
	Vx	5.716	10.822	12.579	21.147	24.845
	Vv	5.635	10.687	12.419	20.831	24.507
30°	Pure FG	7.838	14.378	18.612	26.165	33.908
	Vu	7.397	13.576	17.567	24.705	32.008
	Vo	7.714	14.150	18.331	25.735	33.363
	Vx	7.526	13.813	17.860	25.153	32.575
	Vv	7.429	13.628	17.641	24.802	32.140
45°	Pure FG	11.639	20.597	30.176	37.612	51.010
	Vu	10.981	19.450	28.472	35.511	48.148
	Vo	11.462	20.258	29.729	36.990	50.189
	Vx	11.165	19.802	28.940	36.157	49.002
	Vv	11.031	19.523	28.601	35.651	48.350

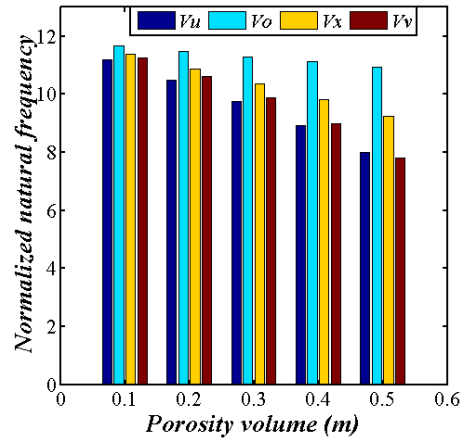


Figure 6.3: Effect of porosity volume on natural frequency of porous plate

Table 6.10: Effect of thickness ratio on natural frequency of porous FGSME plate (SSSS, $\alpha = 45^0$, $\eta = 2$, porosity factor, $m= 0.1$, $b/a = 1$)

	a/h	Mode				
		1	2	3	4	5
Pure	10	8.301	13.734	17.162	19.834	20.307
	20	9.641	16.141	25.487	25.522	34.326
	50	10.994	18.488	29.038	32.362	45.733
	100	11.843	20.904	30.694	38.190	51.825
V_u	10	7.853	12.995	16.242	18.761	19.219
	20	9.117	15.265	24.105	24.143	32.486
	50	10.392	17.483	27.451	30.610	43.246
	100	11.193	19.772	29.014	36.117	49.000
V_o	10	8.161	13.497	16.709	19.307	19.930
	20	9.490	15.889	25.078	25.093	33.419
	50	10.829	18.206	28.612	31.825	45.018
	100	11.667	20.568	30.251	37.572	51.009
V_x	10	7.997	13.240	16.708	19.303	19.607
	20	9.273	15.527	24.528	24.588	33.418
	50	10.564	17.777	27.895	31.167	43.990
	100	11.377	20.121	29.477	36.758	49.849
V_y	10	7.889	13.052	16.252	18.777	19.294
	20	9.165	15.344	24.227	24.257	32.505
	50	10.453	17.576	27.611	30.760	43.476
	100	11.261	19.870	29.188	36.304	49.271

Table 6.11: Effect of aspect ratio on natural frequency of porous FGSMEE plate(SSSS, $\alpha = 45^0$, $\eta = 2$, porosity factor, $m = 0.1$, $a/h = 100$)

Porosity type	b/a	Modes				
		1	2	3	4	5
Pure FG	0.5	37.168	45.862	68.340	97.869	115.791
	1	11.843	20.904	30.694	38.190	51.825
	1.5	7.321	13.981	20.881	27.029	32.750
	2	5.908	10.313	18.594	19.189	25.384
	2.5	5.275	8.359	14.660	17.697	22.131
	3	4.912	7.209	11.990	17.261	20.320
V_u	0.5	35.133	43.366	64.646	92.529	109.570
	1	11.193	19.772	29.014	36.117	49.000
	1.5	6.920	13.221	19.738	25.549	30.958
	2	5.585	9.751	17.576	18.134	23.997
	2.5	4.987	7.903	13.855	16.728	20.919
	3	4.643	6.815	11.332	16.316	19.207
V_o	0.5	36.605	45.136	67.191	96.447	113.621
	1	11.667	20.568	30.251	37.572	51.009
	1.5	7.209	13.765	20.577	26.604	32.271
	2	5.817	10.155	18.332	18.901	25.009
	2.5	5.197	8.233	14.443	17.452	21.810
	3	4.841	7.101	11.814	17.025	20.029
V_x	0.5	35.719	44.120	65.838	94.010	111.684
	1	11.377	20.121	29.477	36.758	49.849
	1.5	7.037	13.446	20.056	25.991	31.458
	2	5.679	9.914	17.850	18.434	24.388
	2.5	5.069	8.035	14.082	16.984	21.254
	3	4.717	6.928	11.516	16.563	19.511
V_v	0.5	35.341	43.601	64.954	93.055	110.022
	1	11.261	19.870	29.188	36.304	49.271
	1.5	6.960	13.291	19.856	25.701	31.143
	2	5.617	9.804	17.682	18.249	24.138
	2.5	5.016	7.948	13.941	16.829	21.045
	3	4.670	6.854	11.402	16.414	19.323

6.3.2 Static characteristics of porous FGSMEE plate

The behaviour of the porous FGSMEE plate subjected to static load is studied in this section. The effect of skew angle on the various porosity distributions is investigated. A comparison study of the porous and non-porous plate is carried out to highlight the influence of porosity on the structural behaviour of the skew plate. In addition, the geometric parameters influencing the structural behaviour are also assessed. The static characteristic of porous FGMEE plate with different porosity distributions, porosity volume, and different gradient index has been analysed by considering the uniformly distributed sinusoidal load across the plate area. The geometrical parameters considered for the study are: $\eta = 2$, $a/h = 100$, $b/a = 1$ and $m = 0.1$. The effect of boundary conditions, thickness ratio, and aspect ratio affecting the primary quantities (displacements and potentials) and the secondary quantities (Stresses, electric displacement and magnetic induction) of the porous FGMEE plate are investigated. Figure 6.4(a) – (k) present the effect of different porosity distribution on the various static characteristics of porous FGMEE plate. It can be seen from Figure 6.4(a) that the Vv porosity distribution has the highest u -displacement while the Vu and Vx distributions witnessed nearly identical behaviour. The characteristic behaviour of v -displacement and w -displacement in Figure 6.4(b) and (c) is similar to that of the u -displacement. It is important to note that the u -displacement clearly displays only bending, while v -displacement majorly witnesses stretching. It can also be seen that the stretching is more dominant for Vu , Vo and Vx porosity distributions. However, the predominant contribution of bending along with the stretching is observed for Vv distribution.

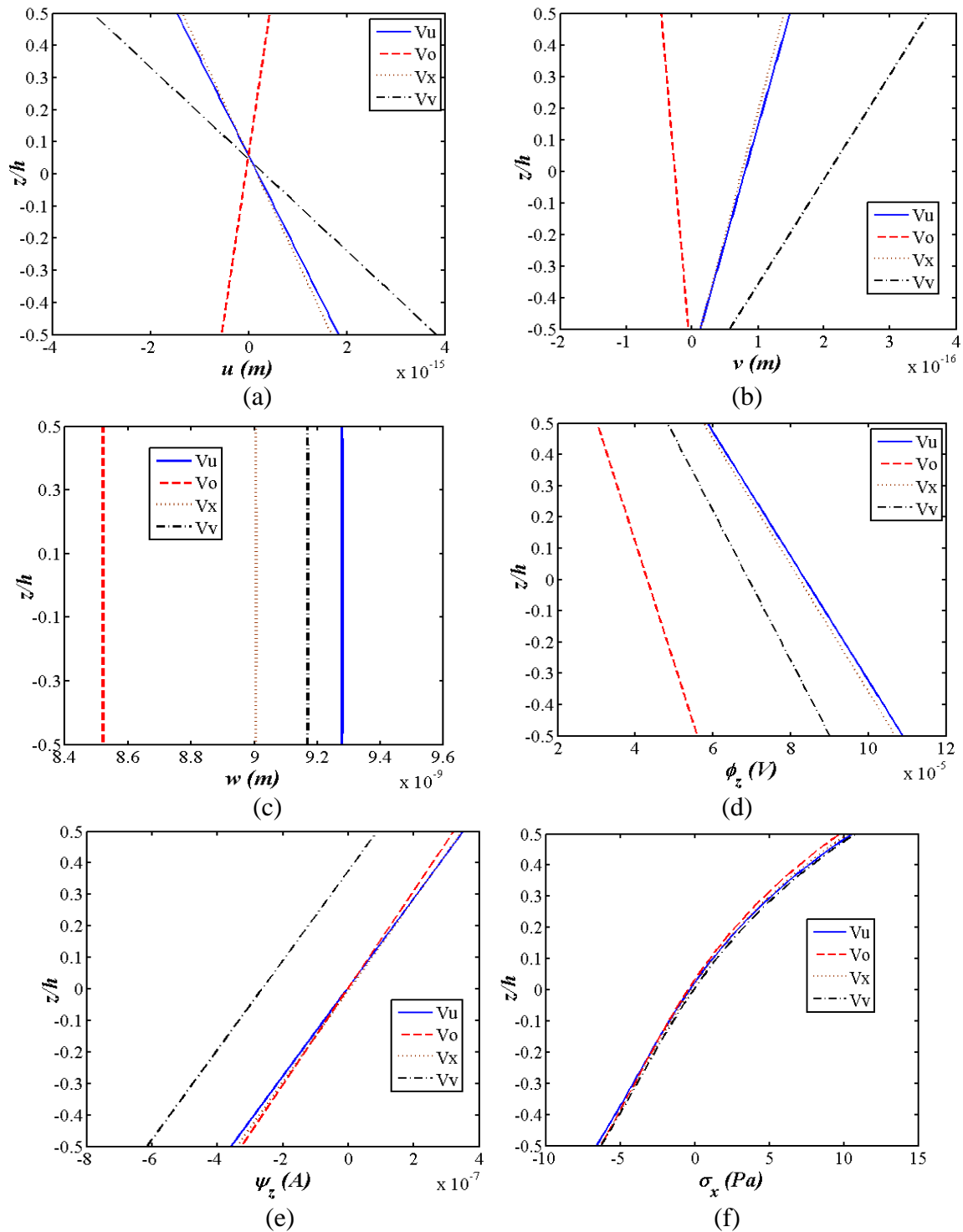
The characteristics of electric potential and magnetic potential for different porosity distribution are displayed in Figure 6.4(d) and (e). It can be seen from Figure 6.4(d) that different porosity distribution has significant influence on the electric potential. Further, it can also be seen that the largest electric potential is witnessed for Vu porosity distribution while the lowest is observed for Vo distribution. The magnetic potential in Figure 6.4(e) displays identical characteristics for Vu , Vo and Vx porosity distributions while the Vv distribution witnessed the largest magnetic potential. Figure 6.4(f) – (i) display the effect of porosity distribution on various stress quantities and a meagre influence of porosity distribution on stresses is observed. The effect of porosity distribution on magnetic induction is shown in Figure 6.4(j). The Vu , Vo and Vx porosity distributions display identical characteristics, and witness no major difference among

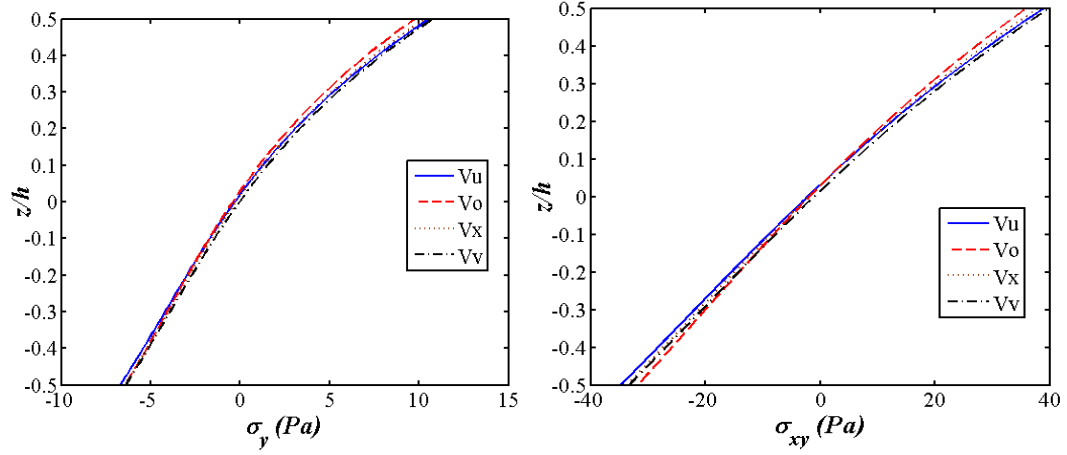
them. However, the V_v porosity distribution possesses least magnetic induction and displays nearly identical magnetic induction at the top and the bottom of the plate. Furthermore, the effect of porosity distribution on the electric displacement is presented in Figure 6.4(k). It may be observed from the figure that the V_u and V_x distribution show identical characteristics. It is also noticed that the largest electric displacement is obtained for V_u while the lowest is recorded for V_o .

The effect of skew angle and porosity distribution is depicted in Figure 6.5 – Figure 6.15. Figure 6.5(a) – (c) present u displacement for three different skew angles. A distinctive behaviour is evident for every porosity distribution with the largest displacement being associated with V_v distribution and the lowest with V_o . However, V_u and V_x distributions display an identical behaviour. It is interesting to note that the increase in skew angle results in lower u displacement and the lowest displacement is witnessed for $\alpha = 45^\circ$. The v displacement characteristics of the plate are shown in Figure 6.6(a) – (c). It can be observed from these figures that the increase in skew angle increases the stretching and reduces the bending in the porous FGSME plate. It may also be observed from these figures that the v displacement display combined stretching and bending for $\alpha = 15^\circ$. However, for $\alpha = 45^\circ$, stretching contributes majorly to the v displacement. In addition, irrespective of skew angle, every porosity distribution produced unique behaviour with the largest displacement being seen for V_v distribution and the lowest with V_o . Figure 6.7 (a) – (c) presents the w displacement characteristics of the porous FGSME plate for different skew angles. It can be observed from the plots that the increase in skew angle decreases the w displacement. In addition, it can be noticed that the V_u FGSME plate experiences largest displacement, while the V_o plate experiences the lowest displacement.

The electric potential ϕ presented in Figure 6.8 (a) – (c) decreases with the increase in skew angle. These figures also suggest that the porosity distributions display significant influence on the electric potential. The magnitude of the characteristic curve of electric potential for V_u and V_x distribution is nearly identical. However, V_o distribution registers the lowest electric potential. The increase in skew angle decreases the magnetic potential as shown in Figure 6.9 (a) – (c). Among the porosity distributions considered, V_v registers the largest magnetic potential while for the other distributions display nearly identical behaviour. The stress components presented in Figure 6.10 – Figure 6.13 decreases with the increase in skew angle. It can also be seen that the porosity

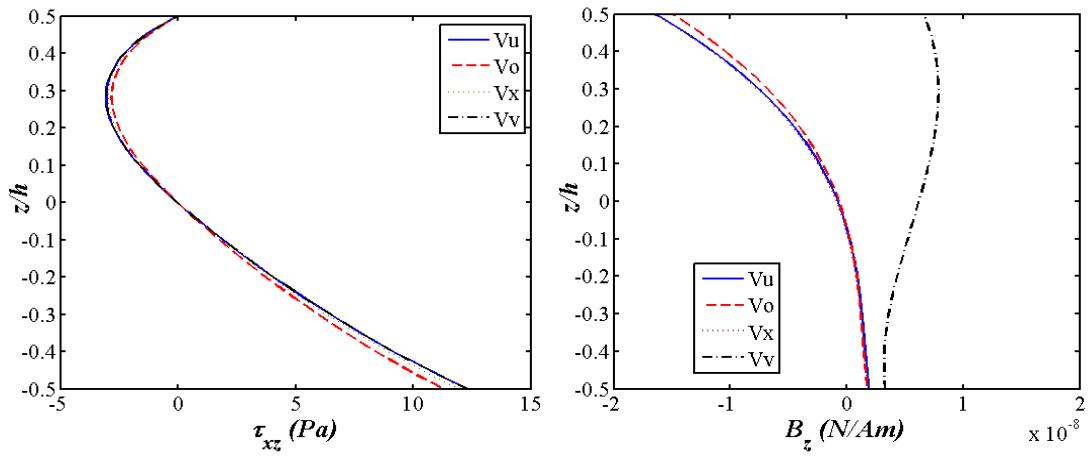
distributions have a minor influence on the stress magnitudes. Figure 6.14 (a) – (c) suggest that the magnetic induction significantly increases with the increase in skew angle. It is also interesting to note that V_v distribution registers the largest magnetic induction while the other distributions attain nearly identical magnitudes. A significant influence of porosity distributions on the electric displacement is seen from Figure 6.15 (a) – (c).





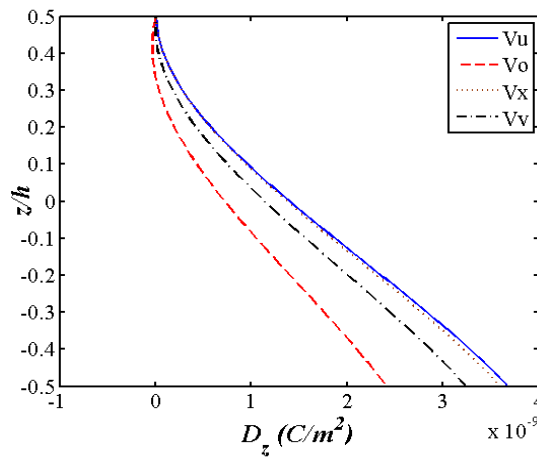
(g)

(h)



(i)

(j)



(k)

Figure 6.4: Effect of different porosity distribution on (a) u (b) v (c) w (d) ϕ_z (e) ψ_z (f) σ_x (g) σ_y (h) σ_{xy} (i) τ_{xz} (j) B_z (k) D_z

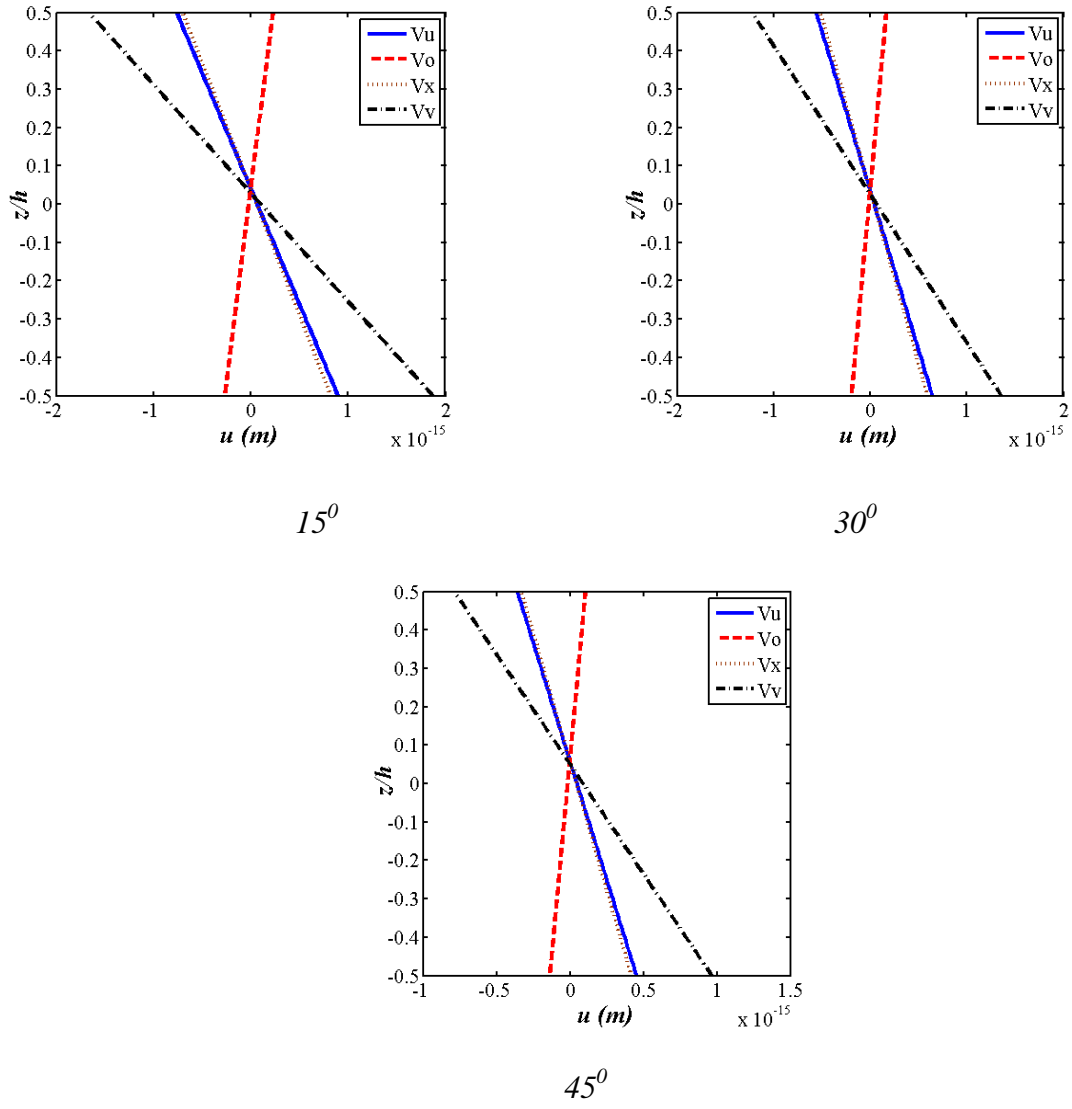
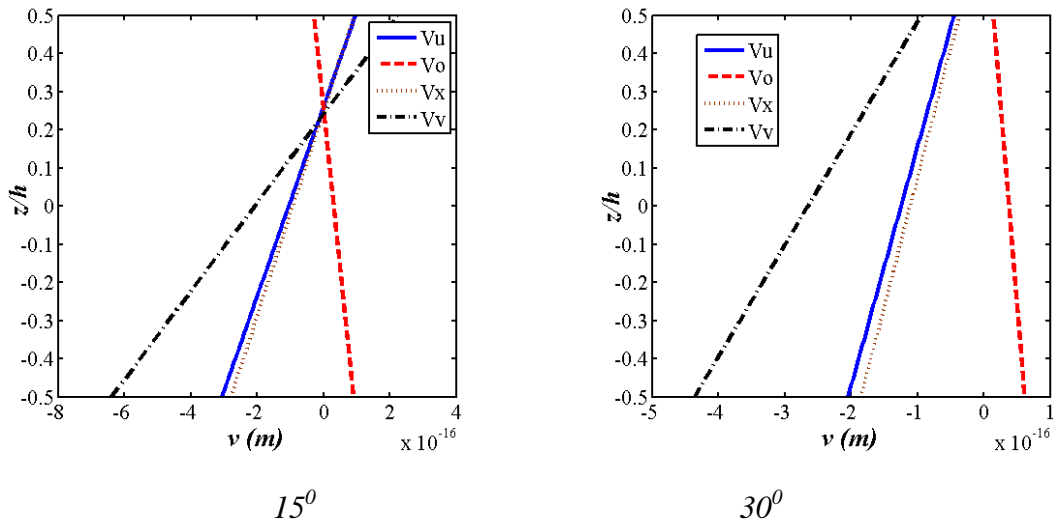
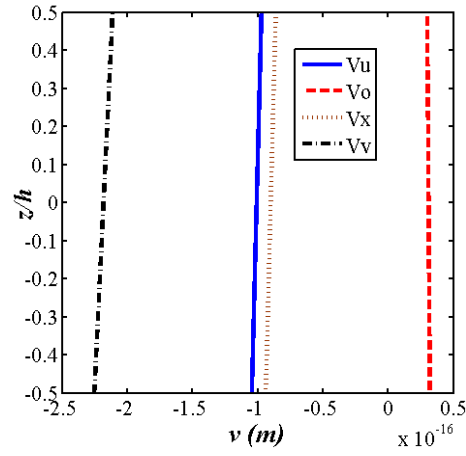


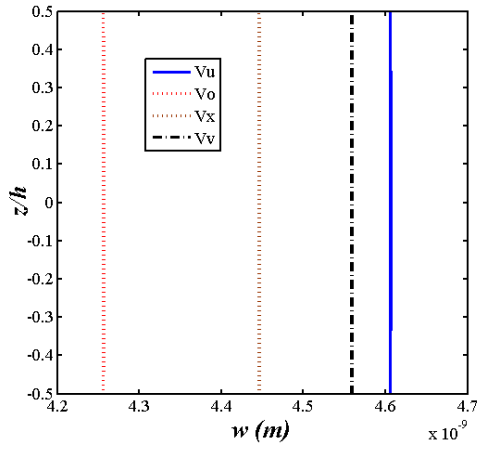
Figure 6.5: Effect of porosity distribution on porous FGSMEE plate for u ($\eta = 2$)



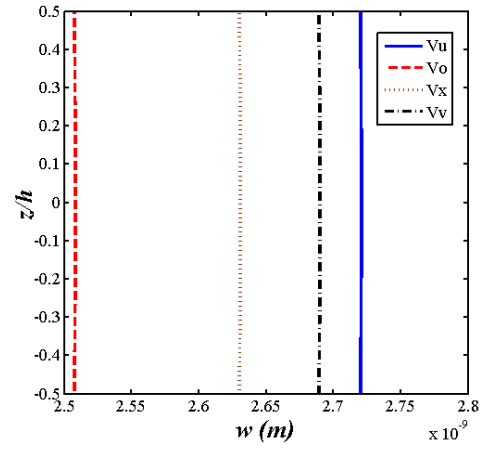


45^0

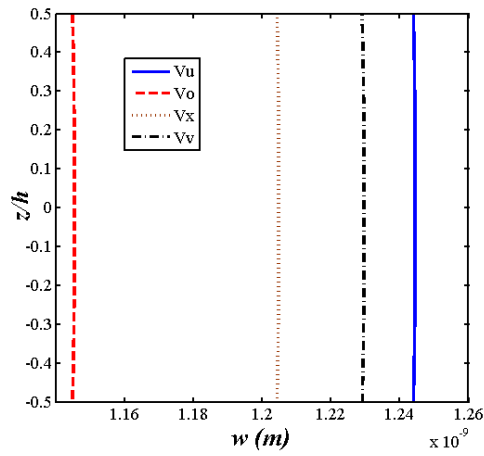
Figure 6.6: Effect of porosity distribution on porous FGSMEE plate for v ($\eta = 2$)



15^0



30^0



45^0

Figure 6.7: Effect of porosity distribution on porous FGSMEE plate for w ($\eta = 2$)

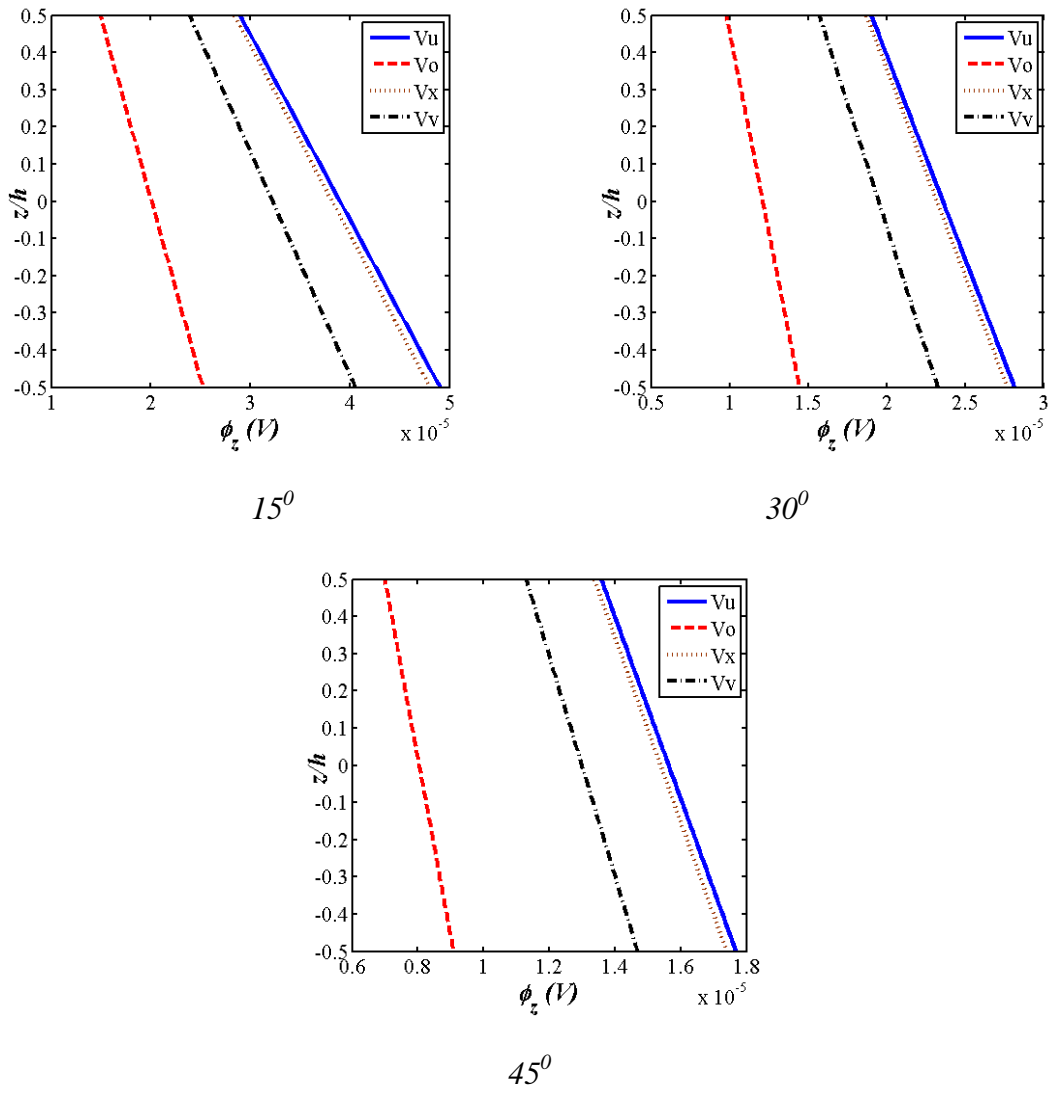
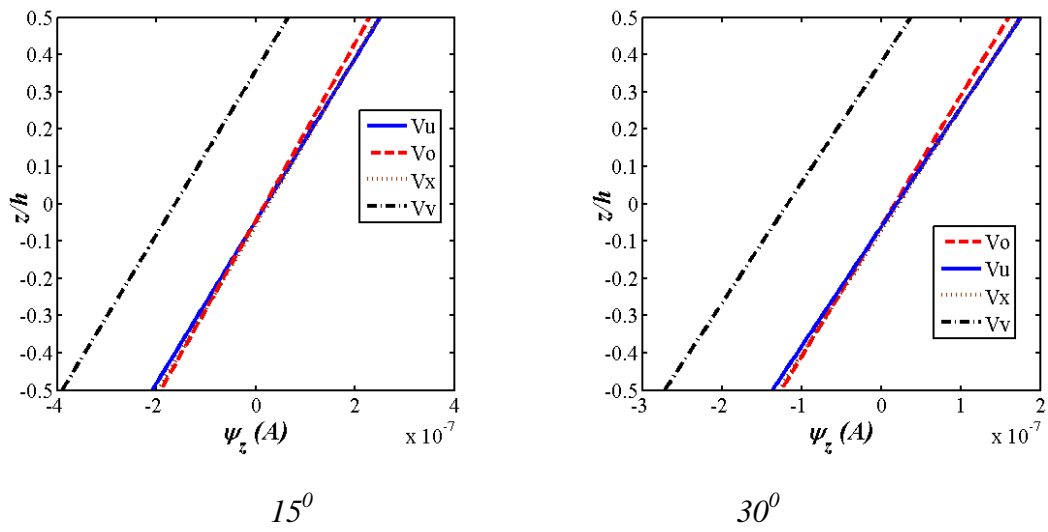
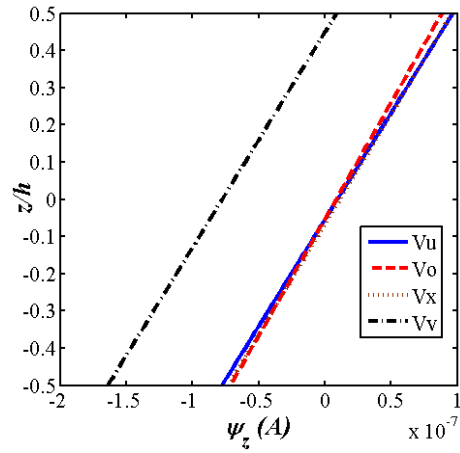


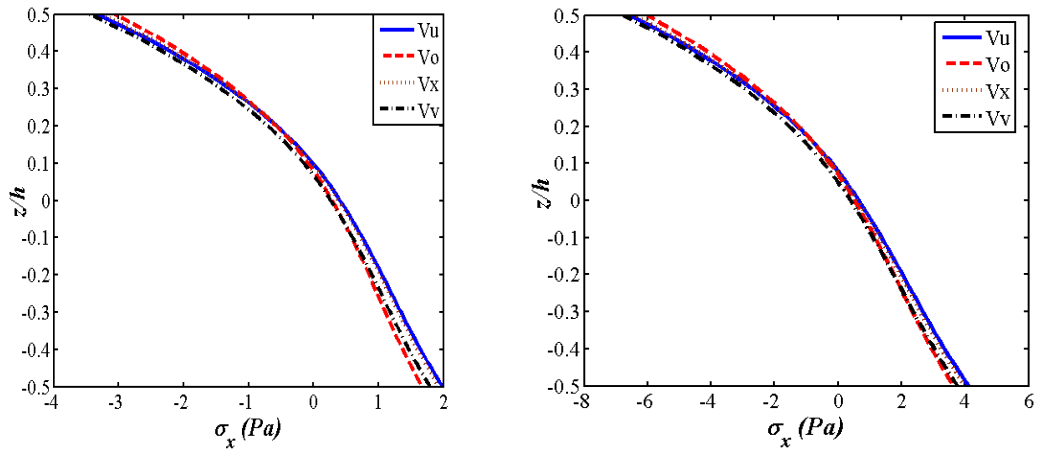
Figure 6.8: Effect of porosity distribution on porous FGSMEE plate for ϕ ($\eta = 2$)





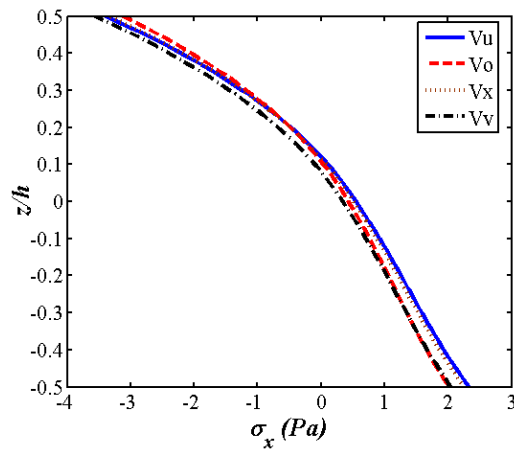
45°

Figure 6.9: Effect of porosity distribution on porous FGSMEE plate for ψ ($\eta = 2$)



15°

30°



45°

Figure 6.10: Effect of porosity distribution on porous FGSMEE plate for σ_x ($\eta = 2$)

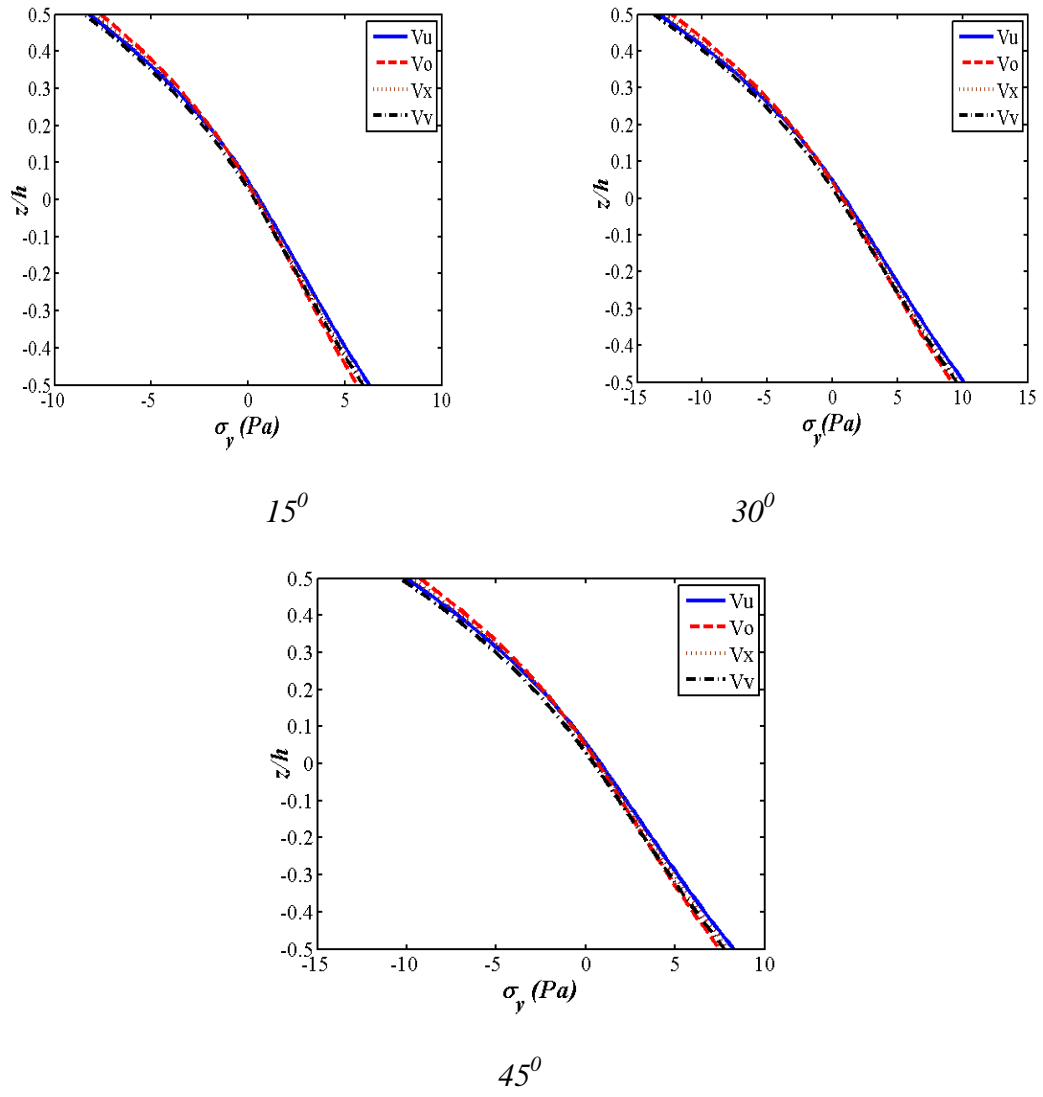
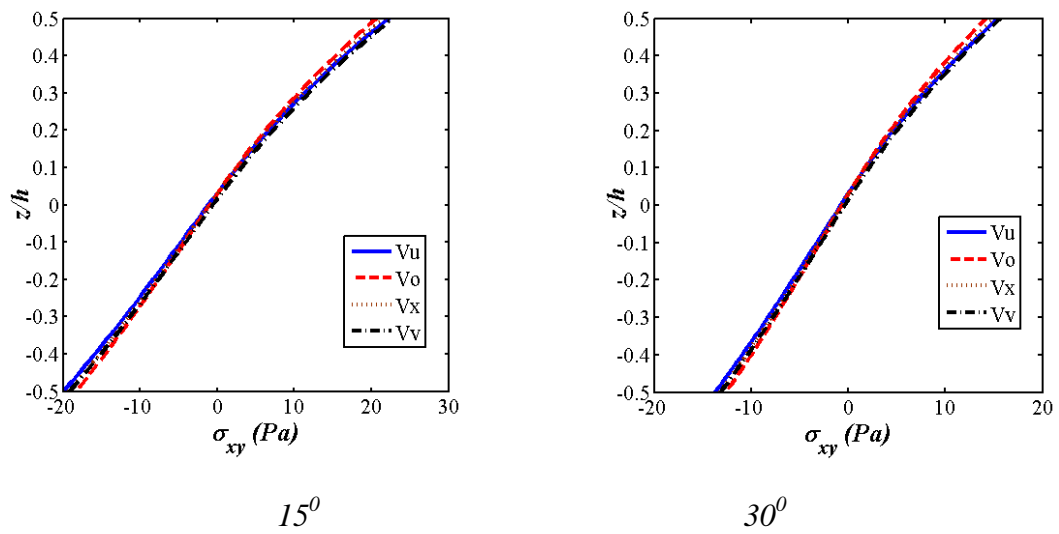


Figure 6. 11: Effect of porosity distribution on porous FGSMEE plate for σ_y ($\eta = 2$)



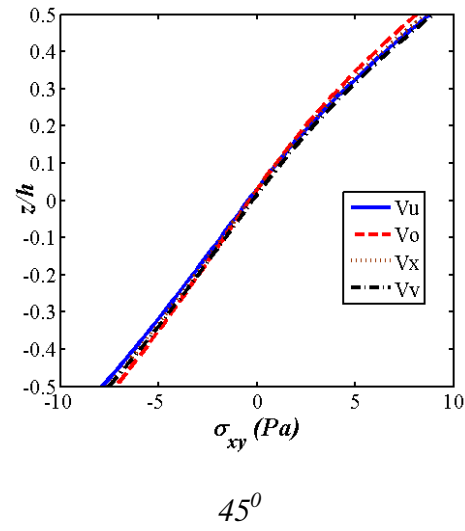


Figure 6.12: Effect of porosity distribution on porous FGSMEE plate for σ_{xy} ($\eta = 2$)

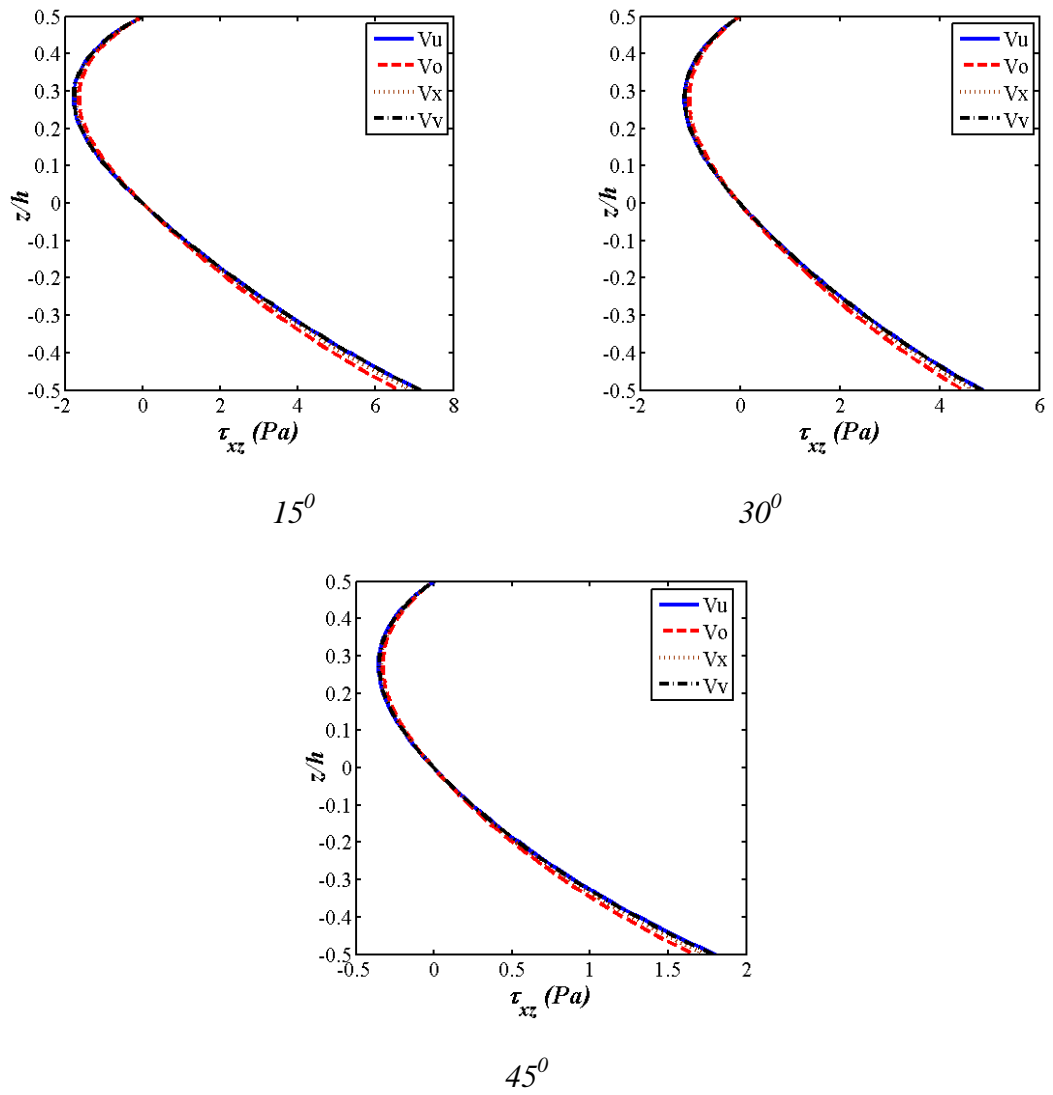


Figure 6.13: Effect of porosity distribution on porous FGSMEE plate for τ_{xz} ($\eta = 2$)

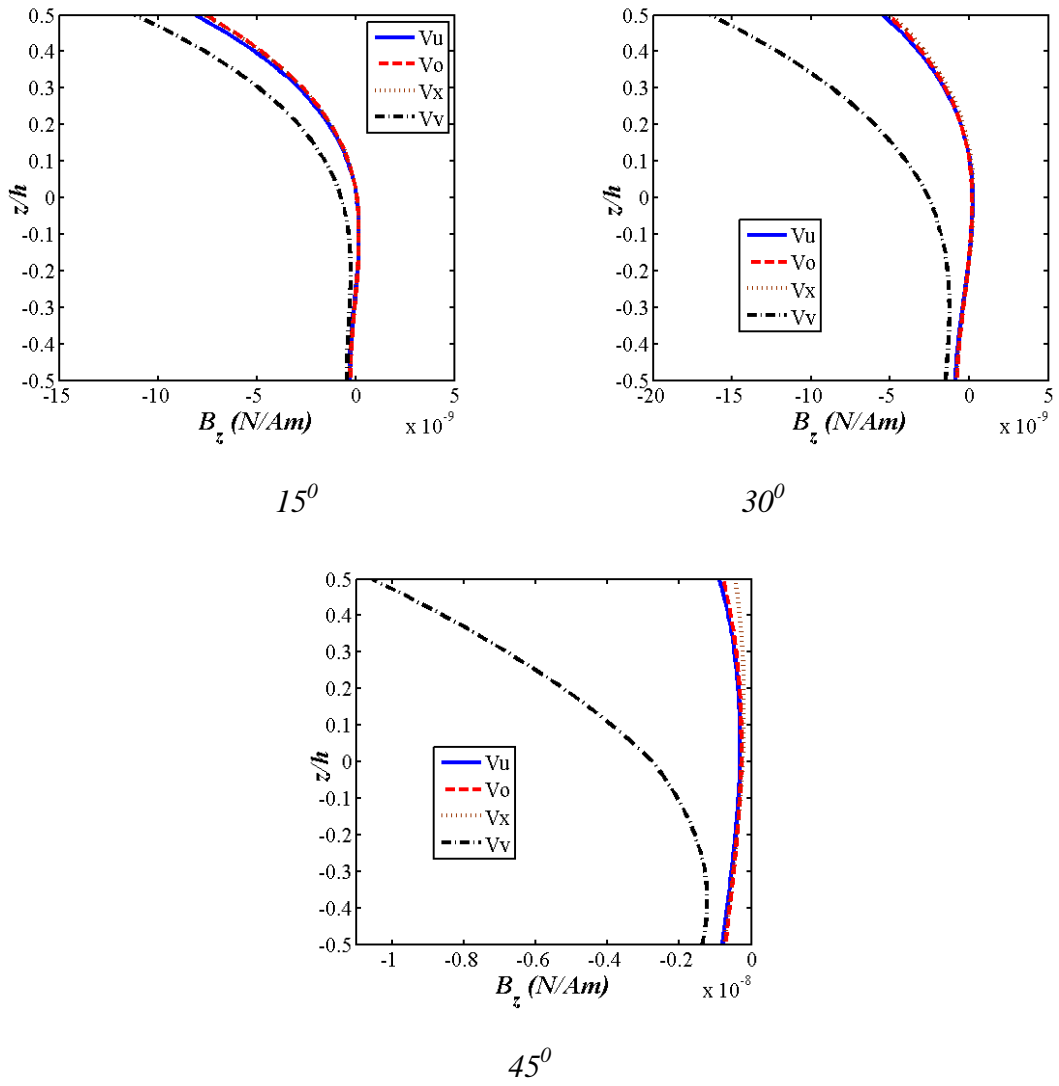
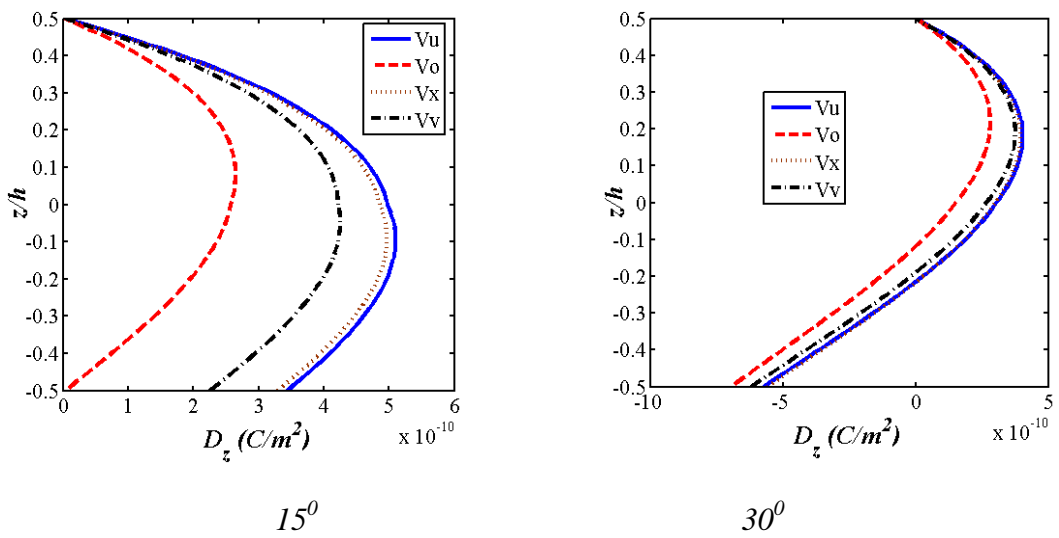


Figure 6.14: Effect of porosity distribution on porous FGSMEE plate for B_z ($\eta = 2$)



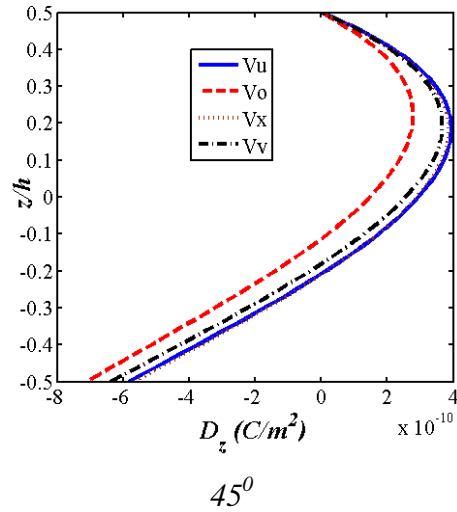
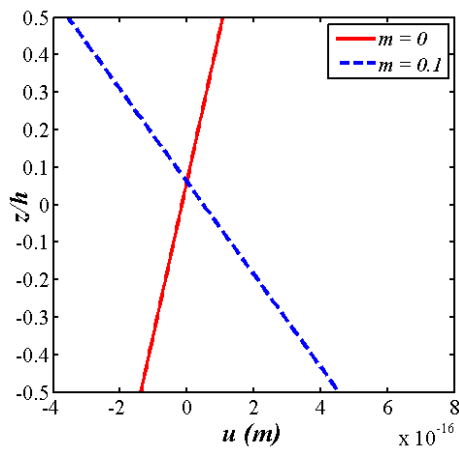
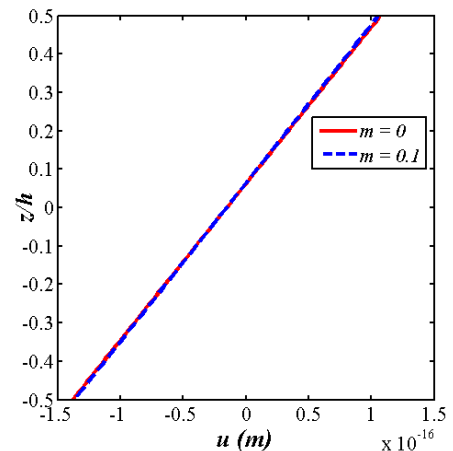


Figure 6.15: Effect of porosity distribution on porous FGSMEE plate for D_z ($\eta = 2$)

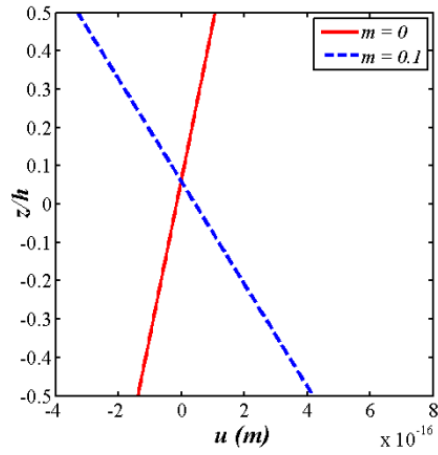
A comparison study of porous and nonporous FGSMEE plate subjected to static load is performed. The skew angle for the plate is taken as 45° and rest of the geometrical conditions are considered similar to previous analysis. Figure 6.16 –Figure 6.25 present the comparison study of porous and non-porous plate via primary quantities (u , v , ϕ , and ψ) and secondary quantities (stresses, magnetic induction, and electric displacement) for four different porosity distributions. Displacements, electric potential, and electric displacement are higher for Vu , Vx , and Vv distributions over the non-porous plate while for Vo distribution a meagre influence is seen. The magnetic potential increases for Vv distribution while Vu , Vo , and Vx porous plate produce no major influence in comparison with the non-porous plate. The influence of porosity on the stresses is negligible. Magnetic induction is higher for non-porous plate than the porous plate for Vu , Vo , and Vv while for the Vx porous plate, major influence has not been seen.



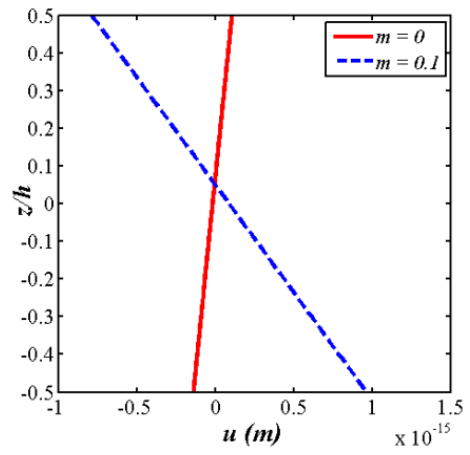
(a) Vu



(b) Vo

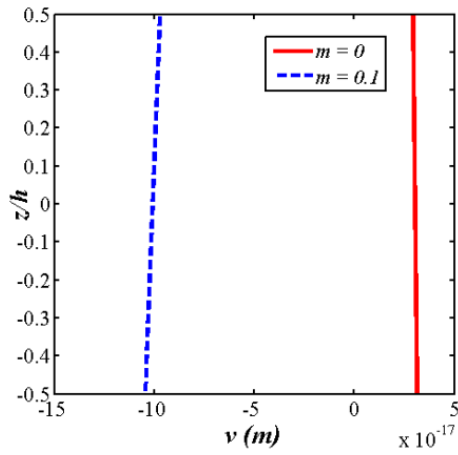


(c) V_x

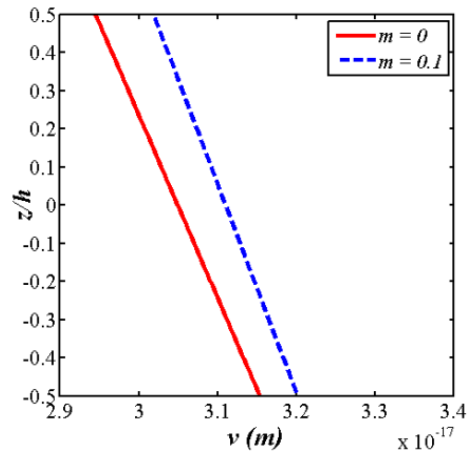


(d) V_v

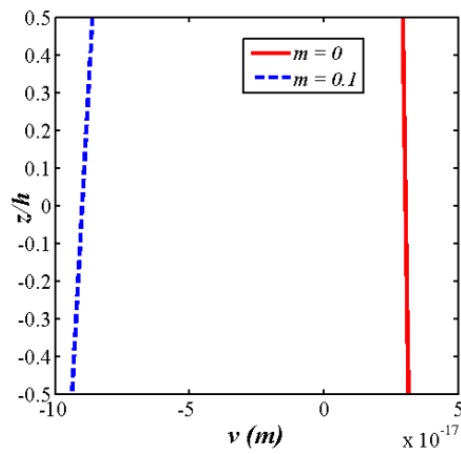
Figure 6.16: Comparison of porous and non-porous plate for u ($\eta = 2$; $\alpha = 45^\circ$)



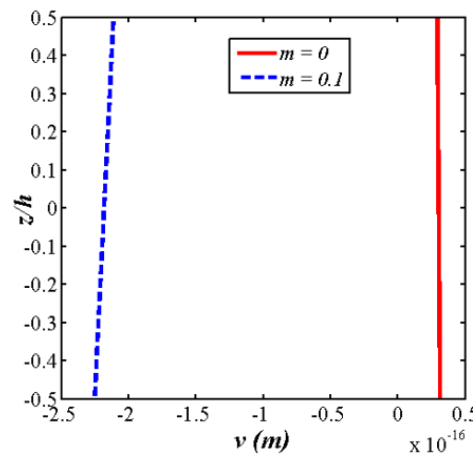
(a) V_u



(b) V_o

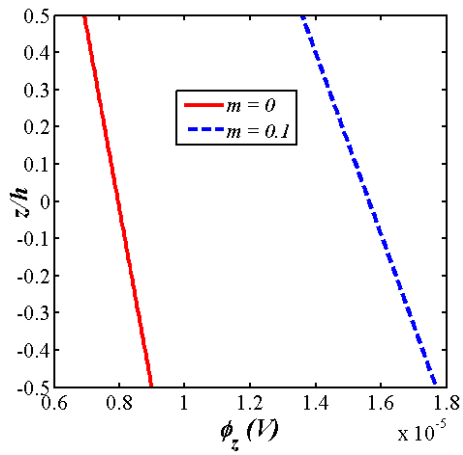


(c) V_x

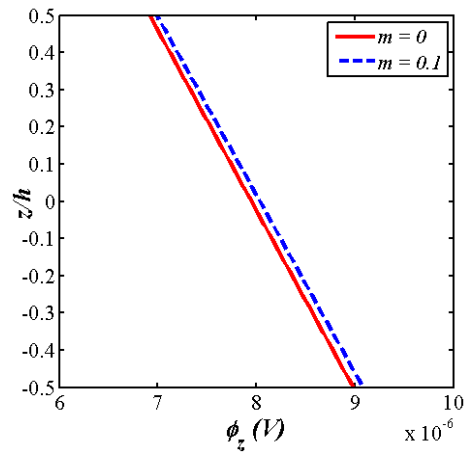


(d) V_v

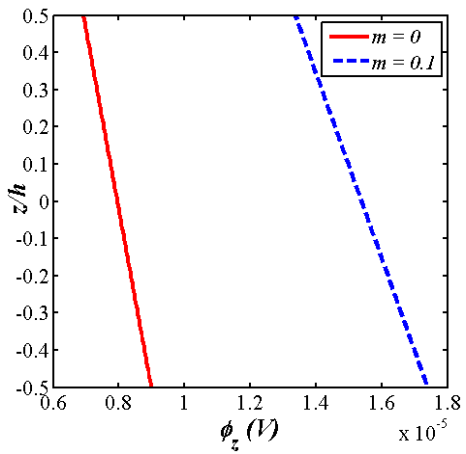
Figure 6.17: Porous and non-porous plate for v displacement ($\eta = 2$; $\alpha = 45^\circ$)



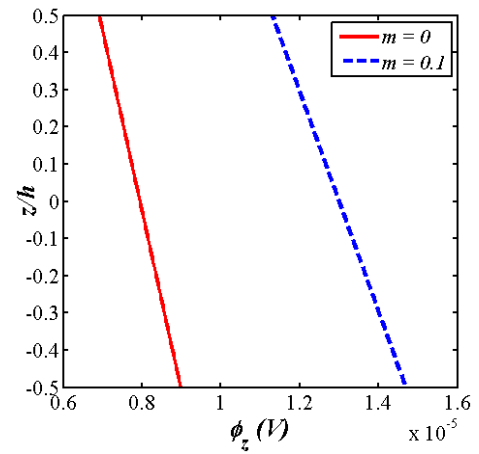
(a) Vu



(b) Vo

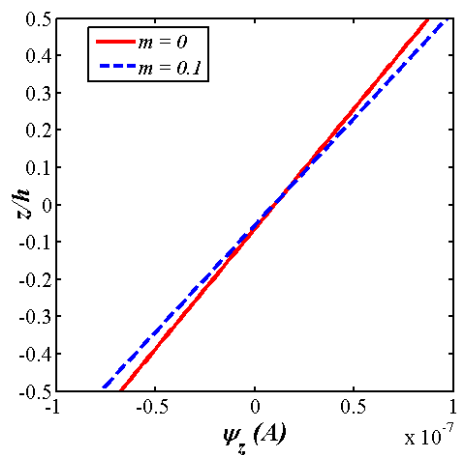


(c) Vx

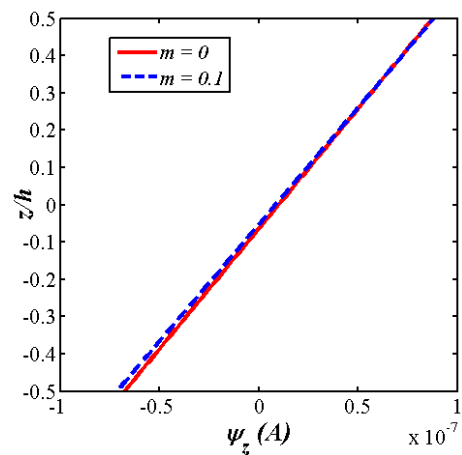


(d) Vv

Figure 6.18: Comparison of porous and non-porous plate for ϕ ($\eta = 2$; $\alpha = 45^\circ$)



(a) Vu



(b) Vo

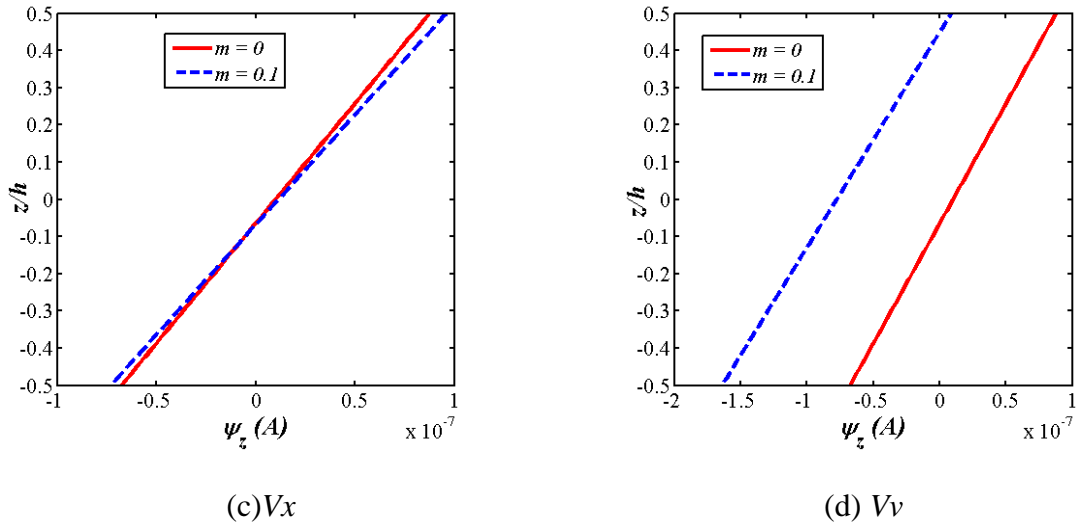


Figure 6.19: Comparison of porous and non-porous plate for ψ ($\eta = 2$; $\alpha = 45^\circ$)

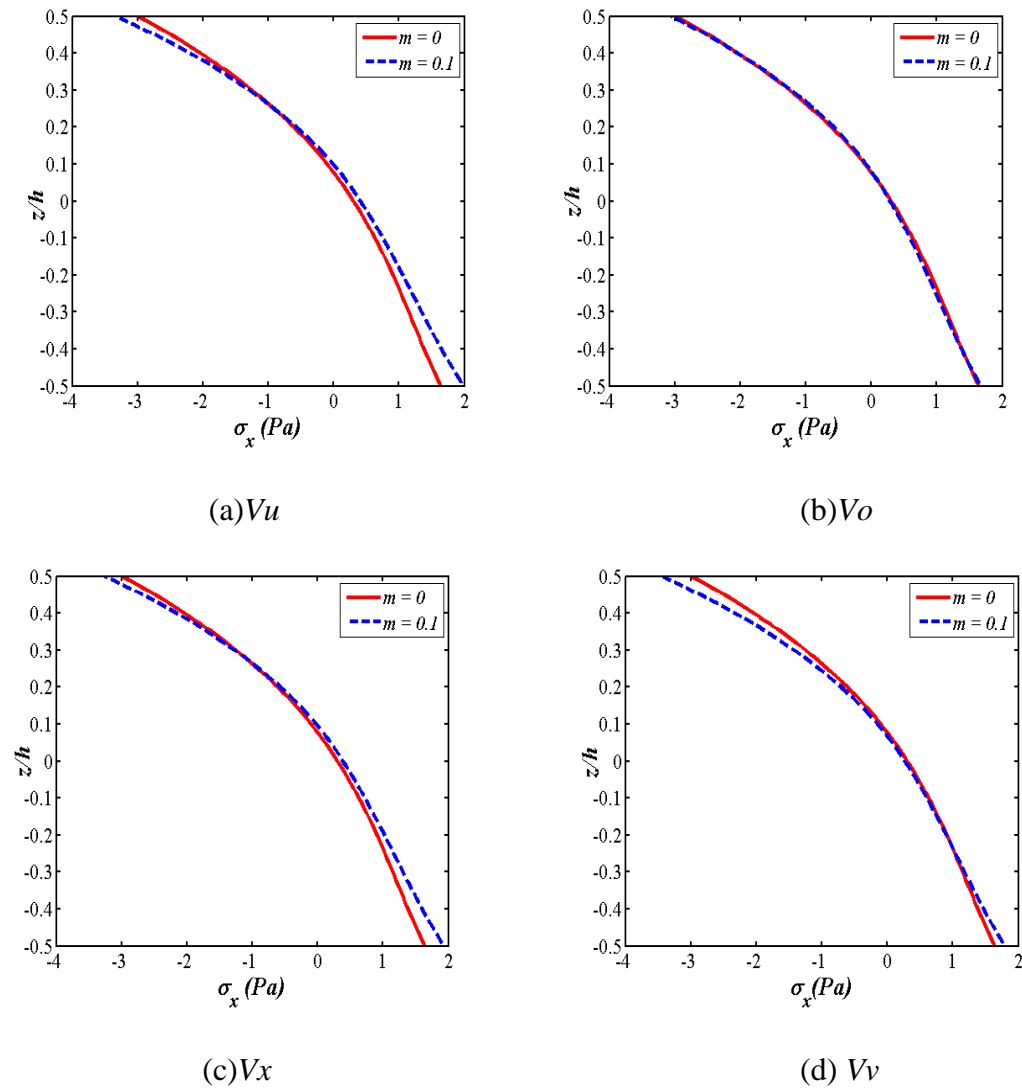
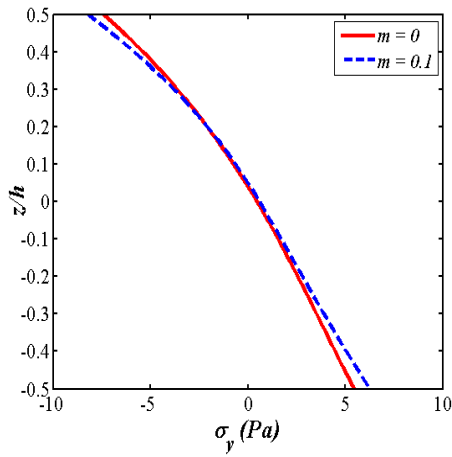
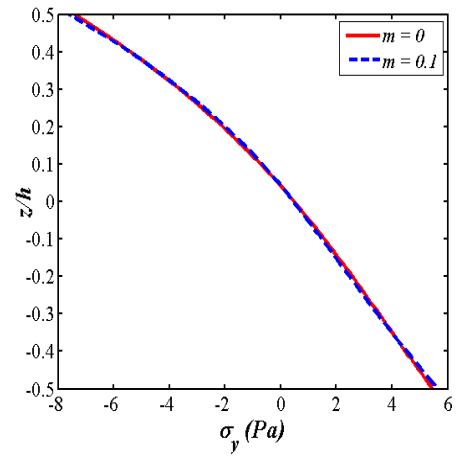


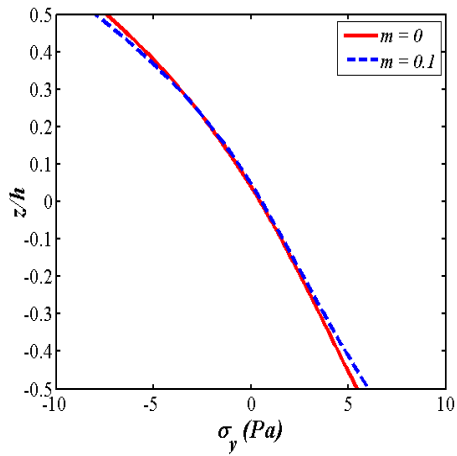
Figure 6.20: Comparison of porous and non-porous plate for σ_x ($\eta = 2$; $\alpha = 45^\circ$)



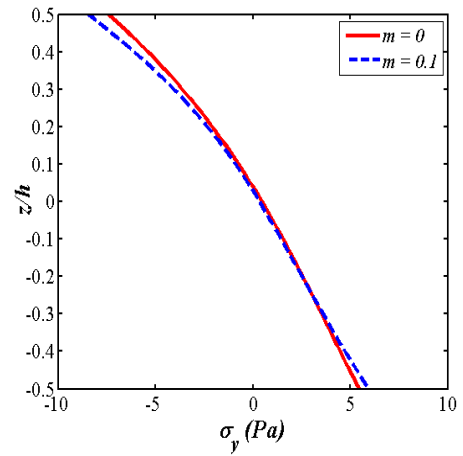
(a) Vu



(b) Vo

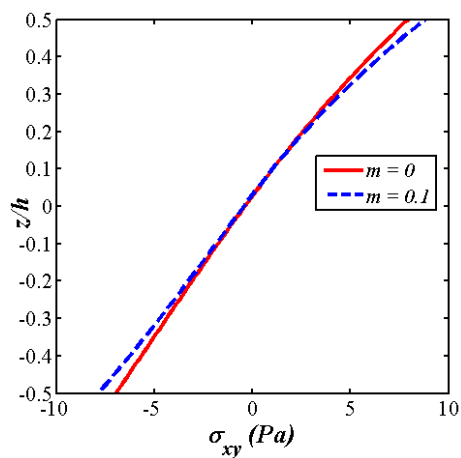


(c) Vx

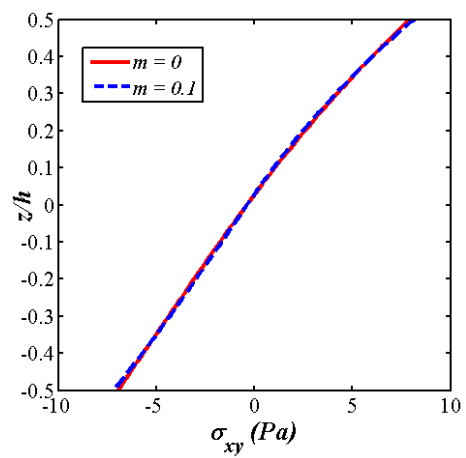


(d) Vv

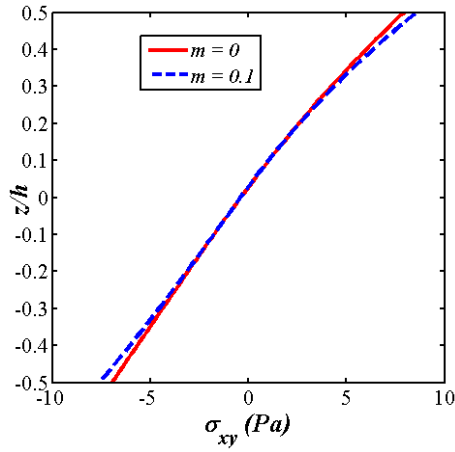
Figure 6.21: Comparison of porous and non-porous plate for σ_y ($\eta = 2$; $\alpha = 45^\circ$)



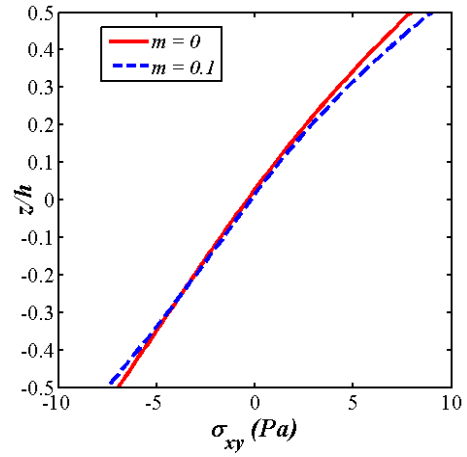
(a) Vu



(b) Vo

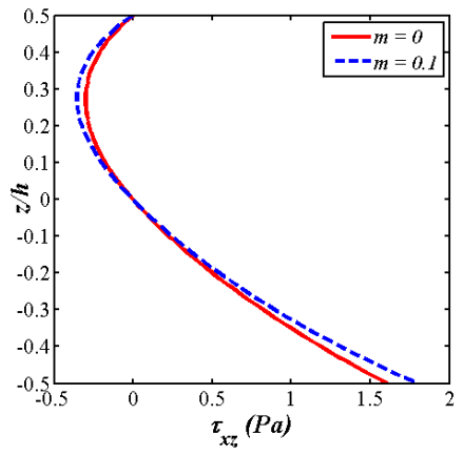


(c) V_x

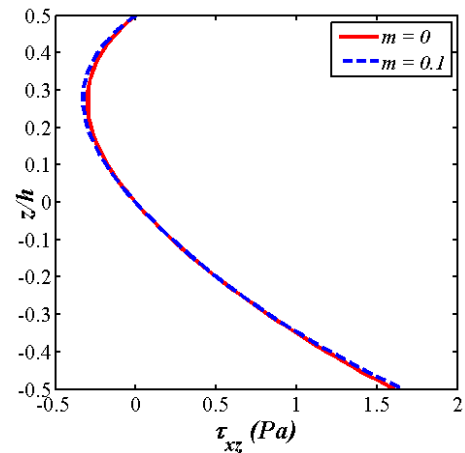


(d) V_v

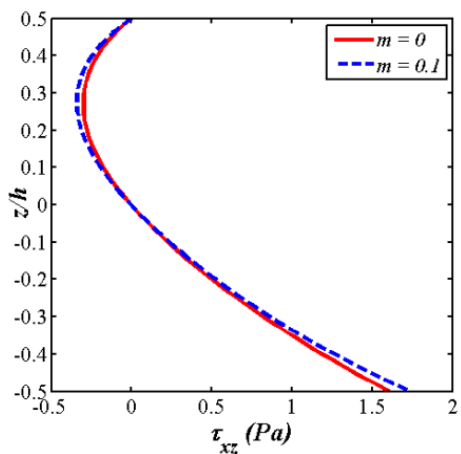
Figure 6.22: Comparison of porous and non-porous plate for σ_{xy} ($\eta = 2$; $\alpha = 45^0$)



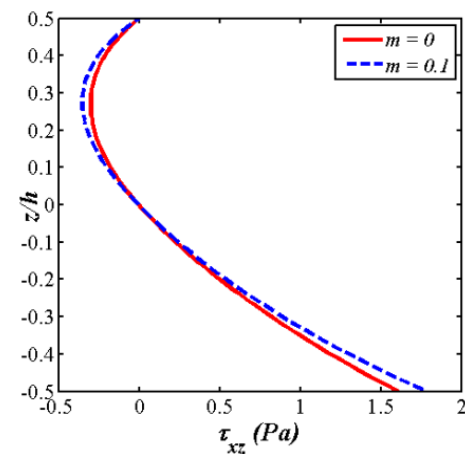
(a) V_u



(b) V_o

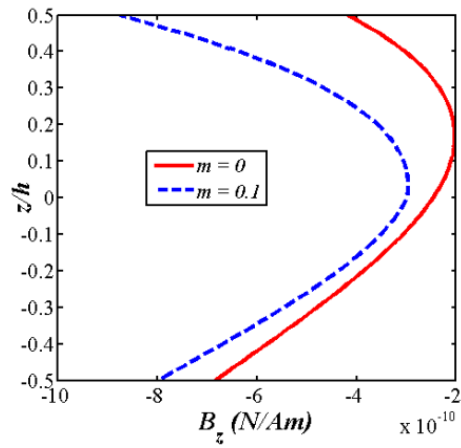


(c) V_x

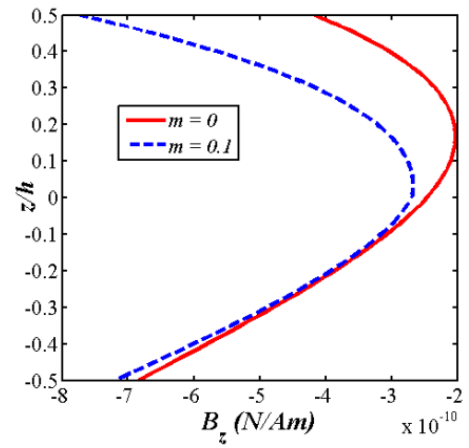


(d) V_v

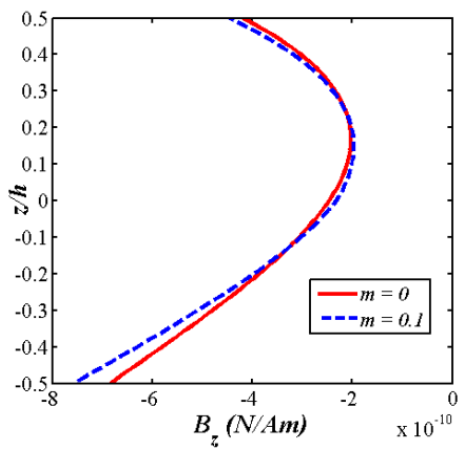
Figure 6.23: Comparison of porous and non-porous plate for τ_{xz} ($\eta = 2$; $\alpha = 45^0$)



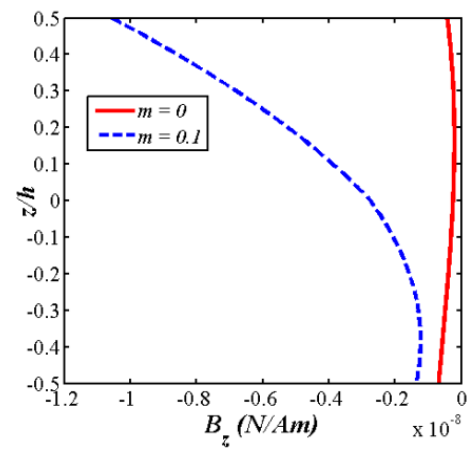
(a) V_u



(b) V_o

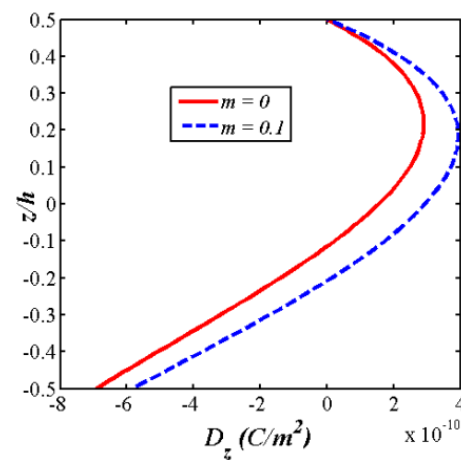


(c) V_x

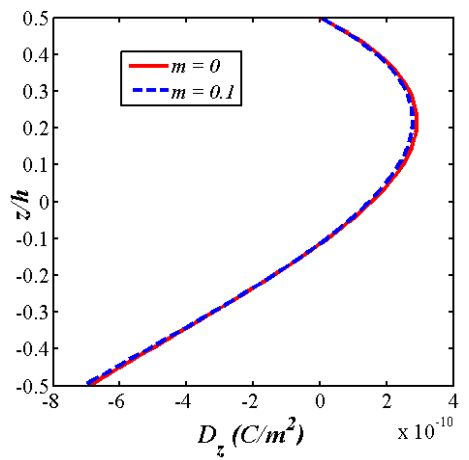


(d) V_v

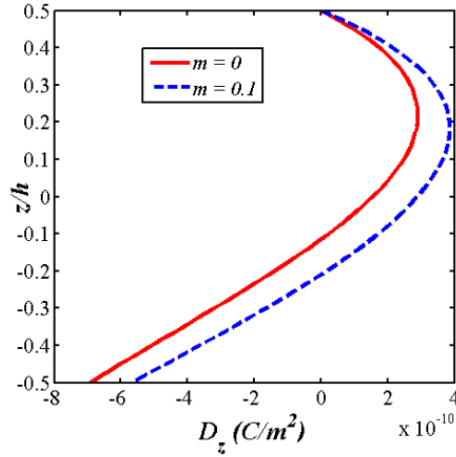
Figure 6.24: Comparison of porous and non-porous plate for B_z ($\eta = 2$; $\alpha = 45^\circ$)



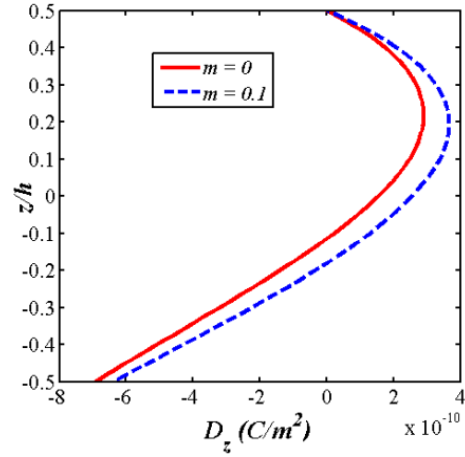
(a) V_u



(b) V_o



(c) V_x

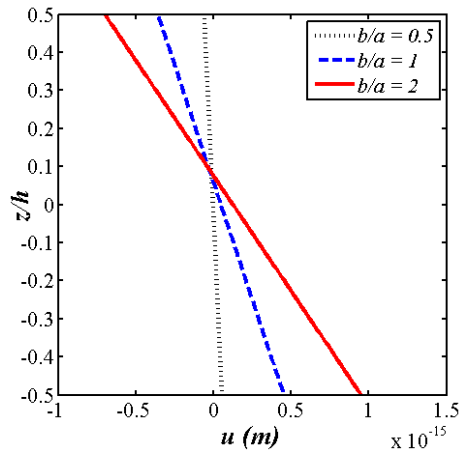


(d) V_v

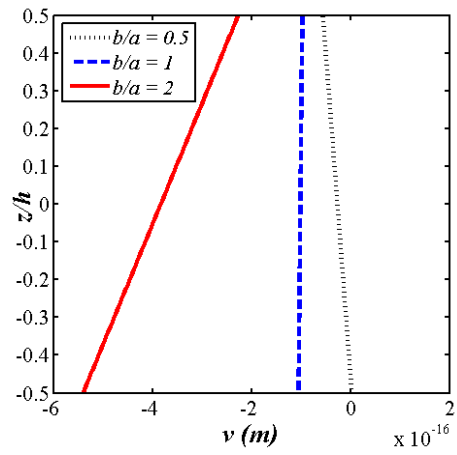
Figure 6.25: Comparison of porous and non-porous plate for D_z ($\eta = 2$; $\alpha = 45^\circ$)

The geometrical parameters influencing the static behaviour of porous FGSME plate is presented in Figure 6.26 – Figure 6.29. The primary quantities (u , v , ϕ , and ψ) and the secondary quantities (stresses, magnetic induction, and electric displacement) investigated for different aspect ratios are presented in Figure 6.26(a) – (j). These figures suggest that the increase in aspect ratio increases the primary and secondary quantities. Further, increase in lateral dimensions increases the influence of porosity on FGSME plate. Similarly, the static characteristics of porous FGME plates are studied for different thickness ratios. Figure 6.27(a) – (j) suggest that the porosity largely affects the thin plate over thick plates. In addition, boundary conditions affecting the plate characteristics for static load are presented in Figure 6.28(a) – (j). It can be observed from these figures that the simply supported plate produces larger displacements, potentials, stress, magnetic induction, and electric displacement over clamped plates. The influence of volume of porosity on the static behaviour of porous FGSME plate is also studied. The different porosity distributions studied in the present analysis are shown in Figure 6.29 – Figure 6.38. It may be noticed from these figures that the higher volume of porosity results into higher displacements, potentials, stresses, magnetic induction, and electric displacement for V_u , V_x , and V_v porosity distributions. However, the influence of porosity volume on V_o porosity distribution is found to be ineffective for porosity volume, $m > 0.2$. It can also be noticed from the Figure 6.29 – Figure 6.38 that the higher porosity volume effectively brings down the stiffness of the plate thereby results in higher primary and secondary quantities. The negligible influence of higher porosity volume (i.e., $m > 0.2$) on V_o suggests that the existence of porosity near to the bottom and top

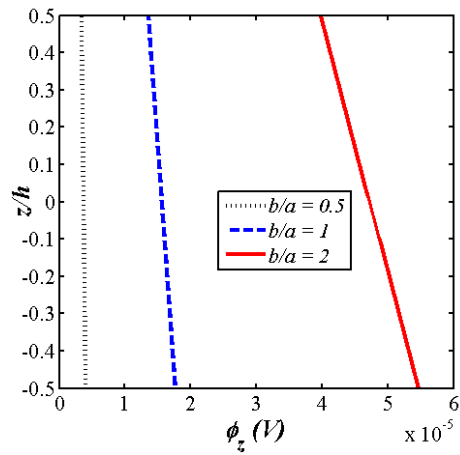
surface are more prone to higher displacement and stresses over porosity distributions near to mid-plane.



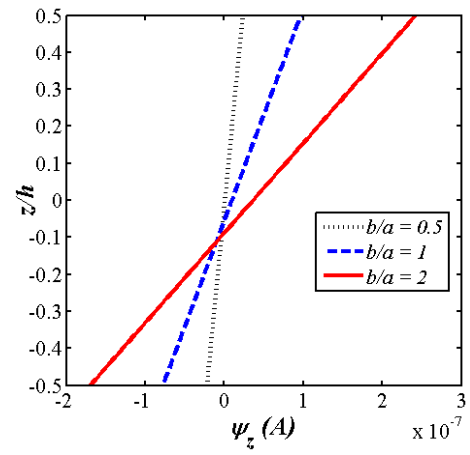
(a)



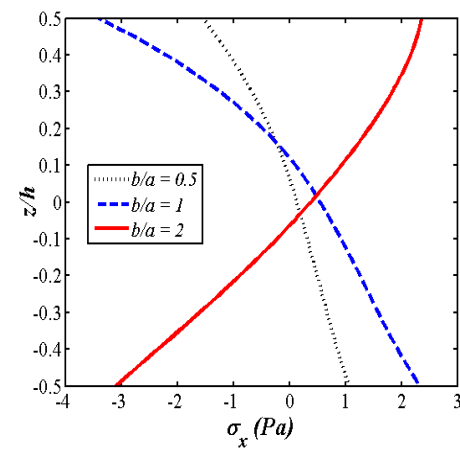
(b)



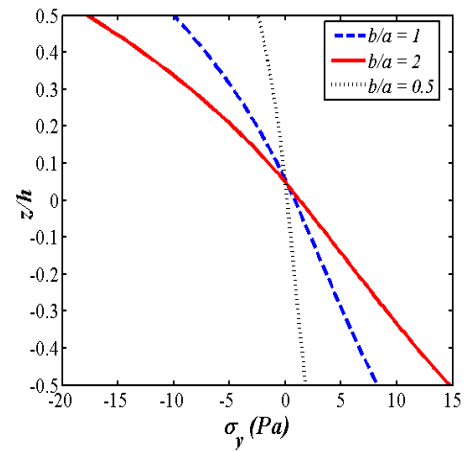
(c)



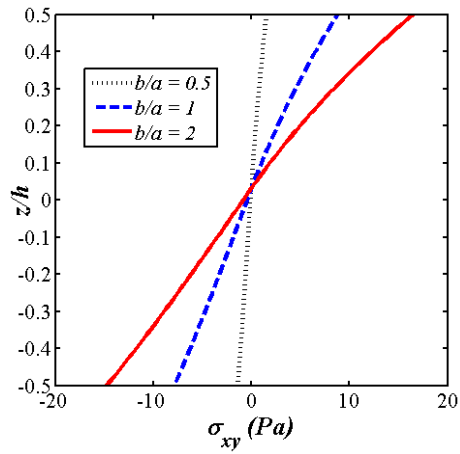
(d)



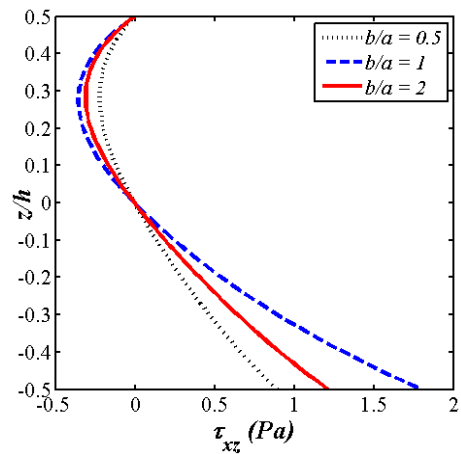
(e)



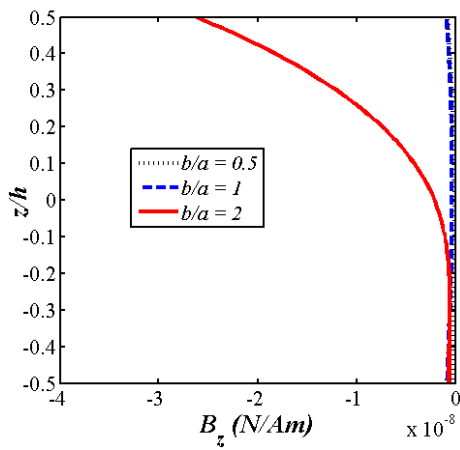
(f)



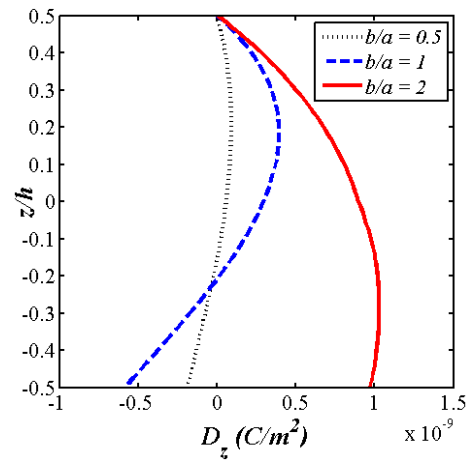
(g)



(h)

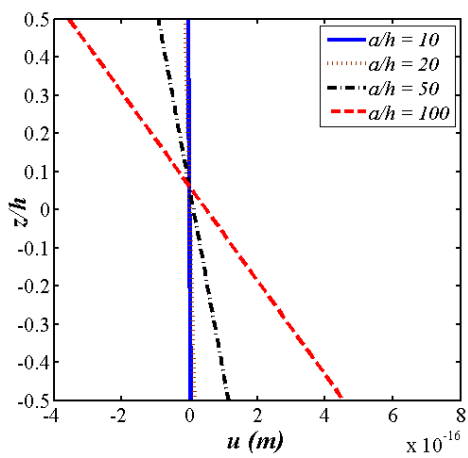


(i)

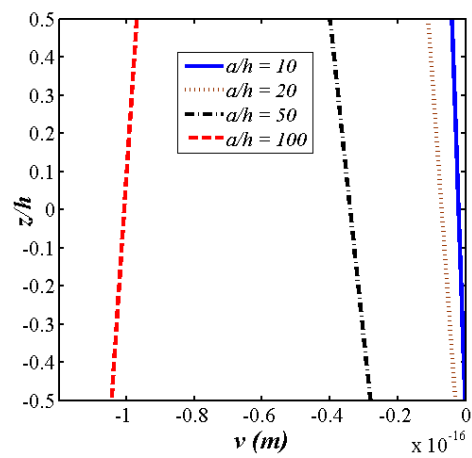


(j)

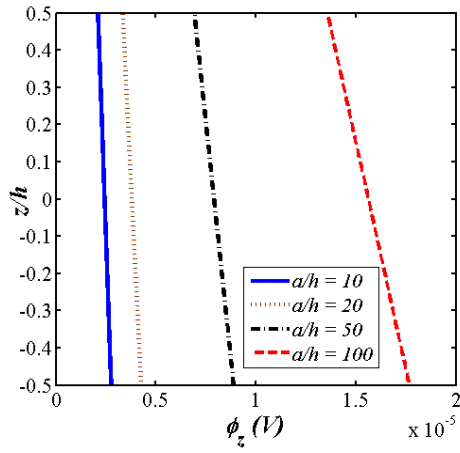
Figure 6.26: Effect of aspect ratio on ($\eta = 2$; Vu ; $\alpha = 45^\circ$) (a) u (b) v (c) ϕ_z (d) ψ_z (e) σ_x (f) σ_y (g) σ_{xy} (h) τ_{xz} (i) B_z (j) D_z



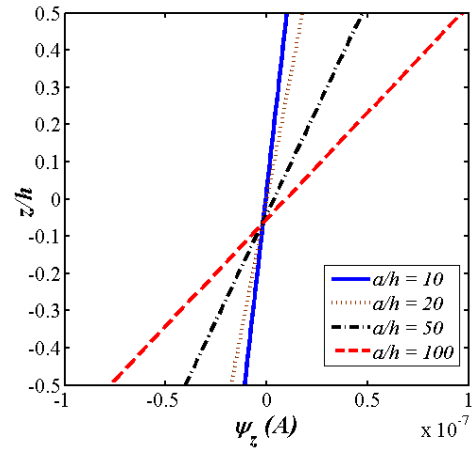
(a)



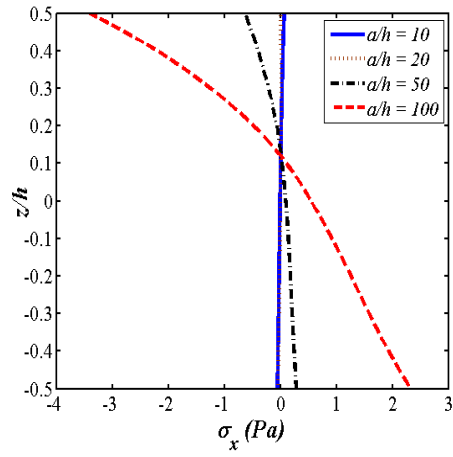
(b)



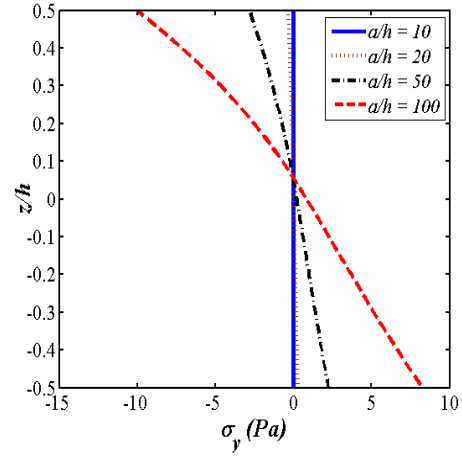
(c)



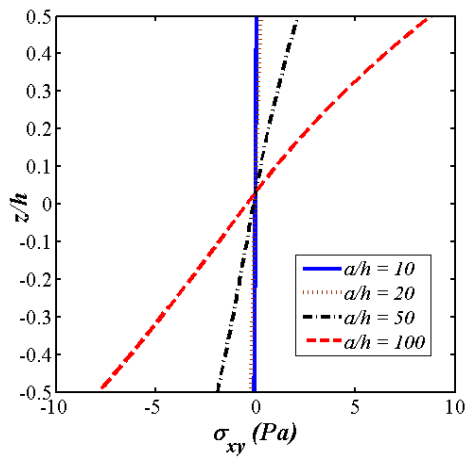
(d)



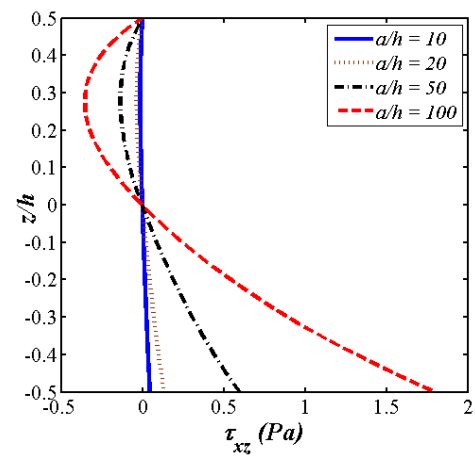
(e)



(f)



(g)



(h)

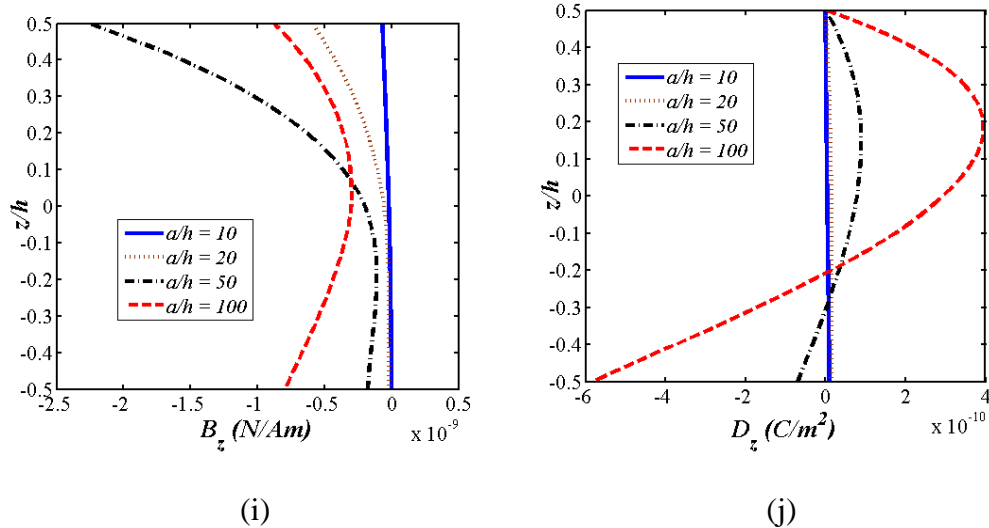
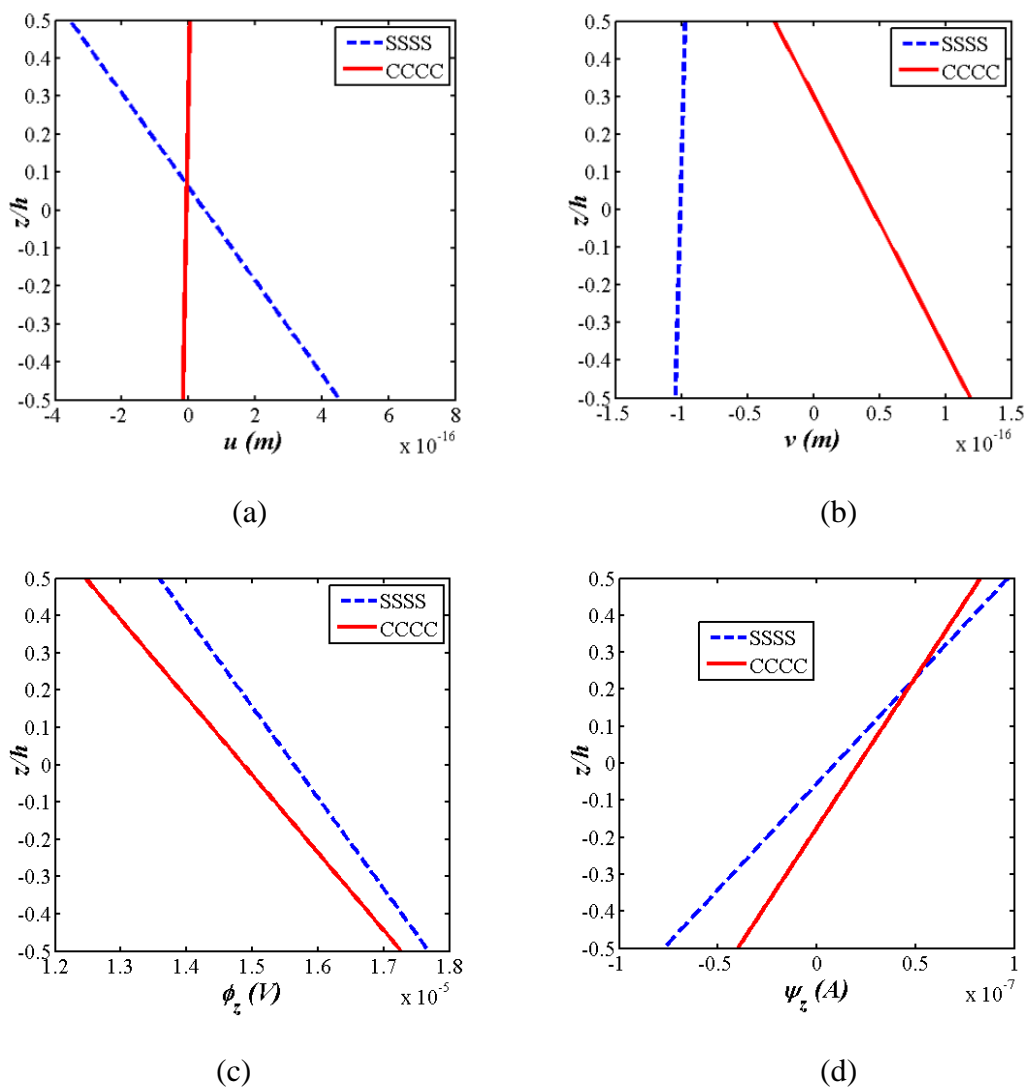
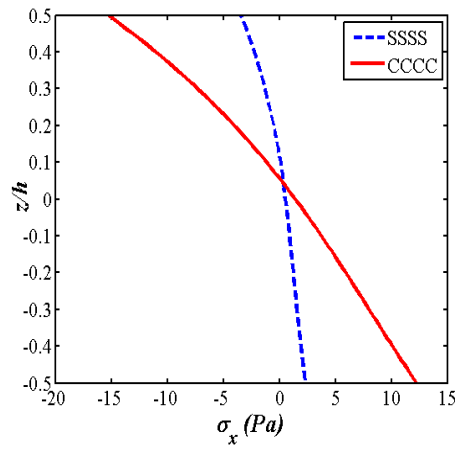
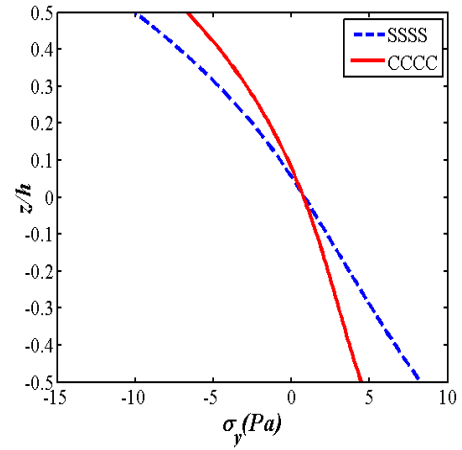


Figure 6.27: Effect of thickness ratio on ($\eta = 2$; Vu ; $\alpha = 45^\circ$) (a) u (b) v (c) ϕ_z (d) ψ_z (e) σ_x (f) σ_y (g) σ_{xy} (h) τ_{xz} (i) B_z (j) D_z

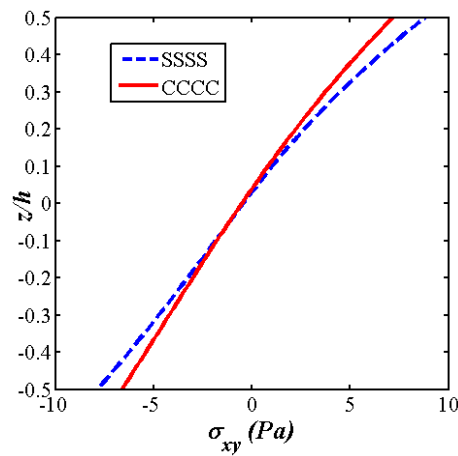




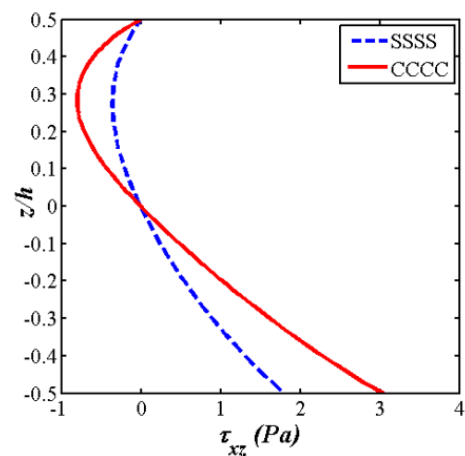
(e)



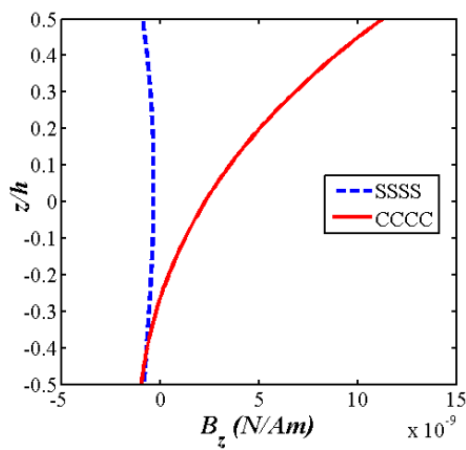
(f)



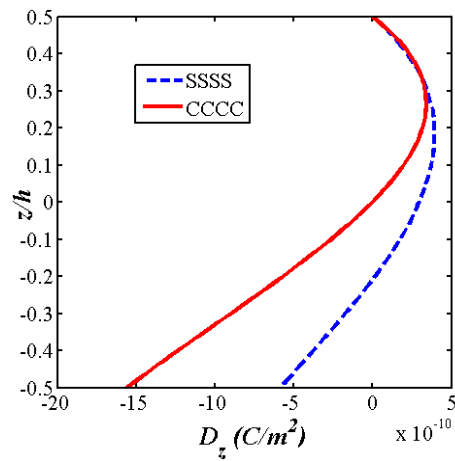
(g)



(h)

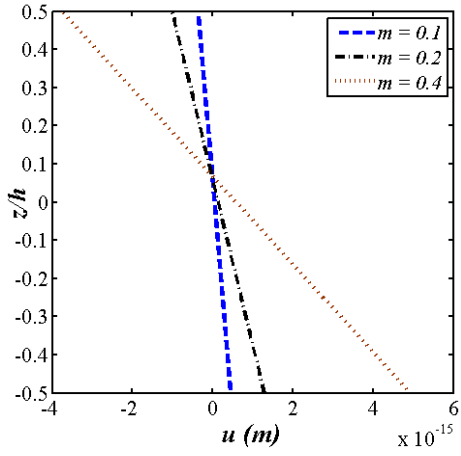


(i)

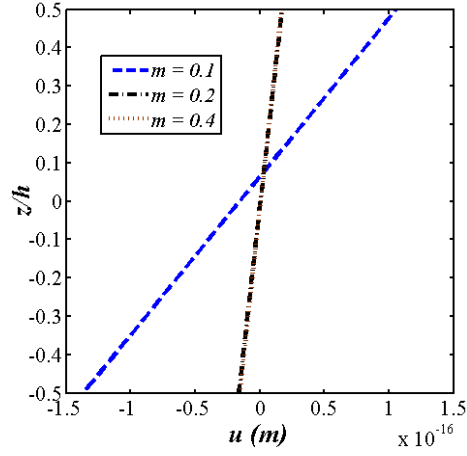


(j)

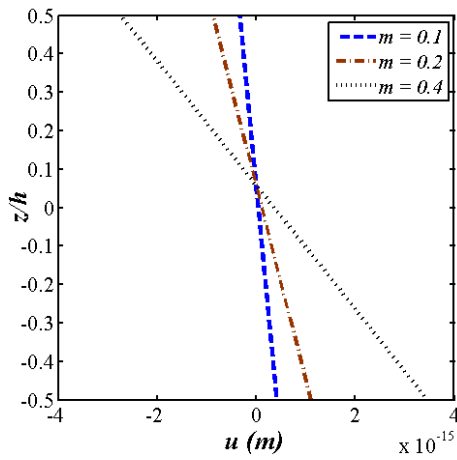
Figure 6.28: Effect of boundary condition on ($\eta = 2$; Vu ; $\alpha = 45^\circ$) (a) u (b) v (c) ϕ_z (d) ψ_z (e) σ_x (f) σ_y (g) σ_{xy} (h) τ_{xz} (i) B_z (j) D_z



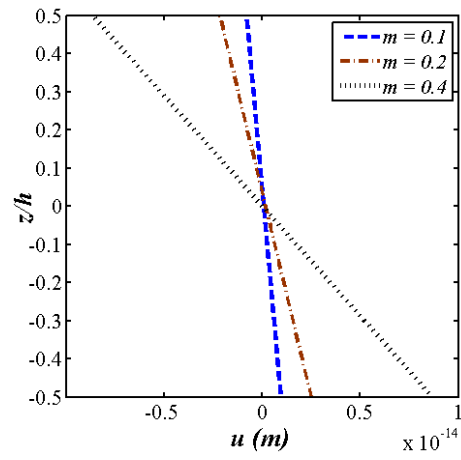
(a) Vu



(b) Vo

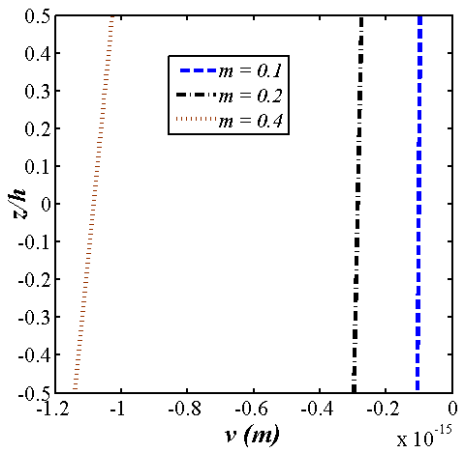


(c) Vx

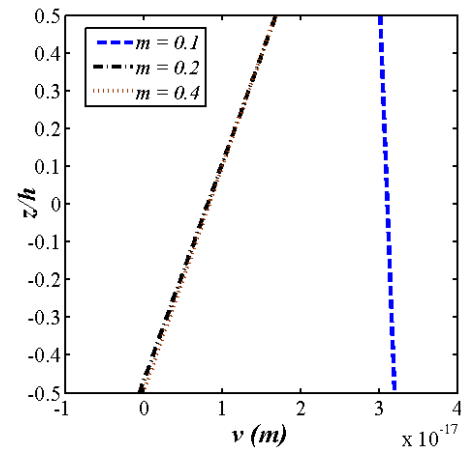


(d) Vv

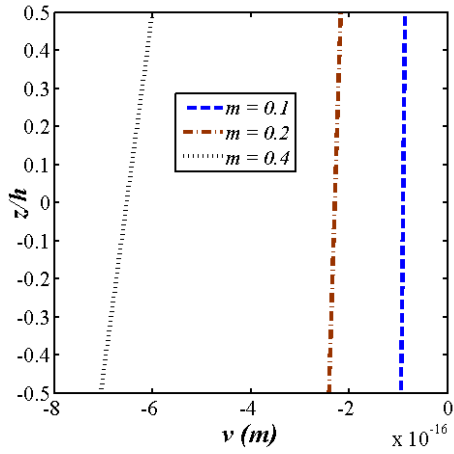
Figure 6.29: Effect of porosity volume on u ($\eta = 2$; $\alpha = 45^0$)



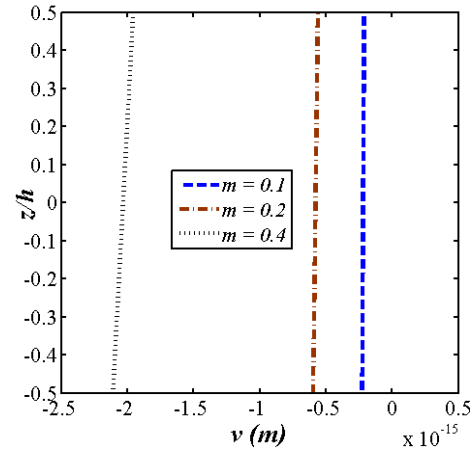
(a) Vu



(b) Vo

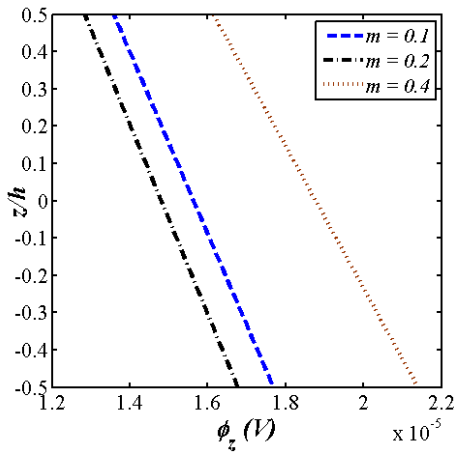


(c) V_x

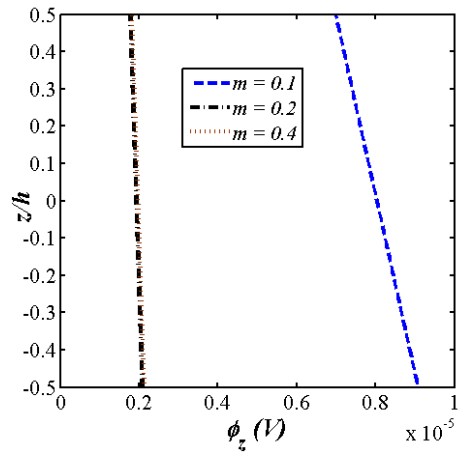


(d) V_v

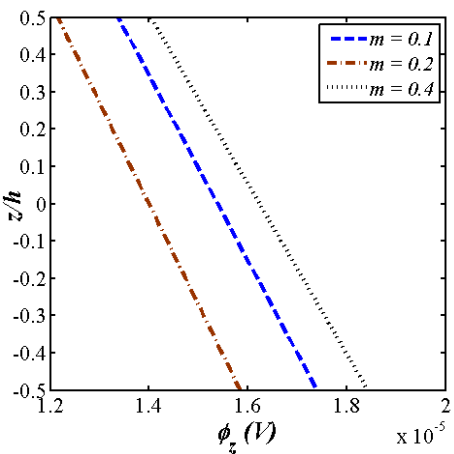
Figure 6.30: Effect of porosity volume on v ($\eta = 2$; $\alpha = 45^0$)



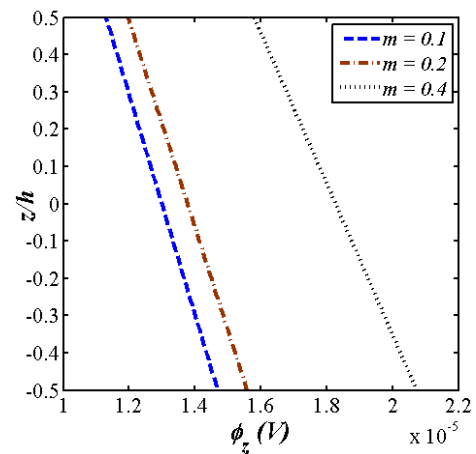
(a) V_u



(b) V_o

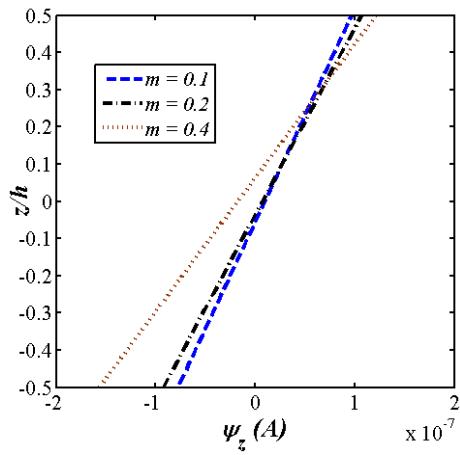


(c) V_x

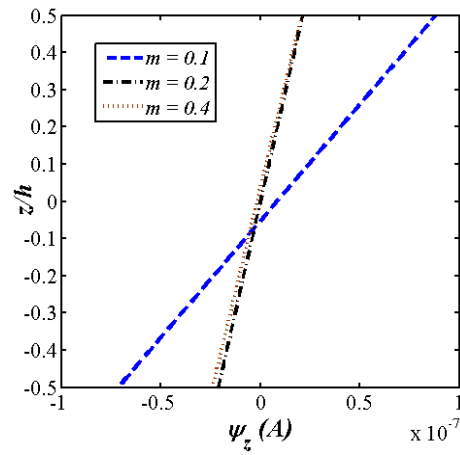


(d) V_v

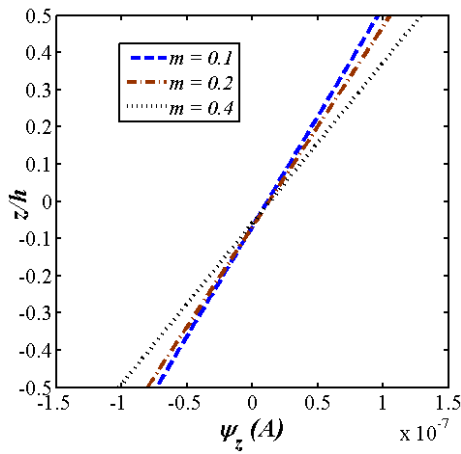
Figure 6.31: Effect of porosity volume on ϕ ($\eta = 2$; $\alpha = 45^0$)



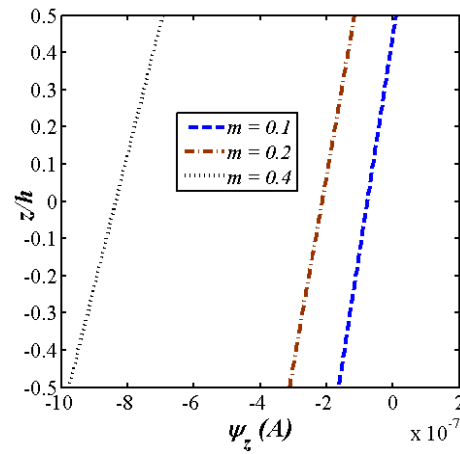
(a) V_u



(b) V_o

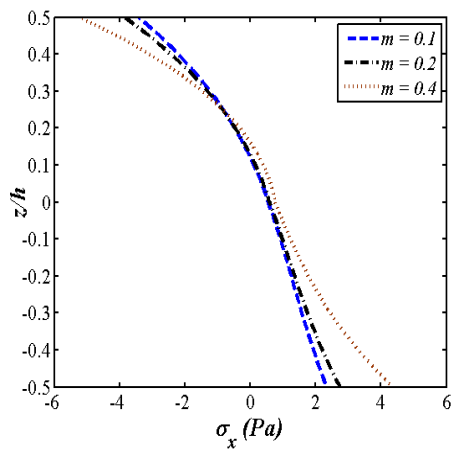


(c) V_x

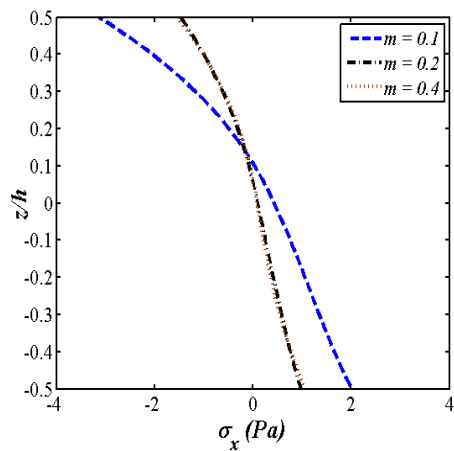


(d) V_v

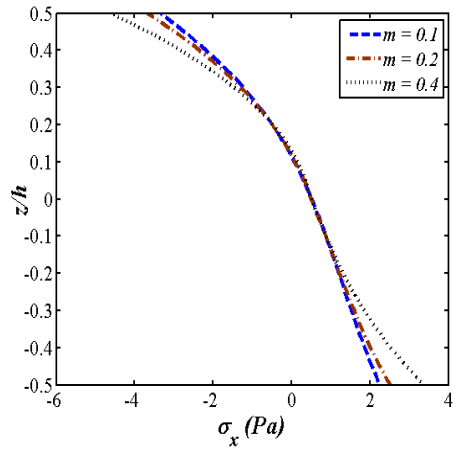
Figure 6.32: Effect of porosity volume on ψ ($\eta = 2$; $\alpha = 45^\circ$)



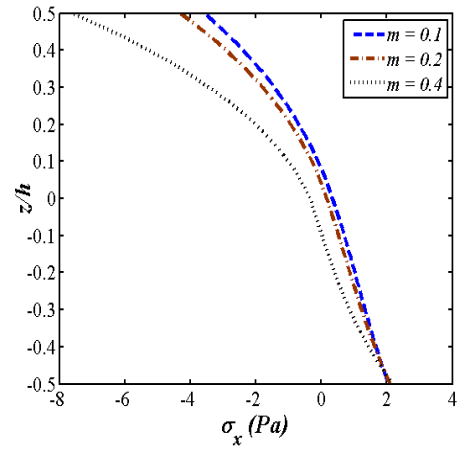
(a) V_u



(b) V_o

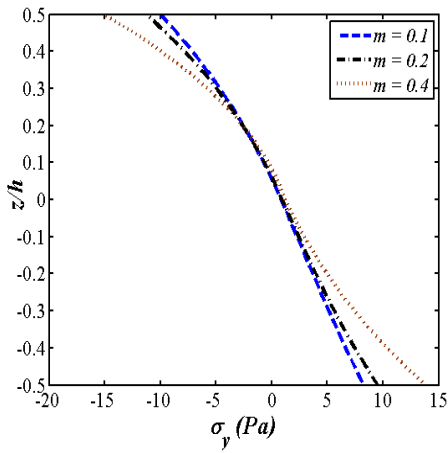


(c) V_x

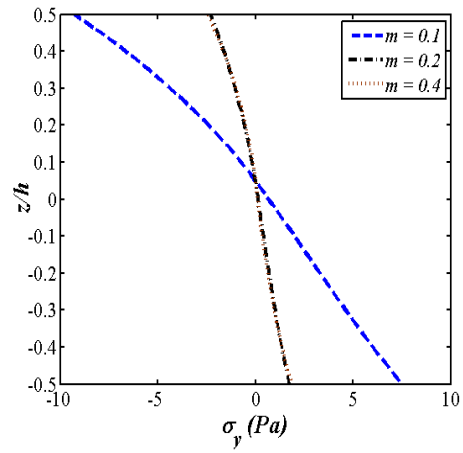


(d) V_v

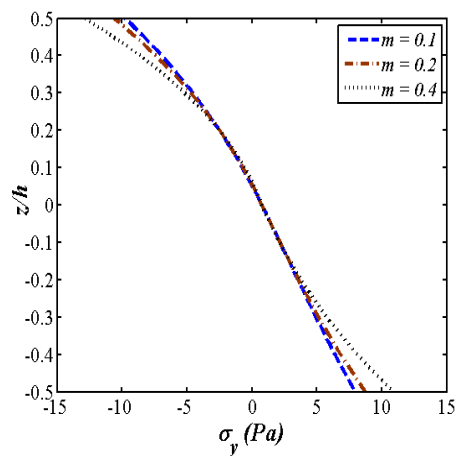
Figure 6.33: Effect of porosity volume on σ_x ($\eta = 2$; $\alpha = 45^\circ$)



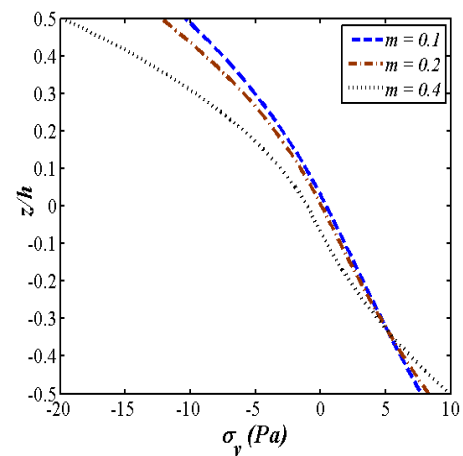
(a) V_u



(b) V_o

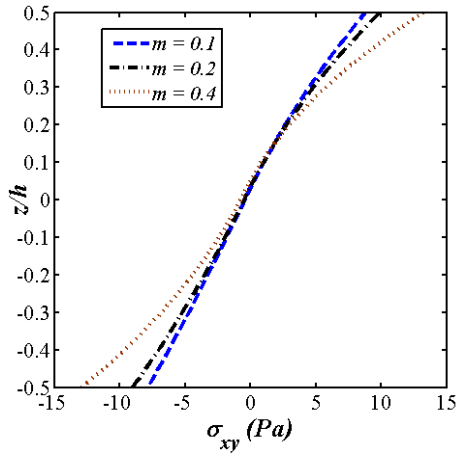


(c) V_x

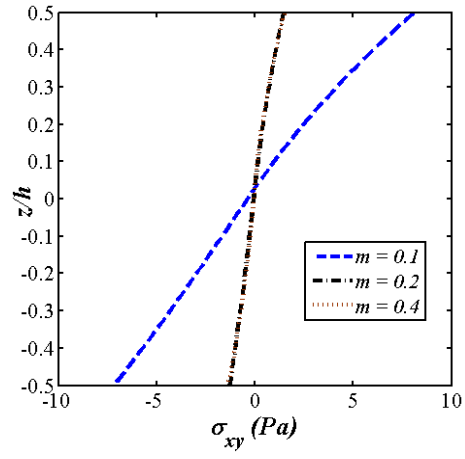


(d) V_v

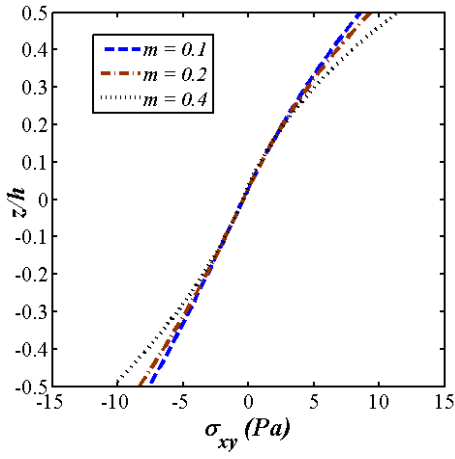
Figure 6.34: Effect of porosity volume on σ_y ($\eta = 2$; $\alpha = 45^\circ$)



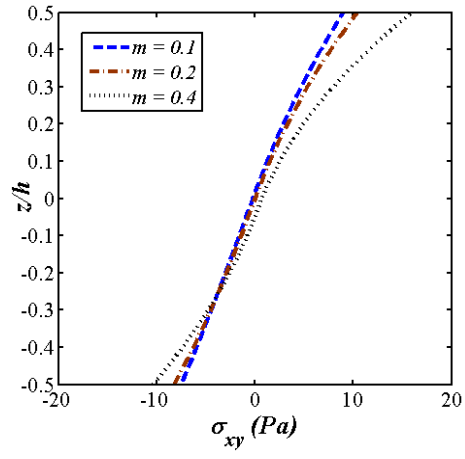
(a) V_u



(b) V_o

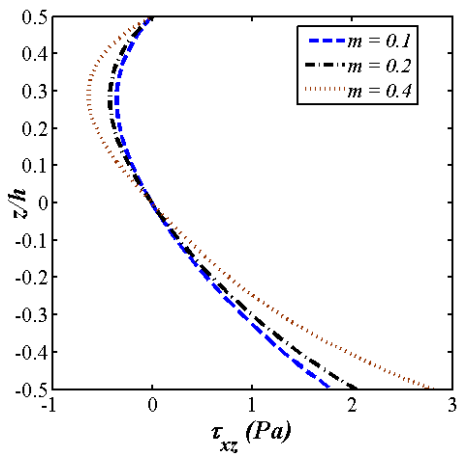


(c) V_x

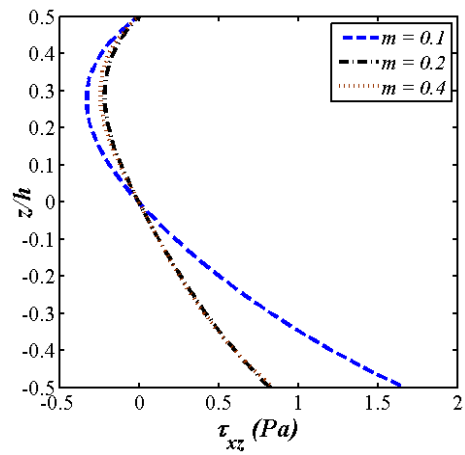


(d) V_v

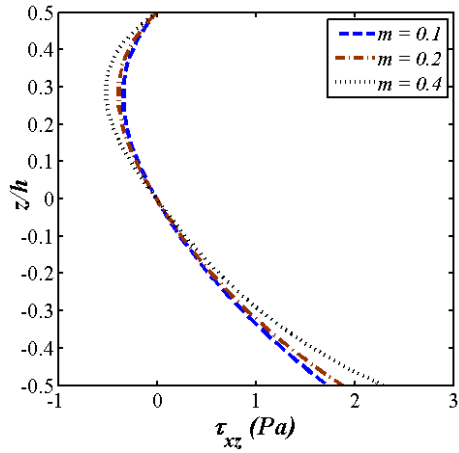
Figure 6.35: Effect of porosity volume on σ_{xy} ($\eta = 2$; $\alpha = 45^\circ$)



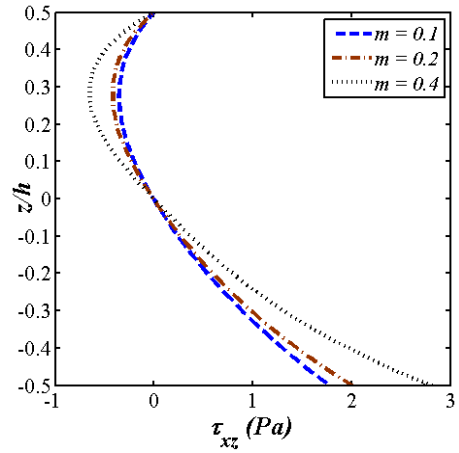
(a) V_u



(b) V_o

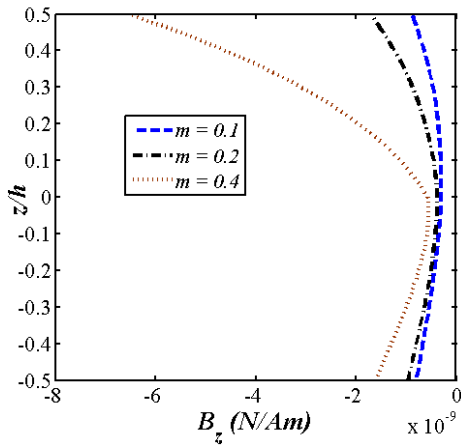


(c) V_x

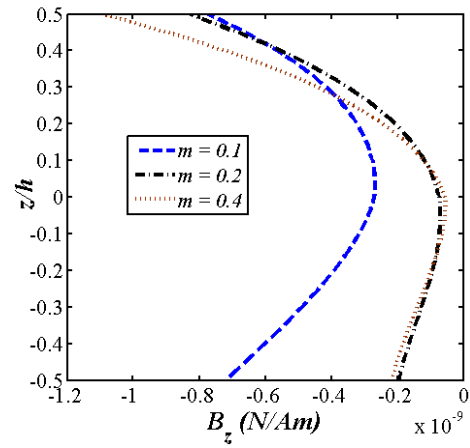


(d) V_v

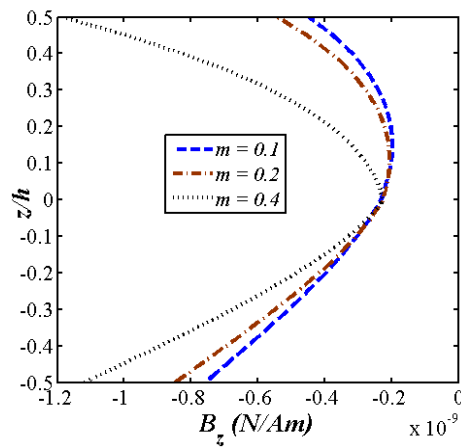
Figure 6.36: Effect of porosity volume on τ_{xz} ($\eta = 2$; $\alpha = 45^\circ$)



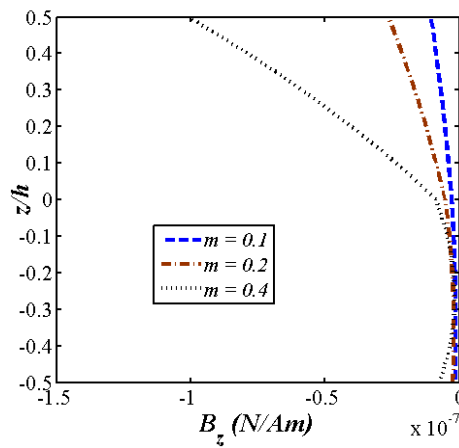
(a) V_u



(b) V_o



(c) V_x



(d) V_v

Figure 6.37: Effect of porosity volume on B_z ($\eta = 2$; $\alpha = 45^\circ$)

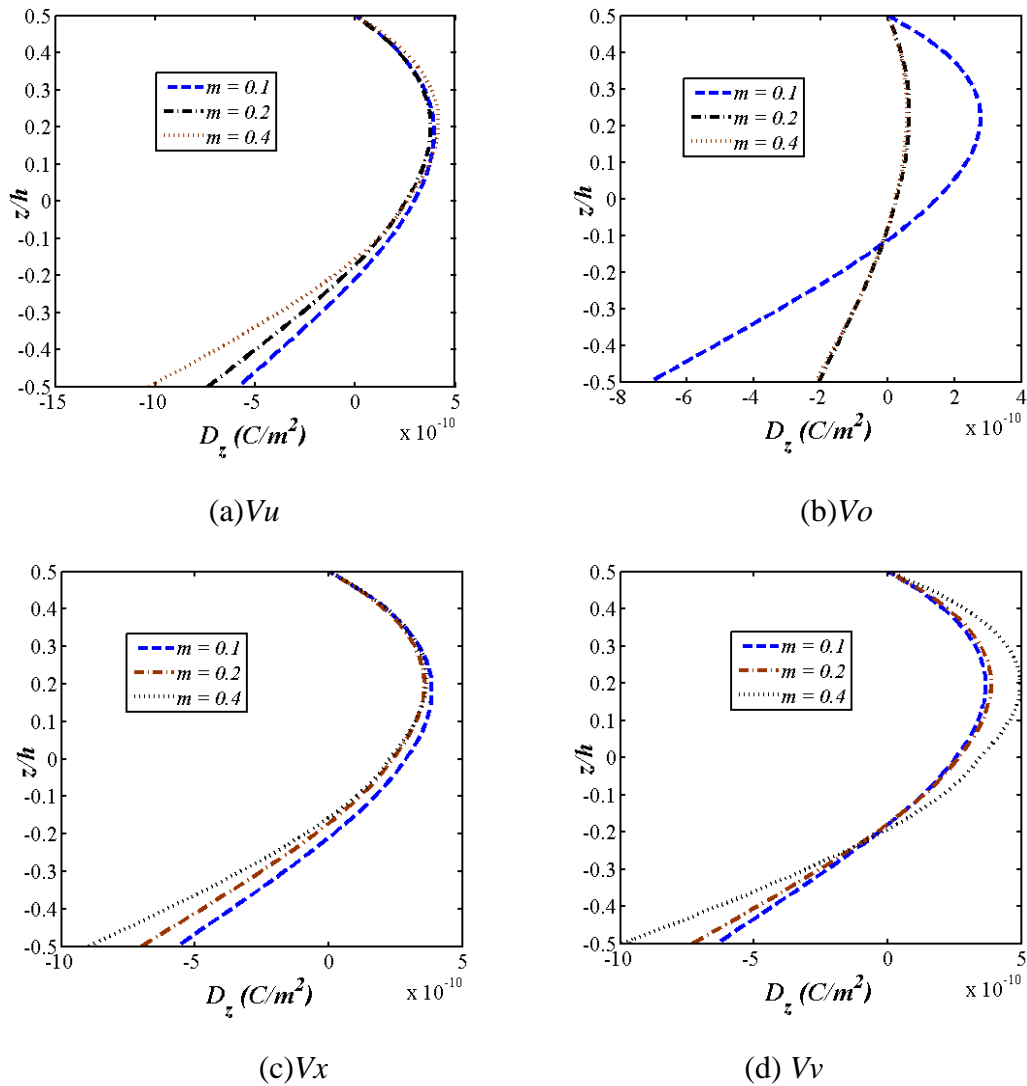


Figure 6.38: Effect of porosity volume on D_z ($\eta = 2$; $\alpha = 45^\circ$)

6.4. CONCLUSIONS

The static and free vibration responses of porous FGSMEE plate are studied using a finite element formulation. The porosity is accounted for local density and implemented using the modified power law. The influence of skew angle and porosity on the natural frequency of the FGMEE plate has been studied. The inclusion of porosity brings down the natural frequency in comparison with non-porous plates. The porosity distribution pattern Vo exhibits the least influence on the natural frequency while Vu displays the largest effect for all the skew angle of the FGSMEE plate. In addition, the increase in gradient index and porosity volume meagrely affects Vo distribution in the skew plate. The presence of larger porous density near to the top and the bottom surface significantly influences the free vibration behaviour of the plate. It is also observed that the increase in

thickness ratio increases the natural frequency while the increase in aspect ratio decreases the natural frequency.

The static studies reveal that the increase in skew angle decreases the u - and w -displacement and the porosity distribution V_v exhibits the largest displacement while the V_o has the lowest. The electric potential and the magnetic potential decrease with the increase in skew angle. The lowest electric potential is noticed for V_o and V_v porosity pattern, respectively. It is also observed that the porosity displays a negligible influence on the stresses, whereas the stress magnitude decreases with the increase in skew angle. The comparison study between porous and non-porous plate display the considerable influence of porosity on the structural characteristics of FGSME plate. Higher porosity volume results in higher displacements, potentials, stresses, magnetic induction, and electric displacement for V_u , V_x , and V_v porous skew plate.

Chapter 7

CONCLUSIONS AND FUTURE SCOPE

This chapter encapsulates the major outcomes of the present research work and the future possible improvements on the analysis of magneto-electro-elastic (MEE) skew structures.

7.1 Major findings

This dissertation deals with the analysis of geometrical changes and porosity on the structural behaviour of rectangular, skew multilayered and functionally graded skew magneto-electro-elastic plates. The finite element model has been developed using shear deformation theory to evaluate the structural behaviour of MEE, SMEE, and FGSMEE plates. The numerical analysis is carried out to investigate on the static, free vibration and buckling behaviour of multilayered rectangular and skew MEE plates. The significance of stacking sequence and geometrical parameters such as aspect ratio, width to thickness ratio, boundary conditions etc., on the buckling behaviour of MEE plates is well established. The buckling mode shapes are extensively drawn to understand and establish the plate buckling region. It is observed that the skew plate holds higher buckling strength over rectangular MEE plate and the stacking sequence displayed significant influence on the buckling characteristics of rectangular and skew multilayered MEE plate.

Further, the static responses and the natural frequencies of the SMEE plate are significantly influenced by changes in plate geometry in terms of skew edges. The aspect ratio, thickness ratio and the boundary conditions are found to be critical in assessment of static characteristics and free vibrations. The research has also been devoted for the structural behaviour assessment of skew functionally graded MEE plates. The functional variation of the material is considered along the thickness direction and the transformation matrix is established to account the skew edges of the plate. The present results reveal that the natural frequencies of the skew FGMEE plate increase with increase in skew angle.

Further analysis revealed that the variables corresponding to static behaviour such as displacement, potentials, stresses, electric displacement, and magnetic

induction are significantly influenced by geometrical changes (skew edges) of the plate. Special attention has been paid to consider the porosity defects in the FGSMEE plate. The porosity is accounted as local density via modified power law. Four porosity distributions are assumed and their influence on the structural behaviour of FGME plate is investigated. The influence of skew angle on the porous FGME plate is evaluated and considerable influence on static and free vibration characteristics is observed.

The major outcomes drawn from the present research work are outlined as follows:

1. The buckling strength and the natural frequency of the multilayered SMEE plate increases with increase in the skew angle. However, for $\alpha = 45^\circ$, the increase in natural frequency is rapid. This enrichment of frequency and buckling parameter is associated with the increase in the stiffness of the plate. This may be attributed to the reduction in parallel distance between the non skew edges with the increase in skew angle.
2. Under the biaxial compression, the critical buckling loads halved in comparison with uniaxial compression and their corresponding mode shapes are also affected by the type of compression applied. In addition, buckling load decreases with increase in aspect ratio and span to thickness ratio of the MEE plate.
3. The displacements and the electric potential for multilayered SMEE plate are lower at higher skew angles while the magnetic potential is higher for $\alpha = 45^\circ$.
4. The magnitude of the normal stresses and transverse shear stresses decreases with the increase in a skew angle which may be attributed to the increase in stiffness of the plate with increase in the skew angle.
5. The F/B/F SMEE plate exhibits higher buckling strength and natural frequency than the B/F/B SMEE plate. Further, the natural frequency decreases with the increase in power-law index values. It may be due to the higher concentration of CoFe_2O_4 in the F/B/F plate which leads to higher natural frequency.

6. The power-law index η exhibits major influence on the electric potential while its influence on the magnetic potential is minimal in the FGSMEE plate.
7. The porosity in FGSMEE plate brings down the natural frequency in comparison with non-porous plates.
8. The porosity distribution pattern V_u displays significant effect on the natural frequency of the FGMEE plate for all the skew angles while V_o exhibit the least influence on the natural frequency. This is due to the presence of larger porosity near the top and bottom surfaces of the V_u type distributions.
9. The increase in skew angle in the porous FGSMEE plate decreases the u -displacement. However, the porosity distribution V_v exhibits the largest displacement while the V_o distribution shows the least.
10. The electric potential and the magnetic potential for porous FGSMEE plate decreases with the increase in skew angle and the lowest electric potential and magnetic potential are noticed for V_o and V_v distributions, respectively.
11. The boundary condition, the aspect ratio, and the stacking sequence exhibit noticeable influence on the static fields, natural frequency, and buckling load.

7.2 Scope for the future work

The basic purpose of this Thesis has been fulfilled by the contributions presented in the preceding chapters of this dissertation. However, there is still scope for further research which facilitates the enhancement of performance of MEE smart structures. Among them, few possible future research scopes have been outlined as follows:

1. An experimental investigation of the influence of skew angle and the porosity on MEE plates holds a potential scope for research.
2. Analysis of buckling behaviour of skew nano-MEE plate using Erignan's theory will showcase the influence of non-local parameter on buckling behaviour.

Appendix:

The nodal strain-displacement matrices $[b_{bt}]$, $[b_{br}]$, $[b_{st}]$ and $[b_{sr}]$ appearing in the Eq. (2.20) are given by

$$[b_{bt}] = [b_{bt1} \ b_{bt2} \ b_{bt3} \ b_{bt4}], \quad [b_{br}] = [b_{br1} \ b_{br2} \ b_{br3} \ b_{br4}],$$

$$[b_{st}] = [b_{st1} \ b_{st2} \ b_{st3} \ b_{st4}] \quad \text{and} \quad [b_{sr}] = [b_{sr1} \ b_{sr2} \ b_{sr3} \ b_{sr4}]$$

The various sub-matrices $[b_{tbi}]$, $[b_{rbi}]$, $[b_{tsi}]$ and $[b_{rsi}]$ ($i = 1, 2, 3, 4$) are as follows

$$[b_{tbi}] = \begin{bmatrix} \frac{\partial n_i}{\partial x} & 0 & 0 \\ 0 & \frac{\partial n_i}{\partial y} & 0 \\ 0 & 0 & 0 \\ \frac{\partial n_i}{\partial y} & \frac{\partial n_i}{\partial x} & 0 \end{bmatrix}, \quad [b_{rbi}] = \begin{bmatrix} \frac{\partial n_i}{\partial x} & 0 \\ 0 & \frac{\partial n_i}{\partial y} \\ \frac{\partial n_i}{\partial y} & \frac{\partial n_i}{\partial x} \end{bmatrix}, \quad [b_{tsi}] = \begin{bmatrix} 0 & 0 & \frac{\partial n_i}{\partial x} \\ 0 & 0 & \frac{\partial n_i}{\partial y} \end{bmatrix} \quad \text{and} \quad [b_{rsi}] = \begin{bmatrix} n_i & 0 \\ 0 & n_i \end{bmatrix}.$$

Similarly, the nodal strain-displacement matrices $[b_{tb}]$, $[b_{rb}]$, $[b_{ts}]$ and $[b_{rs}]$ corresponding to chapter 3 are given by

$$[b_{tb}] = [b_{tb1} \ b_{tb2} \ \dots \ b_{tb8}], \quad [b_{rb}] = [b_{rb1} \ b_{rb2} \ \dots \ b_{rb8}],$$

$$[b_{ts}] = [b_{ts1} \ b_{ts2} \ \dots \ b_{ts8}] \quad \text{and} \quad [b_{rs}] = [b_{rs1} \ b_{rs2} \ \dots \ b_{rs8}]$$

The various sub-matrices $[b_{tbi}]$, $[b_{rbi}]$, $[b_{tsi}]$ and $[b_{rsi}]$ ($i = 1, 2, 3, \dots, 8$) are as follows

$$[b_{tbi}] = \begin{bmatrix} \frac{\partial n_i}{\partial x} & 0 & 0 \\ 0 & \frac{\partial n_i}{\partial y} & 0 \\ \frac{\partial n_i}{\partial y} & \frac{\partial n_i}{\partial x} & 0 \end{bmatrix}; \quad [b_{tsi}] = \begin{bmatrix} 0 & 0 & \frac{\partial n_i}{\partial x} \\ 0 & 0 & \frac{\partial n_i}{\partial y} \end{bmatrix};$$

$$[b_{rbi}] = \begin{bmatrix} \frac{\partial n_i}{\partial x} & 0 & 0 & 0 \\ 0 & \frac{\partial n_i}{\partial y} & 0 & 0 \\ \frac{\partial n_i}{\partial y} & \frac{\partial n_i}{\partial x} & 0 & 0 \\ 0 & 0 & n_i & 0 \\ 0 & 0 & 0 & n_i \end{bmatrix}; \quad [b_{rsi}] = \begin{bmatrix} n_i & 0 & 0 & 0 \\ 0 & n_i & 0 & 0 \\ 0 & 0 & \frac{\partial n_i}{\partial x} & 0 \\ 0 & 0 & \frac{\partial n_i}{\partial y} & 0 \\ 0 & 0 & 0 & \frac{\partial n_i}{\partial x} \\ 0 & 0 & 0 & \frac{\partial n_i}{\partial y} \end{bmatrix}$$

REFERENCES

- Aboudi, J., (2018). “The transient response of multiferroic composites”. *International Journal of Engineering Science*, **124**, 64-84.
- Adineh, M., Kadkhodayan, M. (2017). “Three-dimensional thermo-elastic analysis and dynamic response of a multi-directional functionally graded skew plate on elastic foundation”. *Composites Part B: Engineering*, **125**, 227-240.
- Ahmed, A. and Kapuria, S. (2017). “Third order theory based quadrilateral element for delaminated composite plates with a hybrid method for satisfying continuity at delamination fronts”. *Composite Structures*, **181**, 84-95.
- Alaimo, A., Milazzo, A. and Orlando, C. (2013). “A four-node MITC finite element for magneto-electro-elastic multilayered plates.” *Computers and Structures*, **129**, 120-33.
- Alibeigi, B., Beni, Y.T. and Mehralian, F. (2018). “On the thermal buckling of magneto-electro-elastic piezoelectric nanobeams”. *The European Physical Journal Plus*, **133**(3), p.133.
- Annigeri, A.R., Ganesan, N. and Swarnamani, S. (2006a). “Free vibrations of clamped–clamped magneto-electro-elastic cylindrical shells”. *Journal of Sound and Vibration*, **292**(1), 300-314.
- Annigeri, A.R., Ganesan, N. and Swarnamani, S. (2006b). “Free vibrations of simply supported layered and multiphase magneto-electro-elastic cylindrical shells. *Smart Materials and Structures*, **15**(2), 459.
- Annigeri, A.R., Ganesan, N. and Swarnamani, S. (2007). “Free vibration behaviour of multiphase and layered magneto-electro-elastic beam”. *Journal of Sound and Vibration*, **299**(1), 44-63.
- Ansari, R., Hasrati, E., Gholami, R. and Sadeghi, F. (2015a). “Nonlinear analysis of forced vibration of nonlocal third-order shear deformable beam model of magneto–electro–thermo elastic nanobeams”. *Composites Part B: Engineering*, **83**, 226-241.
- Ansari, R., Gholami, R. and Rouhi, H. (2015b). “Size-dependent nonlinear forced vibration analysis of magneto-electro-thermo-elastic Timoshenko nanobeams based upon the nonlocal elasticity theory”. *Composite Structures*, **126**, 216-226.

- Ansari, R and Gholami, R. (2016). "Size-dependent buckling and postbuckling analyses of first-order shear deformable magneto-electro-thermo elastic nanoplates based on the nonlocal elasticity theory." *International Journal of Structural Stability and Dynamics*, **10**, 1750014 (26 pp).
- Ansari, R. and Gholami, R. (2016a). Nonlocal free vibration in the pre-and post-buckled states of magneto-electro-thermo elastic rectangular nanoplates with various edge conditions. *Smart Materials and Structures*, **25**(9), 095033.
- Ansari, R. and Gholami, R., (2016b). "Nonlocal nonlinear first-order shear deformable beam model for post-buckling analysis of magneto-electro-thermo-elastic nanobeams". *Scientia Iranica. Transaction F, Nanotechnology*, **23**(6), 3099.
- Ansari, R. and Gholami, R. (2016c). "Size-dependent nonlinear vibrations of first-order shear deformable magneto-electro-thermo elastic nanoplates based on the nonlocal elasticity theory". *International Journal of Applied Mechanics*, **8**(4), 1650053.
- Ardestani, M.M., Zhang, L.W., Liew, K.M. (2017). "Isogeometric analysis of the effect of CNT orientation on the static and vibration behaviors of CNT-reinforced skew composite plates. *Computer Methods in Applied Mechanics and Engineering*, **317**, 341-379.
- Asemi, K., Sattar, J. S., Manouchehr, S. and Mojtaba, S. (2014). "Dynamic and static analysis of FGM skew plates with 3d elasticity based graded finite element modelling." *Latin American Journal of Solids and Structures*, **11**, 504 – 533
- Ashour, A. S. (2009). "The free vibration of symmetrically angle-ply laminated fully clamped skew plates." *Journal of Sound and Vibration*, **323**(1-2), 444-450.
- Azam, M.S., Ranjan, V. and Kumar, B. (2017). "Free Vibration Analysis of Rhombic Plate with Central Crack". *International Journal of Acoustics & Vibration*, **22**(4).
- B**abu, S. C. and Kant, T. (1999). "Two shear deformable finite element models for buckling analysis of skew fibre-reinforced composite and sandwich panels." *Composite Structures*, **46**(2), 115-124.
- Babaei, M.H. and Chen, Z.T. (2008). "Analytical solution for the electromechanical behaviour of a rotating functionally graded piezoelectric hollow shaft". *Archive of Applied Mechanics*, **78**(7), 489-500.

- Badri, T.M. and Al-Kayiem, H.H. (2013). “Analytical solution for simply supported and multilayered Magneto-Electro-Elastic Plates”. *Asian journal of scientific research*, **6**, 236-244.
- Barandiaran, J. M., Kurlyandskaya, G. V., de Cos D., García-Arribas, A. and Vas’kovskiy, V. O. (2009 b). “Multilayer magnetoimpedance sensor for nondestructive testing”. *Sensor Letters*, **7**, 374–377.
- Barati, M.R., Shahverdi, H. (2017). “Aero-hygro-thermal stability analysis of higher-order refined supersonic FGM panels with even and uneven porosity distributions”. *Journal of Fluids and Structures*, **73**, 125-136.
- Barati, M.R., Shahverdi, H., Zenkour, A.M. (2017). “Electro-mechanical vibration of smart piezoelectric FG plates with porosities according to a refined four-variable theory”. *Mechanics of Advanced Materials and Structures*, **24**(12), 987-998.
- Bhangale, R.K. and Ganesan, N. (2005). “Free vibration studies of simply supported non-homogeneous functionally graded magneto-electro-elastic finite cylindrical shells”. *Journal of Sound and Vibration*, **288**(1), 412-422.
- Bhangale, R.K. and Ganesan, N. (2006). “Static analysis of simply supported functionally graded and layered magneto-electro-elastic plates”. *International Journal of Solids and Structures*, **43**(10), 3230-3253.
- Biju, B., Ganesan, N. and Shankar, K. (2009). “Finite element formulation using magnetic vector potential approach: effects of displacement current in magneto-electro-elastic cylindrical shells”. *Smart Materials and Structures*, **19**(1), 015009.
- Biju, B., Ganesan, N. and Shankar, K. (2010). “Harmonic Response of Magneto-electro-elastic Sensors Bonded to Cylindrical Shells”. *Sensors & Transducers*, **116**(5), 89.
- Biju, B., Ganesan, N. and Shankar, K. (2011). “Dynamic response of multiphase magneto-electroelastic sensors using 3D magnetic vector potential approach”. *IEEE Sensors Journal*, **11**(9), 2169-2176.
- Biju, B., Ganesan, N. and Shankar, K. (2012). “Dynamic analysis of magneto-electro-elastic cylindrical shells by quasi-static and fully dynamic electromagnetic theories”. *Multidiscipline Modeling in Materials and Structures*, **8**(3), 403-416.

- Boomgaard, V. J. and Born, R. A. (1978), “Sintered magnetoelectric composite material BaTiO₃-Ni (Co, Mn)Fe₂O₄”. *Journal of Materials Science*, **13**(7), 1538-48.
- Buchanan, G. R. (2004). “Layered versus multiphase magneto-electro-elastic composites.” *Composites Part B-Engineering*, **35**(5), 413–420.
- Butalia, T. S., Kant, T. and Dixit, V. D. (1990). “Performance of Heterosis Element for Bending of Skew Rhombic Plates.” *Computers and Structures*, **34**, 23-49.
- Carman, G.P., Cheung, K.S. and Wang, D. (1995). “Micro-mechanical model of a composite containing a conservative nonlinear electro-magneto-thermo-mechanical material”. *Journal of Intelligent Material Systems and Structures*, **6**(5), 691-699.
- Carrera, E., Brischetto, S., Fagiano, C. and Nali, P. (2009). “Mixed multilayered plate elements for coupled magneto-electro-elastic analysis”. *Multidiscipline Modeling in Materials and Structures*, **5**(3), 251-256.
- Chang, T.P., (2013). “On the natural frequency of transversely isotropic magneto-electro-elastic plates in contact with fluid”. *Applied Mathematical Modeling*, **37**(4), 2503-2515.
- Chakraverty, S. and Pradhan, K.K. (2018). “Flexural vibration of functionally graded thin skew plates resting on elastic foundations”. *International Journal of Dynamics and Control*, **6**(1), 97-121.
- Chen, J.Y., Heyliger, P.R. and Pan, E. (2014). “Free vibration of three-dimensional multilayered magneto-electro-elastic plates under combined clamped/free boundary conditions”. *Journal of Sound and Vibration*, **333**(17), 4017-4029.
- Chen, W.Q., Lee, K.Y. and Ding, H.J. (2005). “On free vibration of non-homogeneous transversely isotropic magneto-electro-elastic plates”. *Journal of Sound and Vibration*, **279** (1), 237-251.
- Chen, J., Chen, H., Pan, E. and Heyliger, P.R. (2007). “Modal analysis of magneto-electro-elastic plates using the state-vector approach”. *Journal of Sound and Vibration*, **304**(3), 722-734.
- Cook, A.C. and Vel, S.S. (2013). “Multiscale thermopiezoelectric analysis of laminated plates with integrated piezoelectric fiber composites”. *European Journal of Mechanics-A/Solids*, **40**, 11-33.

- D**aga, A., Ganesan, N. and Shankar, K. (2008). “Transient response of magneto-electro-elastic simply supported cylinder using finite element”. *Journal of Mechanics of Materials and Structures*, **3**(2), 375-389.
- Daga, A., Ganesan, N. and Shankar, K. (2009a). “Behaviour of magneto-electro-elastic sensors under transient mechanical loading”. *Sensors and Actuators A: Physical*, **150**(1), 46-55.
- Daga, A., Ganesan, N. and Shankar, K. (2009b). “Transient dynamic response of cantilever magneto-electro-elastic beam using finite elements”. *International Journal for Computational Methods in Engineering Science and Mechanics*, **10**(3), 173-185.
- Dai, H.L., Hong, L., Fu, Y.M. and Xiao, X. (2010). “Analytical solution for electromagnetoelastoelectric behaviours of a functionally graded piezoelectric hollow cylinder”. *Applied Mathematical Modelling*, **34**(2), 343-357.
- Dai, T. and Dai, H.L. (2017). “Analysis of a rotating FGMEE circular disk with variable thickness under thermal environment”. *Applied Mathematical Modeling*, **45**, 900-924.
- Davi, G. and Milazzo, A. (2011). “A regular variational boundary model for free vibrations of magneto-electro-elastic structures”. *Engineering Analysis with Boundary Elements*, **35**(3), 303-312.
- Dong, C.Y. (2008). “Vibration of electro-elastic versus magneto-elastic circular/annular plates using the Chebyshev–Ritz method”. *Journal of Sound and Vibration*, **317**(1), 219-235.
- E**brahimi, F., Naei, M. H., Rastgoo, A. (2009), “Geometrically nonlinear vibration analysis of piezoelectrically actuated FGM plate with an initial large deformation”. *Journal of Mechanical Science and Technology*, **23** (8), 2107–2124.
- Ebrahimi, F and Mohammad, R. B. (2016). “Static stability analysis of smart magneto-electro-elastic heterogeneous nanoplates embedded in an elastic medium based on a four-variable refined plate theory.” *Smart Materials and Structures*, **25**, 105014 (21pp)
- Ebrahimi, F. and Barati, M.R., (2016a). “An exact solution for buckling analysis of embedded piezoelectro-magnetically actuated nanoscale beams”. *Advanced Nano Research*, **4**(2), 65-84.

- Ebrahimi, F. and Barati, M.R. (2016b). "Temperature distribution effects on buckling behaviour of smart heterogeneous nanosize plates based on nonlocal four-variable refined plate theory". *International Journal of Smart and Nano Materials*, 7(3), 119-143.
- Ebrahimi, F. and Barati, M.R. (2016c). "Buckling analysis of smart size-dependent higher order magneto-electro-thermo-elastic functionally graded nanosize beams". *Journal of Mechanics*, **33**(1), 23-33.
- Ebrahimi, F. and Barati, M.R. (2016d). "Electromechanical buckling behaviour of smart piezoelectrically actuated higher-order size-dependent graded nanoscale beams in thermal environment". *International Journal of Smart and Nano Materials*, 7(2), 69-90.
- Ebrahimi, F. and Barati, M.R. (2016e). "A unified formulation for dynamic analysis of nonlocal heterogeneous nanobeams in hygro-thermal environment". *Applied Physics A*, **122**(9), 792.
- Ebrahimi, F. and Barati, M.R. (2016f). "Dynamic modeling of a thermo-piezo-electrically actuated nanosize beam subjected to a magnetic field". *Applied Physics A*, **122**(4), 451.
- Ebrahimi, F., Barati, M.R. (2017). "Porosity-dependent vibration analysis of piezo-magnetically actuated heterogeneous nanobeams". *Mechanical Systems and Signal Processing*, **93**, 445-459.
- Ebrahimi, F., Jafari, A., Barati, M.R. (2017). "Vibration analysis of magneto-electro-elastic heterogeneous porous material plates resting on elastic foundations". *Thin-Walled Structures*, **119**, 33-46.
- Ebrahimi, F., Jafari, A., Barati, M.R. (2017). "Free vibration analysis of smart porous plates subjected to various physical fields considering neutral surface position". *Arabian Journal of Science and Engineering*, **42**(5), 1865-1881.
- Ebrahimi, F. and Barati, M.R. (2017). "Buckling analysis of piezoelectrically actuated smart nanoscale plates subjected to magnetic field". *Journal of Intelligent Material Systems and Structures*, **28**(11), 1472-1490.
- F**arajpour, A., Yazdi, M.H., Rastgoo, A., Loghmani, M. and Mohammadi, M. (2016). "Nonlocal nonlinear plate model for large amplitude vibration of magneto-electro-elastic nanoplates". *Composite Structures*, **140**, 323-336.

Farajpour, A. and Rastgoo, A. (2017). “Size-dependent static stability of magneto-electro-elastic CNT/MT-based composite nanoshells under external electric and magnetic fields”. *Microsystem Technologies*, **23**(12), 5815-5832.

Farajpour, A., Rastgoo, A. and Farajpour, M.R. (2017). “Nonlinear buckling analysis of magneto-electro-elastic CNT-MT hybrid nanoshells based on the nonlocal continuum mechanics”. *Composite Structures*, **180**, 179-191.

García-Arribas, A., Gutiérrez, J., Kurlyandskaya, G. V., Barandiarán, J. M., Svalov, A., Fernández, E. and Bravo-Imaz, I. (2014). “Sensor applications of soft magnetic materials based on magneto-impedance, magneto-elastic resonance and magneto-electricity.” *Sensors (Basel)*, **14**(5), 7602–7624.

García-Macías, E., Castro-Triguero, R., Flores, E.I.S., Friswell, M.I. and Gallego, R. (2016). “Static and free vibration analysis of functionally graded carbon nanotube reinforced skew plates”. *Composite Structures*, **140**, 473-490.

Garg A. K., Khare, R. K. and Kant, T. (2006). “Free vibration of skew fiber-reinforced composite and sandwich laminates using a shear deformable finite element model.” *Journal of Sandwich Structures and Materials*, **8**, 33-53.

Grover, N., Maiti, D. K., and Singh, B. N. (2014). “An efficient C^0 finite element modeling of an inverse hyperbolic shear deformation theory for the flexural and stability analysis of laminated composite and sandwich plates.” *Finite Elements in Analysis and Design*, **80**, 11–22.

Haitao, D., Wei, C. and Mingzhi, L. (2008). “Static/dynamic analysis of functionally graded and layered magneto-electro-elastic plate/pipe under Hamiltonian system”. *Chinese Journal of Aeronautics*, **21**(1), 35-42.

Heshmati, M. and Daneshmand, F. (2018). A study on the vibrational properties of weight-efficient plates made of material with functionally graded porosity. *Composite Structures*, **200**, 229-238.

Heyliger, P.R. and Pan, E. (2004). “Static fields in magneto-electroelastic laminates”. *The American Institute of Aeronautics and Astronautics Journal*, **42**(7), 1435 – 1443.

- Houmat, A. (2015). "Nonlinear free vibration analysis of variable stiffness symmetric skew laminates." *European Journal of Mechanics-A/Solids*, **50**, 70–75.
- Huang, D.J., Ding, H.J. and Chen, W.Q. (2007). "Analytical solution for functionally graded magneto-electro-elastic plane beams". *International Journal of Engineering Science*, **45**(2), 467-485.
- Hu, H. T., Yang, C. H., and Lin, F. M. (2006). "Buckling analyses of composite laminate skew plates with material nonlinearity". *Composites Part B-Engineering*, **37**(1), 26 –36.
- Hu, H. T. and Tzeng, W. L. (2000). "Buckling analysis of skew laminate plates subjected to uniaxial inplane loads." *Thin Walled Structures*, **38**(1), 53 –77.
- Huang, D.J., Ding, H.J. and Chen, W.Q. (2010). "Static analysis of anisotropic functionally graded magneto-electro-elastic beams subjected to arbitrary loading". *European Journal of Mechanics-A/Solids*, **29**(3), 356-369.
- J**abbari, M. and Barati, A.R. (2015). "Analytical Solution for the Thermopiezoelectric Behaviour of a Smart Functionally Graded Material Hollow Sphere Under Radially Symmetric Loadings". *Journal of Pressure Vessel Technology*, **137**(6), 061204.
- Jafari, N. and Azhari, M. (2017). "Bending Analysis of Moderately Thick Arbitrarily Shaped Plates with Point Supports Using Simple Hp Cloud Method". *Iranian Journal of Science and Technology, Transactions of Civil Engineering*, **41**(4), 361-371.
- Jamalpoor, A., Ahmadi-Savadkoobi, A. and Hosseini-Hashemi, S. (2016). "Free vibration and biaxial buckling analysis of magneto-electro-elastic microplate resting on visco-Pasternak substrate via modified strain gradient theory". *Smart Materials and Structures*, **25**(10), 105035.
- Jandaghian, A.A. and Rahmani, O. (2016). "Free vibration analysis of magneto-electro-thermo-elastic nanobeams resting on a Pasternak foundation". *Smart Materials and Structures*, **25**(3), 035023.
- Jian, A. and Ding, H. (2007). "Analytical solutions for density functionally gradient magneto-electro-elastic cantilever beams". *Smart Structures and Systems*, **3**(2), 173-188.
- Jiang, J.P. and Li, D.X. (2007). "A new finite element model for piezothermoelastic composite beam". *Journal of Sound and Vibration*, **306**(3), 849-864.

- Jiangyi, C., Hualing, C. and Ernian, P. (2006). “Free vibration of functionally graded, magneto-electro-elastic, and multilayered plates”. *Acta Mechanica Solida Sinica*, **19**(2), 160-166.
- Joodaky, A. and Joodaky, I. (2015). “A semi-analytical study on static behavior of thin skew plates on Winkler and Pasternak foundations”. *International Journal of Mechanical Sciences*, **100**, 322-327.
- K**amali, M., Shamsi, M. and Saidi, A.R. (2018). “Postbuckling of magneto-electro-elastic CNT-MT composite nanotubes resting on a nonlinear elastic medium in a non-uniform thermal environment”. *The European Physical Journal Plus*, **133**(3), p.110.
- Kanasogi, R. M. and Ray, M. C. (2013). “Active constrained layer damping of smart skew laminated composite plates using 1–3 piezoelectric composites”. *Journal of Composites*, Doi:10.1155/2013/824163.
- Kattimani, S.C. and Ray, M.C. (2014a). “Smart damping of geometrically nonlinear vibrations of magneto-electro-elastic plates.” *Composite Structures*, **114**(1), 51–63.
- Kattimani, S.C. and Ray, M.C. (2014b). “Active control of large amplitude vibrations of smart magneto – electro – elastic doubly curved shells.” *International Journal of Mechanics and Materials in Design*, **10**(4), 351–378.
- Kattimani, S.C. and Ray, M.C. (2015). “Control of geometrically nonlinear vibrations of functionally graded magneto-electro-elastic plates.” *International Journal of Mechanical Sciences*, **99**, 154–167.
- Kattimani, S.C. (2017a). “Geometrically nonlinear vibration analysis of multiferroic composite plates and shells.” *Composite Structures*, **163**, 185-194.
- Kattimani, S.C. (2017b). “Active damping of multiferroic composite plates using 1-3 Piezoelectric composites”. *Smart Materials and Structures*, **26**(12), 125021.
- Khor, K.A., Gu, Y.W. (2000). “Effects of residual stress on the performance of plasma sprayed functionally graded $ZrO_2/NiCoCrAlY$ coatings”. *Material Science and Engineering: A*, **277**(1), 64-76.
- Kiani, Y. (2016). “Free vibration of FG-CNT reinforced composite skew plates”. *Aerospace Science and Technology*, **58**, 178-188.

- Kiani, A., Sheikhhoshkar, M., Jamalpoor, A. and Khanzadi, M. (2018). “Free vibration problem of embedded magneto-electro-thermo-elastic nanoplate made of functionally graded materials via nonlocal third-order shear deformation theory”. *Journal of Intelligent Material Systems and Structures*, **29**(5), 741-763.
- Koma, Y. A. and Zimcik, D. G. (2003). “Applications of Smart Structures to Aircraft for Performance Enhancement.” *Canadian Aeronautics and Space Journal*, **49**(4), 163-172.
- Kulikov, G.M. and Plotnikova, S.V. (2017). “An analytical approach to three-dimensional coupled thermoelectroelastic analysis of functionally graded piezoelectric plates”. *Journal of Intelligent Material Systems and Structures*, **28**(4), 435-450.
- Kumar, R.S. and Ray, M.C. (2013). “Active control of geometrically nonlinear vibrations of doubly curved smart sandwich shells using 1–3 piezoelectric composites”. *Composite Structures*, **105**, 173-187.
- Kumar, A., Panda, S. K., and Kumar, R. (2015). “Buckling behaviour of laminated composite skew plates with various boundary conditions subjected to linearly varying in-plane edge loading.” *International Journal of Mechanical Sciences*, **100**, 136–144.
- Kumar, A.M.S., Panda, S. and Chakraborty, D. (2016). “Piezo-viscoelastically damped nonlinear frequency response of functionally graded plates with a heated plate-surface”. *Journal of Vibration and Control*, **22**(2), 320-343.
- Kumar, R., Mondal, S., Guchhait, S., Jamatia, R. (2017). “Analytical Approach for Dynamic Instability Analysis of Functionally Graded Skew Plate under Periodic Axial Compression”. *International Journal of Mechanical Sciences*, **130**. 41-51.
- Kumaravel, A., Ganesan N and Sethuraman, R. (2007). “Steady-state analysis of a three-layered electro-magneto-elastic strip in a thermal environment. *Smart Materials and Structures*, **16**(2), 282–295.
- Kumaravel, A., Ganesan, N. and Sethuraman, R. (2007). “Buckling and vibration analysis of layered and multiphase magneto-electro-elastic beam under thermal environment”. *Multidiscipline Modeling in Materials and Structures*, **3**(4), 461-476.

- Kumaravel, A., Ganesan, N. and Sethuraman, R. (2010). “Buckling and vibration analysis of layered and multiphase magneto-electro-elastic cylinders subjected to uniform thermal loading”. *Multidiscipline Modeling in Materials and Structures*, **6**(4), 475-492.
- Kurlyandskaya, G. V., deCos, D. and Volchkov, S. O. (2009 a). “Magneto-sensitive transducers for nondestructive testing operating on the basis of the giant magnetoimpedance effect: a review” *Russian Journal of Non-destructive Testing*, **45**, 377–98.
- Kuang, Z.B. (2011). “Physical variational principle and thin plate theory in electro-magneto-elastic analysis”. *International journal of solids and structures*, **48**(2), 317-325.
- Kuang, Z.B. (2014). “An applied electro-magneto-elastic thin plate theory”. *Acta Mechanica*, **225**(4-5), 1153-1166.
- Lage, R.G., Soares, C.M., Soares, C.M. and Reddy, J.N. (2004). “Layerwise partial mixed finite element analysis of magneto-electro-elastic plates”. *Computers & Structures*, **82**(17), 1293-1301.
- Liew, K. M. and Wang, C. M. (1993). “Vibration Studies on Skew Plates: Treatment of Internal Line Supports. *Computers and Structures*, **49**,941-951.
- Li, Y.S., Ma, P. and Wang, W. (2016). “Bending, buckling, and free vibration of magneto-electro-elastic nanobeam based on nonlocal theory”. *Journal of Intelligent Material Systems and Structures*, **27**(9), 1139-1149.
- Liu, M.F. (2011). “An exact deformation analysis for the magneto-electro-elastic fiber-reinforced thin plate”. *Applied Mathematical Modelling*, **35**(5), 2443-2461.
- Li, Y. S. and Zhang, J. (2014). “Free vibration analysis of magneto-electro-elastic plate resting on a Pasternak foundation.” *Smart Materials and Structures*, **23**, 025002 (9pp).
- Li, Y. S., Cai, Z. Y. and Shi, S. Y. (2014). “Buckling and free vibration of magneto-electro-elastic nanoplate based on nonlocal theory.” *Composite Structures*, **111**(1), 522–529.
- Luccioni, L. X. and Dong, S. B. (1998). “Levy-type finite element analyses of vibration and stability of thin and thick laminated composite rectangular plates, *Composites Part B-Engineering*, **29**, 459-475.

- Mandal, A., Ray, C. and Halder, S. (2017). ‘Free vibration analysis of laminated composite skew plates with cut-out’. *Archive of Applied Mechanics*, **87**(9), 1511-1523.
- McGee, O. G., Graves, W. D., Butalia, T. S. and Owings, M. I. (1994). “Natural vibrations of shear deformable rhombic plates with clamped and free edge conditions”. *Computers and Structures*, **53**, 679-694.
- Miehe, C., Vallicotti, D. and Teichtmeister, S. (2016). “Homogenization and multiscale stability analysis in finite magneto-electro-elasticity. Application to soft matter EE, ME and MEE composites”. *Computer Methods in Applied Mechanics and Engineering*, **300**, 294-346.
- Milazzo, A. Orlando, C. and Alaimo, A. (2009). "An analytical solution for the magneto-electro-elastic bimorph beam forced vibrations problem." *Smart Materials and Structures*, **18**(8), 08501296.
- Milazzo, A. (2012). “An equivalent single-layer model for magneto-electro-elastic multilayered plate dynamics”. *Composite Structures*, **94**(6), 2078-2086.
- Milazzo, A. (2013). “A one-dimensional model for dynamic analysis of generally layered magneto-electro-elastic beams”. *Journal of Sound and Vibration*, **332**(2), 465-483.
- Milazzo, A. (2014). “Large deflection of magneto-electro-elastic laminated plates.” *Applied Mathematical Modelling*, **38**(5), 1737–1752.
- Mohammadimehr, M., Okhravi, S.V. and Akhavan Alavi, S.M. (2018). “Free vibration analysis of magneto-electro-elastic cylindrical composite panel reinforced by various distributions of CNTs with considering open and closed circuits boundary conditions based on FSDT”. *Journal of Vibration and Control*, **24**(8),1551-1569.
- Mohazzab, A.H. and Dozio, L. (2015). “A spectral collocation solution for in-plane eigenvalue analysis of skew plates”. *International Journal of Mechanical Sciences*, **94**, 199-210.
- Moita, J.M.S., Soares, C.M.M. and Soares, C.A.M. (2009). “Analyses of magneto-electro-elastic plates using a higher order finite element model”. *Composite Structures*, **91**(4), 421-426.

Moshtagh, E., Pan, E. and Eskandari-Ghadi. M. (2018). "Shear excitation of a multilayered magneto-electro-elastic half-space considering a vast frequency content". *International Journal of Engineering Science*, **123**, 214-235.

Naghsh, A. and Azhari, M. (2015). "Non-linear free vibration analysis of point supported laminated composite skew plates". *International Journal Non-Linear Mechanics*, **76**, 64-76.

Nair, P. S. and Durvasula, S. (1973). "Vibration of Skew Plates". *Journal of Sound and Vibration*, **26**, 1-19.

Nan, C.W. (1994). "Magnetoelectric effect in composites of piezoelectric and piezomagnetic phases". *Physical Review B*, **50**(9), 6082.

Nan, C. W., Bichurin, M. I., Dong, S., Viehland, D., and Srinivasan, G. (2008). "Multiferroic magnetoelectric composites: Historical perspective, status, and future directions." *Journal of Applied Physics*, **103**(3).

Narendar, S. (2016). "Wave dispersion in functionally graded magneto-electro-elastic nonlocal rod". *Aerospace Science and Technology*, **51**, 42-51.

Pan, E. (2001). "Exact solution for simply supported and multilayered magneto-electro-elastic plates". *Journal of Applied Mechanics*, **68**(4), 608-618.

Pan, E. and P. R. Heyliger. (2002), "Free vibrations of simply supported and multilayered magneto-electro-elastic plates." *Journal of Sound and Vibration*, **252**(3), 429-442.

Pan, E. and Heyliger, P.R. (2003). "Exact solutions for magneto-electro-elastic laminates in cylindrical bending". *International Journal of Solids and Structures*, **40**(24), 6859-6876.

Pan, E. and Han, F. (2005). "Exact solution for functionally graded and layered magneto-electro-elastic plates". *International Journal of Engineering Science*, **43**(3), 321-339.

Panda, S. and Ray, M.C. (2008). "Active constrained layer damping of geometrically nonlinear vibrations of functionally graded plates using piezoelectric fiber-reinforced composites". *Smart Materials and Structures*, **17**(2), 025012.

- Panda, S. and Ray, M.C. (2009). "Active control of geometrically nonlinear vibrations of functionally graded laminated composite plates using piezoelectric fiber reinforced composites". *Journal of Sound and Vibration*, **325**(1), 186-205.
- Parida, S. and Mohanty, S.C. (2017). "Thermoelastic vibration analysis of functionally graded skew plate using nonlinear finite element method. *Journal of Thermal Stresses*". **40**(9), 1111-1133.
- Parida, S. and Mohanty, S.C. (2018). "Free Vibration Analysis of Functionally Graded Skew Plate in Thermal Environment Using Higher Order Theory". *International Journal of Applied Mechanics*, **10**(01), 1850007.
- Peng, X., Yan, M., Shi, W. (2007). "A new approach for the preparation of functionally graded materials via slip casting in a gradient magnetic field". *Scripta Materialia*, **56**(10), 907-909.
- Phoenix, S.S., Satsangi, S.K. and Singh, B.N. (2009). "Layer-wise modelling of magneto-electro-elastic plates". *Journal of Sound and Vibration*, **324**(3-5), 798-815.
- R**amirez, F., Heyliger, P.R. and Pan, E. (2006a). "Free vibration response of two-dimensional magneto-electro-elastic laminated plates". *Journal of Sound and Vibration*, **292**(3), 626-644.
- Ramirez, F., Heyliger, P.R. and Pan, E. (2006b). "Discrete layer solution to free vibrations of functionally graded magneto-electro-elastic plates". *Mechanics of Advanced Materials and Structures*, **13**(3), 249-266.
- Rao, M.N., Schmidt, R. and Schröder, K.U. (2015). "Geometrically nonlinear static FE-simulation of multilayered magneto-electro-elastic composite structures". *Composite Structures*, **127**, 120-131.
- Ray, M.C. and Pradhan, A.K. (2008). "Performance of vertically and obliquely reinforced 1–3 piezoelectric composites for active damping of laminated composite shells". *Journal of Sound and Vibration*, **315**(4), 816-835.
- Ray, M.C. and Shivakumar, J. (2009). "Active constrained layer damping of geometrically nonlinear transient vibrations of composite plates using piezoelectric fiber-reinforced composite". *Thin-Walled Structures*, **47**(2), 178-189.

- Razavi, S. and Shooshtari, A. (2014). "Free vibration analysis of a magneto-electro-elastic doubly-curved shell resting on a Pasternak-type elastic foundation". *Smart Materials and Structures*, **23**(10), 105003.
- Razavi, S and Shooshtari, A. (2015a). "Nonlinear free vibration of magneto-electro-elastic rectangular plates." *Composite Structures*, **119**, 377–384.
- Razavi, S. and Shooshtari, A. (2015b). "Nonlinear free vibration of rectangular magneto-electro-elastic thin plates." *IJE Transact. A: Basics*, **28**(1), 136-144.
- Reddy JN (2004). *Mechanics of laminated composite plates and shells: theory and analysis*. CRC press. LLC.
- Ruan, M., Wang, Z.M. (2016). "Transverse vibrations of moving skew plates made of functionally graded material". *Journal of Vibration and Control*, **22**(16), 3504-3517.
- Schmid, H. (2008). "Some symmetry aspects of ferroics and single phase multiferroics." *Journal of Physics: Condensed Matter*, **20**(43).
- Schmid, H. (1994). "Multi-ferroic magnetoelectrics." *Ferroelectrics*, **162**(1), 317-38.
- Setoodeh, A.R. and Shojaee, M. (2016). "Application of TW-DQ method to nonlinear free vibration analysis of FG carbon nanotube-reinforced composite quadrilateral plates". *Thin-Walled Structures*, **108**, 1-11.
- Shahverdi, H., Barati, M.R. (2017). "Vibration analysis of porous functionally graded nanoplates". *International Journal of Engineering Sciences*, **120**, 82-99.
- Shafiei, N., Mirjavadi, S.S., MohaselAfshari, B., Rabby, S., Kazemi, M. (2017). "Vibration of two-dimensional imperfect functionally graded (2D-FG) porous nano-/micro-beams". *Computer Methods in Applied Mechanics and Engineering*, **322**, 615-632.
- Shenas, A.G., Malekzadeh, P. (2016). "Free vibration of functionally graded quadrilateral microplates in thermal environment". *Thin-Walled Structures*, **106**, 294-315.
- Shojaee, M., Setoodeh, A.R. and Malekzadeh, P. (2017). "Vibration of functionally graded CNTs-reinforced skewed cylindrical panels using a transformed differential quadrature method". *Acta Mechanica*, **228**(7), 2691-2711.
- Shooshtari, A. and Razavi, S. (2015). "Nonlinear vibration analysis of rectangular magneto-electro-elastic thin plates". *IJE transactions A: Basics*, **28**(1), 139-147.

Shooshtari, A. and Razavi, S. (2017). “Vibration of a multiphase magneto-electro-elastic simply supported rectangular plate subjected to harmonic forces”. *Journal of Intelligent Material Systems and Structures*, **28**(4), 451-467.

Singha, M. K., and Daripa, R. (2007). “Nonlinear vibration of symmetrically laminated composite skew plates by finite element method.” *International Journal Non-Linear Mechanics*, **42**(9), 1144–1152.

Seifried, S., Winterer, M., Hahn, H. (2001). “Nanocrystalline gradient films through chemical vapor synthesis”. *Scripta Materialia*, **44**(8), 2165-2168.

Suchtelen, J. (1972). “Product properties: a new application of composite materials.” *Philips Research Report*, **27**, 28.

Song, C., Xu, Z., Li, J. (2007). ”Structure of in situ Al/Si functionally graded materials by electromagnetic separation method”. *Materials and Design*, **28**(3), 1012-1015.

Thang, P.T., Nguyen-Thoi, T., Lee, D., Kang, J. and Lee, J. (2018). “Elastic buckling and free vibration analyses of porous-cellular plates with uniform and non-uniform porosity distributions”. *Aerospace Science and Technology*, **79**, 278-287.

Tsai, Y.H. and Wu, C.P. (2008). “Dynamic responses of functionally graded magneto-electro-elastic shells with open-circuit surface conditions”. *International Journal of Engineering Science*, **46**(9), 843-857.

Upadhyay, A. K. and Shukla, K. K. (2012). “Large deformation flexural behavior of laminated composite skew plates: an analytical approach”. *Composite Structures*, **94**, 3722-3735.

Vinyas, M. and Kattimani, S.C. (2017a). “Hygrothermal analysis of magneto-electro-elastic plate using 3D finite element analysis”. *Composite Structures*, **180**, 617-637.

Vinyas, M. and Kattimani, S.C. (2017b). “Static analysis of stepped functionally graded magneto-electro-elastic plates in thermal environment: A finite element study”. *Composite Structures*, **178**, 63-86.

- Vinyas, M. and Kattimani, S.C. (2017c). “Static behavior of thermally loaded multilayered Magneto-Electro-Elastic beam”. *Structural Engineering and Mechanics*, **63**(4), 481-495.
- Vinyas, M. and Kattimani, S.C. (2017d).” A Finite element based assessment of static behavior of multiphase magneto-electro-elastic beams under different thermal loading”. *Structural Engineering and Mechanics*, **62**(5), 519-535.
- Vinyas, M. and Kattimani, S.C. (2017e). “Static studies of stepped functionally graded magneto-electro-elastic beam subjected to different thermal loads”. *Composite Structures*, **163**, 216-237.
- Vuksanović, D. (2006). “Linear analysis of laminated composite plates using single layer higher-order discrete models.” *Composite Structures*, **48**, 205-211.
- Wang, J., Chen, L. and Fang, S. (2003). “State vector approach to analysis of multilayered magneto-electro-elastic plates”. *International Journal of Solids and Structures*, **40**(7), 1669-1680.
- Wang, J., Qu, L. and Qian, F. (2010). “State vector approach of free-vibration analysis of magneto–electro-elastic hybrid laminated plates”. *Composite structures*, **92**(6), 1318-1324.
- Wang, R., Han, Q. and Pan, E. (2010). “An analytical solution for a multilayered magneto-electro-elastic circular plate under simply supported lateral boundary conditions”. *Smart materials and Structures*, **19**(6), 065025.
- Wang, S. (1997). “Buckling analysis of skew fibre-reinforced composite laminates based on first-order shear deformation plate theory.” *Composite Structures*, **37**(1), 5-19.
- Wang, J. and Zhao, J. (2017). “Investigating the effect of SPRM on mechanical strength and thermal conductivity of highly porous alumina ceramics”. *Ceramics International*, **43**(18), 16430-16435.
- Wankhade, R. L. (2011). “Geometric nonlinear analysis of skew plates using finite element method”. *International Journal of Advanced Engineering Technology*, **2**, 154-163.

- Watanabe, Y., Eryu, H., Matsuura, K. (2001). "Evaluation of three-dimensional orientation of Al₃Ti platelet in Al-based functionally graded materials fabricated by a centrifugal casting technique". *Acta Materialia*, **49**(5), 775-783.
- Wattanasakulpong, N., Prusty, B.G., Kelly, D.W., Hoffman, M. (2012). "Free vibration analysis of layered functionally graded beams with experimental validation". *Materials and Design*, **36**, 182-190.
- Watts, G., Pradyumna, S. and Singha, M.K. (2018). "Free vibration analysis of non-rectangular plates in contact with bounded fluid using element free Galerkin method". *Ocean Engineering*, **160**, 438-448.
- Wu, C.P., Chen, S.J. and Chiu, K.H. (2010). "Three-dimensional static behavior of functionally graded magneto-electro-elastic plates using the modified Pagano method". *Mechanics Research Communications*, **37**(1), 54-60.
- Wu, C., Li, Y., Cheng, X. and Xie, S. (2018). "Microstructural evolution and oxidation behavior of TiB₂/SiC/B₄C composite fabricated by reactive spark plasma sintering". *Journal of Alloys and Compounds*, **765**, 158-165.
- Xue, Y., Jin, G., Ding, H. and Chen, M. (2018). "Free vibration analysis of in-plane functionally graded plates using a refined plate theory and isogeometric approach". *Composite Structures*, **192**, 193-205.
- Xu, X.J., Deng, Z.C., Zhang, K. and Meng, J.M. (2016). "Surface effects on the bending, buckling and free vibration analysis of magneto-electro-elastic beams". *Acta Mechanica*, **227**(6), 1557-1573.
- Yuan, G. L., Or, S. W., Liu, J. M. and Liu, Z. G. (2006). "Structural transformation and ferroelectromagnetic behavior in single-phase Bi_{1-x}Nd_xFeO₃ multiferroic ceramics." *Applied Physics Letters*, **89**(5).
- Yu, J. and Wu, B. (2009). "Circumferential wave in magneto-electro-elastic functionally graded cylindrical curved plates". *European Journal of Mechanics-A/Solids*, **28**(3), 560-568.

- Yu, H., Wu, L. and Li, H., (2014). “A domain-independent interaction integral for magneto-electro-elastic materials”. *International Journal of Solids and Structures*, **51**(2), 336-351.
- Zhao, X., Li, X.Y. and Li, Y.H. (2017). “Axisymmetric analytical solutions for a heterogeneous multi-ferroic circular plate subjected to electric loading”. *Mechanics of Advanced Materials and Structures*, 1-10.
- Zhang, R., Duan, Y., Or, S. W. and Zhao, Y. (2014). “Smart elasto-magneto-electric (EME) sensors for stress monitoring of steel cables: design theory and experimental validation.” *Sensors* (Basel), **14**(8), 13644–13660.
- Zheng, M., He, C., Lu, Y. and Wu, B., (2018). “State-vector formalism and the Legendre polynomial solution for modelling guided waves in anisotropic plates”. *Journal of Sound and Vibration*, **412**, 372-388.
- Zenkour, A.M. (2018). “A quasi-3D refined theory for functionally graded single-layered and sandwich plates with porosities”. *Composite Structures*, **201**, 38-48.
- Zheng, H., Wang, J., Lofland, S. E., Ma, Z., Mohaddes-Ardabili, L. and Zhao, T. (2004). “Multiferroic BaTiO₃- CoFe₂O₄ nanostructures.” *Science*, **303**(5658), 661-3.
- Zhong, Z. and Shang, E.T. (2005). “Exact analysis of simply supported functionally graded piezothermoelectric plates”. *Journal of Intelligent Material Systems and Structures*, **16**(7-8), 643-651.
- Zhong, Y., Qin, W., Yu, W., Zhou, X. and Jiao, L. (2015). “Variational asymptotic homogenization of magneto-electro-elastic materials with coated fibers”. *Composite Structures*, **133**, 300-311.
- Zhou, Y. and Zhu, J. (2016). “Vibration and bending analysis of multiferroic rectangular plates using third-order shear deformation theory”. *Composite Structures*, **153**, 712-723.
- Zhu, J., Lai, Z., Yin, Z., Jeon, J., Lee, S. (2001). “Fabrication of ZrO₂-NiCr functionally graded material by powder metallurgy”. *Material Chemistry and Physics*, **68**(1), 130-135.

List of Publications based on PhD Research Work

Sl. No.	Title of the paper	Authors (In the same order as in the paper, underline research scholar's name)	Name of the Journal/ Conference/ Symposium Vol. No. Pages	Month & Year of Publication	Category *
1	Buckling characteristics and static studies of multilayered magneto-electro-elastic plate	<u>Kiran M. C.</u> and S. C. Kattimani	Structural Engineering Mechanics	September 2017	1
2	Buckling analysis of skew magneto-electro-elastic plates under in-plane loading	<u>Kiran M. C.</u> and S. C. Kattimani	Journal of Intelligent Material Systems and Structures	January 2018	1
3	Porosity influence on structural behaviour of skew functionally graded magneto-electro-elastic plate	<u>Kiran M. C.</u> , S. C. Kattimani and Vinyas M.	Composite Structures	February 2018	1
4	Free vibration and static analysis of functionally graded skew magneto-electro-elastic plate	<u>Kiran M. C.</u> and S. C. Kattimani	Smart Structures Systems	February 2018	1
5	Assessment of porosity influence on vibration and static behaviour of functionally graded magneto-electro-elastic plate: A finite element study	<u>Kiran M. C.</u> and S. C. Kattimani	European Journal of Mechanics / A Solids	April 2018	1
6	Assessment of vibrational frequencies and static characteristics of multilayered skew magneto-electro-elastic plates: A finite element study	<u>Kiran M. C.</u> and S. C. Kattimani	Iranian Journal of Science and Technology: Transactions of mechanical engineering	September 2018	1
7	Free vibration of multilayered magneto-electro-elastic plates with skewed edges using layerwise shear deformation theory	<u>Kiran M. C.</u> and S. C. Kattimani	International Conference on Smart Engineering Materials [ICSEM-2016], RVCE, Bangalore	November 2016	3

BIO-DATA

Name	Kiran M. C.
Father's Name	Chidananda Murthy
Bate of Birth	June 20, 1989
Nationality	Indian
Permanent address	#51, First Stage, First Main, Dr. R. M. L. Nagar, Shivamogga- 577205
Mobile Number	+91-9740912342
Email Id	20.kiranmc@gmail.com

Educational Qualification:

Qualification	University	College	Period	Performance
Ph.D.	National Institute of Technology Karnataka	National Institute of Technology Karnataka	2015-2018	7.77
M.Tech. in Machine Design	Visvesvariah Technological University	STJIT, Ranebennur	2011-2013	75.43%
B. E., Mechanical	Visvesvariah Technological University	JNNCE, Shivamogga	2007-2011	63.2%

I declare that the above information is true and correct to the best of my knowledge

(KIRAN M. C.)